Design of a Single-Particle Detection System for Strong-Field QED Experiments

Dissertation

zur Erlangung des akademischen Grades

doctor rerum naturalium (Dr. rer. nat.)

seit 1558

vorgelegt dem Rat der Physikalisch-Astronomischen
Fakultät der Friedrich-Schiller-Universität Jena

von **Felipe Cezar Salgado**, M. Sc.
geboren am 13.04.1991 in Pindamonhangaba, Brasilien

Gutachter

1. Prof. Dr. Matt Zepf
   Institut für Optik und Quantenelektronik
   Friedrich-Schiller-Universität Jena

2. Prof. Dr. Peter Norreys
   Department of Physics
   University of Oxford

3. Prof. Dr. Brendan Dromey
   Centre for Light Matter Interactions
   Queen's University Belfast

Tag der Disputation: 26. 01. 2023

Abstract

One of the most intriguing physics processes that remain untested is the pure photon electron-positron pair production via quantum-vacuum fluctuations described by the nonlinear Breit-Wheeler theory. These fluctuations generate virtual pairs that can be turned into observable particles by applying strong electric fields above the Schwinger critical limit of 1.3×10^{18} V/m [1, 2]. Despite the advent of high-intense lasers, the critical limit is still far beyond achievable. However, such fields can be achieved on the rest frame of the real particles after the collision of a high-energy γ-ray photons with the laser beam.

To diagnose the created pairs, this thesis describes the design of a particle detection system capable of successfully probing the single leptons created from strong-field quantum electrodynamics (SF-QED) interactions at the upcoming SF-QED experiments E-320 at FACET-II and FOR2783 at CALA. The designed detection system is composed of tracking layers made of LYSO:Ce scintillating screens and a Cherenkov calorimeter that, having their signals combined, can identify a positive event with a confidence level above 99%.

At the E-320 experiment, electron beams generated by the FACET-II linear accelerator with an energy of 13 GeV collide with an intense laser beam of $a_0 \approx 10$, and nonlinear Breit-Wheeler pairs are produced in the nonperturbative full quantum regime of SF-QED interaction ($\chi_e > 1$ and $a_0 > 1$). About 100 electron-positron pairs per shot are expected to be created. According to Monte-Carlo simulations of the experimental layout, the detection system will be placed on a region permeated by a shower of x-rays and few-MeV γ-photons, however, a signal-to-noise ratio of $\text{SNR}_\sigma \approx 18$ on the detectors is achieved.

On the other hand, the FOR2783 experiment is designed to probe the pair-creation process via the nonlinear Breit-Wheeler process for the first time at the ATLAS laser at the Centre of Advanced Laser Applications (CALA). In this experiment, laser-accelerated electron beams with an energy of 2.5 GeV and charge of 10 pC interact with a converter foil to produce bremsstrahlung γ-photons which interact with a laser beam with an intensity of $a_0 \approx 66$. With such experimental conditions, electron-positron pairs are produced in the non-perturbative, quasi-static strong-field regime where $a_0 \gg 1$ and $\chi_\gamma \geqslant 1$, and, a pair yield of about 0.22 pairs per laser shot (≈ 80 pairs/hour) is expected. Monte-Carlo simulations of the full experimental layout foresee a signal-to-noise ratio above 10 on the detectors.

This successfully demonstrates that the detector system designed and built within the scope of this thesis is capable of detecting single particles generated in the non-linear Breit-Wheeler process in a high background noise environment.

Zusammenfassung

Einer der faszinierendsten physikalischen Prozesse, der bis jetzt noch nicht experimentell beobachtet wurde, ist die Erzeugung von Elektronen-Positronen-Paaren durch Vakuumfluktuationen, die durch die nichtlineare Breit-Wheeler-Theorie beschrieben wird. Diese Fluktuationen erzeugen virtuelle Paare, die durch das Anlegen eines starken elektrischen Feldes getrennt und somit detektiert werden können. Dabei muss das elektrische Feld das kritische Schwingerlimit von 1.3×10^{18} V/m [1, 2] übersteigen, das trotz der Entwicklung leistungsstarker Hochintensitätslaser im Laborsytem immer noch jenseits des Erreichbaren liegt. Im Ruhesystem der durch hochenergetische γ-Photonen aus dem Vakuum erzeugten Elektronen-Positronen-Paare kann das Schwingerlimit jedoch mit gegenwärtig zur Verfügung stehender Hochintensitäts-Lasersysteme erreicht werden.

Diese Arbeit beschreibt die Entwicklung eines Systems zur Teilchendetektion, das in der Lage ist einzelne Leptonen erfolgreich zu messen, die durch Starkfeld-Quantenelektrodynamik (SF-QED)-Wechselwirkungen in den bevorstehenden Experimenten E-320 an FACET-II und FOR2783 an CALA erzeugt werden sollen. Das in dieser Arbeit entwickelte Detektorsystem besteht dabei aus mehreren LYSO:Ce-Szintillatoren zur Nachverfolgung der Trajektorien der einzelnen Teilchen sowie eines Cherenkov-Kalorimeters zur Messung derer Energien. Durch die Kombination beider Messmethoden kann dieses System somit ein positives Ereignis, das heißt, ein erfolgreich erzeugtes Elektronen-Positronen-Paar, mit einem Konfidenzniveau über 99% detektieren.

Beim E-320 Experiment stoßen Elektronen, die vom Linearbeschleuniger FACET-II erzeugt werden mit einer Energie von 13 GeV mit einem intensiven Laserstrahl mit $a_0 \approx 10$. Dadurch werden nichtlineare Breit-Wheeler-Paare im nichtperturbativen vollen Quantenregime der SF-QED-Interaktion erzeugt ($\chi_e > 1$ und $a_0 > 1$). Pro Schuss wird dabei voraussichtlich eine Ausbeute von 100 Elektronen-Positronen-Paaren erzielt werden. Mithilfe von Monte-Carlo-Simulationen wurde der gesamte experimentelle Aufbau modelliert und die Stärke des Hintergrundsignals am Detektor abgeschätzt. Dieses besteht aus Röntgen-Photonen und MeV-γ-Photonen und ergibt ein Signal-Rausch-Verhältnis von $\mathrm{SNR}_\sigma \approx 18$ am Detektor.

Das FOR2783-Experiment ist dafür konzipiert, die Paarerzeugung durch den nichtlinearen Breit-Wheeler-Prozess zum ersten mal am ATLAS Laser am CALA zu messen. Hier werden lasererzeugte Elektronen mit einer Energie von 2.5 GeV und 10 pC Ladung

genutzt um mit Hilfe einer Konverterfolie Bremsstrahlungs-γ-Photonen zu erzeugen, die wiederum mit einem Laserpuls mit einer Intensität von $a_0 \approx 66$ interagieren. Mit diesen experimentellen Parametern werden Paare im nichtperturbativen quasistatischen Starkfeld-Regime ($a_0 \gg 1$ und $\chi_\gamma \geqslant 1$) erzeugt und eine Paarausbeute von circa 0.22 Paaren pro Laserschuss (≈ 80 Paare/Stunde) erwartet. Hier ergeben Monte-Carlo-Simulationen des gesamten Experimentes ein Signal-Rausch-Verhältnis von größer 10 auf den Detektoren.

Dies zeigt erfolgreich, dass das im Rahmen dieser Arbeit entworfene und gebaute Detektorsystem in der Lage ist, einzelne Partikel, die im nichtlinearen Breit-Wheeler-Prozess erzeugt werden, in einer Umgebung mit hohem Hintergrundrauschen zu detektieren.

Contents

1. Introduction

Testing the response of physical systems at extreme conditions has historically proven to be one of the most productive avenues to extend our understanding of physics and the accuracy of existing theories. Examples are high energy physics with its extreme particle energies and at the other extreme superconductivity and Bose-Einstein condensates at near zero temperature.

The recent advent of high-intensity laser fields in the next generation of laser facilities, such as CALA [3], ELI [4, 5], Apollon [6], and Corels [7], provides the most powerful electromagnetic fields with intensities up to 10^{23} W/cm^2 in the laboratory [8], corresponding to field strengths of approximately 10^{15} V/m. The strong electromagnetic fields (EM) generated by such powerful laser sources has fundamental phenomena of vacuum quantum electrodynamics (QED) and the largely unexplored regime of strong field QED experimentally accessible.

The relation between the regime of strong field QED and other physics regimes can be visualized using the so-called cube of theories introduced by Ref. [9] and illustrated in figure 1.1. The cube of theories shows the relation between the different physical theories of special relativity, quantum mechanics, and high-intensity fields with its extremes representing theories subjected to tests. The cube is located in a space defined by three orthogonal axes corresponding to special relativity c, quantum mechanics $\hbar$ and EM fields a_0. Each of the vertices of the cube is related to physical parameters and theoretical descriptions, for example, classical mechanics is found at the vertex (0, 0, 0), relativity and high energy physics is represented at the vertex (c, 0, 0), and quantum mechanics is located at (0, $\hbar$, 0) . The cube also represents the theories that unifies two or more effects, such as classical electrodynamics at the vertex (c, 0, a_0), atomic, molecular, and optical physics at vertex (0, $\hbar$, a_0), and quantum field theory at the vertex (c, $\hbar$, 0). Note that, if high-intensity fields are added in the quantum field theory, a physical regime known as strong-field quantum electrodynamics (SF-QED) is located at vertex (c, $\hbar$, a_0). Designing experiments to test physics in this extreme regime is the aim of the work presented in this thesis.

The variable a_0 represents the normalized amplitude of the electromagnetic field and describes the interaction between a charged particle with the EM field. The value
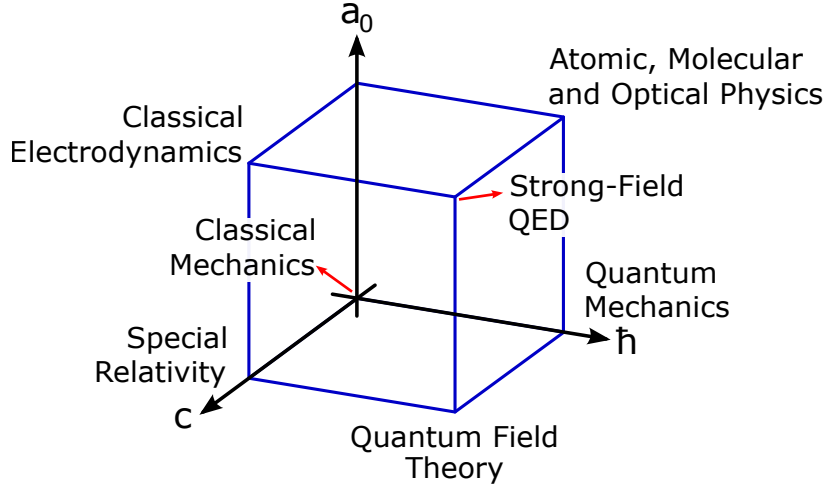
Figure 1.1.: Cube of theories adapted from Ref. [9]. The cube is located along the axes representing special relativity c, quantum mechanics $\hbar$ and high-intensity fields a_0. Each vertex of the cube represents a physical theory: $(0, 0, 0)$ is classical mechanics, $(c, 0, 0)$ is special relativity, $(0, \hbar, 0)$ is quantum mechanics, $(c, 0, a_0)$ is classical electrodynamics, $(0, \hbar, a_0)$ is atomic, molecular, and optical physics, $(c, \hbar, 0)$ is quantum field theory, and finally, $(c, \hbar, a_0)$ represents the strong-field quantum electrodynamics (SF-QED) where phenomena that cannot be described by neither classical or perturbative quantum theories are found.

of a_0 is given, in SI units, as

$$a_0 = \frac{e\,\mathrm{E}}{m_e\,c\,\omega_0} = \frac{e\,\mathrm{E}\,\lambda_0}{2\pi\,m_e\,c^2}\,, \tag{1.1}$$

where e is the charge of the electron, E is the electric field amplitude, ω_0 and λ_0 stand for the angular frequency and wavelength of the laser light, respectively, c is the speed of light in vacuum, and m_e is the rest mass of the electron. The a_0 parameter can be interpreted as the energy gain of an electron over a distance of one EM field wavelength in units of the rest mass $m_e\,c^2$, i.e., $\Delta\mathcal{E} = e\,\mathrm{E}\,\lambda_0 \approx a_0\,m_e\,c^2$. Hence, at $a_0 = 1$, relativistic effects become significant in the interaction between the charged particle and the EM field. In equation (1.1), one can substitute the the laser wavelength by the Compton wavelength, $\lambda_0 \longrightarrow \lambdabar_c = h/(2\pi\,m_e c) = 3.861 \times 10^{-13}\,\mathrm{m}$, where $h = 6.626 \times 10^{-34}\,\mathrm{m^2\,kg\,s^{-1}}$ is known as Planck constant. Consequently, one can obtain from equation (1.1) the electromagnetic field strength capable of performing a work of $m_e\,c^2$ over a Compton wavelength such that $e\,\mathrm{E_c}\,\lambdabar_c = m_e\,c^2$ [9]. Therefore, the

field strength required to perform the such work is given as

$$E_c = \frac{m_e^2 c^3}{e\,\hbar} \approx 1.32 \times 10^{16}\,\mathrm{V\,cm^{-1}}\,, \tag{1.2}$$

where $\hbar = h/(2\pi)$ is the reduced Planck constant. Hence, electric fields E with the same order of magnitude of E_c, which is also known as the Schwinger critical field, enables the study of novel physical processes found at the strong-field QED vertex of the cube of theories.

As the field strength increases towards E_c, the strong-field leads to significant non-linearities in the optical properties of vacuum. These nonlinearities can be dispersive, e.g., vacuum birefringence, or absorptive, where the background field induces the tunneling of electron-positron pairs out of the quantum vacuum - process known as the Schwinger pair production, which is discussed in detail in section 2.3.3.

Although the peak intensity lasers can reach have significantly increased due to the Chirped pulse amplification (CPA) technique to values up to 10^{23} W/cm^2, it is still orders of magnitude below the intensity given by the critical field of about 10^{29} W/cm^2. Therefore, a solution to achieve stronger EM fields is to collide the intense laser field with high energy γ-rays or relativistic electron beams of Lorentz-factor $\gamma \gg 1$ with a collision angle θ between them. Such collision geometry is illustrated in figure 1.2. In the electron's rest frame, the relativistic particle will "see" an electric field Lorentz-boosted by $E_* = \gamma\,E\,(1-\cos\theta)$ which can reach the magnitude of the Schwinger critical field for realistic parameter sets, thus making strong-field phenomena accessible in the laboratory. For example, assume a laser beam of intensity of 10^{21} W/cm^2, which corresponds to an electric field of approximately 10^{14} V/m, colliding with an 2.5 GeV electron beam ($\gamma \approx 4892$) at an angle $\theta = 180°$ (head-on collision). The Lorentz-boosted electric field seen by the electron beam at its rest frame is $E_* \approx 10^{18}$ V/m which is at the same order of magnitude of the Schwinger critical field E_c.
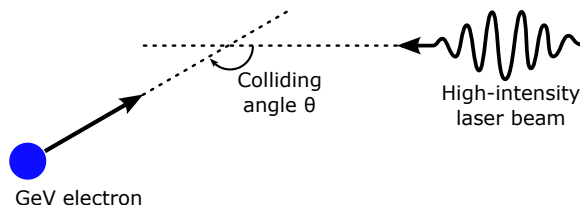
Figure 1.2.: Collision geometry between an ultra-relativistic electron with a high-intensity laser beam. The collision angle between them is given by θ. For head-on collisions, $\theta = 180°$.

Investigating the interaction between strong-fields and particles is relevant to un-

derstand astrophysical phenomena that were before not accessible, for example, the electron-positron pair creation close to black holes' event horizon [10–12], pair production at the surface of magnetars [13–15], and the absorption of high-energy photons as they propagate in the universe [16]. However, one of the many challenges while realizing strong-field quantum electrodynamics (SF-QED) experiments under laboratory conditions is to detect the electron-positron pairs created during the processes in an environment permeated by intense background radiation. Therefore, in this thesis, a single-particle detection system with superior performance and capable of substantially rejecting background radiation is designed and calibrated for being used in the upcoming SF-QED experiments.

In this introductory chapter, the history of quantum electrodynamics (QED) and how strong-fields were later incorporated in the QED theory are briefly explained. Further, the current experiments proposed to test the predictions of SF-QED are introduced. As already mentioned, the collision of relativistic electrons and high-intensity laser fields is required to enable strong-field QED studies. Therefore, the generation of ultra-relativistic electron beams using conventional and laser-driven plasma accelerators followed by the development of high-intensity lasers are also discussed. At the end of the chapter, an outline of the next chapters of this thesis is given.

1.1. The Birth of Quantum Electrodynamics (QED)

It was in 1926 that Schrödinger published his theory to solve the energy states of the hydrogen atom [17]. However, the proposed theory was inconsistent with special relativity and could not be used in situations where the particles were traveling close to the speed of light or if interactions between them occur. Two years later, in 1928, Paul Dirac proposed a new equation that incorporates the interaction between particles and special relativity while searching for methods to calculate the spontaneous radiation emission rate of atoms when undergoing a transition from a higher to lower excitation states [18]. The equation also introduced the idea of creation and annihilation of particles that allowed Dirac to find solutions for his new equation corresponding to electrons with negative energies at empty spaces. This new set of solutions introduced the concept of the Dirac sea with the vacuum being considered as a state where all negative energy particles are located. If a hole is found in the negative energy state of the quantum vacuum, it corresponds to an electromagnetic field that behaves as if it were a positively charged particle. A hole in the sea is found to have the same mass as an electron and therefore was initially called anti-electron. However, in 1932,

Carl Anderson, while performing experiments to investigate cosmic rays, observed unexpected tracks of particles which later were attributed to anti-electrons, or, the term he coined, positrons [19, 20].

The Dirac sea allowed electron and positron pair creation and annihilation by radiation without introducing concepts of field quantization, later known as quantum field theory (QFT). But years later, Furry and Oppenheimer demonstrated that when quantizing the radiation field in Dirac's equation, the creation, and annihilation of particle and anti-particles are naturally incorporated in the theory [21, 22]. Introducing QFT into the relativistic quantum theory of Dirac, charged particles could interact between them by continuously exchanging radiation, namely photons, considered as virtual particles. These new type of particles cannot be directly observed otherwise the energy conservation law would be violated, but their effect is visible in many observables.

Also in 1934, Gregory Breit and John Wheeler calculated the electron-positron creation from the collision of 2 photons which creates a hole and an electron in the Dirac sea [23]. Such process is considered the inverse of the electron-positron annihilation of the Dirac sea and is named the Breit-Wheeler process. Experiments have been proposed to investigate the pair creation through the Breit-Wheeler process [24, 25], however, no successful results have been reported so far.

Up to now, quantum field theory has successfully incorporated the creation and annihilation of matter and anti-matter. However, a major problem has already been reported during its development in yearly 1930 by Oppenheimer while he calculated the effect of quantum electromagnetic fields on the energy levels of atomic electron [26]. He found that is impossible to eliminate the interaction of the charge with its field and energy shifts were predicted to be infinite. The same problems with infinite energy levels were also later reported by Dancoff when calculating the scattering of electrons [27].

Different ideas on how to solve the problem of infinities were proposed by different authors [28–31], but the most accepted method was introduced by Weisskopf in 1936 [32] where the infinities were eliminated by redefining the physical parameters to compensate the effects of self-interactions. The newly proposed method was named renormalization. The first experimental evidence of the effect of the electron self-energy initially proposed by Oppenheimer was successfully realized by Lamb and Retherford in 1947 using microwaves to stimulate transitions between the hydrogen energy levels $^2S_{1/2}$ and $^2P_{1/2}$ [33]. But only a few months later a theoretical description of the effect was announced by Hans Bethe where he used non-relativistic quantum mechanics

with the mass renormalization method to calculate the self-energy correction and the hydrogen fine structure predicted by the Lamb and Retherford experiment [34].

It was in the late 1940s that three systematic formulations of QFT based on previous theoretical work were proposed. These formulations, each independently presented by Tomonaga (1946) [35], Julian Schwinger (1948) [36, 37] and Richard Feynman (1949) [38–40], provide a method of treating the infinities however, the method proposed by Feynman presented a unique set of rules that allowed to draw diagrams representing how energy and momentum could flow through intermediate states, namely through virtual particles. The rules established an easy calculation algorithm to evaluate the probability of a process to occur and automatically ensures the elimination of the infinities problem. The method proved so efficient and easy that is nowadays taught in standard QFT textbooks, e.g., Refs. [41, 42]. The three formulations were, in 1949, proved to be equivalent by Freeman Dyson [43, 44] where graphical rules similar to the ones proposed by Feynman could be achieved by the methods proposed by Tomonaga and Schwinger. The introduction of such formulations is considered a big step to establish the theory that is known as quantum electrodynamics (QED) which describes the interaction between light and matter and it is in full agreement with quantum mechanics and special relativity. The importance of such methods was recognized in 1965 by awarding the Nobel prize to Tomonga, Schwinger, and Feynman for their contributions to the mass renormalization and quantum electrodynamics.

1.2. Strong-Field Quantum Electrodynamics

Quantum electrodynamics is considered one of the most successful theory of physics [45]. It predicted the anomalous magnetic dipole moment (g-2) with high precision [46] and the fine structure constant $\alpha \approx 1/137$ [47]. However, non-perturbative features arise in the presence of strong background electromagnetic fields, and a new branch of QED is derived, known as strong-field quantum electrodynamics (SF-QED) as already introduced in the cube of theories in figure 1.1.

In the theory of strong-field QED, the electromagnetic field F_{SF-QED} is divided into two parts, a classical field F and a quantized radiation F_{rad}, such that $F_{SF-QED} = F + F_{rad}$. The quantization of the radiation leads to a definition of the vacuum state without any real particle but containing fluctuations of virtual electron-positron pairs when no external field is applied. By applying an external field, the virtual pairs form dipoles aligned in the same direction of the external field, and vacuum

anisotropy is observed. If the applied field is strong enough, above the Schwinger critical field $E_c \approx 1.32 \times 10^{18}\,\mathrm{V\,m^{-1}}$, the virtual particles acquire energies above $m_e c^2$ over a distance of the Compton wavelength $\lambda_c = h/(m_e c) = 2.426 \times 10^{-12}\,\mathrm{m}$, where $h = 6.626 \times 10^{-34}\,\mathrm{m^2\,kg\,s^{-1}}$ is the Planck constant, $m_e = 9.109 \times 10^{-31}\,\mathrm{kg}$ stands for the rest mass of an electron and c is the speed of light in vacuum. If the field strength overcomes the critical field, it deforms the Dirac sea, and a particle can tunnel from the negative to the positive continuum through the energy gap creating real particle and anti-particle pairs. This mechanism is named Schwinger pair production and it is discussed in detail in chapter 2, section 2.3.3.

Furry picture

To evaluate the interaction between the external strong background field and the particles, an interaction picture, namely Furry picture, was developed by Wendell H. Furry in 1934 [48]. This new interaction picture treats classically the applied background field, i.e., the particle-field interaction leaves the field unchanged, and results in exact solutions of the equations of motion.

The QED Lagrangian density in the Furry picture is represented by [49]

$$\mathcal{L}_{\mathrm{QED}}^{\mathrm{Furry}} = \overline{\Psi}^{\mathrm{FP}}(i\slashed{\partial} - e\slashed{A}^{\mathrm{e}} - m_e)\Psi^{\mathrm{FP}} - \frac{1}{4}F_{\mu\nu}F^{\mu\nu} - e\overline{\Psi}^{\mathrm{FP}}\slashed{A}\Psi^{\mathrm{FP}}\,, \qquad (1.3)$$

where $\slashed{A}$ is the quantized fields, i.e., the photon fields, Ψ^{FP} is the quantized fermion states, $\slashed{A}^{\mathrm{e}}$ is the external classical field, and e is the electron charge. One can obtain a similar equation to the Dirac equation for the bound states Ψ^{FP} coupled to the background field $\slashed{A}^{\mathrm{e}}$ for $\partial^2 A = 0$ [49],

$$(i\slashed{\partial} - e\slashed{A}^{\mathrm{e}} - m_e)\Psi^{\mathrm{FP}} = 0\,. \qquad (1.4)$$

Equation (1.4) was first solved exactly by Volkov by considering the external fields as plane-waves and only one propagation direction [49, 50]. However, when the external background fields are produced by a laser, they are considered as oscillatory fields and infinite plane waves, and a faithful representation of the background field is required. The best approximation up to now to solve the SF-QED problem is given by the locally constant field approximation (LCFA) [49, 51–53], but attempts to provide corrections on the approximations already have been proposed [54, 55].

Different processes can be studied by applying the SF-QED theory in particles immersed in strong-background fields, for example, nonlinear (inverse) Compton

scattering and nonlinear Breit-Wheeler pair creation [2], which are studied in detail in chapter 2.

Important Parameters in Strong-Field QED Theory

Two important parameters in SF-QED theory are the quantum nonlinearity parameter of a electron χ_e or χ_γ for a high-energy photon, where the particles are immersed in a background field [2]. Assume the collision of a particle with a laser beam forming a collision angle θ between them as already seen in figure 1.2. In the co-moving frame (COM) of the electron, the particle "sees" a boosted electric field of the laser of $\mathrm{E}_* = \gamma_e \, \mathrm{E} \, (1 - \cos\theta)$, where γ_e is the Lorentz-factor of the particle. The ratio χ_e between the boosted electric field of the laser beam and the Schwinger critical field is given as

$$\chi_e = \frac{\mathrm{E}_*}{\mathrm{E_c}} = \gamma_e \, \frac{\mathrm{E}}{\mathrm{E_c}} \, (1 - \cos\theta) = \mathrm{a}_0 \, \gamma_e \, \frac{\hbar \, \omega_o}{m_e \, c^2} (1 - \cos\theta) \,, \tag{1.5}$$

where γ_e is the Lorentz factor of the electron, $\hbar \, \omega_0$ is angular frequency of the background laser field assumed to be monochromatic with amplitude E in the laboratory frame, m_e is the rest mass of the electron, and θ is the collision angle between electron-laser beam (for head-on collision $\theta = 180°$). As the boosted laser field E_* approaches the critical field $\mathrm{E_c}$, the parameter $\chi_e \sim 1$, and the electron immersed in the strong background field starts to emit photons with significant energies relative to its kinetic energy, and radiation reaction effects on the particle must be taken into account in the particle motion [2].

Similarly, one can define the parameter χ_γ which can be interpreted as the ratio between of the boosted laser electric field in the co-moving frame of the created electron and positron from quantum vacuum $\mathrm{E}_*^\gamma = \gamma_\gamma \, \mathrm{E} \, (1 - \cos\theta)$ and the Schwinger field [2]. Hence, the definition of χ_γ is given as

$$\chi_\gamma = \frac{\mathrm{E}_*^\gamma}{\mathrm{E_c}} = \gamma_\gamma \, \frac{\mathrm{E}}{\mathrm{E_c}} \, (1 - \cos\theta) = \mathrm{a}_0 \, \frac{\hbar^2 \, \omega_0 \, \omega_\gamma}{m_e^2 \, c^4} (1 - \cos\theta) \,, \tag{1.6}$$

where $\gamma_\gamma = \hbar \, \omega_\gamma / m_e$, $\hbar \, \omega_\gamma$ is the energy of the high-energy photon, and ω_0 is the laser field frequency. Again, as the boosted laser electric field approaches the critical field, the vacuum becomes nonlinear and electron-positron can be created.

A third and useful parameter is the Lorentz invariant dimensionless amplitude of the laser field given by a_0 which have been previously introduced in equation (1.1). As discussed, the parameter a_0 can be interpreted as the energy gained by an electron

in units of its rest mass $m_e c^2$ over a wavelength when particle propagates in a linear motion,

$$\Delta\mathcal{E} = e \, \mathrm{E} \, \lambda_0 = 2\pi \, \mathrm{a}_0 \, m_e \, c^2 \, . \tag{1.7}$$

A further important interpretation of the parameter a_0 is that it corresponds to the energy absorbed by the particle over a Compton wavelength in units of the laser photon energy. This interpretation of a_0 will be discussed later in chapter 2 in the context of Compton Scattering, section 2.2.

1.3. Strong-field QED Experiments

Achieving χ_e and χ_γ above unity to access SF-QED processes, is a formidable challenge as they require both an ultra-relativistic electron beam (either for the interaction or as source of high energy photons) and an intense laser. A number of experiments have been proposed that allow ultra-relativistic electron beams to interact with high-intensity tightly focused laser beams [3, 56–63].

The Experiment-144 (E-144) at SLAC was the first SF-QED experiment combining intense laser fields and ultra-relativistic electron beams from an RF accelerator structure [57–59]. In this experiment, about 100 electron-positron pairs created through the nonlinear Breit-Wheeler process in the perturbative regime ($\chi_\mathrm{e} < 1$ and $\mathrm{a}_0 < 1$) were detected. The pair creation was achieved by colliding electron bunches with energies up to 49.1 GeV with a focused laser field with a root mean square (RMS) normalized field strength of $\mathrm{a}_0^\mathrm{RMS} = 0.3$ leading to a $\chi_\mathrm{e}^\mathrm{RMS} \approx 0.3$. The electron-laser collision produced high-energy photons through Compton scattering and these photons while still immersed in the laser field produced the electron-positron pairs by nonlinear Breit-Wheeler - a two step process in this configuration.

Experiments have also been proposed to investigate SF-QED process through the interaction of ultra-relativistic electrons in nuclear fields of crystals [64–66] or using all-optical setups to produce GeV-class electron beams through laser wakefield acceleration (LWFA) to interact them with high-intensity laser beams [60, 61, 67, 68]. The first all-optical SF-QED experiment was performed at the Astra-Gemini laser system at the Rutherford Appleton Laboratory (RAL), where electron beams up to 2 GeV interacted with intense laser pulses of $\mathrm{a}_0 = 10$, and signatures of radiation reaction in the non-perturbative moderate quantum regime were first observed ($\chi_\mathrm{e} < 1$ and $\mathrm{a}_0 > 1$) [60, 61].

Currently there are several projects internationally that aim to investigate SF-QED effects in the non-perturbative full quantum regime ($\chi_e > 1$, $\chi_\gamma > 1$, and $a_0 > 1$) through electron-laser and photon-laser interactions. The generation of the ultra-relativistic electron bunches required for the realization of these experiments can be achieved by using linear accelerators with radio-frequency (RF) cavities as proposed by the Experiment-320 (E-320) [62], and the LUXE collaboration [63], or by plasma-based accelerators in all-optical setups as planned by the project FOR2783/E3 from the Quantum Vacuum Research Unit [3]. In figure 1.3 a), the different regimes of electron-laser interactions of several experiments are highlighted. For comparison, the dependence of the parameter χ_γ on the γ-photon energy and the normalized field strength a_0 for photon-laser collision experiments is presented in figure 1.3 b). Note that to achieve $\chi_\gamma > 1$, the field strength a_0 must be higher than the field strength required to reach $\chi_e > 1$ in electron-laser collisions.

Despite the advanced technology used to produce the ultra-relativistic electron bunches required to collide with the high-intense laser beams, the number of particle pairs expected to be created by the SF-QED interactions remains small. The design of a detection system capable of detecting the few created pairs in an intense background originated by the primary electron beam and γ-rays of the experiments presents a challenge that will be further explored in this thesis.

1.4. Generation of Ultra-Relativistic Electron Beams

The first essential requirement to trigger SF-QED interaction in the laboratory is the generation of ultra-relativistic electron bunches that will collide with high-intensity laser beams. In the SF-QED experiments discussed in this thesis, relativistic electron bunches are generated either by conventional or plasma-based accelerators. Hence, in this section, these two methods of generating such relativistic electron bunches are briefly introduced.

Conventional Particle Accelerators

According to the Lorentz equation of motion, charged particles are accelerated under the influence of an external electric field potential gradient [69]. Based on this theory, a number of different approaches can be taken to accelerate particles to high energy, with the first particle accelerator demonstrated Cockcroft and Walton in 1932 [70, 71]. The Cockcroft-Walton particle accelerator used capacitor banks to generate electric
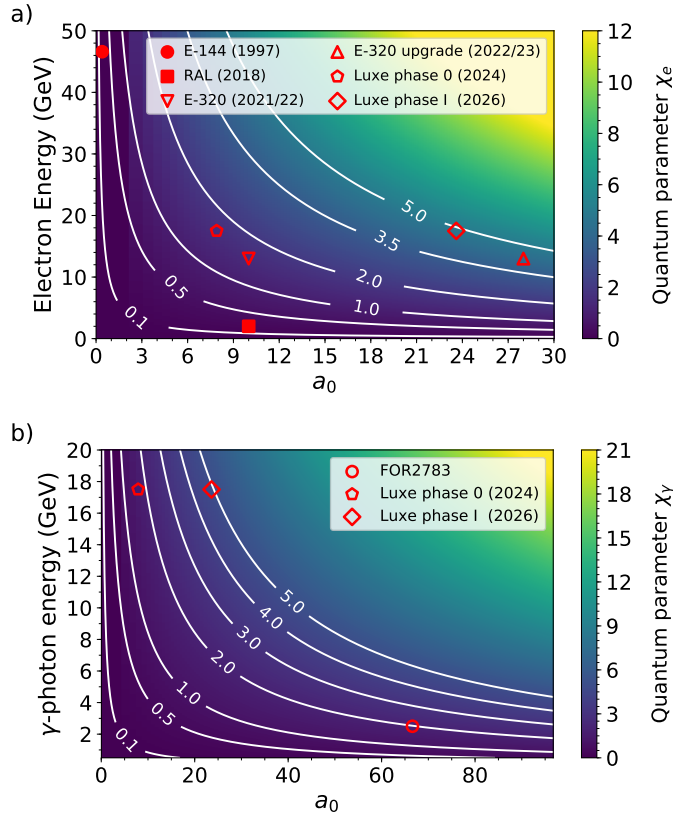
Figure 1.3.: a) Electron quantum parameter χ_e for different normalized laser strength a_0 and incoming electron energies. To date, the regime $\chi_e > 1$ is still unexplored. The filled red markers indicates the already performed experiments: (circle) Experiment-144 (E-144), 1997 [57, 59]; (square) RAL, 2018 [61]. The open markers shows the upcoming SF-QED experiments: (down-pointing triangle) Experiment-320 (E-320), 2021/2022 [62]; (up-pointing triangle) Experiment-320 upgrade, 2022/2023 [62]; (pentagon) LUXE phase 0, 2024 [63]; (diamond) LUXE phase 1, 2026 [63]. The Experiment-320 will probe the non-perturbative full quantum regime of interaction ($\chi_e > 1$ and $a_0 > 1$). b) Dependence of χ_γ on γ-ray energy and a_0 for $\lambda = 800$ nm. The nonlinear Breit-Wheeler pair-creation from pure quantum vacuum remain untested. The open circle marker indicates the FOR2783 experiment, which is designed to probe such regime with γ-photons of energy $E_\gamma = 2.5$ GeV colliding with an intense laser beam of $a_0 = 66$ ($I = 9.5 \times 10^{21}$ W/cm^2) [3]. The pentagon open marker represents the LUXE phase 0, 2024 [63], and the open diamond marker shows LUXE phase 1, 2026 [63]. Note that to achieve $\chi_\gamma > 1$ in photon-laser interactions, the field strength a_0 must be higher than the field strength required to reach $\chi_e > 1$ in electron-laser collisions.

field potential differences to accelerate Helium nuclei up to 3 MeV.

This basic approach remains in use to this current day (most prominently in Tandem Accelerators), but has been superseded for higher energy particle beams. Technological advances in the field of superconducting magnets and radio-frequency (RF) technology allowed the construction of small RF-cavities capable of generating strong fields in small spaces [72], and circular geometries for particle accelerators became accessible. In circular accelerators, also known as synchrotrons, particle beams are accelerated in closed-loop paths defined by magnets, and, due to the cyclic motion of the particles and continuous transverse acceleration, radiation from the particles is emitted. The radiation power emitted by an accelerated particle in a synchrotron is given by the well-known Larmor formula $\mathrm{P_{Larmor}} \propto \mathcal{E}^4/(m^4\,R^2)$, where $\mathcal{E}$ is the energy of the particle, m is the mass of the accelerated particle, and R represents the bend radius of the cyclic motion [69]. Thus, for the acceleration of particles to happen in a synchrotron, the rate at which the particle loses energy should be slower than the rate of energy gain through acceleration. Hence, to increase the limit that a particle can be accelerated, the emitted radiated power $\mathrm{P_{Larmor}}$ must be reduced by using heavier particles (protons or ions) or by increasing the radius of the cyclic motion.

Circular accelerators are great devices to investigate different interactions between particles through the collision of particles. For example, the Large Hadron Collider (LHC) at CERN, a circular particle accelerator with 27 km circumference, was commissioned in 2008 to mainly study the generation of mass of elementary particles by the Higgs mechanism via electroweak symmetry breaking by colliding relativistic protons and ions [73–77]. Currently, an even larger circular accelerator, the Future Circular Collider (FCC-hh) [78], with about 100 km circumference is envisioned to reach center-of-mass collision energy of 100 TeV between hadrons, an increase of 7× from the center-of-mass collision energy of 14 TeV of the LHC [see 79, page 801]. The FCC-hh is planned to investigate phenomena that the current Standard Model does not explain such as the evidence of dark matter, the mass of neutrinos, and the predominance of matter of anti-matter.

Different from hadron colliders, lepton colliders are also exciting platforms to investigate interactions between particles and their point-like interactions of fundamental particles have been the driver of experiments to develop the standard model. Lepton colliders are frequently linear accelerators and achieve smaller center-of-mass energies. For example, the Stanford Linear Collider (SLC) was designed to study the Z-boson by colliding electrons and positrons with a center-of-mass energy of about 80 GeV [80]. As the technology advances, future linear particle accelerator colliders of electrons

and positrons have also been proposed, e.g., the Compact Linear Collider (CLIC) and the International Linear Collider (ILC). Both linear accelerators are planned to be longer than the original Stanford Linear Collider by about ten times which enable center-of-mass collision energy of $> 1\,\text{TeV}$ making it possible to study, for example, the coupling between the Higgs boson with fermions and bosons through the Higgsstrahlung process, and to realize precision measurements of the top quark mass through electron-positron collisions [81–83].

Laser-driven Plasma Accelerators

The upcoming particle accelerators and colliders enables the high-energy physics community to perform particle colliding experiments with high center-of-mass energy to study physics beyond the Standard Model. However, the construction of such facilities becomes costly and large areas are required for their infrastructure. Plasma-based accelerators offer an interesting alternative compared to conventional RF-cavity accelerators to reach high-energy particles for collision at lower costs, smaller footprints, and naturally synchronized too [84].

Laser wakefield accelerators (LWFA) generates electrons by propagating high-intensity laser pulses in a plasma. The accelerating structure is formed by ponderomotive pressure which separates the electrons aside from the ions of the atoms since the ions are much heavier than the negative charges and have more inertia. If the duration of the laser pulse is short enough, the radiation pressure force ceases as the pulse propagates through the plasma, and a restoring force between the electrons and the background of heavy ions becomes responsible to accelerate back the electrons. Now, the background electrons perform an oscillatory motion with a frequency given by the plasma frequency, and a density wave travels behind the laser pulse, both at the same velocity. The density wave generates an electric field, a so called laser wakefield, which moves along with the laser pulse accelerating the electrons up to GeV energies. This plasma acceleration method is known as laser wakefield acceleration (LWFA) and was first proposed by Tajima and Dawson in 1979 [85]. The LWFA method of generating ultra-relativistic electron beam is capable of achieving electric field gradients on the order of ~ 100 GV/m in plasma with densities of 10^{18} cm^{-3} which corresponds to about three orders of magnitude higher than gradients produced by conventional RF-accelerators.

Figure 1.4 shows 2D particle-in-cell (PIC) simulations of a plasma wake driven by propagating laser pulses with different intensities a_0. As the intensity increases, the

oscillation of the plasma wake increases until electrons become trapped and accelerated as they 'surf' on the plasma wake. The white streamlines represent the motion of the electrons in the co-moving frame of the system. For detailed reference on the laser wakefield acceleration method for obtaining high-energetic electron beams, please see references [67, 86–88].

The LWFA method has been successfully used to accelerate electron beams from 100's of MeV up to few-GeV [89, 90]. However, much work is still in progress to improve the quality of the beam, i.e., injection mechanism [91], emittance [92, 93], energy spread [94].

1.5. High-intensity Lasers

The second essential requirement for enabling SF-QED processes is the generationg of high-intensity laser pulses. The advent of the chirped pulse amplification method increased the peak intensities of laser pulses exponentially from 10^{14} W/cm^2 up to $> 10^{21}$ W/cm^2 [95, 96] which is enough to reach quantum parameters χ_e and χ_γ larger than the unity and access SF-QED phenomena by interacting the high-intensity laser beam with GeV-particles.

To reach high intensities using CPA, an input pulse provided by a mode-locked laser is stretched by gratings with negative group velocity dispersion (GVD). The negative GVD promotes the higher frequencies components of the laser light to propagate longer optical paths and therefore to exit the system after the lower frequencies, which follows a shorter optical path. As result, the laser pulse is now stretched in time and positively chirped. The stretched pulse propagates through an amplification medium extracting the energy pumped and stored in the material. After exiting the medium, gratings with positive GVD matched with the previous negative group dispersion applied compress back the pulse[1], and a high-intensity pulse is obtained. The steps of the CPA method are illustrated in figure 1.5. The steps here described for the CPA method were first introduced by Donna Strickland and Gérard Mourou in 1985 [97], who were awarded the 2018 Nobel Prize recognition of the CPA method.

For the amplification to be successful, three main requirements need to be fulfilled: (i) the amplification medium should have superior energy storage, (ii) the laser pulse fluence should be large enough to efficiently extract the maximum energy stored

---

[1]A perfect matched GVD between the stretcher and compressor gratings is difficult to achieve and, as consequence, the now amplified but uncompensated GVD laser pulse presents low-intensity pedestals on its temporal contrast.
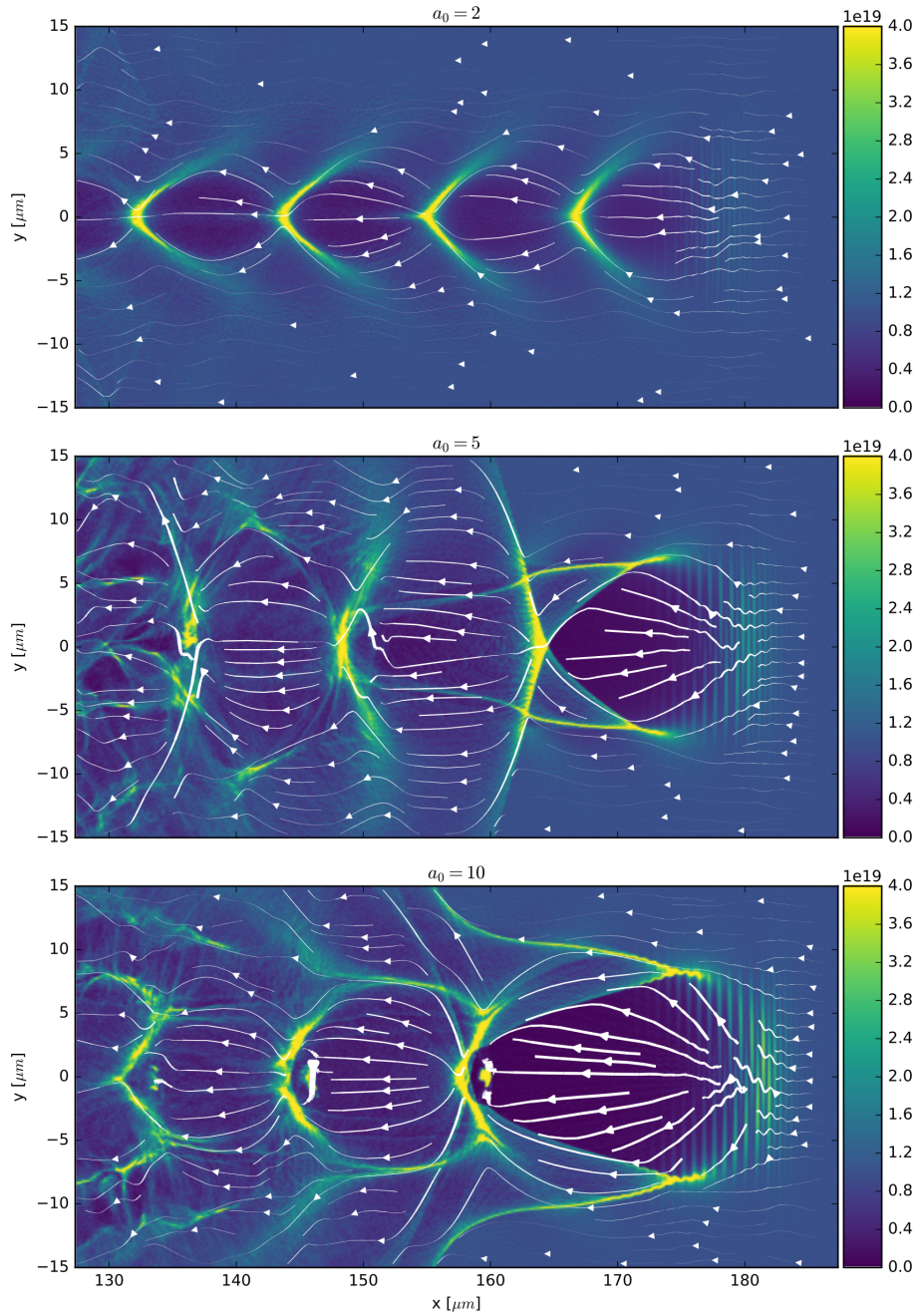
Figure 1.4.: Particle-in-cell simulations of the plasma wake driven by the propagation of a laser pulse with different intensities a_0. As the laser intensity increases from $a_0 = 2$ to $a_0 = 10$, the oscillations of the plasma wake also increase until electrons are trapped and accelerated as they were 'surfing' on the plasma wake. The white streamlines represent the motion of the electrons in the co-moving frame of the system. The image was taken from Ref. [87]. For a detailed explanation of the laser wakefield acceleration method (LWFA), please see references [67, 86, 87].

15
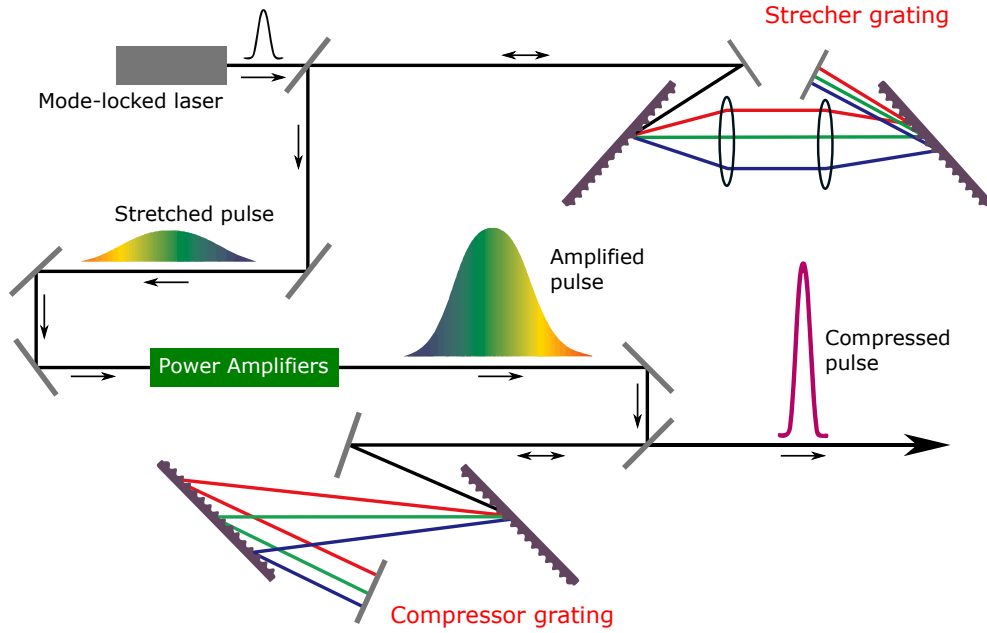
Figure 1.5.: Basic sketch of the chirp Pulse Amplification (CPA) method. A mode-locker laser generates a short duration and low energy laser pulse. The pulse is first stretched by a grating (stretcher grating) for then to propagate through a gain medium amplifier, for example, Ti:Sa crystals, where it extracts the energy stored in the material. As consequence, the energy of the stretched laser pulse is amplified. And finally, the long and energetic laser pulse is compressed back retrieving its short duration characteristic before exiting the CPA system. Image adapted from Ref. [98].

in the gain medium, and (iii) the pulse duration should be as short as possible to maximize the peak power, i.e., the gain medium bandwidth should be broad enough to accommodate the laser pulse spectrum [95, 96].

Typically, the laser systems used on the SF-QED experiments use the solid-state material Titanium-sapphire (Ti:Sa) as amplification medium due to its superior energy storage, and high damage threshold in comparison with other gain media, such as alexandrite, Nd:glass, Yb:glass [99, 100]. The high energy gain extracted from Ti:Sa medium by employing laser pulse fluences of about $1\,\mathrm{J/cm^2}$ at $800\,\mathrm{nm}$ [95, 96, 101, 102] allows reaching laser peak powers above few-petawatt which is fundamental for enabling SF-QED interactions.

In this thesis, the laser systems of the E-320 and FOR2783 experiments are based on the CPA technique and have Ti:Sa as gain medium which means that its laser pulse of duration of approximately 25 to 30 fs have a central wavelength of about 800 nm.

1.6. Thesis Outline

This work focuses on designing a single-particle detection system for upcoming strong-field QED experiments E-320 at FACET-II at the SLAC National Laboratory and the FOR2783 at the Centre for Advanced Laser Applications (CALA). The detector development presents the challenge of detecting single-particles while being insensitive to the background radiation (composed of photons and particles) which is inherent to experiments with high-energy electrons beams and a beam dump placed close to the interaction and detection regions.

Chapter 2 presents a review of the theory required to understand the interaction between light and matter. It starts by describing the relevant radiation mechanism originated from particle-matter interactions, such as bremsstrahlung, scintillation mechanisms, and Cherenkov radiation. Reviewing such mechanism allow understanding the development of the detectors and the design of the SF-QED experiments. Then, the interaction between particles and electromagnetic fields are briefly discussed. The particle-light interaction is an important step in producing high-energy γ-photons required to trigger pair production. Finally, a review of particle pair production is given, specially the nonlinear Breit-Wheeler pair production process which is used for generating the leptons to be diagnosed by the designed single-particle detectors introduced in chapter 3.

Role of the author: In this chapter the underlying physical processes are described. The derivations and plots shown in the chapter were performed by the author unless stated.

Chapter 3 introduces the single-particle detection system designed to detect single-particle hits of the pairs created via the nonlinear Breit-wheeler process in the upcoming strong-field experiments. A calibration of the Cherenkov calorimeter and the LYSO tracking layers is also provided. The design of the detector as well as its calibration described in this chapter has been previously published by the author in Ref. [103].

Role of the author: the single-particle detection system introduced in this chapter was designed, simulated, and built by the author with valuable inputs of collaborators from the Experiment-320 at FACET-II. After the construction of the single-particle detection system, the author led an experimental campaign at the ELBE radiation source at the Helmholtz-Zentrum Dresden Rossendorf to calibrate the response of

the detectors. All data analysis of the calibration campaign have been analyzed and interpreted by the author.

Chapter 4 presents the Experiment-320 at FACET-II at SLAC in detail. The results of particle-in-cell simulations of the interaction between monoenergetic 13 GeV electron bunches from the linear accelerator and the laser pulse with $a_0 = 10$ are shown. In this experiment, electron-positron pairs are produced in a two step process: high-energy photons are emitted by the electrons after interacting with the laser beam and, while the emitted photons are still immersed in the strong laser field, they promote the creation of electron-positron pairs from the quantum vacuum. The generated positrons will be diagnosed by the single-particle detection system described in chapter 3. Using Monte-Carlo simulations, the background radiation at the detectors is estimated, and systematic analysis of the signal-to-noise ratio of the Cherenkov calorimeter and the signal expected from the LYSO tracking screens is performed. The work described in this chapter has been previously published by the author in Ref. [103].

Role of the author: in the Experiment-320 at FACET-II, the author was responsible to coordinate the design of the single-particle detection system to be used in the experiment. The author also performed the estimation of the signal-to-noise ratio and the sources of background radiation on the single-particle detectors with the input of the simulation results provided by M. Tamburini and Monte-Carlo simulations of the complete experimental geometry performed by G. Sarri and N. Cavanagh. Additionally, the author also collaborated on the design of the optical setup inside the experimental vacuum chamber as well as the design and construction of components that are essential for the electron-laser collision, such as the motorized off-axis parabola mounts, common base plate for the setup, and target alignment holder.

Chapter 5 describes the upcoming FOR2783 experiment for probing the nonlinear Breit-Wheeler in the non-perturbative regime at the Centre for Advanced Laser Applications (CALA). A theoretical calculation of the expected pair yield is given and, also using Monte-Carlo simulations, the background radiation and the signal-to-noise ratio at the detectors are estimated. The work described in this chapter has been previously published by the author in Ref. [3].

Role of the author: in this chapter, the author performed all the theoretical calculations for estimating the pair production yield and the GEANT4 Monte-Carlo simulations of the complete experimental layout at CALA. The results obtained from these simulations as well as the expected signal-to-noise ratio on the single-particle

detectors was evaluated by the author. Moreover, the design of the single-particle detectors, experimental layout, and components was performed by the author with valuable inputs from K. Grafenstein, Prof. Karsch, and Prof. Zepf.

Chapter 6 summarizes the conclusions of this thesis, including preliminary measurements of background radiation at the E-320 experiment, and provides an outlook of research opportunities that are possible with SF-QED experiments.

2. Theory

This chapter briefly introduces the theory[1] required for designing the single-particle detection system and the upcoming SF-QED experiments E-320 and FOR2783.

We start by describing the radiation mechanisms originated from particle-matter interactions that are relevant for this work. Bremsstrahlung radiation is an important step to generate high-energy γ-photons required to trigger the nonlinear Breit-Wheeler pair production process in all-optical experiments. Then, the generation of scintillation and Cherenkov radiation is explained. Both radiation mechanisms are fundamental for designing the single-particle detection system as will be seen in chapter 3.

After introducing the pertinent radiation mechanisms from particle-matter interactions, the emission of high-energy photons through light-matter interactions is studied. As mentioned already, high-energy photons are essential to trigger the nonlinear Breit-Wheeler pair creation. Differently from the all-optical FOR2783 experiment where γ-photons are generated via bremsstrahlung radiation, in the Experiment-320 at SLAC, the required high-energy photons are created by interacting the accelerated electron bunches from the FACET-II linear accelerator with a high-intensity laser beam. The process that describes such interaction is known as nonlinear inverse Compton scattering (NICS). Nonetheless, to understand the NICS process, we start the chapter by describing the scattering process between light and matter from a classical perspective - known as Thomson scattering, where a low-energy photon collides elastically with an electron initially at rest. Then, we slowly develop the scattering model by increasing the energy of the incoming photon such that quantum mechanical effects cannot be neglected anymore (Compton scattering). Since we are interested in generating high-energy photons, we proceed by introducing the inverse process of the Compton scattering, where, now, a low-energy photon interacts with a high-energy electron (linear inverse Compton scattering). Finally, after we have laid the fundamentals of how to generate high-energy photons using linear inverse Compton scattering, the concept of the nonlinear inverse Compton scattering is introduced. In the NICS process, a highly energetic electron is immersed in an intense laser background, and multiple low-energy photons from the background field interact with the relativistic particle. As consequence of this interaction, a photon with significant energy relative to the kinetic energy of the incoming electron is emitted.

---

[1]The theory presented in this chapter uses rationalized natural units ($\hbar = c = 1$) unless otherwise noted.

After understanding the different mechanisms that generate γ-photons, we conclude this chapter by introducing the different theories of pair creation mechanisms that supports the explanation of the nonlinear Breit-Wheeler process. Pair production is one of the most iconic predictions in quantum electrodynamics where light is transformed into matter. Hence, learning how the pair creation processes works, allow us to correctly predict the number of pairs expected from the SF-QED experiments and the signal produced in the designed single-particle detectors as is shown in the next chapters 4 and chapter 5.

2.1. Particle-Matter Interactions: Radiation Mechanisms

In this section, we introduce three different radiation processes from particle-matter interactions: bremsstrahlung, scintillation and Cherenkov radiation. All three process, as already discussed, are essential for the design of the FOR2783 SF-QED experiment and the single-particle detectors.

As an electron propagates through matter, it slows down through scattering, and the particle can lose its energy mainly by emission of Cherenkov or bremsstrahlung radiation, or deposition of energy in the material, or production of secondary particle showers. The two common ways that an electron or positron loses its energy as it propagates inside a material are the following:

(i) The moving particle can ionize the medium by removing a bound electron from the medium's atom or by exciting an atomic electron to a higher orbital or free state. As the excited electron returns to its ground state, photons are emitted, usually in the visible spectrum. Note that the ionization of the medium is not limited to the primary incoming high-energy particle. In most of the cases, the secondary particles[2] created by the propagation of the high-energy particle inside the material are the ones that mostly ionize the medium.

(ii) The free-moving particle can interact with the Coulomb field of an atomic nucleus. As consequence, it slows down leading to a change in its propagation direction. The

---

[2]As a high-energy particle enters a material, the particle starts to interact with the matter. Photons interact predominantly via Bethe-Heitler pair production [69] while charged particles, electrons and positrons, interact via bremsstrahlung. Both processes, Bethe-Heitler pair production and bremsstrahlung, continue to take place and lead to a cascade (shower) of particles of decreasing energy until the processes thresholds are not satisfied anymore. These low-energy particles originated from the cascade process are known as secondary particles.

deceleration experienced by the particle leads to the emission of a photon. This
process is named bremsstrahlung and will be further discussed. In addition, the
bremsstrahlung radiation emitted inside the material can also generate electron-
positron pairs while still within the material by Bethe-Heitler process - these
particles are known as secondary radiation. These secondaries are likely to ionize
the medium the same way as described in the item (i) above, and, consequently,
scintillation light is also emitted.

The energy loss by the moving particle after penetrating the material is dependent
on its initial energy and target properties. To quantify the amount of energy loss, the
mass stopping power coefficient S (given in units of $\mathrm{MeV\,cm^2\,g^{-1}}$) is frequently used.
The coefficient S is given as the sum of the collision S_c and radiation S_r stopping
powers: $S = S_c + S_r$ and accounts for the energy loss per unit length due to the
ionization and excitation of the atoms (case (i) above), whereas the radiation stopping
power quantifies the amount energy loss per unit length through the radiation emitted
by bremsstrahlung due to the interactions of the particle with the Coulomb field of
the material atoms (case (ii) above). Methods to calculate the stopping powers are
found in Refs. [104, 105], and are not explicitly discussed in this thesis. However, one
can easily obtain the stopping powers for different elements and materials using the
ESTAR NIST database [106].

Figure 2.1 shows the stopping powers for three different materials that are pertinent
for designing the experiments and the single-particle detectors described in this thesis:
Tungsten (density of $\rho_W = 19.3\,\mathrm{g\,cm^{-3}}$), LYSO ($\rho_{LYSO} = 7.15\,\mathrm{g\,cm^{-3}}$), and F2 lead-
glass ($\rho_{F2} = 3.6\,\mathrm{g\,cm^{-3}}$). From the plots in figure 2.1, Tungsten is an excellent source
of γ-radiation due to its high radiation stopping power, which is explained by its higher
density compared to the other two materials (assuming that all materials have the
same thickness). On the other hand, LYSO and F2 lead-glass are materials with lower
densities and, therefore, have higher collision stopping powers which is advantageous for
depositing energies that later are transformed into scintillation light (in case of LYSO)
or for stopping the particle by dissipating its energy through Cherenkov radiation (in
case of the F2 lead-glass).

2.1.1. Bremsstrahlung Radiation

An important step in all-optical SF-QED experiments, such as the FOR2783 experiment,
is the generation of bremsstrahlung radiation (from German: "breaking radiation").
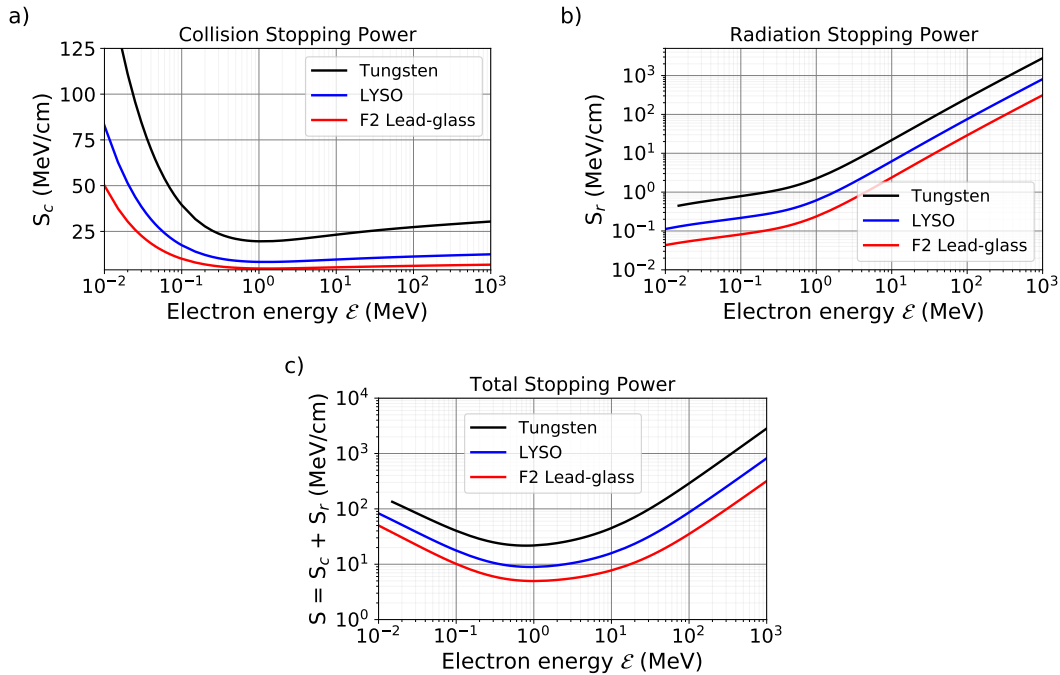Through bremsstrahlung radiation, the high-energy γ-photons required to trigger the

Figure 2.1.: Stopping powers for three different materials: Tungsten ($\rho_W = 19.3\,\mathrm{g\,cm^{-3}}$), LYSO ($\rho_{LYSO} = 7.15\,\mathrm{g\,cm^{-3}}$), and F2 lead-glass ($\rho_{F2} = 3.6\,\mathrm{g\,cm^{-3}}$). As seen in plots a) and b), Tungsten presents higher collision and radiation energy losses due to its high density. As a consequence, Tungsten is considered an excellent source of bremsstrahlung compared to low-density materials. The total stopping power, which is the sum of the collision S_c and S_r stopping powers, of the different materials is shown in (c). Data is taken from the ESTAR NIST database [106].

pair production process via nonlinear Breit-Wheeler in the photon-laser collisions are produced. Therefore, we study the bremsstrahlung radiation process in this section.

This interaction between a charged particle and the material through which it propagates can be seen, in the classical picture, as the deceleration of the particle as it passes through the Coulomb field of the material's atoms. As the particle interacts with the Coulomb field, it slows down and radiation is emitted. However, one can also analyze it using quantum electrodynamics by calculating the cross-section of the process using the diagram in figure 2.2. According to the diagram, an electron transfers energy to a virtual photon from the Coulomb field before emitting a photon. The cross-section of the bremsstrahlung process allows us to calculate the number of photons N_γ emitted with energy ω_γ by the process using the following equation [104],

$$\frac{\mathrm{d}N_\gamma}{\mathrm{d}\omega_\gamma} = \frac{L}{L_{\mathrm{rad}}}\frac{1}{\omega_\gamma}\left[\frac{4}{3} - \frac{4}{3}\frac{\omega_\gamma}{\mathcal{E}_0} + \left(\frac{\omega_\gamma}{\mathcal{E}_0}\right)^2\right], \qquad (2.1)$$

where a particle with initial energy $\mathcal{E}_0$ propagates through a material of radiation length L_{rad} and thickness L. The radiation length is a characteristic amount of the material which indicates the mean distance that an electron propagates until its energy is reduced to $(1/e)$ of its original value $\mathcal{E}_0$. The method to analytically calculate the L_{rad} of a material is given in details in Refs. [104, 107] and in Appendix C.
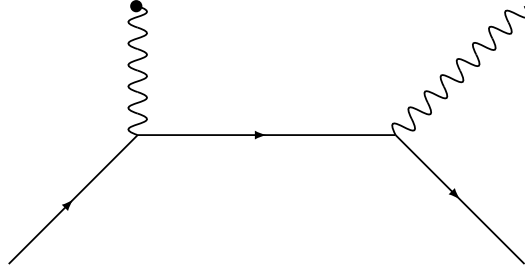

Figure 2.2.: Feynman diagram for bremsstrahlung. An electron transfer momentum to a virtual photon from the Coulomb field of an atom before emitting a photon. This diagram allows to calculate the bremsstrahlung cross-section and estimate radiated spectrum as given in equation (2.1).

A useful simulation tool frequently used to predict the bremsstrahlung radiation spectrum produced by an incoming particle is the GEANT4 framework [108–110]. Figure 2.3 shows a comparison between the theoretical spectrum using equation (2.1) and the simulated results from GEANT4, both calculated for a collimated electron beam of $2.5\,\text{GeV}$ and $10\,\text{pC}$ of charge interacting with a tungsten target with different thicknesses. At first, we note a good agreement between the analytical and simulation solutions, especially at low energies and thin material thicknesses. However, as the material length increases, the simulation spectrum curve becomes rounded at the high-energies due to the multiple scattering occurring inside the material that softens the high-energy photons. Unfortunately, the analytical model does not include the multiple scattering occurring inside the material unlike the GEANT4 simulations, which capture the effect in detail.

2.1.2. Scintillation Mechanisms in Materials

As previously discussed, a high-energy particle propagating through a material generates a cascade of secondary particles that lose their energy by ionizing the medium. As the excited atomic electrons return to their ground states, scintillation light is emitted. In this thesis, we detect scintillation light originated by positrons and electrons propagating through pixelated LYSO crystal screens which are a fundamental part of the detection system designed for the upcoming SF-QED experiments.
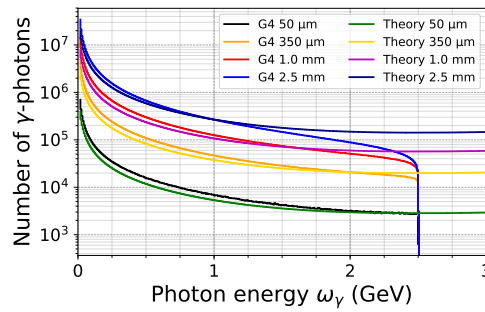
Figure 2.3.: Bremsstrahlung spectrum for a collimated electron beam of 2.5 GeV and a charge of 10 pC interacting with a tungsten target with several thicknesses. As the thickness increases, multiple scattering inside the material occurs softening the high-energy photons emitted. The analytical model does not include this effect, but the GEANT4 simulations captures the high-energy photons softening in detail.

The ionization process is taken into account when calculating the collision stopping power of the material meaning that energy from the particle is absorbed and later reemitted as visible light, namely scintillation light, or converted to heat. Depending on the material (scintillator) nature, organic or inorganic, different mechanisms of emitting scintillation light are possible.

Organic materials are usually hydrocarbon compounds that present luminescence due to transitions of free valence electrons between π-orbitals of the molecules [111, 112]. Organic scintillators are usually less costly than inorganic materials, and their optical absorption and emission spectra are tuned easily [113]. In addition, most of the organic scintillators offer faster decay times on the order of a few nanoseconds [114]. Often, organic materials are employed in the detection of neutrons, protons, and alpha particles [115, 116].

The second type of scintillator, namely inorganic scintillators, is composed of crystals. Inorganic materials present higher densities and, therefore, higher stopping powers than organic materials. Higher scintillation yields than organic materials are also possible using crystals. However, the usual decay time of the inorganic materials is about 2-3 orders of magnitude higher than most of organic ones. Moreover, the scintillation mechanism is also different from the organic materials. Two types of ionization mechanisms are possible inside the inorganic materials: as a particle enters the crystal, it ionizes the atomic electron from the valence band to the conduction band producing a free electron and a hole; or an exciton is created by exciting an electron from the valence band to the exciton band, and the electron/hole formed remain as

a pair that can move within the crystal [111, 112]. Now, if a crystal incorporates a dopant, the forbidden energy gap can contain electronic levels that act as luminescence centers or impurity traps. If an electron finds its way to one of the holes of the luminescence center and make the transition to its ground state, scintillation light is emitted. Figure 2.4 illustrates the scintillation mechanism in the inorganic materials in a simplified manner.
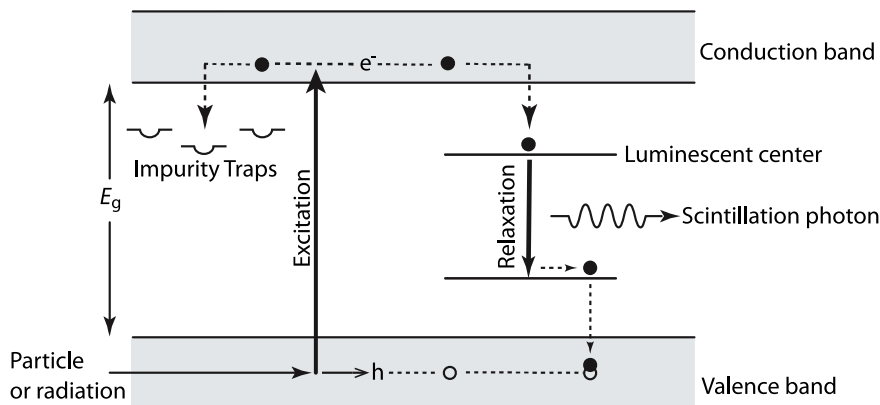
Figure 2.4.: Band structure of an inorganic crystal. An incoming particle, usually secondary radiation originated from the primary high-energy particle, ionizes the atoms and molecules of the crystal, and electron-holes pairs or excitons are formed. Luminescence centers in the material are formed due to dopants added to the material, and holes can migrate to such centers. Excited electrons can fall into the holes in the luminescence centers and make the transition to their ground states by emitting scintillation light. Figure taken from Ref. [117, 118].

The ratio between the number of scintillation photons emitted and energy lost (also referred to as energy deposited) by the incoming particle is commonly given as a property of the scintillator named light yield with units photons/keV or photons/MeV. In this thesis, three main scintillator materials are used to detect radiation are: LYSO [119], Lanex (Gadox), and CsI:Tl [120, 121]. Table 2.1 presents the scintillation characteristics of these three materials. LYSO and CsI crystals exhibit fast decay times with high light yield, hence, being beneficial for detecting single-particle hits using intensified charge-coupled (ICCD) gated cameras. On the other hand, Lanex screens are widely used as the standard method to diagnose the charge and spectrum of electron beams [122–124]. The applications of these scintillation materials on the proposed particle detectors in this work are investigated in the later chapters.

Material	Chemical Formula	Density (g/cm^3)	Yield (photons/MeV)	Decay Time at 1/e (ns)	Emission Peak
LYSO	Lu$_{1.8}$Y$_{0.2}$SiO$_5$:Ce	7.1	2.5 - 45 $\times 10^4$	40 - 45	420 nm
CsI	CsI:Tl	4.5	6.6×10^4	800	550 nm
Lanex	Gd$_2$O$_2$S:Tb	7.3	6.0×10^4	10^6	545 nm

Table 2.1.: Properties of inorganic crystals (LYSO, CsI and Lanex) that are commonly used in detect particles. LYSO and CsI crystals are commonly used to detect single-particles hits due to their high scintillation yield. Lanex screens are widely used to probe with high precision the spectrum and charge of electron beams. Data from the table was collected from Refs. [119–121, 125–134].

2.1.3. Cherenkov Radiation

Another important process due to the interaction of a relativistic particle through a medium is the emission of Cherenkov radiation, which is widely used to diagnose particles in high-energy physics experiments [135–139] and also implemented in our detection system to determine the energy of the single-particle propagating through the detectors.

The first observation of Cherenkov radiation was made by Čerenkov in 1934 while investigating the emission of a weak blue-light in a solution of uranyl salt that was irradiated by γ-photons from a radioactive radium source [140, 141]. At first, Čerenkov assumed that the blue light emission was due to the interaction of the γ-photons with the uranyl salt. However, subsequently, it was discovered that the light emission occurred due secondary electrons generated by the irradiation of γ-photons on the sample [141], and, the emitted light was polarized, propagating within a small cone in the same direction as the secondary electrons.

A theory explaining the phenomena was derived a few years later, in 1937, by Frank and Tamm [142], who presented a correct interpretation for the experiments of Čerenkov. According to their theory, a charged particle propagating through a dielectric medium can emit radiation if its velocity is greater than the phase velocity of light in the medium - known as Cherenkov radiation threshold, i.e., $v_{\mathrm{particle}} \gtrsim c/n(\omega)$, where $n(\omega)$ is the refractive index of the dielectric medium dependent on the frequency of the light. Alternatively, the Cherenkov radiation threshold can also be expressed in

terms of the particle energy $\mathcal{E}$ required to produce the effect [143, 144],

$$\mathcal{E} \approx m_e \left(\frac{1}{\sqrt{1 - 1/n^2}} - 1 \right) . \tag{2.2}$$

To understand how the Cherenkov radiation is formed, we follow the explanation given by Jelley [144]. Localized dipoles are formed along the propagation path inside the medium of a charged particle. As these atoms are depolarized, radiation is emitted. Now, depending on the speed of the particle, the emitted radiation by these localized dipoles can interfere constructively or destructively. For a low particle velocity, i.e., $v_{\mathrm{particle}} < c/n$, the polarized dipoles are distributed symmetrically around the trajectory of the particle and its instantaneous position. Due to their symmetry along the particle's path, the radiation emitted after the depolarization of the dipoles interferes destructively, and no radiation is observed. On the other hand, if the particle velocity is larger than the speed of light inside the material $v_{\mathrm{particle}} \gtrsim c/n$, the polarization symmetry along the trajectory is broken and phase-matching between the induced radiating dipoles is achieved. Consequently, the emitted radiation interferes constructively giving rise to the so-called Cherenkov radiation.

By analyzing the location where the emitted wavefronts interfere constructively, one notices that the Cherenkov light propagates within a cone defined by the half angle θ_{Ch}. Figure 2.5 shows how the Cherenkov cone is defined. The half angle θ_{Ch} is given as [141, 145],

$$\cos \theta_{\mathrm{Ch}} = \frac{1}{\beta \, n(\omega)} , \tag{2.3}$$

where $\beta = c/n$, and it is analogous to the angle that a supersonic boom propagates where the generated waves cannot propagate forward from the particle.

To evaluate the energy radiated per unit distance by the moving particle with charge zq as it propagates in the medium, we employ the Frank-Tamm formula (here given in rationalized natural units) [69, 142],

$$\frac{\mathrm{d}\,\mathcal{E}_{\mathrm{rad}}}{\mathrm{d}\,x} = (zq)^2 \int_{n(\omega)>1/\beta} \omega \left(1 - \frac{1}{\beta^2 \, n^2(\omega)} \right) \mathrm{d}\omega . \tag{2.4}$$

The Frank-Tamm formula in equation (2.4) can be rewritten in terms of the number of photons radiated within a wavelength range. This way of expressing the formula is particularly interesting when designing detectors that use the Cherenkov radiation mechanism to diagnose single-particles. With the number of photons emitted, one can predict the response of such detectors and evaluate, for example, the signal-to-
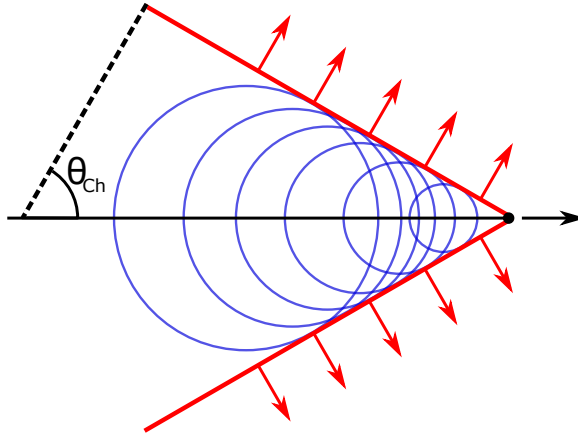
Figure 2.5.: Formation of the Cherenkov radiation as a relativistic charged particle propagates inside a medium. Along with the propagation of the particle, circular wavefronts (blue circles) traveling slower than the moving particle are formed. These wavefronts interfere constructively due to phase-matching and are confined to a cone (defined by the red lines in the figure) that resembles a supersonic boom, where the generated waves cannot propagate forward from the particle.

noise ratio expected for particle detection. The number of photons emitted within a wavelength range is calculated as[3],

$$\frac{\mathrm{d}\,N_{\mathrm{Ch}}}{\mathrm{d}x} = 2\pi\alpha\,z^2 \int_{\lambda_1}^{\lambda_2} \frac{\sin^2\theta_{\mathrm{Ch}}}{\lambda^2}\,\mathrm{d}\lambda\,. \tag{2.5}$$

As an example, assume a relativistic charged particle ($z = 1$, $\beta \approx 1$) propagating through a medium with refractive index of $n = 1.6$ constant within the range $250\,\mathrm{nm}$ to $500\,\mathrm{nm}$. The Cherenkov half-angle is $\theta_{\mathrm{Ch}} \approx 51°$. By applying equation (2.5), the number of photons per unit distance propagated by the particle is $(\mathrm{d}N_{\mathrm{Ch}}/\mathrm{d}x) \approx 920 \sin^2\theta_{\mathrm{Ch}} \approx 555$ photons/cm.

2.2. Light-Matter Interactions: Radiation Mechanisms

After describing the relevant radiation emission mechanisms from particle-matter interactions in the previous section, we introduce now the generation of γ-photons through light-matter interactions. Understanding how the emission of high-energy photons by colliding electrons and laser beams occurs lets us explain how pairs are

---

[3]Note that equation (2.5) is given in SI units. Since the number of photons is closely related to its detection in experiments, it is more intuitive to evaluate it in units that are easy to use in the laboratory.

created in the Experiment-320 at FACET-II. However, before we describe how the emission of γ-photon takes place, we start by analyzing the elastic scattering of low energy photons by a free electron at rest using classical electromagnetism. Then, we increase the energy of the photon such that quantum mechanical effects cannot be neglected anymore and should be included in the model, consequently, transforming the collision between both particles becomes inelastic. This inelastic scattering process is known as Compton scattering.

Nonetheless, we are interested in the emission of high-energy photons through the collision between relativistic electrons and a laser beam, similar to the E-320 experiment. Therefore, we proceed by reviewing the inverse process of Compton scattering, known as inverse Compton scattering (ICS) process, in which an ultra-relativistic electron transfers momentum to a low energy photon, resulting in the emission of a high-energy photon. At last, we improve the ICS model to include the interaction and absorption of many low-energy photons by the relativistic electron by analyzing electron-laser interactions. This improved model is known as nonlinear inverse Compton scattering and is the main mechanism used at the Experiment-320 at FACET-II to generate high-energy photons that will trigger the nonlinear Breit-Wheeler pair production.

2.2.1. Thomson Scattering

As a particle initially at rest interacts with a low-intensity light beam, it accelerates to velocities much smaller than the speed of light (non-relativistic motion). In this particular case, the particle oscillates linearly in phase with the oscillating electric field of the wave, and, consequently, the radiation emitted by the electron will have the same frequency as the incident wave but remitted in a different direction. This process is known as elastic scattering or Thomson scattering.

To evaluate this process, the non-relativistic equation of motion of a charged particle[4] is used to obtain the trajectories of the particle which are later plugged into the Liénard–Wiechert potentials[5] to calculate the radiation spectrum and its angular distribution [69, 146]. Another way to characterize the process is through the concept of cross-sections, i.e., the ratio between the scattered energy and the incident energy

---

[4]The equation of motion for a charged particle and its trajectories are shown in Appendixes A and B.

[5]In a Lorentz gauge, the Liénard–Wiechert potentials are used to describe the classical electric and magnetic fields generated by an accelerated charge in terms of a vector potential and a scalar potential. For details, please see [69, 146].

flux. The Thomson scattering cross-section of an electron with charge e is given as [69]

$$\sigma_0 = \frac{8\pi}{3} \frac{\alpha^2}{m_e^2} = 1.7 \times 10^{-15}\,\mathrm{eV}^{-2}\,, \tag{2.6}$$

where $\alpha \approx 1/137$ is the fine-structure constant. The Thomson cross-section in SI units[6] is $\sigma_0 = 6.65 \times 10^{-25}\,\mathrm{cm}^2$.

2.2.2. Compton Scattering

The Thomson scattering formulation previously presented is only valid for low photon energies, i.e., low wave frequencies. As soon as the frequency increases, i.e., the energy of the incident photons ω_i becomes larger, on the order of the rest mass m_e of the electron, quantum mechanical effects start to play a role, and the scattering process should be now analyzed using the kinematics of the collision between a single photon and the particle. In this case, the photon transfers energy to the particle and, consequently, is scattered with lower energy. Hence, this type of collision is inelastic in terms of momentum. This quantum mechanical view of the photon-electron scattering is referred to as Compton scattering. From the kinematics evaluation of the collision, the ratio between the final ω_f and initial ω_i photon energies is given by [69]

$$\frac{\omega_f}{\omega_i} = \frac{1}{1 + \frac{\omega_i}{m_e}\left(1 - \cos\theta\right)} \tag{2.8}$$

where θ is the angle between the incident and scattered photons.

By assuming that an electron initially at rest interacts with an unpolarized photon with Lorentz-factor $\gamma_p = \omega/m_e$, quantum field theory can be used to evaluate the cross-section of the inelastic scattering process. By employing QFT, the cross-section was first calculated by Klein and Nishina (KN) in 1929 [147], and is given by[7]

$$\sigma_{KN} = \frac{3}{4}\sigma_0 \left\{ \frac{1 + \gamma_p}{\gamma_p^3}\left[\frac{2\gamma_p(1 + \gamma_p)}{1 + 2\gamma_p} - \ln(1 + 2\gamma_p)\right] + \frac{\ln(1 + 2\gamma_p)}{2\gamma_p} - \frac{1 + 3\gamma_p}{(1 + 2\gamma_p)^2} \right\}. \tag{2.9}$$

---

[6]In SI units, the Thomson cross-section is calculated as:

$$\sigma_0 = \frac{8\pi}{3}\left(\frac{\alpha\,\hbar\,c}{m_e\,c^2}\right)^2 = \frac{8\pi}{3}\,\mathrm{r_e^2} = 6.65 \times 10^{-25}\,\mathrm{cm}^2\,, \tag{2.7}$$

where $\mathrm{r_e} \approx 2.818 \times 10^{-15}\,\mathrm{m}$ is the classical electron radius.

[7]For details on the calculation steps, please see quantum field theory textbooks, e.g., Refs. [41, 42, 148].

The Feynman diagram that represents the Compton scattering process is illustrated in figure 2.6.
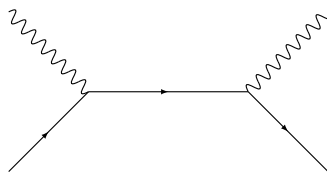

Figure 2.6.: Feynman diagram for the Compton scattering process.

Note that if one takes the non-relativistic limit where $\gamma_p \ll 1$, the Klein-Nishina cross-section σ_{KN} is reduced to the Thomson cross-section $\sigma_{KN} \approx \sigma_0$ [42, 148]. On the other hand, at high photon energies $\gamma_p \gg 1$, the KN cross-section tends to zero $\sigma_{KN} \to 0$ showing that highly energetic photons are much less likely to scatter. Figure 2.7 plots the ratio σ_{KN}/σ_0 where the values of the cross-section at the γ_p limits is observed.
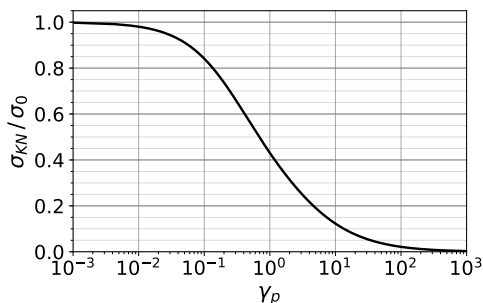
Figure 2.7.: Klein-Nishina cross-section for the interaction of a photon of energy $\gamma_p = \omega/m_e$ with an electron initially at rest. In the non-relativistic limit $\gamma_p \ll 1$, the Klein-Nishina cross-section reduces to the Thomson scattering cross-section. On the other hand, photons with high energies $\gamma_p \gg 1$, the cross-section tends to zero $\sigma_{KN} \to 0$ which shows that highly energetic photons are much less likely to scatter.

2.2.3. Linear Inverse Compton Scattering

In the previous section 2.2.2, Compton scattering with the transfer of momentum from a high-energy photon to a particle initially at rest was introduced. However, the transfer of momentum can also occur from a relativistic electron to a low energy photon, namely inverse linear Compton scattering (ILCS), so that $\omega_i + e^- \to \omega + e^-$. The modeling of the ILCS process is also possible using the kinematic method, where

now we look into the rest frame of the electron. Assume an electron with initial energy $\mathcal{E}_i$ and Lorentz-factor of $\gamma = \mathcal{E}_i / m_e$ and a low energy photon ω_i propagating with an angle θ with respect to the electron propagation direction. The photon experiences a relativistic Doppler-shift in the rest frame of the electron so that its initial energy becomes $\omega_i' = \gamma \omega_i (1 - \beta \cos \theta)$. The same boost to the electron rest frame can be applied to its incident angles such that [149–151]

$$\sin \theta' = \frac{\sin \theta}{\gamma (1 + \beta \cos \theta)} \tag{2.10a}$$

and

$$\cos \theta' = \frac{\cos \theta + \beta}{1 + \beta \cos \theta} . \tag{2.10b}$$

After boosting the incident angles of the photon to the rest frame of the electron, the energy of the scattered photon can also be calculated using the same kinematics method introduced for evaluating the Compton scattering condition in equation (2.8),

$$\frac{\omega_f'}{\omega_i'} = \frac{1}{1 + \frac{\omega_i'}{m_e} (1 - \cos \alpha')} , \tag{2.11}$$

where α' is the scattering angle in the rest frame of the electron depending on the azimuthal angles ϕ_i' and ϕ_f' of incident and scattered photon also in the electron rest frame,

$$\cos \alpha' = \cos \theta_i' \cos \theta_f' + \sin \theta_i' \sin \theta_f' \cos(\phi_i' - \phi_f') . \tag{2.12}$$

The spectrum of the scattered radiation of the inverse linear Compton scattering is given by the spectral emissivity $I(\omega_f)$ as given in Refs. [149, 150],

$$I(\zeta) = \frac{3\sigma_T}{16} N(\omega_i) \left[2\zeta^2 \ln \left(\frac{\zeta}{4} \right) + \zeta^2 + 4\zeta - \frac{\zeta^3}{2} \right] , \tag{2.13}$$

where $N(\omega_i)$ is the number density of photons and $\zeta = \omega_f / (\gamma^2 \omega_i)$. Figure 2.8 plots the emissivity as function of the α parameter. From the emissivity spectrum, one finds that a photon can acquire the maximum energy of $\omega_{f,\max} \approx 4\gamma^2 \omega i$ in the laboratory frame for head-on collision between the photon and the electron [149, 150]. Note that the emitted photon suffers a Doppler shift and have a higher energy than the incoming low-energy photon ωi by a factor $\approx 4\gamma^2$.

To illustrate the linear ICS process with parameters that are commonly used on SF-QED experiments using electron-laser collisions, assume a laser photon of energy $1.55\,\mathrm{eV}$ colliding with a counter propagating ($\theta = 180°$) electron of energy $2.5\,\mathrm{GeV}$,

which corresponds to a Lorentz factor of $\gamma \approx 4892$. The initial energy of the photon is first boosted to the rest frame of the electron such that $\omega_i' = 15.16\,\text{keV}$. Note that $\omega_i \ll m_e$, therefore, equation (2.11) can be simplified to $\omega_f' \approx \omega_i'$. To find the photon energy after the interaction in the laboratory frame of reference, a second Lorentz boost is necessary such that $\omega_f = \gamma \omega_f' \left(1 + \beta \cos\theta_f'\right)$ which now can also be simplified to

$$\omega_f = 4\gamma^2 \omega_i \,, \tag{2.14}$$

for a relativistic particle where $\beta \approx 1$ and head-on collision. Hence, the energy of the photon in the laboratory frame after interaction with the relativistic electron is $\omega_f = 148.4\,\text{MeV}$. Note that the maximum energy transfer between the relativistic electron and the low-energy photon occurs at head-on collision, agreeing with the maximum energy transfer previously predicted using the emissivity spectrum.
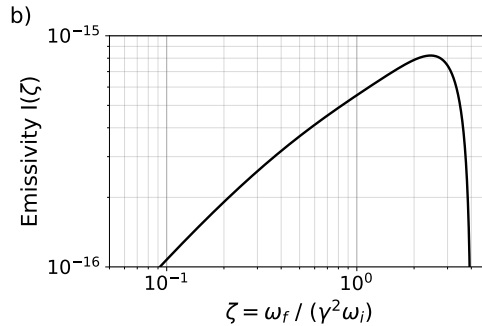
Figure 2.8.: Emissivity of the inverse Compton scattering (ICS) process. The maximum energy that a photon can acquire, $\omega_{f,\,\text{max}} = 4\gamma^2 \omega_i$, after the interaction with a relativistic electron is only possible for head-on collisions between both particles and axial re-emission.

2.2.4. Nonlinear Inverse Compton Scattering

As seen in the previous section, the interaction of a single-particle with a single photon was easily described by the kinematics of the process and by QFT to obtain their corresponding cross-sections. Now, the question is: what happens if a single-particle is immersed in an intense background laser field which contains many photons similarly to the electron-laser collision in the E-320 experiment? In this particular case, the relativistic electron traveling within this intense laser background field starts to absorb many low-energy photons of energy ω_L from the laser beam such that $n\,\omega_L + e^- \rightarrow \omega_f + e^-$ giving rising to nonlinear effects on the electron motion. This process is known as nonlinear inverse Compton Scattering (NLCS).

The kinematics for the nonlinear inverse Compton scattering is similar to the linear inverse Compton scattering process, and can be easily deduced by substituting the incoming photon energy ω_i in equation (2.11) by $n\,\omega_i$, $\omega_i \to n\,\omega_i$, where n is the number of incoming photons interacting with the relativistic particle. By performing such substitution, we assume that all incoming photons have the same energy and propagate parallel to each other. Then, the energy of the scattered photon in the rest frame of the relativistic electron becomes,

$$\frac{\omega'_f}{\omega'_i} = \frac{n}{1 + \frac{n\,\omega'_i}{m_e}\left(1 - \cos\alpha'\right)}\,, \tag{2.15}$$

One can boost back the energy of the emitted photon to the laboratory frame. By doing so, the relativistic mass increase effect should be also taken into account by replacing $m_e \to m_* = m_e\sqrt{1 + a_0^2}$ [152–154]. Hence, the scattered photon energy in the laboratory frame becomes [152–155]:

$$\frac{\omega_f}{\omega_i} = \frac{2\,n\,\gamma^2}{1 + a_0^2/2 + (\gamma\theta_0)^2}\left(1 - \cos\theta\right), \tag{2.16}$$

where θ_0 is the emission angle, θ is the photon-electron collision angle, γ is the Lorentz-factor of the relativistic particle, and a_0 is the normalized field strength defined previously in equation (1.1). Similar to the linear inverse Compton scattering case, the maximum photon energy obtained from equation (2.16) is given again by $\omega_{f,\max} \approx 4\gamma^2\omega i$, and is only possible for head-on collision where $\theta = 180°$ and on-axis emission angle $\theta_0 = 0$. Any deviation from the collision or emission angle, the scattered photon suffers a Doppler redshift to lower photon energies, i.e. lower frequencies. For the case where $a_0 < 1$ most of the emitted radiation goes to the fundamental harmonic $n = 1$ [153], however, as $a_0 \sim 1$, the emission of harmonics starts to play a role such that, at the limit where $a_0 \gg 1$, the emitted radiation is composed by several harmonics that are redshifted due to the term $a_0^2/2$ in equation (2.16). In addition, at this limit of $a_0 \gg 1$, the total number of harmonics that contributes significantly to the emission spectrum is proportional to $\sim a_0^3$, and the envelope over the emitted spectrum becomes similar to a synchrotron radiation spectrum [152, 153].

The number of absorbed photons by the relativistic particle over a Compton wavelength can be estimated by using the definition of the normalized field strength a_0. To this end, we first calculate the ratio between the laser wavelength λ_0 and the reduced

Compton wavelength $\lambdabar_c$,

$$\lambda_0 = 2\pi \frac{m_e \, c^2}{\hbar \, \omega_0} \lambdabar_c \, . \tag{2.17}$$

Then, by substituting equation (2.17) into equation (1.7), one obtains the work performed by the laser field over a Compton wavelength, i.e., the energy absorbed from the laser field by the particle over a distance given the reduced Compton wavelength to emit a high-energy photon:

$$\Delta \mathcal{E}_{\text{abs}} = e \, \text{E} \, \lambdabar_c = a_0 \, \hbar \, \omega_0 \, . \tag{2.18}$$

Note that, in equation (2.18), a_0 can be approximated as number of absorbed photons n from the laser field.

Although we can analyze the process in terms of its kinematic, the complete description of the electron-laser interaction can be studied using the Furry picture introduced in section 1.2 [48]. Using the Feynman diagram[8] of the nonlinear inverse Compton Scattering illustrated in figure 2.9, the differential scattering rate of the process for a circularly polarized laser field averaged over the spin states of the electron[9] is given as [2, 156],

$$\frac{\text{dW}_n}{\text{d}x} = \frac{\alpha m_e^2}{4\mathcal{E}} \left[-4\text{J}_n^2(z) + a_0^2 \left(1 - x + \frac{1}{1-x} \right) \left(\text{J}_{n-1}^2(z) + \text{J}_{n+1}^2(z) - 2\text{J}_n^2(z) \right) \right] , \tag{2.19}$$

where $x = \omega_f / \mathcal{E}$ is the ratio between the energy of the scattered photon ω_f and the energy of the electron $\mathcal{E}$, a_0 is the normalized field strength, and $\text{J}_n(z)$ is the Bessel function of first kind of order n with argument z given by,

$$z = \frac{2a_0}{\sqrt{1 + a_0^2}} \frac{\sqrt{x \, [nu - (1 + nu)x]}}{u(1-x)} \, ,$$

with

$$u = \frac{4\mathcal{E}\omega_L}{m_e^2 (1 + a_0^2)} \, .$$

The order n of the Bessel function $\text{J}_n(z)$ represents the number of background photons that are scattered with the particle. Therefore, the total scattering rate of

---

[8]In the context of the Furry picture in the SF-QED formalism, the double lines represent a particle dressed by the background laser field.

[9]For linearly polarized differential scattering rate of the nonlinear inverse Compton scattering process, please see Refs. [2, 156].

the NICS process is given by the sum

$$\frac{\mathrm{dW}}{\mathrm{d}x} = \sum_n \frac{\mathrm{dW}_n}{\mathrm{d}x} .$$
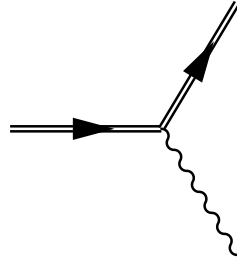(2.20)

Figure 2.9.: Feynman diagram of the nonlinear inverse Compton scattering (NICS) process. An electron immersed in a dense photon background is scattered, and part of its momentum is transferred to a photon. The double line represents an electron dressed in a dense low-energy photon background field.

The scattering rate for the interaction of an electron with initial energy of $\mathcal{E} = 2.5\,\mathrm{GeV}$ colliding with a laser beam with frequency $\omega_L = 1.55\,\mathrm{eV}$ of different a_0 values is shown in figure 2.10. Independently of the a_0 values, the scattering rate rises up to the first Compton edge (n = 1) where it falls sharply. As the interaction of multiple photons occurs with the particle ($n > 1$), the emission of higher harmonics is observed.
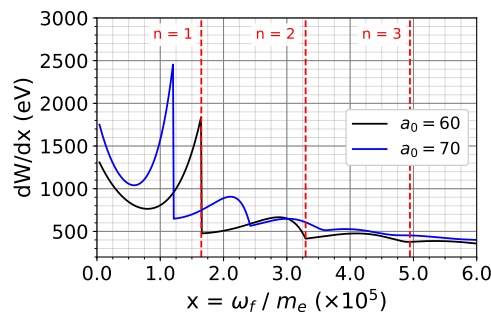
Figure 2.10.: Scattering rate for an electron with energy $\mathcal{E} = 2.5\,\mathrm{GeV}$ interacting with a laser beam of frequency $\omega_L = 1.55\,\mathrm{eV}$ and two different strengths, $a_0 = (60, 70)$. The scattering rate increases up to the first Compton edge (n = 1, dashed line) and then falls sharply. Moreover, the multiple photon scatterings result in higher harmonics scattered photons as $n > 1$. With the increase of the laser intensity a_0 increases, the scattered radiation is Doppler redshifted to lower energies as predicted by equation (2.16).

2.3. Pair Production Mechanisms

To generate an electron-positron pair, high-energy photons are required to overcome the energy threshold of the pair creation processes. As already mentioned, the generation of γ-photons in the FOR2783 experiment is occurs by interacting an electron beam with a converter target which results in a bremsstrahlung γ-beam. On the other hand, at the E-320 experiment at FACET-II, the formation of γ-photons is done by the nonlinear inverse Compton scattering process after the collision of the accelerator electron beam with the intense laser beam.

Now that we understand how the production of the required high-energy photons occurs, we can review the electron-positron pair creation processes. As seen in chapter 1, section 1.1, in 1928 Dirac predicted the existence of two regions, the negative and positive continuum. In both regions, the energy values of the electrons are continuous and due to their finite rest mass m_e, the absolute energy of the particles in both regions should be greater or equal to their rest mass such that $|E| \geq m_e\,c^2$. Therefore, the negative continuum, also called the Dirac sea, has an upper energy limit of $-m_e\,c^2$, and the positive continuum has a lower energy limit of $+m_e\,c^2$.

According to Dirac's theory, the negative energy states are all naturally filled with electrons making it impossible for an electron in the positive continuum to transit to a negative energy state. However, electrons located in the negative continuum have a finite probability of transiting to a positive energy state if energy above the threshold of $2\,m_e\,c^2$ is provided to overcome the potential barrier. As soon as an electron makes the transition from a negative to a positive energy state, it leaves a hole in the negative continuum with the opposite charge of the electron, but the same mass and energy. The hole is interpreted as a real anti-electron, also known as a positron. Whenever a positron that is located in the negative continuum encounters an electron in the positive region, there is a probability for this electron to transit back to the hole defined by the positron. If such transition takes place, energy is released in terms of photons as the electron transits back to the hole in the negative energy state. This recombination process is known as the Dirac annihilation process.

2.3.1. Dirac Electron-Positron Annihilation

The Dirac annihilation process is a process where an electron and positron pair annihilate each other creating two photons:

$$\mathrm{e^+ + e^- \longrightarrow \gamma_1 + \gamma_2}\,.$$

The diagram that describes the pair-annihilation process is shown in figure 2.11 a). One can notice the similarity with the Compton scattering diagram already introduced in section 2.2.2. Both processes are related by the so-called crossing symmetry property where their diagrams have the same number of vertices and lines, but their incoming and outgoing momenta sign and particles are different [42]. The annihilation process is considered spontaneous, i.e., it can occur for any electron-positron pair independently of their energy [157].
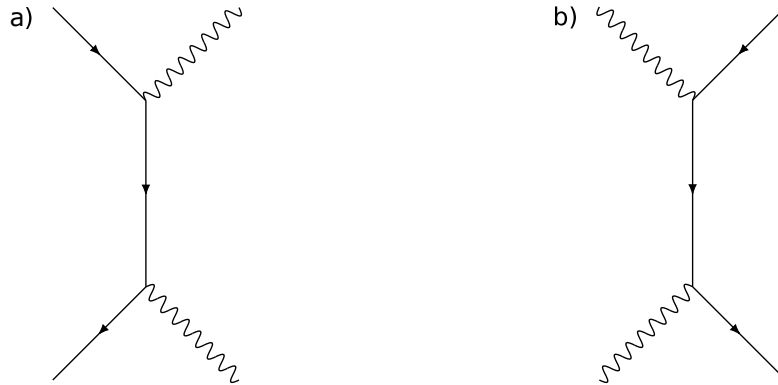

Figure 2.11.: Feynman diagrams of a) Dirac's pair-annihilation process, and b) linear Breit-Wheeler pair production. Both processes are related to each other by crossing symmetry where the same number of vertices and lines are presented, but the momenta of the particles are changed.

From the diagram, one can compute the total cross-section of the pair-annihilation process [42, 148, 158],

$$\sigma_{\mathrm{D}} = \pi \frac{\alpha^2}{m_e^2} \frac{(1 - \hat{\beta})}{4\hat{\beta}^2} \left[(3 - \hat{\beta}^4) \ln \left(\frac{1 + \hat{\beta}}{1 - \hat{\beta}} \right) - 2\hat{\beta}(2 - \hat{\beta}^2) \right] , \qquad (2.21)$$

where $\alpha \approx 1/137$ is the fine-structure constant, $\hat{\beta} = \sqrt{1 - 1/s}$ standing for the center of mass velocity with the energy of the electron or positron at the center of mass given by $s = (\mathcal{E}_{e^-/e^+}/m_e)^2$.

The annihilation cross-section is plotted in figure 2.12 a). At low particle energies, the energy at the center of mass tends to unity $s \to 1$. Consequently, the velocity of the center of mass goes to zero $\hat{\beta} \to 0$, and the cross-section to infinity $\sigma_{\mathrm{D}} \to \infty$ meaning that the electron-positron pairs have an extremely high-probability of generating photon pairs. Now, for high particle energies, the contrary behavior is observed: $s \to 0$ and $\hat{\beta} \to 1$, hence, $\sigma_{\mathrm{D}} \to 0$, indicating a low probability of the particles to create two photons.

2.3.2. Linear Breit-Wheeler Pair Production

The inverse process of the Dirac pair-annihilation is also possible. Photons can excite the electrons from the negative energy state to the positive continuum creating a real electron-positron pair. This inverse process is called linear Breit-Wheeler.

The calculation of the cross-section of the linear Breit-wheeler pair-creation process, described by the Feynman diagram shown in figure 2.11 b), was first performed by Breit and Wheeler in 1934 [23]. Different from the Dirac annihilation effect, the pair-creation process is not spontaneous since electrons and positrons have non-zero masses. Hence, the process features an energy threshold that determines if the photons have sufficient energy to create a pair. The threshold for this process is given by: $\omega_1\omega_2 \gtrsim 2m_e^2/(1 - \cos\theta_{\mathrm{BW}})$, where ω_1 and ω_2 are the photon energies, m_e represents the electron rest mass and θ_{BW} is the collision angle between the photons (for head-on collision, $\theta_{\mathrm{BW}} = 180°$).

The total cross-section of the pair-production process in the center of mass of the collision calculated using the Feynman diagram in figure 2.11 b) is given as[10] [148, 157, 159]:

$$\sigma_{\mathrm{BW}} = \frac{\pi}{2}\frac{\alpha^2}{m_e^2}(1 - \hat{\beta}^2)\left[(3 - \hat{\beta}^4)\ln\left(\frac{1 + \hat{\beta}}{1 - \hat{\beta}}\right) - 2\hat{\beta}(2 - \hat{\beta}^2)\right] = 2\hat{\beta}^2\sigma_{\mathrm{D}}, \qquad (2.22)$$

where the we have the same definitions of $\hat{\beta} = \sqrt{1 - 1/s}$ and $s = \omega_1\omega_2(1 - \cos\theta_{\mathrm{BW}})/(2m_e^2)$. In equation (2.22), note that the linear Breit-Wheeler cross-section is related to the Dirac's pair-annihilation cross-section σ_{D} given in equation (2.21) by a factor of $2\hat{\beta}^2$.

The maximum value of the cross-section is obtained for combinations of photon energies that satisfy the condition where $s = 2$ and $\hat{\beta} = 1/\sqrt{2}$. Independently of the photon energy combination, the maximum Breit-Wheeler cross section is approximately $\sigma_{\mathrm{BW}}^{\max} \approx 170\,\mathrm{mb}$. The small cross-section of the linear Breit-Wheeler makes this process one of the most difficult fundamental QED processes to be observed experimentally on Earth.

2.3.3. Schwinger Pair Production

So far, Heisenberg's uncertainty principle has not been included in the description of the Dirac sea and the quantum vacuum. By doing so, the uncertainty of a photon

---

[10]Equation (2.22) results in cross-section values in units of eV^{-2}. Therefore, we apply the conversion factor of $\approx 3.9 \times 10^{17}$ mb/eV^{-2} on the results presented here to get cross-section values in units commonly used in high-energy physics.
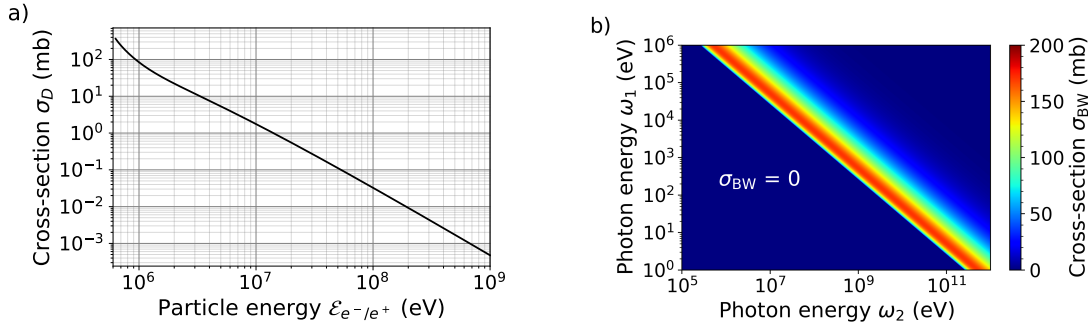
Figure 2.12.: Cross-sections for a) pair annihilation, and b) linear Breit-Wheeler pair production. The cross-section of the pair annihilation process diverges at low particle energies. Hence, low-energy particles have a higher probability of creating photon pairs. This process does not have a threshold to start. On the other hand, the linear Breit-Wheeler pair-production is only possible to occur if the threshold of $\omega_1 \omega_2 \gtrsim m_e^2$ is achieved. The maximum of its cross-section of $\sigma_{\mathrm{BW}}^{\max} \approx 170\,\mathrm{mb}$ is always the same independently of the photon energy combination. Moreover, the region for values of $\sigma_{\mathrm{BW}} = 0$, the energy threshold condition of the process has not been met yet. Note that equation (2.22) results in cross-section values in units of eV^{-2}. Hence, the conversion factor of $\approx 3.9 \times 10^{17}\,\mathrm{mb/eV}^{-2}$ to obtain the cross-section values in units commonly used in high-energy physics is employed.

and electron momenta (and energy) can overcome the pair creation threshold of $2\,m_e\,c^2$ predicted by Dirac's theory causing spontaneous transitions, known as vacuum fluctuations, of electrons from the negative to the positive energy state. Note that the spontaneous transitions are only possible over distances of the reduced Compton wavelength λ_c. These vacuum fluctuations generate virtual particles which can be turned into observable particles by applying a strong electric field on them that is capable of separating both particles apart. This process of turning the virtual pairs from the quantum vacuum by separating them apart using an electric field is called Schwinger pair production[11].

According to Schwinger's theory, the presence of a uniform electric field E in a vacuum accelerates the virtual particle pairs. As the strength of the E-field increases, the virtual pairs acquire energies larger than the pair creation threshold of $2\,m_e\,c^2$ from the field, i.e., the binding energy between the pairs over the Compton wavelength, and become real [162]. The field strength required to transform the virtual particles

---

[11]The Schwinger pair production was first investigated by Sauter in 1936 [160], followed by studies from Heisenberg and Euler in 1936 [161], and later its production rates were computed by Schwinger in 1951 [1].

into measurable real electron-positron pairs was already introduced in chapter 1, equation (1.2), and it is known as the Schwinger critical field E_c. To calculate its value, one needs to evaluate the work performed by the slow varying but strong electric field E_c on a virtual particle over the reduced Compton wavelength which is given as $e\,E_c\,\lambdabar_c = m_e\,c^2$. by substituting the definition of the reduced Compton wavelength $\lambdabar_c = \hbar/(m_e\,c)$ and rearranging the terms, one obtains the field E_c as

$$E_c = \frac{m_e^2\,c^3}{e\,\hbar} \approx 1.32 \times 10^{16}\,\mathrm{V\,cm^{-1}}\,, \tag{2.23}$$

According to the theory derived by Schwinger [1], the probability of the particles to become real $P_{e^-e^+}$ is proportional to [1, 162, 163],

$$P_{e^-e^+} \propto \exp\left(-\pi\,\frac{E_c}{E}\right)\,, \tag{2.24}$$

where E is the strength of the electric field applied to the quantum vacuum. Note that the value of the critical field is extremely large, indicating that for very small electric field strengths, i.e., $E \ll E_c$, the pair creation effect is exponentially suppressed. However, for fields E on the order of the critical field or larger, the Schwinger pair production starts to become accessible.

The Schwinger pair production can be seen as the tunneling of an electron from the negative to the positive continuum through the energy gap which is deformed by the critical field E_c applied on the quantum vacuum [164]. Figure 2.13 a) illustrates how the tunneling of an electron from the negative to the positive continuum via the Schwinger pair creation mechanism occurs. Hence, the Schwinger pair production effect can also be understood through an analogy with the atomic ionization process predicted by Keldysh [165] since both phenomena describe the tunneling of particles mediated by an electric field [162, 165, 166].

In the atomic ionization process, an alternating electric field $E = E_0 \cos(\omega t)$ acting over an atom with biding energy $\mathcal{E}_b$ defines the tunneling frequency of the ionization as $\omega_T = eE_0/\sqrt{2m_e\mathcal{E}_b}$ which defines the typical tunneling time of the interaction between the particle and the potential. Keldysh predicted two physical regimes that are defined by the Keldysh parameters [162, 165]:

$$\gamma_K = \frac{\omega}{\omega_T} = \frac{\omega\sqrt{2m_e\mathcal{E}_b}}{eE_0}\,. \tag{2.25}$$

For the case that $\gamma_K \ll 1$, the electric field E is considered to be instantaneous,
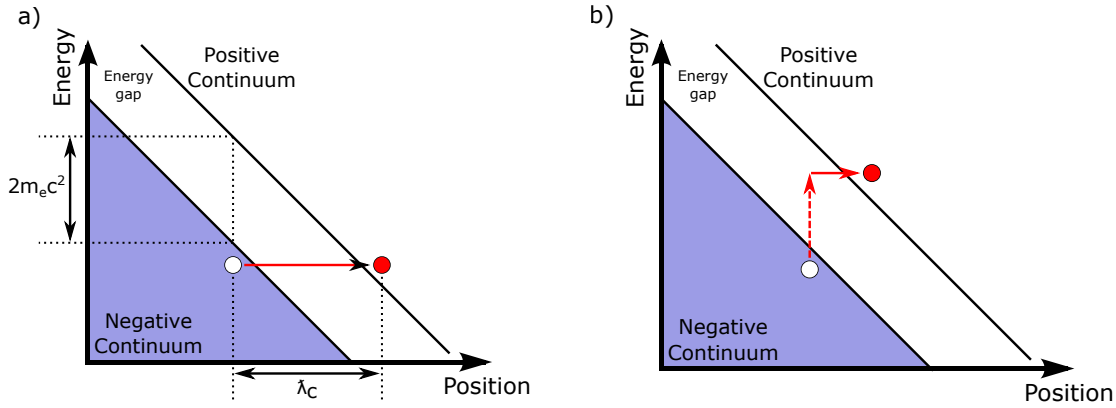
Figure 2.13.: a) Schwinger pair production mechanism is seen as the tunneling of an electron from the negative energy state to the positive continuum through the energy gap which is deformed by the critical field E_c. b) Tunneling of an electron from the negative to the positive continuum via the dynamically assisted Schwinger pair production process. Here, a slow varying but strong background field deforms the energy gap between the negative and positive continuum while the fast but weak field lifts the electron from the negative energy state to a position within the energy gap. Now, the tunneling length is shorter than the reduced Compton wavelength, and, therefore, the pair creation probability increases.

and particle tunneling is permitted. This case is called the non-perturbative regime. On the other limit, $\gamma_K \gg 1$, the electric field varies quickly, and tunneling is not possible anymore. Thus, ionization is only possible through the absorption of many photons. Therefore, the regime is named the multi-photon ionization regime. Ionization probabilities P_{ion} were also calculated by Keldysh for each parameter γ_K limit[162, 165]:

$$
P_{\text{ion}} \propto \begin{cases} \exp\left(-\dfrac{4}{3}\dfrac{\sqrt{2m_e}\mathcal{E}_b^{3/2}}{eE_0}\right) & , \text{for } \gamma_K \ll 1 \,(\text{non-perturbative regime}) \,, \\[2em] \left(\dfrac{eE_0}{2\omega\sqrt{2m_e\mathcal{E}_b}}\right)^{2\mathcal{E}_b/\omega} & , \text{for } \gamma_K \gg 1 \,(\text{perturbative regime}) \,. \end{cases} \tag{2.26}
$$

The Keldysh method can be extended to pair-production as shown by different authors [162, 166–170]. Starting with an oscillating electric field $E = E_0 \cos(\omega t)$ and binding energy of $\mathcal{E}_b = 2m_e$ as the threshold condition, the tunneling frequency for the pair-production becomes $\omega_{\text{p.p.}} = eE_0/m_e$. And, analogously, one can define a parameter $\gamma_{\text{p.p.}}$ as,

$$\gamma_{\text{p.p.}} = \frac{\omega}{\omega_{\text{p.p.}}} = \frac{m_e\,\omega}{e\,E_0} = \frac{1}{\text{a}_0}\,. \tag{2.27}$$

Equation (2.27) has a similar form to the Keldysh parameter for atomic ionization in equation (2.25). However, the parameter $\gamma_{\text{p.p.}}$ is inversely proportional to the normalized field strength $\text{a}_0 = e\,E_0/(m_e\,\omega)$. The two physical regimes possible with this analogy are:

(i) As a_0 becomes smaller than the unit, $\text{a}_0 \lesssim 1$, $\gamma_{\text{p.p.}} \geq 1$, and the pair production process occurs in the perturbative regime, also known as the multi-photon regime. Here, multiple photons (usually optical photons with energy ω_0) are required to interact with a single high-energy photon (e.g. a high-energy bremsstrahlung photon ω_γ) to satisfy the threshold limit of the production process of $(N\omega_0)\,\mathcal{E}_\gamma \geq m_*^2$ to generate an electron-positron pair, where N is the number of low energy photons of energy ω_0 and $m_* = m_e\sqrt{1 + \text{a}_0^2/2}$ is the intensity-dependent effective mass of the leptons [2, 171].

(ii) On the other limit, which $\text{a}_0 \gg 1$, the parameter $\gamma_{\text{p.p.}}$ becomes very small, $\gamma_{\text{p.p.}} \ll 1$, and the pair production process is said to be in the non-perturbative regime. In this case, the electric field is also considered constant and it is typically required a large number of laser photons to deform the energy gap between the negative and positive continuum to overcome the threshold of pair production [3]. The probability rates for the non-perturbative regime are calculated using the SF-QED framework and are strongly dependent on the χ_γ parameter previously given in equation (1.6). The pair creation in the non-perturbative regime, namely the nonlinear Breit-Wheeler process, is introduced in the next section.

2.3.4. Nonlinear Breit-Weeler Pair Production

The pair creation via the Schwinger mechanism is yet to be achieved in the laboratory since the strong Schwinger critical field is orders of magnitude far from be reached, even with the use of the upcoming intense lasers at facilities such as ELI [4, 5] and Apollon [6]. To enhance the pair production probability of the Schwinger mechanism, one can combine a slow varying but strong background field with a fast but weak field to increase the pair production probabilities. This method is called dynamically assisted Schwinger pair production [172–179].

The slow varying but strong background field deforms the energy gap between the negative and positive continuum while the fast but weak field lifts the electron from the negative energy state to a position within the energy gap. Now, the tunneling length is shorter than the reduced Compton wavelength as required by the Schwinger critical field, and, therefore, the pair creation probability increases by orders of magnitude due to its exponential dependence on the tunneling length [180]. Figure 2.13 b) illustrates the dynamically assisted Schwinger mechanism.

The nonlinear Breit-Wheeler can be interpreted as an assisted Schwinger mechanism where the strong varying but strong background field of $a_0 \gg 1$ is produced by an intense laser, and the fast varying but weak field is obtained from a highly-energetic γ-photon, which, in our case, is produced via bremsstrahlung in the FOR2783 experiment and nonlinear inverse Compton scattering in the E-320 project.

As mentioned before, due to large value of a_0, the nonlinear Breit-Wheeler is considered a non-perturbative, quasi-static strong-field regime. In this interaction regime, the electric field is treated as a constant, and the process evaluated with the SF-QED framework. The diagram representing this effect is illustrated in figure 2.14 where a highly-energetic photon interacts with an extremely large number of laser photons and an electron-positron pair is generated.
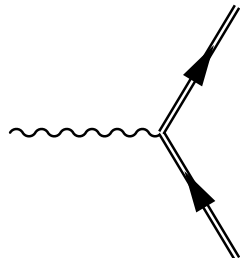
Figure 2.14.: Feynman diagram of the nonlinear Breit-Wheeler pair production. A highly-energetic photon interacts with an extreme large number of laser photons and an electron-positron pair is created. The double lines represents the Volkov dressed states of the particles by the laser field.

Assuming a γ-photon of energy ω_γ colliding with a laser beam of intensity I with photon energy of ω_0, the pair-production probability rate for the nonlinear BW process is given, in rationalized units and for linearly polarized laser light, as [2, 3]

$$\frac{\mathrm{d}\,\mathrm{P}}{\mathrm{d}\,t} = -\frac{\alpha\,m_e^2\,\chi_\gamma}{16\,\omega_\gamma} \int_{z_0}^{\infty} \mathrm{d}z\,\frac{8u+1}{\sqrt{z}\sqrt{u^3(u-1)}}\mathrm{Ai}'(z)\,, \qquad (2.28)$$

where $z_0 = (4/\chi_\gamma)^{2/3}$, $u = (z/z_0)^{3/2}$, and χ_γ is the quantum nonlinear parameter

introduced in equation (1.6). Integrating equation (2.28) over a laser pulse cycle, the pair conversion probability per cycle P is obtained. At low values of $\chi_\gamma \ll 1$, the probability exhibits an exponential suppression of $P \sim \chi_\gamma \exp\left(-8/3\chi_\gamma\right)$ which is similar to the ionization suppression introduced in equation (2.26). On the other limit, $\chi_\gamma \gg 1$, the pair conversion probability rate scales as $P \sim \chi_\gamma^{2/3}$ which is considered equivalent to the ionization over-the-barrier limit. Figure 2.15 a) shows the pair conversion probability per laser cycle for different γ-photon energies as function of the laser intensity. The exponential suppression is clearly seen at low laser intensities.
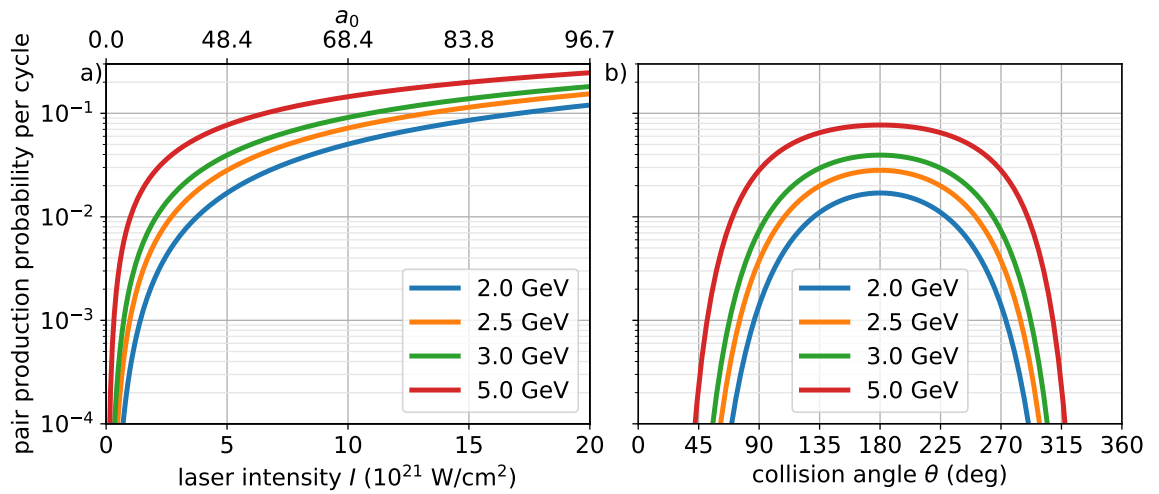
Figure 2.15.: Pair conversion probability per laser cycle assuming $\omega_0 = 1.55\,\text{eV}$: a) for a head-on collision between different colliding γ-photon energies as function of the laser intensity; b) for different colliding angles θ and a constant laser intensity of $I = 5 \times 10^{21}\,\text{W}\,\text{cm}^{-2}$. Figure adapted from my recent publication Ref. [3].

In figure 2.15 b), the influence of the colliding angle θ between the γ-photon and the laser beam is also presented. At head-on collisions ($\theta = 180°$), the pair conversion probability presents its maximum value. However, by decreasing the angle to about $\theta = 150°$, the conversion probability does not reduce significantly. This fact gives flexibility when designing nonlinear BW experiments as discussed in Ref. [3].

3. Single Particle Detection System for SF-QED Experiments

A precondition for SF-QED experiments is the collision of high-energy electron beams with intense laser pulses to generate the high-energy γ-photons required to trigger the pair production process via nonlinear Breit-Wheeler. Once the γ-photons are created through bremsstrahlung or nonlinear inverse Compton scattering, the primary electron beam is cooled down at beam dumps located close to the area where the detectors are found. The cooling down of the electron beam at the dump produces a shower of low-energy secondary particles with an energy of few-MeV that is backscattered towards the detectors acting as background radiation. In the particular case of all-optical SF-QED experiments, such as the FOR2783 experiment, the γ-beam produced via bremsstrahlung becomes an additional source of background radiation when the photons are also cooled down. Depending on the level of the background radiation that reaches the detectors, the signal of a Breit-Wheeler particle cannot be distinguishable from the background and therefore not detected.

In both experiments, E-320 and FOR2783, a small number of nonlinear Breit-Wheeler process pairs are expected as to be seen in the following chapters. Therefore, the detector development for SF-QED experiments presents the challenge of not only being capable of rejecting low-energy background radiation but also it should be able to detect single-particle hits.

Despite the challenges mentioned above, this chapter introduces the single-particle detection systems designed for the upcoming SF-QED experiments, E-320 at FACET-II (SLAC) and FOR2783 at the ATLAS-3000 laser system at CALA, that are successfully capable of detecting single-particle hits with a high confidence level of $> 99\%$ while being insensitive to the background radiation inherent to the SF-QED experiments.

Both systems introduced here share the same construction features and detection method. The systems comprise two LYSO pixelated crystal screens and a Cherenkov calorimeter where most of the energy of the incoming particle is deposited inside and converted into Cherenkov light that is detected by photomultiplier tubes (PMTs). Finally, a calibration of the single-particle detection system performed at the ELBE radiation source at the Helmholtz-Zentrum Dresden-Rossendorf (HZDR) is provided.

3.1. Single-Particle Detection System for the Experiment-320 at FACET-II

The detection system designed for the Experiment-320 at FACET-II comprises two pixelated LYSO:Ce screens to provide high spatial resolution and tracking information of the single-particle propagating trough the system, and a Cherenkov calorimeter segmented into detection channels.

After an electron-positron pair (also referred to as signal particle from now on) is created via the nonlinear Breit-Wheeler process, it propagates until a dipole magnet that deflects the positron toward the single-particle detection system. The positron interacts first with the pixelated scintillating screens and then the Cherenkov calorimeter. As the particle propagates through the screens, scintillation light is generated and then imaged by a highly-sensitive camera. The position of the scintillation light on both screens allows us to retrieve the trajectory of the incoming particle and ensure that the single-particle hit is indeed from a signal particle and not a high-energy background radiation particle. After the positron has propagated through the screens, it reaches the Cherenkov calorimeter, where its energy is fully deposited in one of the active channels generating an electromagnetic shower of secondary particles that produces Cherenkov photons inside the device. Photomultiplier tubes at the rear of each detection channel of the calorimeter detect the Cherenkov photons.

The detection system is placed about 3.6 meters from the dipole magnet. The screens are located in front of the calorimeter with a separation between them of about 33 cm and are imaged by an optical system made of a large plano-convex condenser lens (PCX lens), image intensifier, and a single-photon sensitive Hamamatsu ORCA FLASH4 camera [181]. Figure 3.1 a) presents the setup of the single-particle detection system for the E-320 collaboration. A detailed view of the calorimeter is shown in figure 3.1 b) where the incident particle range of $2.5 - 5.6 \, \text{GeV}$ expected to be deflected towards the detectors is highlighted, please see chapter 4 for details on the particle detection range and dipole magnet configuration.

3.1.1. Pixelated LYSO:Ce Tracking Layers

The pixelated scintillating screens used on the detection system are made of LYSO:Ce crystals. These crystals are ideal to use in SF-QED experiments as tracking layers due to its high scintillating yield of about 25 photons/keV and fast decay time of approximately 40 ns which is beneficial to reject noise on the detectors originated from

a)

Cherenkov
calorimeter

LYSO 2

Mirrors

LYSO 1

Positron
dispersion

5.6 GeV

2.5 GeV

PCX condenser
lens

Gated image
intensifier

ORCA Flash4v3
camera

b)

PMTs

Reference
channels (blue)

5.6 GeV

2.5 GeV

Central detection
channels (red)

Reference
channels (blue)
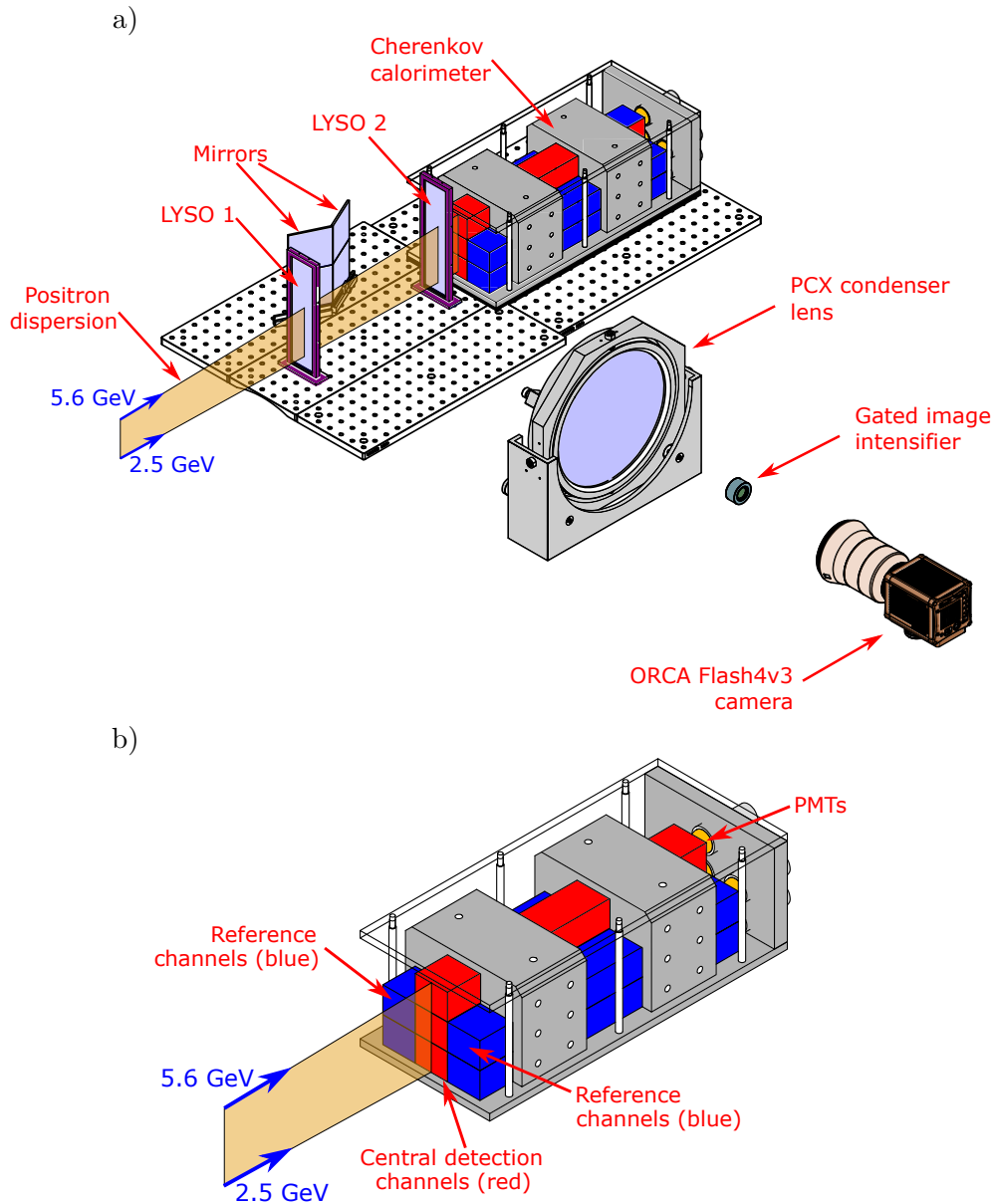
Figure 3.1.: a) Design of the single-particle detection system for E-320 at FACET-II. The incident single GeV-positron travels through two pixelated LYSO scintillating screens which provide particle tracking and high-resolution spectral information before entering the Cherenkov detector at one of its lead-glass detection channels where its energy is fully deposited. b) Detailed view of the Cherenkov detector. The background reference channels, where no signal particle is expected to strike, are shown in blue. The central detection channel of the detector, in which signal leptons are deflected, is illustrated in red. The Cherenkov photons produced inside the lead-glass channel are detected by photomultiplier tubes (PMTs) at the rear of each channel. The positron direction of dispersion is within the yellow area with limits of 2.5 - 5.6 GeV.

far away sources, for example, in the case of the E-320 project, the noise created by backscattered radiation from the main beam dump which is located about 9 meters downstream from the detectors.

An alternative to the LYSO screens is the use of silicon tracking layers which have been widely used in high-energy physics experiments (see Ref. [182] for a review). Silicon detectors are pixelated arrays resembling CMOS chips with pixel sizes on the order of a few micrometers and thickness of 100's-µm. They usually have nanoseconds temporal resolution and are only sensitive to high-energy charged particles [25] since high-energy photons have a very low probability of absorption due to the thin thickness of the silicon layers. Despite the advantages of silicon tracking layers, one would need large strips of silicon detectors in the E-320 and FOR2783 experiments to cover the large deflection trajectories suffered by the signal particles due to the dipole magnets. Hence, the use of large strips of silicon detectors would elevate the costs of the detection system. In contrast, the LYSO pixelated crystal screens designed for our single-particle detection system present an effective cost-benefit solution for tracking layers in comparison with the silicon detectors due to their high-spatial resolution and capability of providing single-particle tracking information.

Both LYSO scintillating screens used in the E-320 detection system have overall dimensions of $40\,\mathrm{mm} \times 200\,\mathrm{mm} \times 4\,\mathrm{mm}$ with crystal pixel sizes of $2\,\mathrm{mm} \times 2\,\mathrm{mm} \times 4\,\mathrm{mm}$ which is enough to provide a high spatial resolution and tracking information on the single-particles propagating through the detectors. A pixelated screen is presented in figure 3.2. To image both screens, a plano-convex (PCX) lens (diameter of 250 mm and focal length of 400 mm) is placed about 800 mm distant from the screens, and an image intensifier imaging the entire active region of the screens are placed 270 mm after the PCX lens. The intensifier is essential in the imaging system to amplify and gate the light signal of the screens. The output of the gated image intensifier is imaged by a Hamamatsu ORCA camera with an f/1.4 macro-lens of 28 mm focal length. The camera is placed about 250 mm after the intensifier to maximize the photon collection and efficiency of the system.

Knowing the position of the components of the imaging system of the system, the number of scintillation photons $\mathrm{N}_{\mathrm{LYSO}}^{1,2}$ detected for each of the screens (screen-1 or 2) is calculated as

$$\mathrm{N}_{\mathrm{LYSO}}^{1,2} = \mathrm{N}_{\mathrm{scin}}^{1,2} \cdot \mathrm{CE}_{\mathrm{PCX}} \cdot \mathrm{G}_{\mathrm{int}} \cdot \mathrm{CE}_{\mathrm{orca}} \cdot \mathrm{QE}_{\mathrm{orca}}\,, \tag{3.1}$$

where $\mathrm{CE}_{\mathrm{PCX}}$ is the collection efficiency of PCX condenser lens calculated as $\mathrm{CE}_{\mathrm{PCX}} =$
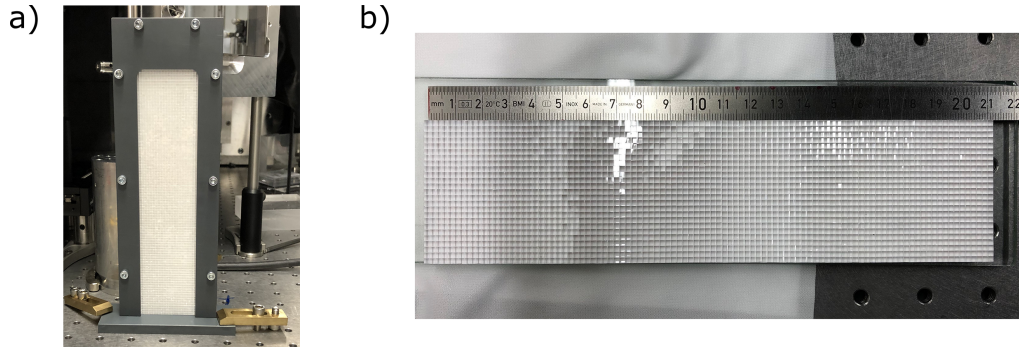
a)

b)

Figure 3.2.: LYSO screen designed for the E-320 single-particle detection system. In a) the screen is placed in its holder and b) shows the screen dimensions of $40\,\text{mm} \times 200\,\text{mm} \times 4\,\text{mm}$ with crystal pixel sizes of $2\,\text{mm} \times 2\,\text{mm} \times 4\,\text{mm}$.

$(\pi \cdot 125^2)/(800^2)/(4\pi) = 6.1 \times 10^{-3}$, CE_{Orca} is the collection efficiency of the camera $\text{CE}_{Orca} = (\pi \cdot 20^2)/(250^2)/(4\pi) = 1.6 \times 10^{-3}$, $\text{QE}_{Orcas} \approx 0.4$ is the quantum efficiency of the ORCA-Flash camera at the scintillation light wavelength of 410 nm [181]. The constant $\text{G}_{int} = 10^3$ represents the dual microchannel plate (MCP) gain of the image intensifier applied. Note that the quantum efficiency of the intensifier is already taken into account in the G_{int} value.

3.1.2. Description of the Cherenkov Calorimeter

The Cherenkov calorimeter, which is placed after the second LYSO screen, is made of up to 7 detection channels of $50\,\text{mm} \times 40\,\text{mm} \times 400\,\text{mm}$ Schott F2 lead-glass wrapped in enhanced specular (ESR) foils to prevent cross-talk of the optical Cherenkov photons between the channels. F2 lead-glass has been already used in several past experiments as the choice of dielectric material for producing Cherenkov radiation due to its linear response at measurements of particle energies between $1\,\text{GeV}$ and $4\,\text{GeV}$ and absence of scintillation light [183, 184]. The lack of scintillation light favors our detection system to reject low-energy background radiation which is unable to generate scintillation light inside the glass and does not produce Cherenkov photons that can be mistaken as the signal of a Breit-Wheeler GeV-particle. Moreover, the glass features a radiation length of $X_0 = 3.14\,\text{cm}$ and a Molière radius of $\text{R}_\text{M} = 3.4\,\text{cm}$ in which about 90% of the transverse secondary shower is contained within the material. The length of a 400 mm of a detection channel is designed to contain the full longitudinal particle shower produced by an incident GeV-signal particle. It means that the total path length of the secondary particles of the electromagnetic shower is proportional to the energy of the incoming signal particle, and, consequently, the total number of Cherenkov

light produced inside the glass is proportional to the energy of the incident particle. As an example, figure 3.3 shows a GEANT4 simulation of the longitudinal profile of a particle shower produced by a 3 GeV particle hit centrally on an F2 lead-glass detection channel. As observed, the lateral shower is well contained within the Molière radius and the longitudinal shower within the 400 mm channel length.
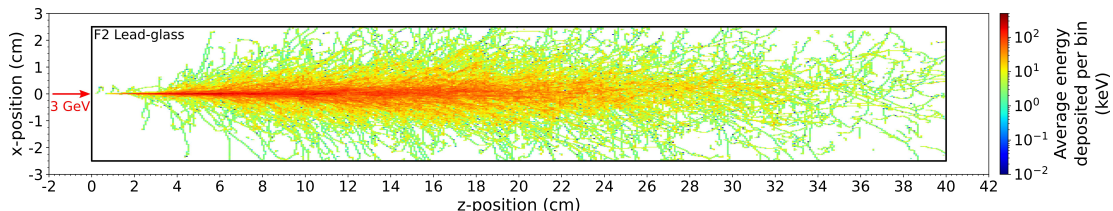

Figure 3.3.: GEANT4 simulation of the longitudinal shower profile after a 3 GeV positron hit centrally on a single detection channel of F2 lead-glass block 50 mm × 40 mm × 400 mm. The lateral electromagnetic shower is well contained within the Molière radius ($R_M = 3.4$ cm) and the longitudinal shower within the 400 mm length of the channel. Each bin has an area of 0.1 mm^2.

The Cherenkov calorimeter designed for the E-320 project is divided into two main regions: the background (reference) channels and the active area where the positrons signal particles are incident. Both regions are shown in detail in figure 3.1 b). The active area of the detector is composed by the central three detection channels which sums up to a total area of $3 \cdot (40\,\text{mm} \cdot 50\,\text{mm}) = 6000\,\text{mm}^2$. On the other hand, the background channels are responsible for monitoring the background levels at the detector on a shot-to-shot basis and for providing better discrimination of background events against single hits on the active detection channels. Detection of the Cherenkov radiation produced on each of the channels is achieved by a photomultiplier tube (PMT) [185] connected at the rear of each lead-glass channel through an index-matching gel (refractive index of about 1.5). The chosen PMTs are capable of single-photon detection in the spectral range of about 300 nm to 550 nm with a maximum gain of 1×10^6 and rise time of $< 3\,\text{ns}$. Such features are essential to detect the low Cherenkov light produced in the channels and to allow rejection of the background noise by also temporal gating the PMT signal acquisition.

The number of detected photons by the photomultiplier tubes (PMTs) N_{det} is given by the sum of the number of signal photons produced by a single-particle hit N_{sig} plus the number of photons produced by the background noise N_{bg} and the expected

uncertainty $<\sigma_{\text{det}}>^2 = \sigma_{\text{sig}}^2 + \sigma_{\text{bg}}^2$,

$$N_{\text{det}} = N_{\text{sig}} + N_{\text{bg}} \pm <\sigma_{\text{det}}> \ . \tag{3.2}$$

Hence, the number of signal photons produced N_{sig} is easily calculated by subtracting the number of detected photons by the PMTs by the number of background photons which are monitored on a shot-to-shot basis at the reference channels of the calorimeter: $N_{\text{sig}} = N_{\text{det}} - N_{\text{bg}} \pm <\sigma>$ where its uncertainty is given by propagating the variances such that $<\sigma>^2 = <\sigma_{\text{sig}}>^2 + 2 <\sigma_{\text{bg}}>^2$. After calculating the number of signal photons produced N_{sig} with its variance given as $<\sigma_{\text{sig}}> = \sqrt{N_{\text{sig}}}$. The energy of the single-particle which hit the calorimeter is obtained by using the calibration curve $\mathcal{E} = (N_{\text{sig}}/0.13)^{(1/1.04)}$ which will be introduced later in this chapter in section 3.3.

3.1.3. Event Identification and Rejection

Now that the single-particle detection system and the signal expected from the scintillation screens and the Cherenkov calorimeter have been introduced, we discuss in this section how to identify a signal event that propagates through the system.

Identifying a positive event requires both scintillation screens, LYSO 1 and LYSO 2, to record an event above the threshold that corresponds to a possible track originated at the interaction point, and, in addition, the calorimeter channel on the corresponding track must record an event. Consequently, the identification of a positive event has a high confidence level of $> 99\%$.

False-positive events are therefore only possible if the calorimeter measures a sufficiently high signal above the background. Since the background is presumed to consist of a bath of many low energy events, as will be seen in the following chapters 4 and 5, monitoring the background radiation noise and comparing it with the signal channels of the calorimeter prevent false positives from arising from the low energy background.

To evaluate the real false-positive rate, one needs to analyze the probability of giving a matching false-positive on the Cherenkov channel, i.e., high energy events localized on one detector (or split event). To quantify this probability, the background radiation level of hard γ-photons in FACET-II and CALA needs to be known. Thus, background radiation measurements will be performed at both facilities during the commission of the experiments.

3.2. Single-Particle Detection System for the FOR2783 experiment at CALA

Following the same design concept of the single-particle detector for the Experiment-320 at FACET-II, the system designed for the FOR2783 project has also two LYSO screens and a Cherenkov calorimeter behind the screens. However, here a coincidence measurement between the electrons and positrons generated due to the SF-QED interactions is possible due to the combination of separator and collimator magnets. The arrangement of the detectors is shown in figure 3.4. The LYSO screens and its imaging system are omitted from the figure for better visualization, however they are an essential part of the detection system.
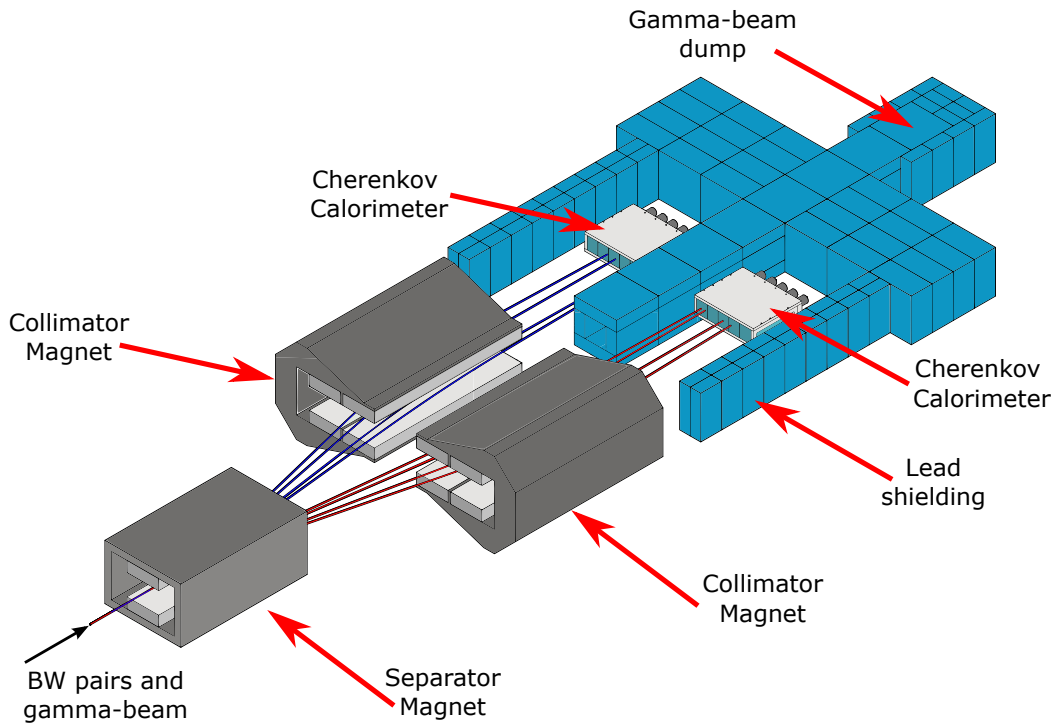
Figure 3.4.: Single-particle detection system for the FOR2783 project. A separator magnet deflects the charged particles towards collimator magnets that directs them to the detectors. The bremsstrahlung γ-beam continues to propagate in a straight path towards the gamma-beam dump. Blue trajectories are the electrons and red trajectories represents the positrons.

The Cherenkov calorimeter designed for the FOR2783 experiment is composed of 5 detection channels also made of Schott F2 lead-glass. Each lead-glass has dimensions of $60\,\mathrm{mm}\,(\text{height}) \times 50\,\mathrm{cm}\,(\text{width}) \times 200\,\mathrm{mm}\,(\text{length})$. Note that the length of the calorimeter channels is half of the E-320 Cherenkov detector, but, despite the shorter

length, the electromagnetic shower produced by an incident signal particle on the detector is still contained within the lead-glass channel since the expected signal particles have less energy compared to the signal expected from the E-320 project.

The pixelated LYSO screens used on the diagnostics have a larger overall dimension of 60 mm (height) × 20 cm (width) × 4 mm (depth) with crystal pixel size also of 2 mm × 2 mm × 4 mm. The screens are image by a single-photon sensitive camera 4Picos capable of gating times down to 200 ps [186] attached to a f/1.4 macro lens placed about 870 mm away from the screens. Here, a combination of PCX lens and image intensifier is not necessary since the camera is capable of amplifying the scintillation photon signal due to an already built-in dual multi-channel plate (MCP). Calibration of the 4Picos cameras to be utilized in the experiment are presented in Appendix D.

In this case, the response of the LYSO screens can be calculated using the LYSO crystal absolute light efficiency Y_{LYSO}^{eff} (given in units of photons/sr/pC), and taking into account the light collection solid angle Ω, the transmission efficiency of the lens used on the 4Picos camera T_{lens}:

$$N_{ph,\,det} = Y_{LYSO}^{eff} \cdot \Omega \cdot \frac{1.602 \times 10^{-19}}{10^{-12}} \cdot T_{lens} \,. \qquad (3.3)$$

Note that the term $(1.602 \times 10^{-19}/10^{-12})$ represents the charge of a single electron or positron given in picocoulombs.

The Cherenkov calorimeter is also arranged in a different configuration from the detector proposed for the E-320 experiment. Here, the calorimeter is composed of five Schott F2 lead-glass detection channels with dimensions 60 mm (height) × 50 mm (width) × 200 mm (depth) each. Note that the expected particle energy incident on the calorimeter lies in the range between 300 MeV and 1.5 GeV (detailed explanation given in chapter 5) therefore the length of each channel is shortened by half of the length of the E-320 calorimeter since the incident particles are not required to propagate any further to deposit its entire energy in the glass. Note that the active area of the calorimeter is now also larger, given by $5 \cdot (50\,mm \cdot 60\,mm) = 1500\,mm^2$, and no channel for shot-to-shot background level measurement is present. In this case, the background noise is monitored constantly by turning off the collider laser after a set of shots to inhibit the SF-QED interaction between the γ-photons and allow the bremsstrahlung γ-ray to propagate directly towards the gamma-dump. Any produced background is then recorded for the later data evaluation and quantification of false-positive hits on the detectors. The detection of the Cherenkov photons at the calorimeter is also made by photomultiplier tubes attached at the rear of each lead-glass using index-matching

gel between the components.

The evaluation of the response of the Cherenkov calorimeter follows the method presented in the previous section 3.1.2. The total number of signal photons produced N_{sig} by a signal particle is calculated by subtracting the number of detected photons N_{det} on the PMTs by the number of background photons N_{bg} such that $N_{sig} = N_{det} - N_{bg} \pm <\sigma>$ where the uncertainty is obtained by propagating the variances as $<\sigma>^2 = <\sigma_{sig}>^2 + 2<\sigma_{bg}>^2$. Finally, the energy of the incident signal particle is calculated using the calibration curve of the calorimeter.

To identify a positive event and to prevent false-positive hits, we follow the same method previously explained in section 3.1.3. For a positive event to happen, the signal obtained from the scintillating screens should be above the threshold consistent with a possible track of a signal particle. In addition, the Cherenkov calorimeter should also record a signal on the detection channel corresponding to the same particle track. Thus, by performing this analysis, the confidence level of a positive event is above $> 99\%$.

3.3. Calibration of the Cherenkov Calorimeter Detector

The Cherenkov calorimeter of the Experiment-320 was calibrated at the ELBE radiation source at the Helmholtz-Zentrum Dresden-Rossendorf (HZDR) using the linear accelerator dark current. The calibration results obtained for a single detection channel of the E-320 calorimeter are also valid for the detector designed for the FOR2783 project since they share the same construction features and detection principles.

The accelerator provides single monoenergetic 27 MeV electrons from its dark current with an electron weighted average rate of (0.156 ± 0.005) electrons/RF cycle. The dark current was irradiated into the central channel of the calorimeter which was placed about 43.5 cm away from the $100\,\mu m$ thick beryllium exit window of the accelerator. The passage of the single electrons through the exit window does not produce significant secondary radiation that can significantly influence the calibration measurements since the total stopping power of the thin exit beryllium window is only about 36 keV for 27 MeV primary electrons. The dark current of the accelerator was characterized using radiochromatic films (RCFs) [187], and the weighted average of two calibration values was calculated. For details on the measurement of the dark current, please see Ref. [103] published by the author.

Figure 3.5 shows the calibration setups of the Cherenkov calorimeter and the light yield of the LYSO screens implemented at ELBE.
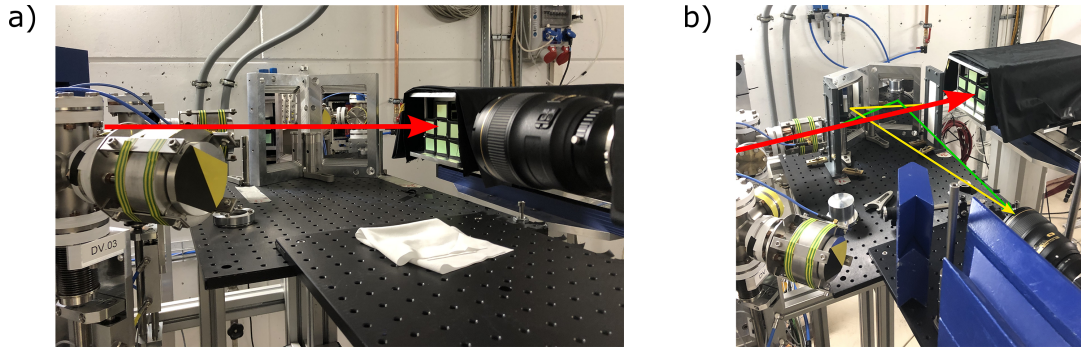
Figure 3.5.: a) Calibration setup of the Cherenkov calorimeter with the dark current of the ELBE accelerator irradiating over a detection channel. b) Calibration setup of the LYSO crystal light yield using a 5.6 pC electron beam of 27 MeV to generate scintillation light imaged by a camera. The red arrow represents the path of the electron beam, the green arrow shows the path of the scintillation light of LYSO screen-1 after the accelerator exit window, and the yellow arrow indicates the path of the light from LYSO screen-2.

For the calibration of the Cherenkov calorimeter, the gain of the photomultiplier tubes was set to 4×10^6, corresponding to a voltage across the cathode and anode of the PMT of 10^3 V, and a total of 10^4 events, i.e., signal traces of the PMTs, were recorded using PicoScopes [188] digitizers at a high sampling rate. The evaluated number of Cherenkov photons detected by the PMTs as well as the recorded decay times of the signals are shown in the histograms in figure 3.6. An average of 4 Cherenkov photons are recorded by the photomultiplier tube after a single 27 MeV dark current electron hits a single detection channel, and, as seen in figure 3.6 b), the signal produced by the hit of the single-particle produces a signal 1.8 ns long.

GEANT4 Monte-Carlo simulations were performed to compare the calibration results with the designed calorimeter response and evaluate the photon detection efficiency of the device that can later be used to estimate the number of detected Cherenkov photons at different energies. For high fidelity on the number of detected photons, the simulations include the full geometry of the calorimeter and description of the material properties used on the detector. The typical quantum efficiency of the PMT and the photon transmission of the lead-glass over 40 cm length, which are both essential parameters of the calorimeter design and simulations, were included in the Monte-Carlo simulations for the correct estimation of the number of detected photons. Both parameter curves are presented in figure 3.7. The generation of optical photons by the Cherenkov process was only considered in the range of 350 nm to 650 nm in which the combination of the lead-glass transmission spectrum and the PMT quantum efficiency (QE) allows the transport of the optical photons through the system. The
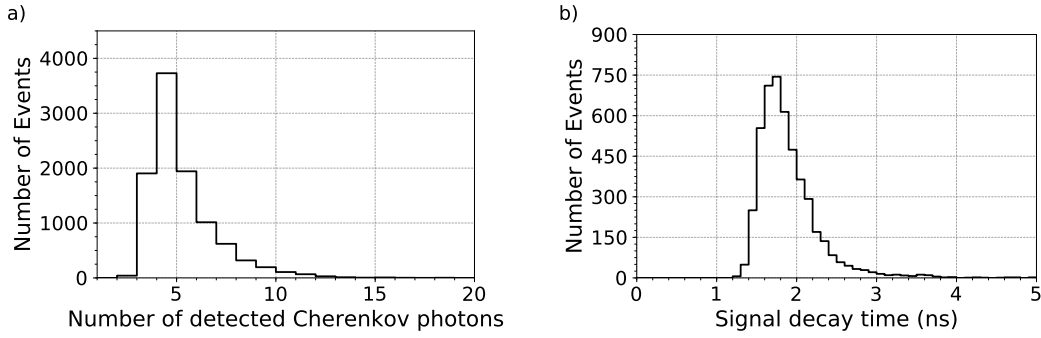
Figure 3.6.: Calibration results of the E-320 Cherenkov calorimeter using the dark current of ELBE accelerator at the Helmholtz-Zentrum Dresden-Rossendorf (HZDR) as source of single 27 MeV electrons. a) Number of detected Cherenkov photons by the photomultiplier tubes of the Cherenkov calorimeter. An average of 4 photons per single electron is detected. b) Decay time of the recorded signal. A single electron hit produces a signal about 1.8 ns long.

simulated distribution of detected photons after a single 27 MeV particle hit in a single Cherenkov detection channel is shown in detail in figure 3.8 a). By fitting a Gaussian curve on the simulated result curve, an average of 17 photons are detected by the PMTs with a variance of $\sigma_{\text{sim}} = 5.5$ photons.
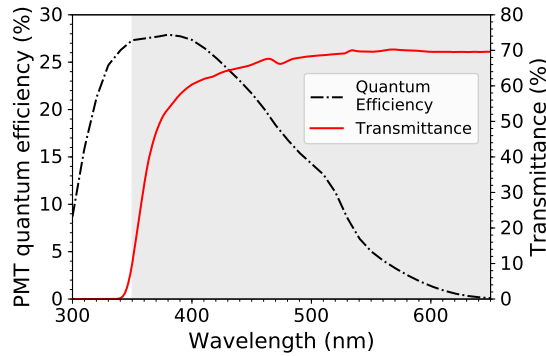
Figure 3.7.: Typical quantum efficiency of the photomultiplier tube (PMT) employed on the Cherenkov calorimeter and the calibrated transmittance of the 40 cm lead-glass. The gray shaded region shows the wavelength region between 350 - 650 nm where both parameters were implemented in the GEANT4 model of the detector to evaluate the number of photons hits on the PMT.

Comparing the simulation results for a single 27 MeV particle hit and the calibration results, we calculate a photon detection efficiency of $\eta \pm \sigma_\eta = (0.23 \pm 0.13)$, where $\eta = 4/17.6 \approx 0.23$ and σ_η is evaluated using error propagation method as $\sigma_\eta =$

$\eta \cdot ((\sqrt{4}/4)^2 + (5.5/17.6)^2)^{1/2} \approx 0.13$.

Based on the photon detection efficiency calculated for the calorimeter, new GEANT4 simulations with different primary single-particle energies in the range between 1 MeV to 4 GeV were performed to predict the number of detected photons by the PMTs. The estimated number of detected Cherenkov photons is presented in figure 3.8 b) with an exponential fit of $N_{SIG} = 0.13 \cdot E^{1.04}$, where E is the energy of the incoming particle in MeV. It is predicted that about 537 photons are detected for an incident 3 GeV single-particle which is expected from the SF-QED experiment at FACET-II. The spectral resolution of the calorimeter depends on the energy of the incoming particle being a representative resolution achieved of 20% better than the 10% possible at high energy range. Rejection of false-positive hits on the calorimeter is possible by combining the reading from the high-spatial resolution provided by the LYSO screens and the number of detected photons by the calorimeter.
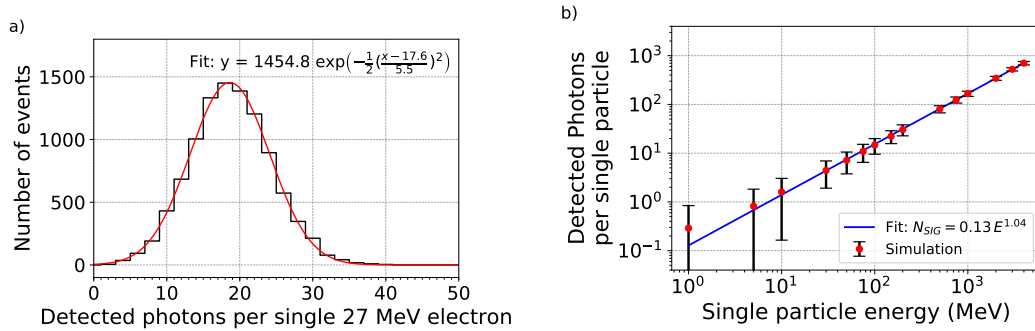
Figure 3.8.: (a) Simulated number of photons detected for a single 27 MeV particle incident centrally on a Cherenkov calorimeter channel. About 17 photons are detected with an RMS variance of 5.5 photons. (b) Calculated number of Cherenkov photons detected per channel for a single incident particle of different energies after the detection efficiency η of 23% and its uncertainty were taken into account. The error bars indicate the standard deviation which determines the energy resolution of the calorimeter. A single 3 GeV particle results in 537 detected photons by the calorimeter. Hence, a single GeV-particle incident on the detector is easily detected by the calorimeter.

To guard against any unknown signal, background level, and non-linearity, calibration of the Cherenkov calorimeter detectors designed for both E-320 and FOR2783 projects are planned during the beamtime, and correction factors will be applied on the given calibration curve in figure 3.8 b).

3.3.1. In-Situ Calibration of the Cherenkov calorimeter detector

At the E-320 experiment, thin foils of high-density materials, for example, tungsten, will be placed on the primary electron beam path. As the electron beam interacts with the thin foil, secondary particles of lower energy than the primary 13 GeV electron beam are produced inside the foil, including electron-positron pairs (mainly via the Bethe-Heitler process). The pairs propagate along the beam path along with the primary electron beam until they reach the main dipole magnet of the experiment. The positrons with energies within the range of 2.5 - 5.6 GeV are deflected towards the detectors producing signals on the scintillating screens and Cherenkov calorimeter. The energy of the deflected positrons is obtained by imaging the screens and analyzing the position where they hit the screens. The signal produced on the Cherenkov calorimeter is compared against the calibrated values and correction factors can be applied to the calibration curves.

A similar correction procedure on the calibration curve of the Cherenkov detectors is performed in The FOR2783 experiment. However, in this case, the detector will be calibrated using a thin back-converter target, e.g., Polytetrafluoroethylene (PTFE), placed on the bremsstrahlung γ-ray path. As the γ-photons interact with the converter target material, secondary pairs are produced via the Bethe-Heitler process. The pairs propagate with the γ-ray beam on the same path as the signal pairs and are deflected towards the single-particle detectors located inside a radiation bunker at CALA. By adjusting the thickness of the PTFE converter foil, one can achieve single-pair production by this method. The energy of the few particles is obtained by evaluating the signal emitted from the scintillating screens, and it is compared against the signal recorded at the calorimeter. By doing so, new correction factors can be calculated and applied at the calibration curve in figure 3.8 b).

3.4. Characterization of the LYSO Crystals

Characterization of the LYSO crystal screens was also performed to determine the crystal scintillation decay time and light yield. In the following sections, both calibrations are presented.

3.4.1. LYSO Decay Time

Using a radioactive Sodium-22 as source of single event hits on the screens, the scintillation light produced by these single events were recorded by photomutiplier

tubes. A total of 1500 PMT traces were recorded and later a curve of the form

$$V = A \left[\exp\left(-\frac{(t - t_0)}{\tau} \right) - \exp\left(-\frac{(t - t_0)}{\tau_p} \right) \right] \Theta(t - t_0) \qquad (3.4)$$

was fitted on each captured trace. Here, the signal amplitude is given by A, the decay time of the signal is represented by τ, τ_P stands for the signal rise time and t_0 is time shift of the signal in the argument of the step-function $\Theta(t)$ which determines where the scintillation signal starts. A single captured trace from the PMT with a fitted curve of the form given in equation (3.4) is presented as example in figure 3.9 a). In addition, the temporal gating window of the screens imaging system and the arrival time of the backscattered noise are also represented in the plot. From the figure, the time window for capturing the LYSO scintillation light ends a few nanoseconds before the arrival of the background noise and, therefore, the acquisition of the scintillation photons without overlapping with the noise is achieved easily.

After analysing all captured traces, the histogram in figure 3.9 b) with all the decay signals τ is plotted. Fitting a Gaussian distribution on the histogram, an average decay time of 42.2 ns with full width at half maximum of 7.1 ns is obtained. Both values are in agreement with measurements reported in the literature [119, 120].
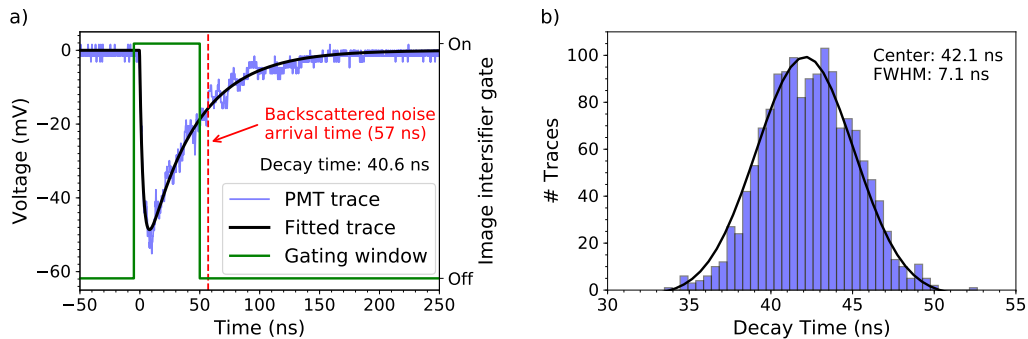
Figure 3.9.: Characterization of the decay time of the LYSO screens using a Sodium-22 as a single event radiation source. (a) Example of a trace captured by the PMTs used to evaluate the decay time of the scintillation signal. The gating window of the imaging system of the screens and the arrival time of the backscattered noise are also plotted demonstrating that scintillation photons can be captured without the influence of the background noise. (b) Histogram distribution of the decay time after 1500 captured traces of single events were analyzed. Performing a Gaussian fit on the distribution, it is found an average decay time of 42.2 ns with FWHM of 7.1 ns is calculated.

3.4.2. LYSO Light Yield

The light yield of the LYSO screens was also characterized in the ELBE radiation source. As shown in figure 3.10, the screens are placed in front of the accelerator exit window and imaged by a Hamamatsu ORCA Flash4 camera attached to a macro lens AF-S NiKKOR 28 mm f/1.4. A monoenergetic electron beam of 27 MeV and 5.6 pC of charge irradiates the screens and the scintillation light captured by the imaging system. In the post-processing of the captured images, only the data from the screen-1 were analyzed for estimating the light yield.
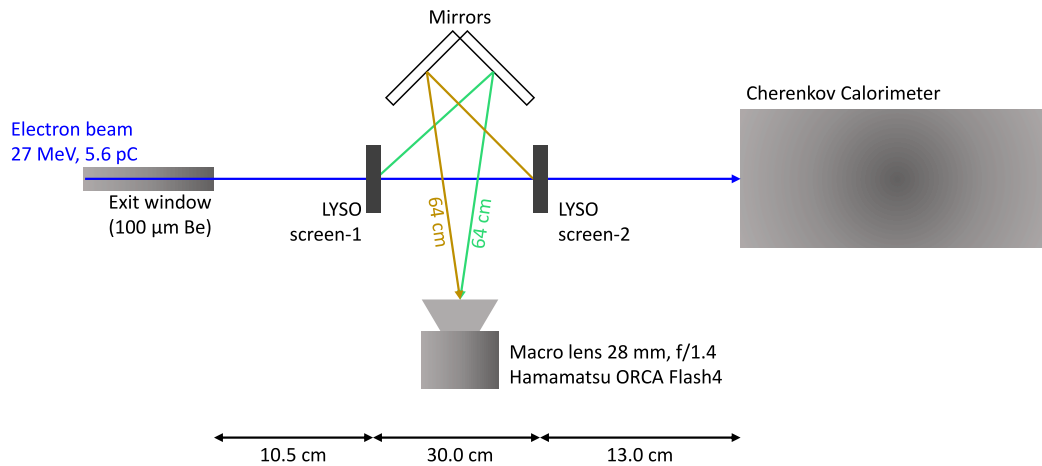

Figure 3.10.: Experimental setup built at the ELBE accelerator for characterizing the light yield of the LYSO crystal screens. A 27 MeV monoenergetic electron beam of 5.5 pC charge irradiates the LYSO screens which are imaged by a highly-sensitive Hamamatsu ORCA Flash4 camera attached to a macro lens of 28 mm focal lens and f/1.4. Only the images from the screen-1 were analyzed for estimating the light yield.

A total of 500 events were captured for the calibration of the crystal light yield. For each image, a region of interest (ROI) was selected and unwarped maintaining the aspect ratio of the screen. An example of an image taken from the first screen is shown in figure 3.11. After, the image counts of each pixel were converted into the number of collected photons using the photon transfer curve of the camera provided by the manufacturer. The absolute scintillation light efficiency of the crystal is then calculated by integrating the number of photons in each pixel and dividing it by the charge of the electron beam, collection solid angle, and transmission losses of the imaging system. A detailed description of the method and the absolute light yield calibration of different crystal screens also performed during the ELBE beamtime is presented in detail in Appendix F.

The average calculated absolute light efficiency of the 500 captured images of the
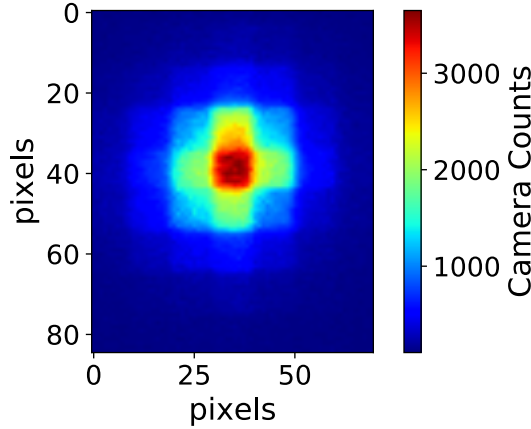
Figure 3.11.: Region of interest of the shot #45 of the LYSO crystal light yield characterization. The scintillation light was captured by the ORCA Flash4 camera with a macro lens of 28 mm focal lens and f/1.4.

LYSO crystal is about $Y_{\text{LYSO}}^{\text{eff}} = 9.08 \times 10^{10}$ photons/sr/pC with standard deviation of $\sigma_{Y_{\text{LYSO}}^{\text{eff}}} = 0.43 \times 10^{10}$ photons/sr/pC. The evaluated light efficiency can also be given in terms of the energy deposited by a single-particle in the crystal. For this purpose, GEANT4 simulations were performed to estimate the amount of energy of a single primary 27 MeV electron is transferred to secondary particles through ionization (stopping power) and bremsstrahlung (radiative power) on the 4 mm LYSO crystal, see figure 3.12 for the simulation results. About $(E_{\text{dep, ioni}}^{\text{LYSO}} \pm \sigma_{E_{\text{dep, ioni}}^{\text{LYSO}}}) = (1.98 \pm 1.41)$ MeV are deposited due to the ionization process for later be transferred into scintillation light and $E_{\text{dep, brems}}^{\text{LYSO}} = (11.34 \pm 3.37)$ MeV is transformed into bremsstrahlung photons.
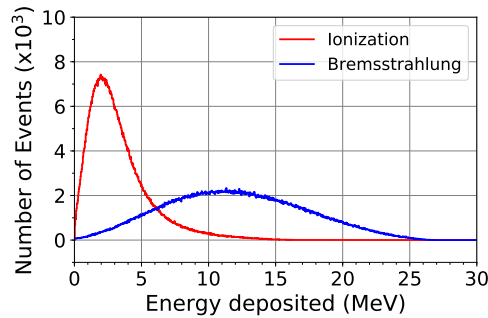
Figure 3.12.: Simulated energy deposited by a single 27 MeV particle into a 4 mm thick LYSO crystal. Approximately (1.98 ± 1.41) MeV are transferred to secondaries that produce scintillation light, and (11.34 ± 3.37) MeV is transferred into bremsstrahlung photons. The simulations were carried out using GEANT4 for a total of 10^6 events.

The light yield is then calculated by converting the $Y_{\text{LYSO}}^{\text{eff}}$ into number of photons

produced by a single-particle in a solid collection angle of 2π sr, and then dividing by the deposited energy for ionization in the material,

$$
Y_{LYSO} = 2\pi \cdot \frac{Y_{LYSO}^{eff}}{E_{dep,\ ioni}^{LYSO}} \cdot \frac{1.602 \times 10^{-19}}{10^{-12}} = 4.62 \times 10^4 \, \frac{photons}{MeV}\,, \qquad (3.5)
$$

where the factor $(1.602 \times 10^{-19}/10^{-12})$ gives the electron charge in units of pC, and 2π is the solid collection angle of the scintillation photon transported to the imaging system that is assumed to be connected directly at the rear of the crystals and capable of detecting all light photons exiting that crystal surface without loss. The uncertainty $\sigma_{Y_{LYSO}}$ on the light yield of the LYSO screen Y_{LYSO} is calculated using error propagation method as

$$
\begin{aligned}
\sigma_{Y_{LYSO}} &= Y_{LYSO} \cdot \left[\left(\frac{\sigma_{Y_{LYSO}^{eff}}}{Y_{LYSO}^{eff}} \right)^2 + \left(\frac{\sigma_{E_{dep,\ ioni}^{LYSO}}}{E_{dep,\ ioni}^{LYSO}} \right)^2 \right]^{1/2} \\
&= 4.62 \times 10^4 \cdot \left[\left(\frac{0.43 \times 10^{10}}{9.08 \times 10^{10}} \right)^2 + \left(\frac{1.41}{1.98} \right)^2 \right]^{1/2} \\
&\approx 3.29 \times 10^4 \ photons/MeV\,.
\end{aligned} \qquad (3.6)
$$

3.5. Conclusions

This chapter introduced the single-particle detection systems designed for the Experiment-320 at FACET-II and FOR2783 project at CALA that are successfully capable of detecting single-particle hits. The proposed detection systems are composed of two pixelated LYSO screens providing high spatial resolution and particle tracking information, and a Cherenkov calorimeter placed behind the second LYSO array.

Using the ELBE radiation source at the Helmholtz-Zentrum Dresden-Rossendorf, the Cherenkov calorimeter was calibrated using the dark current of the ELBE accelerator. Based on the calibration, about 537 photons are detectable for an incident 3 GeV signal positron with a resolution of approximately 20%.

The pixelated LYSO screens, which are placed in front of the calorimeter, were also characterized. The LYSO crystals presented a decay time of about 42.2 ns and scintillation light efficiency of 9.08×10^{10} photons/sr/pC, which corresponds to about 46 photons emitted per keV deposited by the primary particle. The fast decay time of the LYSO crystal is an important feature of the design of the tracking layers since it allows performing temporal gating of the imaging system of the screens and neglects

the noise created by the background radiation originating at regions such as beam dumps.

To identify a positive event with a high confidence level of $> 99\%$, it is required that both scintillation screens of the detection system record an event above the threshold that corresponds to a possible track of a signal particle, and the calorimeter channel on the same track must also record an event. Consequently, false-positive events are only possible if the calorimeter measures a sufficiently high signal above the background. But, by constantly monitoring the background radiation on the detectors, one can distinguish if the high signal is consistent with a signal particle or background radiation.

In the next chapters, the upcoming SF-QED experiments and the expected signals on their respective single-particle detectors are discussed. Estimations on the signal-to-noise ratio of the detectors are calculated based on Monte-Carlo simulations demonstrating that single-particle detection above the noise from the background radiation is possible.

4. Experiment-320: Laser-Electron Interaction in the Non-perturbative Regime

Now that we understand how the nonlinear Breit-Wheeler pairs are created and a single-particle detection system has been designed for detecting such signal particles with a high confidence level, we introduce in this chapter the Experiment-320 (E-320) at the Facility for Advanced Accelerator Experimental Test (FACET-II).

The E-320 is a two-step SF-QED experiment where electron bunches from the FACET linear accelerator interact with a high-intensity laser beam. During the electron-laser interaction, as the first step, high-energy photons are emitted due to the nonlinear inverse Compton scattering process. These high-energy photons, while still immersed in the strong laser field, are capable of producing pairs via the nonlinear Breit-Wheeler mechanism as the second step.

To describe the Experiment-320 and predict the pair creation rate in addition to the signal on the single-particle detectors with high fidelity, we start with a brief description of the FACET-II linear accelerator and the high-power laser system used in the experiment. Then, we present SF-QED simulations of the expected results from the electron-laser interactions. Based on the results obtained from these simulations, Monte-Carlo FLUKA simulations including the entire FACET-II beamline and structure to estimate the background noise level at the single-particle detectors were performed. By analyzing the Monte-Carlo simulations, the expected signal-to-noise ratio of the designed Cherenkov calorimeter was calculated. The detection system is capable of diagnosing single GeV-particles hits with a signal-to-noise ratio of $\mathrm{SNR}_\sigma = 18$ and efficient rejection of background noise. The combination of the calorimeter signal with the LYSO screens allows recording positron spectra with $\Delta\mathcal{E}/\mathcal{E} = 2\%$ even for pair production rates of $\ll 1$ pair per shot.

It is important to remark that the E-320 is composed of collaborators from different affiliations, and here is presented mainly the results obtained from the project for the design of an efficient single-particle detector with a high signal-to-noise ratio. The work performed by the collaborators and used on the detector design by the author is properly assigned through the text. Moreover, the chapter contents presented here are based on the work published by the author in Ref. [103].

4.1. The FACET-II Facility

The Facility for Advanced Accelerator Experimental Test (FACET) is a linear accelerator user facility located at the SLAC National Accelerator Laboratory (USA) [189] that uses the mid-sector of 2 km of the old SLAC LINAC accelerator of 3.2 km. FACET was first commissioned in 2012 to deliver 20 GeV electron bunches with a charge of 3 nC, but in 2016, the facility ended its operations for upgrades on its machinery and for the construction of the upcoming free electron laser at SLAC, namely the Linac Coherent Light Source II (LCLS-II).

After the upgrade, the facility (now known as FACET-II) will generate electron and positron bunches with fs-duration and high-peaks on the order of 200 kA for use in a variety of experiments such as plasma and dielectric wakefield acceleration and strong-field QED [62, 190–194].

The linear accelerator starts with a photoinjector build in an off-axis injection lane capable of generating electron bunches with up to 2 nC charge, bunch duration of < 10 ps and emittance of less than 3 μm-rad. The electron bunches are later compressed by three bunch compressors located along the accelerator beamline such that currents up to 200 kA with energy of 13 GeV are achieved. For more specifications of the FACET-II accelerator, please see Refs. [195, 196].

For the E-320 project, the accelerator will be operating in the single-bunch and high-charge density mode where electron beams of 2 nC charge are accelerated to 13 GeV with energy spread of $\Delta\mathcal{E}/\mathcal{E} \approx 0.1\,\%$. The electron beams are expected to have a root mean square (RMS) length of 250 μm with a Gaussian transverse profile of less than $\sigma_e < 30$ μm and divergence of < 6 μrad. Such parameters are essential for the realization of the E-320 experiment because they allow the electron bunches to complete overlap the focused laser beam during electron-laser collisions and, consequently, to maximize the production of pairs [62].

The high-intensity laser required for the SF-QED collisions is composed of a Vitara oscillator, a Legend Elite regenerative amplifier, and two Thales SAGA pumps. The laser schematic is shown in figure 4.1. After the last amplification and compression stages, the FACET-II laser provides up to 20 TW of power with central wavelength at 800 nm, and pulse duration of $\tau_{\mathrm{laser}} \approx 35$ fs [195].
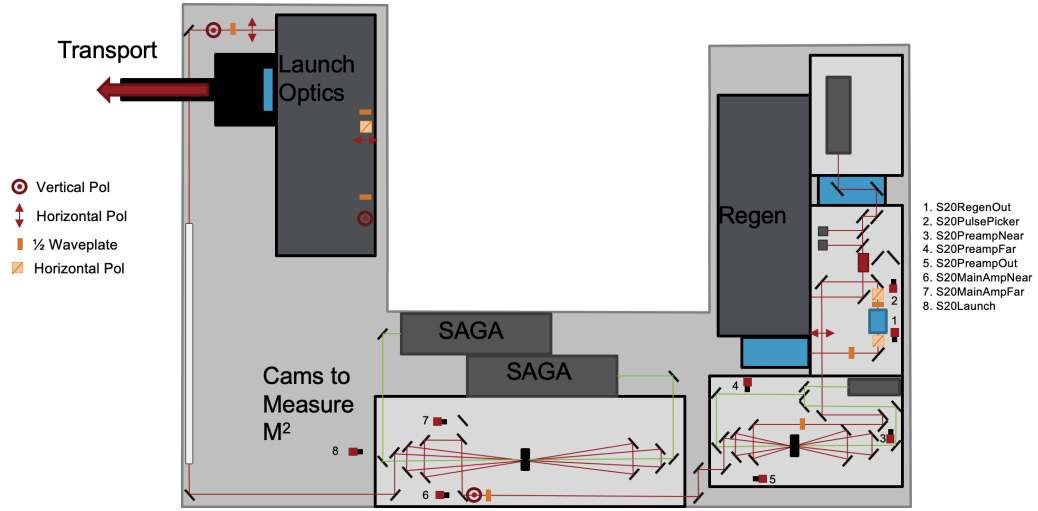
Figure 4.1.: FACET-II experimental laser schematic. After the last amplification stage and compression, the laser can provide up to $20\,\mathrm{TW}$ of power with central wavelength at $800\,\mathrm{nm}$ and pulse duration of $\tau_\mathrm{laser} \approx 35\,\mathrm{fs}$. Figure obtained from Ref. [197]. The transport beamline propagates the laser beam to the tunnel where it is focused before the electron-laser interaction.

4.2. Electron-Laser Interaction Point

Now that the two main ingredients to produce pairs in the experiment were introduced: electron beam from the FACET linear accelerator and the high-intensity laser, the conditions for the collision between the electron bunch and the focused laser beam can be explored. In the experiment-320, the laser beam has flat-top profile with diameter of $40\,\mathrm{mm}$ and is focused by an off-axis parabola (OAP) of f-number ≈ 1.9 to an intensity of $\mathrm{I} = 1.3 \times 10^{20}\,\mathrm{W\,cm^{-2}}$, corresponding to an $\mathrm{a_0} \approx 7.8$. The focused laser beam collides with the electron bunch inside a vacuum chamber at the position named interaction point (IP) at an crossing angle of about $30°$ overlapping spatially with approximately only $1\,\%$ of the electron beam [103]. With such electron beam and laser parameters, a $\chi_\mathrm{e} \approx 1.5$ is achieved. Hence, the E-320 is capable of probing pair creation in the non-perturbative (tunneling) regime.

Figure 4.2 shows the arrangement of the optical components inside the vacuum chamber where the IP is located. The components were developed and manufactured by the thesis' author together with colleagues from the E-320 collaboration. The laser beam enters the vacuum chamber at the top left of the chamber and propagates until the first off-axis parabolic mirror (OAP1) which focuses the beam at the interaction

point. The electron beam generated by the FACET-II accelerator enters also from the left side of the chamber and propagates downstream through the IP for colliding with the focused laser. After the collision, the laser beam is recollimated by a second parabola mirror (OAP2) to later be dumped inside the chamber. The laser beam profile and pointing are monitored in real-time by near-, far-field, and interferometric diagnostics. These laser diagnostics are an important tool to verify the position of the focused laser beam and if the overlap with the electron beam remains correct during the course of the experiment. In addition, to verify the quality and position of the focus spot, an imaging system composed of a Mitutoyo microscope objective of 50× magnification is installed at the E-320 setup.
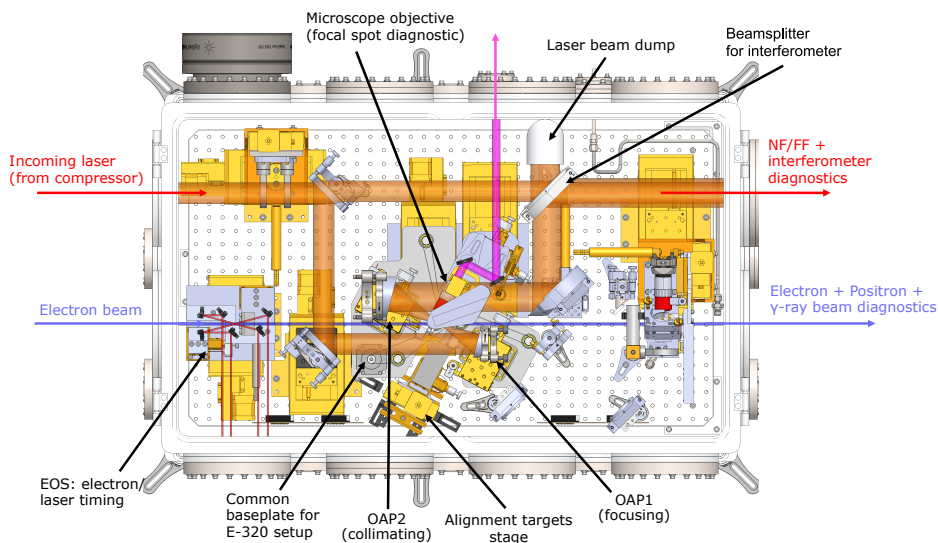
Figure 4.2.: Experimental setup of the E-320. The collimated laser beam enters at the top left side of the vacuum chamber and propagates until the first off-axis parabolic mirror (OAP1) which focuses the beam at the interaction point. The electron bunch also enters at the left side of the chamber, propagating downstream towards the IP for the electron-laser interaction. After the interaction, the laser beam is recollimated by a second parabolic mirror (OAP2) and later dumped inside the chamber. The laser beam profile and pointing are monitored in real-time by near-, far-field, and interferometric diagnostics. Image of the experimental setup provided by Robert Ariniello (CU Boulder).

The spatial overlap of the electron-laser beam is realized by imaging the focus spot and the scintillation light produced by the passage of the electron beam through a 5 μm-thick YAG:Ce screen placed at the focus position. The alignment of the OAPs to each other is fine-tuned by imaging a 2 μm-diameter pinhole and a needle with 5 μm-wide tip. The three alignment components, YAG:Ce screen, pinhole, and

needle, are placed at the same alignment target holder that is fully motorized in XYZ directions. Figure 4.3 shows the designed alignment target holder with the three alignment components.
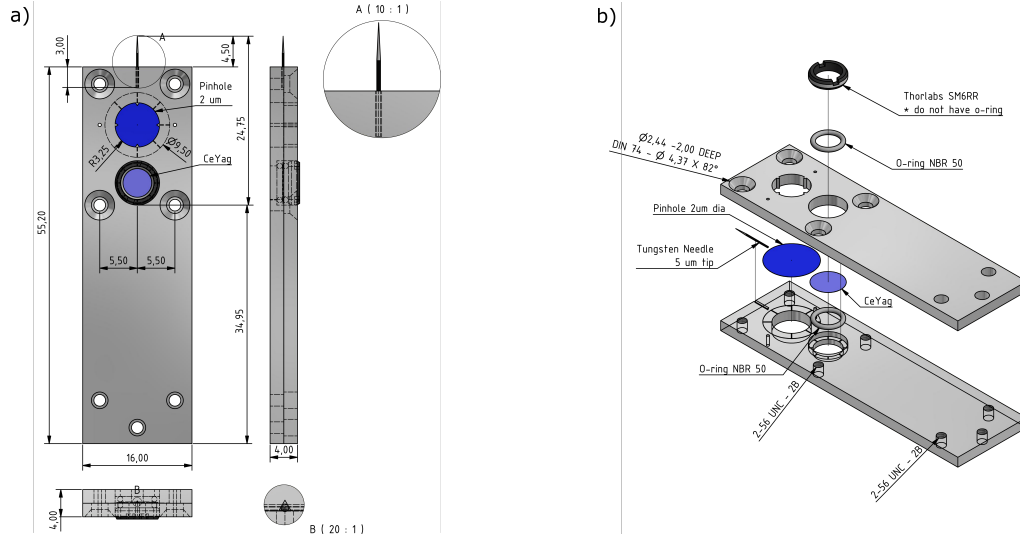
Figure 4.3.: Alignment target holder with the YAG:Ce screen for the spatial overlap of the electron and laser beams, 5 µm-tip needle, and 2 µm diameter pinhole for optical alignment of the focusing and re-collimating OAPs. Figure (a) shows the front view of the holder with its dimensions in millimeters, and (b) shows the exploded view of the holder with details on how the components are mounted.

All the E-320 components required at the IP are placed over a common base plate that offers motions in the x- and y-directions. The motion at the x-direction allows retracting the entire E-320 setup clearing the electron beam path. On the other hand, the vertical motion in the y-direction elevates the entire setup to match the laser and electron beams' heights. The common base plate helps to roughly spatially align the electron beam with respect to the focused laser beam before a finer optimization is performed using the mirrors and OAPs of the laser beam path.

4.3. Simulation Results from the Electron-laser Interaction

In the previous section, the experimental setup of the interaction point of the E-320 was introduced. The next step is to calculate the expected pair yield from the experiment.

To this end, SF-QED Monte-Carlo simulations[1] of the electron-laser collision were performed to using the electron bunch and laser parameters[2] previously presented.

Figure 4.4 shows the simulated electron bunch energy spectrum and divergence after the electron-laser interaction. From the simulation results, one notices the widening of the initial monoenergetic electron bunch with 13 GeV to the range between 1 - 13 GeV. The widening occurs due to the emission of high-energy photons by the inverse nonlinear Compton scattering process previously introduced in section 2.2.4. In addition to the energy spectrum widening, the divergence of the electron beam also increases from $<$ 6 μrad to about 25 μrad at full width at half maximum (FWHM) at the direction of laser polarization which is consequence of the recoil of the electrons.
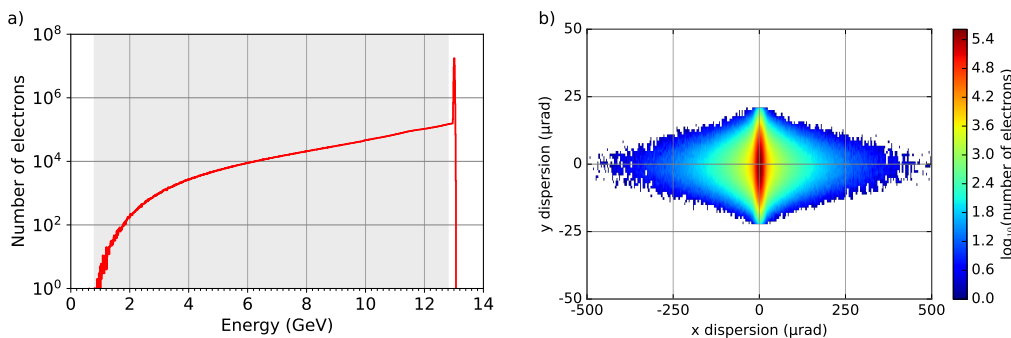
Figure 4.4.: Simulated electron bunch a) energy spectrum (10 MeV bin size) and b) divergence after the interaction with the laser beam. The energy range between 1 - 12.8 GeV (shown within the gray area) corresponds to the energy spectrum used as input on the FLUKA Monte-Carlo simulations presented in section 4.4 for estimating the background noise at the detectors. The divergence of the electron bunch increases from $<$ 6 μrad to approximately 25 μrad at FWHM after the interaction. Figure taken from Ref. [3].

The highly energetic photons emitted during the electron-laser collision have a maximum energy of 12 GeV which is in agreement with the energy conservation law since the maximum energy of the electron beam of 13 GeV limits the maximum photon energy possible. Figure 4.5 shows the energy spectrum as well as the divergence of the photon beam. Most of the photons have energy less than 2 GeV and low divergence. In the x-direction, i.e., at the same direction of the laser light polarization, the photon beam divergence is 134.35 μrad at FHWM. On the other hand, in the y-direction, the FWHM divergence is three orders of magnitude smaller, about 0.64 μrad.

---

[1]Simulations were performed by our collaborator Matteo Tamburini (Max-Planck-Institut für Kernphysik, Germany).

[2]The simulations parameters, which are based on the initial conceptual design phase of the experiment, and the actual experiment parameters will most likely differ from the ones presented here.
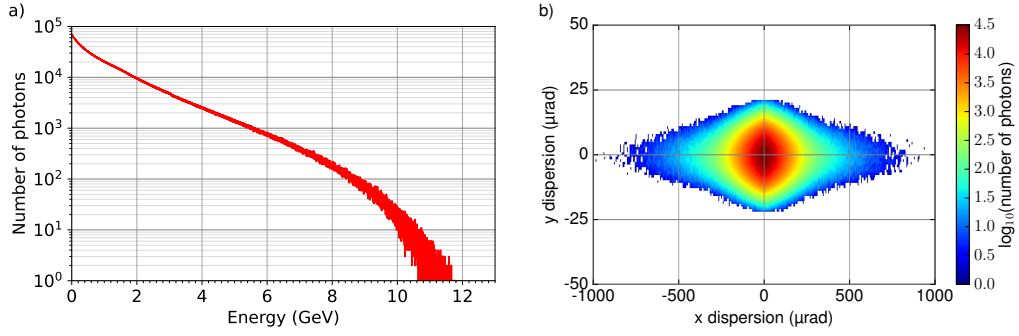
Figure 4.5.: a) Energy spectrum (10 MeV bin size) and b) divergence of the highly energetic photon beam generated after the electron-laser collision. The maximum energy reached by the photon beam is upper limited by the energy of the initial monoenergetic 13 GeV of the incoming electron beam. The divergence of the photon beam in the x-direction, i.e. same direction of the laser polarization, is about 134.35 µrad at FHWM. On the other hand, in the y-direction is much smaller, about 0.64 µrad. Figure taken from Ref. [3].

While still immersed in the high density laser photon background, the γ-photons emitted by the nonlinear inverse Compton scattering interact with the laser optical photons and trigger the nonlinear Breit-Wheeler process generating pairs from the quantum vacuum. According to the simulations, the positrons with energies between 1 - 9 GeV have higher probabilities to be created with an FWHM divergence in the x-direction lower than 1 mrad. Note that the divergence in the y-direction is negligible since it is perpendicular to the laser linear polarization. Figure 4.6 shows the simulated positron spectrum and its divergence in the x-direction.

4.4. Expected Background Noise and Signal-to-Noise Ratio

The next step in the Experiment-320 at FACET-II is to determine the sources of background radiation that can influence the signal on the detectors which can give rise to, for example, false positive events. To this end, we analyze the particle propagation path downstream of the beamline towards the detectors and perform Monte-Carlo simulations that help to identify the sources of background radiation by particles striking mainly the vacuum pipes and supports of the beamline.
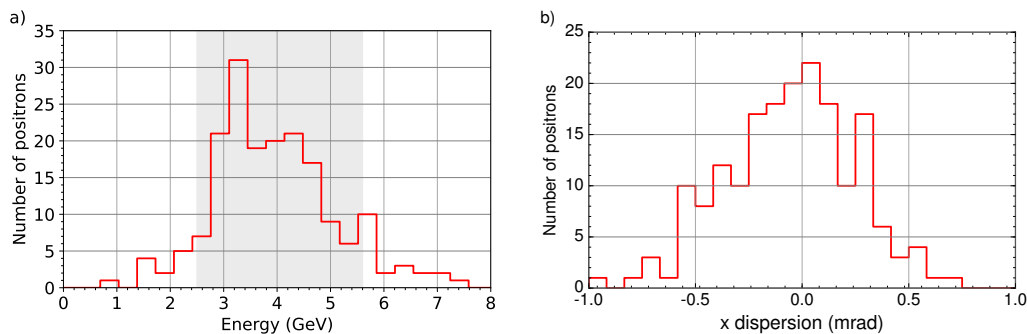
Figure 4.6.: a) Energy spectrum (345 MeV bin size) and b) divergence of the positrons created by the nonlinear Breit-Wheeler process due to the interaction between the high energy γ-photons with the optical laser photons. The detectable energy range by the proposed single-particle detectors between 2.5 - 5.6 GeV for the selected magnet kick of 87.2 MeV is represented by the gray area on the plot. Details on the E-320 single-particle detection system is given in section 4.4. Figure taken from Ref. [3].

4.4.1. Sources of Background Radiation at the Detectors

After the electron-laser interaction, the electron, positron, and photon beams propagate through the FACET-II beamline until they reach a dipole magnet. At the dipole magnet, the charged particles are deflected towards the detectors while the γ-photons continue to travel in a straight path towards a beam dump. The low divergence of the γ-ray beam allows the photons to propagate without any interaction with the beamline walls over several hundreds of meters. Therefore, no background radiation on the detectors originating from the photon beam hitting the beamline pipes is expected.

The dipole magnet has a nominal transverse kick of 87.2 MeV, which is equivalent to a field strength of BL = 0.3 Tm. This setting allows deflecting positrons in the range of 2.5 - 5.6 GeV towards the single-particle detectors which are placed about 3 meters from the magnet. The electrons are deflected within the range of 22 - 65 mrad towards the electron diagnostics located in the electron detection chamber (EDC). The high-energy electrons with 13 GeV that did not interact with the laser at the IP continue to travel with a negligible deflection angle towards the beam dump and also do not contribute to the background at the detectors. The setting of the magnet is adjustable during the experiment, allowing to select the energy range in which particles can be diagnosed. Figures 4.4 a) and 4.6 a) have the expected energy ranges that the detectors are designed to diagnose indicated by a gray shaded area.

Figure 4.7 shows a slice of the FACET-II beamline with the position of the dipole magnet, the single-particle detector for the few positrons, and the electron diagnostics.

After the up-deflection of the positrons by the magnet, the particles propagate through a large chamber named positron detection chamber (PDC) and exit it through an aluminum vacuum exit window of 5 mm thickness before reaching the LYSO screens and the Cherenkov calorimeter. As the particle propagates through the 5 mm thick aluminum window, less than 5% of its energy is lost and, consequently, does not significantly affect the signal at the detectors. The use of thinner exit windows to have less energy loss by the propagating particle, for example, Kapton windows of about 50 μm, were considered in the experiment. However, they can be easily damaged becoming harmful to the vacuum system of the facility. The electrons are deflected downwards and those in the range of 22 - 65 mrad are detected by a high-yield scintillation lanex screen imaged by a high-resolution camera. Electrons deflected at angles larger than 65 mrad strike the beamline supports and vacuum chamber floor creating a source of background radiation that reaches the detectors and cannot be neglected by using the temporal gating method.
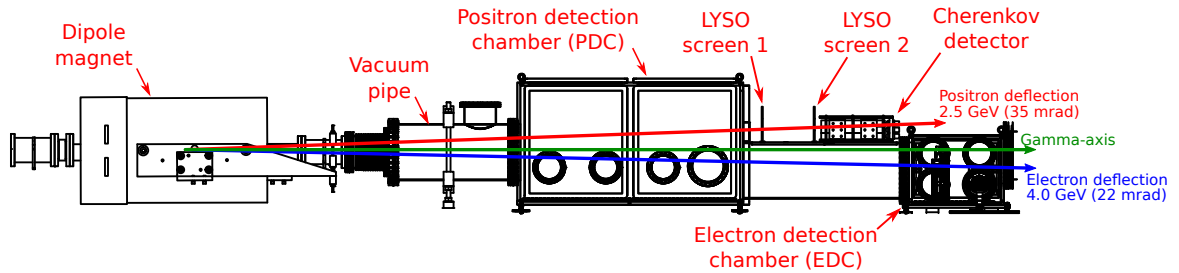
Figure 4.7.: Slice of the FACET-II beamline with the positioning of the single-particle detection system. Positrons are deflected upwards (red trajectory indicates a 2.5 GeV positron) propagating through the positron detection chamber (PDC) before reaching the single-particle detection system. Electrons are deflected downwards and are diagnosed in the electron detection chamber (EDC) by a high-yield scintillation lanex screen imaged by a high-resolution camera (blue trajectory corresponds to a 4.0 GeV electron). The green trajectory represents the low divergence γ-beam. Figure taken from Ref. [3].

About 8.6 meters downstream of the single-particle detectors, the photon beam and the high-energy 13 GeV electrons are cooled down. The interaction of these particles with the dump produces substantial secondary radiation backscattered towards the detectors. The backscattered radiation is also highly energetic, so its suppression is essential for avoiding false positive hits on the single-particle detectors, LYSO, and Cherenkov calorimeter. The hits produced by these high-energy particles can be neglected on the detectors by applying temporal gating on the detectors. The large distance between the position of the detectors and the dump corresponds to

a double-pass delay of 57 ns which is long enough to time gate the LYSO screens (decay time of 42 ns) and the PMTs of the Cherenkov calorimeter. Therefore, the only possible source of background noise on the single-particle detectors is upstream radiation sources that propagate along with the main particle beam and secondary radiation sources located very close to the detectors, such as chamber walls, which arrive within the gating window.

To evaluate the background noise level at the single-particle detectors, FLUKA [198, 199] simulations were performed[3] on the relevant part of the beamline that is shown in figure 4.7. The simulated particle fluence around the detector region is shown in figure 4.8. In the simulation, the electron spectrum presented in figure 4.4 is used as input and only beamline components that contribute significantly to the background noise on the detectors are included. Therefore, the backscattered noise originated at the beam dump is intrinsically suppressed since it arrives on the detectors after the temporal gating window. From the simulations, a shower of secondary particles is created due to the interaction between the low energy electrons deflected at larger angles > 65 mrad and the vacuum chamber floor and walls. Consequently, the shower propagates towards the detectors and cannot be gated away from the signal due to the short distance between their source and the diagnostics.

The calculations presented here are based on the nominal FACET-II design parameters. Imperfect beam transport or generation can lead to a co-propagating halo of radiation resulting in higher backgrounds. See chapter 6 for preliminary data.

4.4.2. Signal-to-Noise Ratio at the Cherenkov Calorimeter Detector

The FLUKA Monte-Carlo simulations also allow to estimate the particle spectrum of the background radiation entering the Cherenkov calorimeter. Figure 4.9 plots the background radiation energy spectrum at the Cherenkov calorimeter, and, as can be seen, the noise is composed mainly by particles with energy lower than 25 MeV. Using the calibration curve of the detector introduced in chapter 3, the particle spectrum is converted into number of produced Cherenkov photons as provided figure 4.9 b). Summing up all the photons, we find that a total of $N_{bg} = 320$ photons with variance of $\sigma_{bg} = 12$ are produced in a calorimeter channel. Now, if we use the calibration curve in figure 3.8 and calculate the number of photons produced for a single 3 GeV

---

[3]The Monte-Carlo FLUKA simulations were performed by our collaborators Niall Cavanagh and Gianluca Sarri from the Queen's University Belfast (QUB), but the interpretation of the data was realized by the author of this thesis.
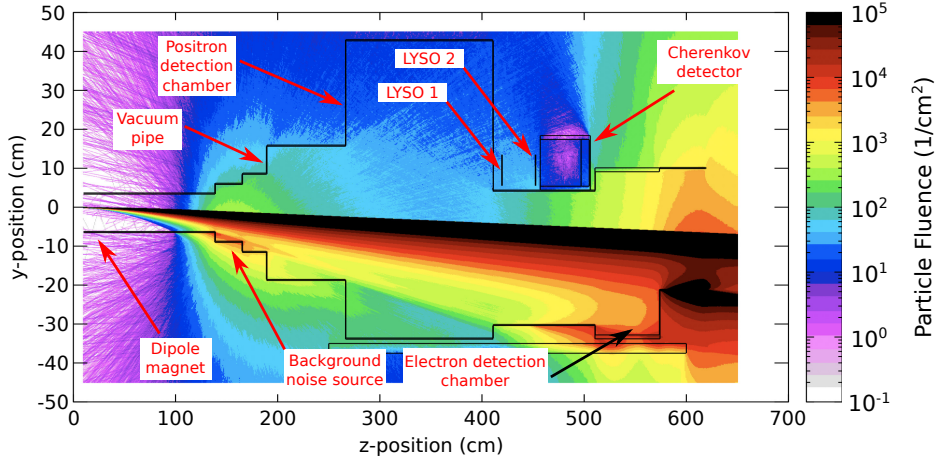
Figure 4.8.: Monte-Carlo simulation of the expected particle fluence (gamma photons, electrons and positrons) at the FACET-II tunnel region around the single-particle detection system. Backscattered radiation from the beam dump is neglected on the simulations since they arrive at the detectors outside of the temporal gating window. Moreover, a shower of secondary particles, considered as background noise, originated from the interaction between the deflected electron beam with the chamber and vacuum pipe walls propagates directly to the detectors. Figure taken from Ref. [3].

particle, which is the typical energy of an expected hit at the calorimeter, we obtain $N_{sig} = 537$ photons. Hence, the signal-to-noise ratio (SNR) of the calorimeter for a single-particle hit at a detection channel in terms of the averaged number of produced photons is $SNR_p = N_{sig}/N_{bg} = 1.7$. The $SNR_p > 1$ indicates that single-particle hits produces about three times more number of Cherenkov photons than the background noise on the calorimeter.

An alternate definition of the SNR measurement SNR_σ in terms of the ratio between the signal and its variance $<\sigma>$ can be introduced as

$$SNR_\sigma = N_{sig}/ <\sigma> . \tag{4.1}$$

This metric indicates how much it is expected the mean number of signal photons to vary. A high SNR_σ value means that the number of expected signal photons for an particle hit do not vary within a large uncertainty range and individual particle hits can be clearly separated from the background.

The variance of the 3 GeV signal of N_{sig} is given by $<\sigma_{sig}> = \sqrt{N_{sig}} \approx 23$. Knowing from the Monte-Carlo simulations that $\sigma_{bg} = 12$, the variance is calculated as $<\sigma> = (23^2 + 2 \cdot 12^2)^{0.5} \approx 29$. And, finally, the alternate definition of the SNR measurement is calculated as $SNR_\sigma = N_{sig} / <\sigma> = 537/29 \approx 18$. The value of
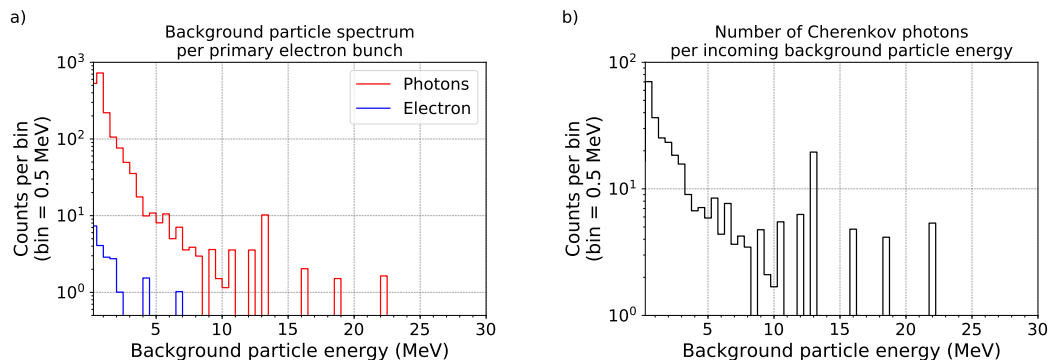
Figure 4.9.: Energy spectrum of the background noise at a single Cherenkov calorimeter channel: a) Background noise particle spectrum, majority of the noise have energies under 25 MeV; b) Number of Cherenkov photons produced per energy of incoming background particle, a total of 320 photons are produced at the single Cherenkov calorimeter channel.

$SNR_\sigma \gg 1$ demonstrates that single-particle hits on the calorimeter detector can easily be separated from the background.

4.4.3. LYSO Screens and Particle Spectra Measurements

From the previous section, the Cherenkov calorimeter exhibits a high signal-to-noise ratio and therefore is capable of detecting single-particle hits in the E-320. The next step is to estimate the signal expected from the LYSO scintillating screens and their ability to diagnose single-particle events.

To diagnose the positrons spectra, the LYSO screens offers a higher spatial resolution than the Cherenkov calorimeter of about 60 MeV at 3 GeV incident particle for the nominal dipole magnet configurations. FLUKA Monte-Carlo simulations were also performed[4] to assess the energy deposited in both crystal screens by high-energy positron propagating through the screens without considering the background noise. The results of the simulations are shown in figure 4.10 and an exponential fit over the simulation points is given.

A 3 GeV positron is expected to deposit about 5.5 MeV at the first scintillation screen and 8.8 MeV at screen-2. The reason for a higher energy deposited at the second LYSO screen is justified by analysing the energy distribution profile at both screens for the single 3 GeV particle hit as given in figure 4.11. After the single-particle strike

---

[4]The FLUKA simulations of the energy deposited on each of the LYSO screens as well as the profile of energy deposited by a single-particle and the background was performed by our collaborators Niall Cavanagh and Gianluca Sarri from Queen's University Belfast (QUB). And, again, the interpretation of the data was realized by the thesis author.
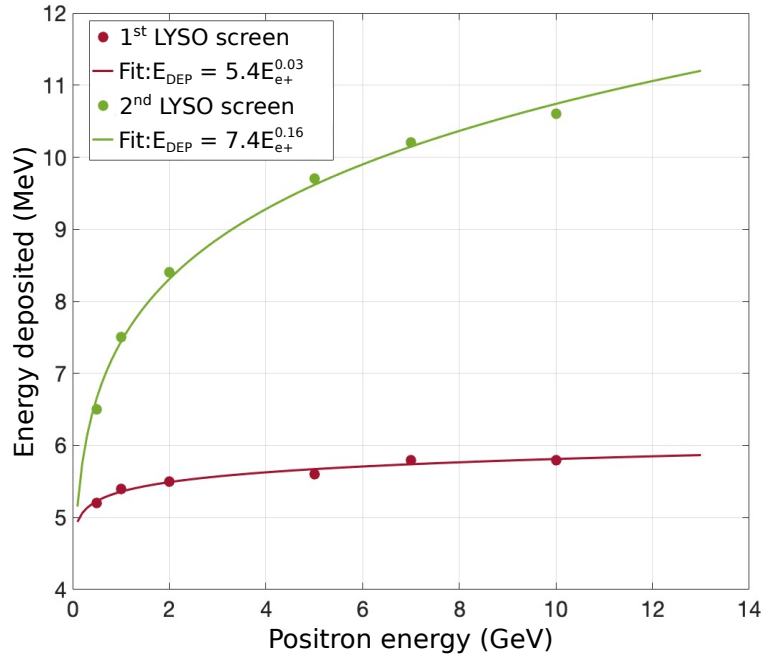
Figure 4.10.: FLUKA simulations of the energy deposited at each LYSO scintillating screen per incoming single-particle. A shower of secondary particles at the first screen is created towards the second screen increasing the energy deposited on it. The typical uncertainty on the data points is on the order of 3-5%.

a crystal at screen-1, a shower of secondary particles is created towards screen-2 and a cluster of crystal pixels is observed, and a higher amount of total deposited energy at the second screen.

The simulations of the energy deposited on each screen enable us to evaluated the expected number of photons detected by the high-resolution low-noise cameras used to capture the scintillation light of the crystals. At the first screen, the 5.5 MeV deposited will produce about $N^1_{scin} \approx 1.4 \times 10^5$ scintillation photons, however, only a fraction is indeed detected by the proposed imaging system. According to the evaluation of the imaging system of the LYSO screens presented in section 3.1.1, equation (3.1), the number of detected photons of screen-1 N^1_{LYSO} is calculated as

$$N^1_{LYSO} = N^1_{scin} \cdot 6.1 \times 10^{-3} \cdot 10^3 \cdot 1.6 \times 10^{-3} \cdot 0.4 \approx 546 \text{ photons}, \qquad (4.2)$$

for a collection efficiency of PCX condenser lens of $CE_{PCX} = 10^{-3}$, collection efficiency of the ORCA-Flash camera of $CE_{Orca} = 1.6 \times 10^{-3}$, quantum efficiency of $QE_{Orcas} \approx 0.4$ at 410 nm, and an image intensifier gain of $G_{int} = 10^3$. Therefore, one expects about approximately 546 photons to be detected from the first LYSO screen. By
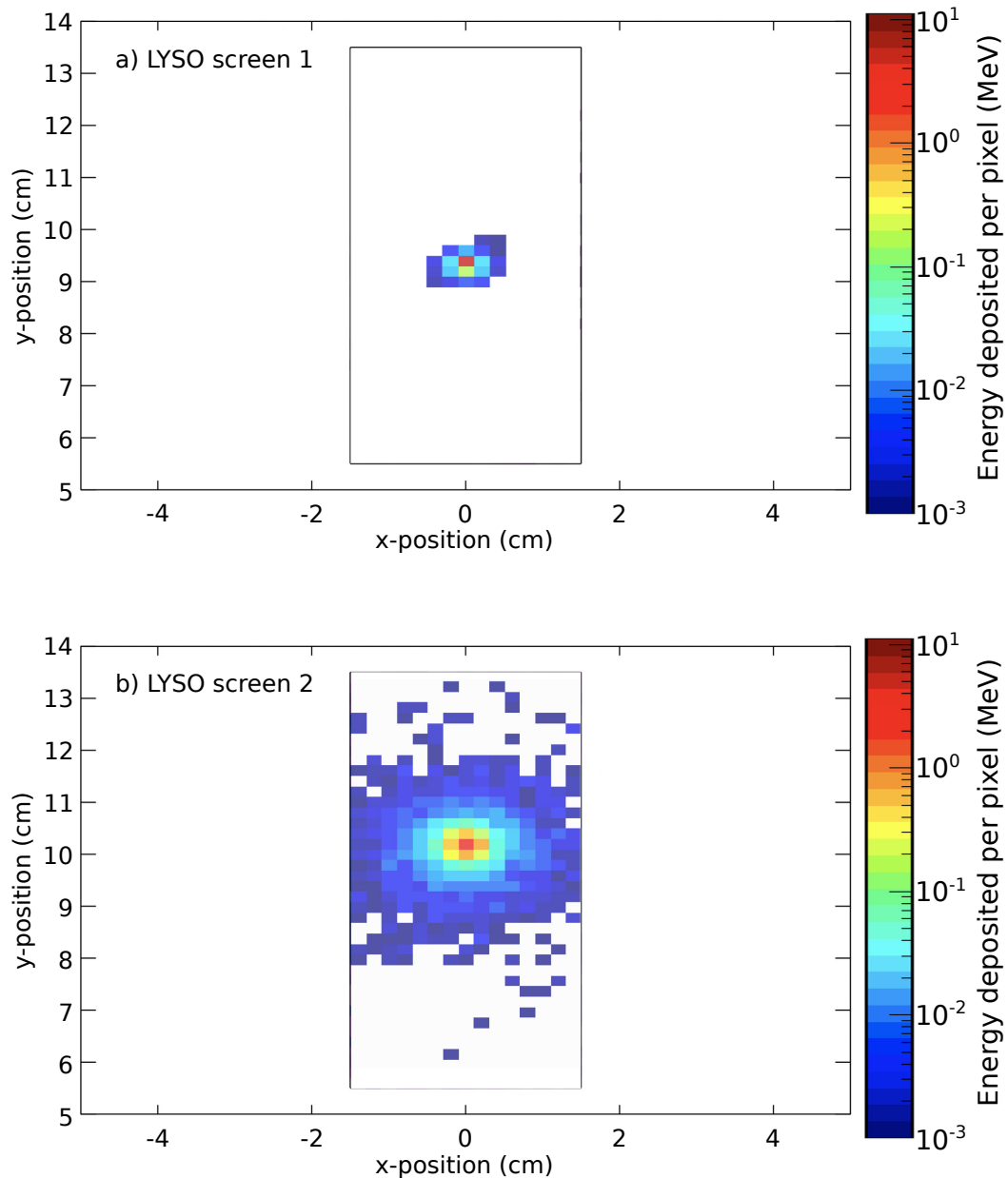
Figure 4.11.: Simulation of a single 3 GeV particle hit on the LYSO screens at the Experiment-320 without considering the background noise: a) LYSO screen 1; b) LYSO screen 2. At the first crystal screen, about 5.5 MeV is deposited in a single pixel at y = 9.4 cm. At screen-2, about 8.8 MeV is deposited. The particle hits screen-2 at the pixel with y = 10.3 cm. Note that the propagation angle of the particle can be estimated to be 28 mrad given the distance between the screens of 330 mm.

applying the same calculation step for the second screen value of energy deposited, the number of scintillation photons emitted is $N_{scin}^2 \approx 2.2 \times 10^5$ photons and about $N_{LYSO}^2 \approx 858$ photons are detected. The uncertainty of the number of detected photons of each LYSO screen is determined by the collection and quantum counting efficiency which are expected to be calibrated after FACET-II be commissioned in the upcoming years.

Background rejection on the screens requires a valid event to follow a particle track to within one pixel and threshold of 3σ of the expected signal level in each of the three detectors, thus only above 99% of events are being considered and $< 1\%$ false negatives hits are expected.

Background simulations on the LYSO screens to determine the noise level were also performed. The background noise is shown in the profile of the screens presented in figure 4.12. Most of the low energy deposited noise on both screens can be rejected based on the energy threshold established. The hot pixels with energy deposited $> 6\%$ shown on screen-1 can be neglected by analysing their tracked pixel and the absence of cluster pixels with > 8.8 MeV deposited on screen-2. In addition, none of the events shown on the screens meet the Cherenkov calorimeter threshold. Finally, the measurement of false-positive events is only possible if the calorimeter measures a sufficiently high signal above the background. However, the FLUKA simulations show that the background noise consists of a shower of low-energy particles which allows the combination of calorimeter reference and signal channels to prevent false-positive events. Therefore, we expect to have zero false positive hits based on the inputs used on the simulations, however, the real rate is yet to be quantified as soon as FACET-II is commissioned and the number of hard background γ-photons is known.

4.5. Conclusions

In this chapter, the design of the Experiment-320 at FACET-II (SLAC) and the implementation of the designed single-particle detection system were introduced. In the E-320, the electron-positron pairs are created in a two-step interaction. First, as the electron beam collides with the high-intense laser beam, high-energy photons are emitted due to the nonlinear inverse Compton scattering. Then, while still immersed in the strong background laser field, the γ-photons trigger the pair production via the nonlinear Breit-Wheeler process.

The detection of the positrons created due to the interaction presents a real challenge and a single-particle detection system with a signal-to-noise ratio above the unity is
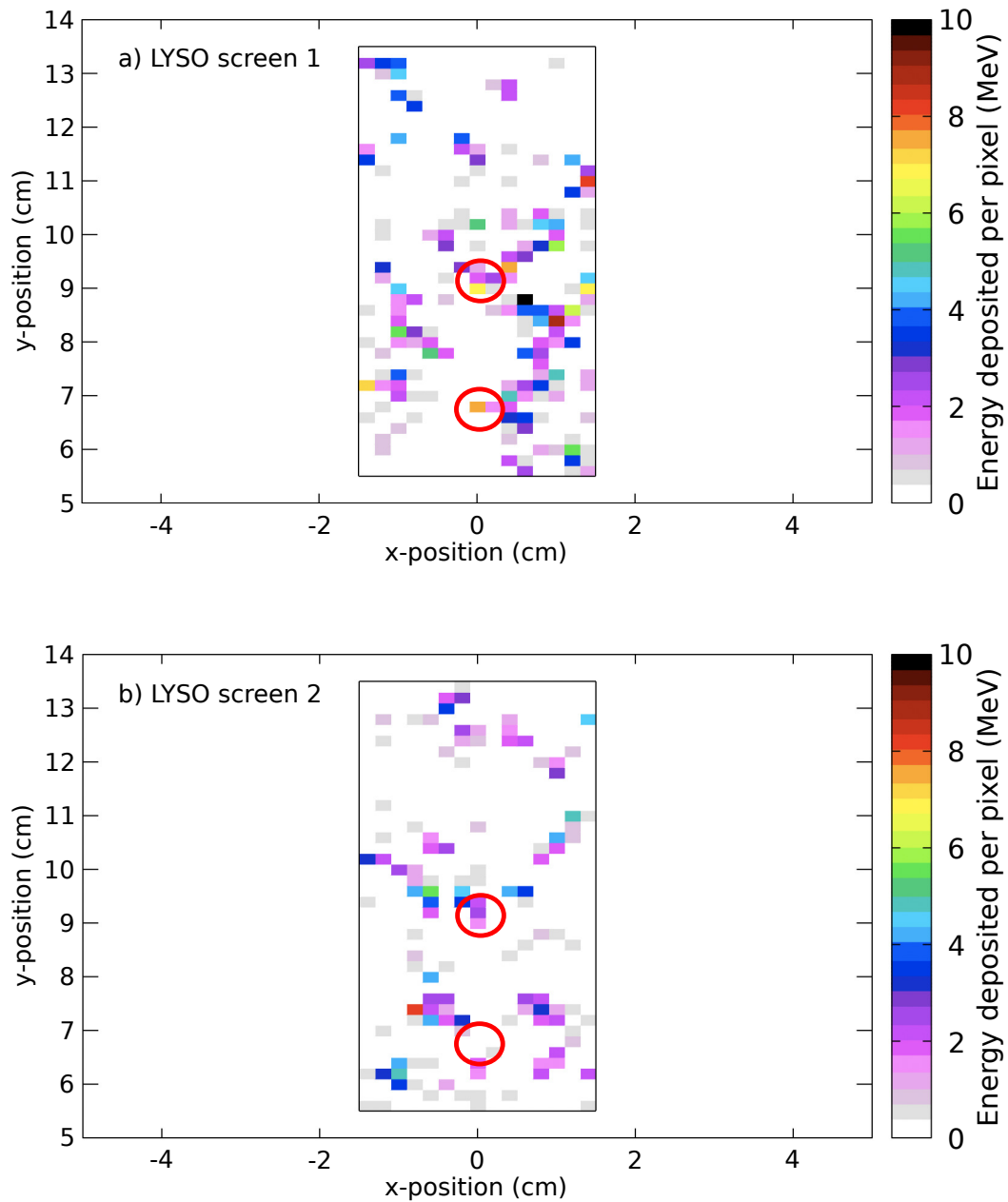
Figure 4.12.: FLUKA simulations of the energy deposited at the LYSO screens due to the background noise at the detection region: a) LYSO screen 1; b) LYSO screen number 2. Most of the background events, except the events highlighted by a red circle on screen-1, can be rejected due to energy deposited threshold per pixel on screen-1 or the absence of > 8 MeV pixel cluster on screen-2. The highlighted pixel in the center of screen-1 and area on screen-2 would be consistent with a > 1 GeV incident positron, however, the calorimeter signal does not match a hit for a GeV-particle. Hence, the hit can be rejected.

required. Monte-Carlo FLUKA simulations were performed by the E-320 collaboration to evaluate the expected performance of the detectors. From the simulations, the background noise at the detectors originated from low-energy electrons striking the vacuum chamber walls, and a shower of low-energy particles propagating directed towards the detectors is generated. The short distance between the source of the background radiation showers and the detector devices makes it difficult for these background particles to be neglected by temporal gating the detectors since particles arrive within the gating window. Differently, the background radiation originating from the beam dump is easily rejected since they take about 57 ns to arrive at the detectors after a signal particle hit.

Moreover, from the simulations, a signal-to-noise ratio of $\mathrm{SNR}_\sigma > 18$ is predicted for the Cherenkov calorimeter in the Experiment-320. The high SNR_σ indicates the capability of the Cherenkov calorimeter in detecting single-particle events above the background noise and its efficient rejection of the low energy background noise.

The LYSO screens performance is also studied, and a resolution of $\Delta\mathcal{E}/\mathcal{E} = 0.02$ in recording the positron spectra for the pair production rates of $\ll 1$ pair per shot was determined.

5. Project FOR2783: Pair Production in the Non-perturbative Regime

In contrast to the E-320, the FOR2783 experiment, which is part of the Research Research Collaboration "Probing the Quantum Vacuum" [200], is an all-optical experiment designed to probe electron-positron pairs created via the nonlinear Breit-Wheeler process for the first time via purely photon and laser beam collisions.

The project FOR2783 is planned to investigate the nonlinear Breit-Wheeler process at the ATLAS-3000 Petawatt laser system at the Centre for Advanced Laser Applications (CALA) [100] through the collision of γ-photons and a high-intensity laser beam, namely collider beam. In the experiment, electron bunches produced by laser-wakefield acceleration (LWFA) [67, 85, 201] interacts with a converter foil to produce bremsstrahlung high-energy γ-photons that collide with the high-intensity laser beam at the interaction point (IP) of the experiment. Note that before the IP, the primary electron beam is deflected outside the bremsstrahlung beam path to guarantee a γ-photon and laser beam collision clean of any charged particle.

This chapter describes the setup and the design steps required to realize the first all-optical nonlinear Breit-Wheeler experiment. We describe the generation of the primary electron beam and the bremsstrahlung γ-beam created through the interaction of the laser-accelerated electron beam and a converter foil. Then, we investigate the pair production yield expected from the interaction of the γ-laser beams at the interaction point. To improve the pair yield expected during the experiments, we analyse the influence of the laser intensity in suppressing or enhancing the creation of the pairs.

To estimate the background radiation on the detectors, we perform GEANT4 Monte-Carlo simulations with the complete layout of the experiment. And, by combining the simulation results and the expected pair yield, the expected signal-to-noise ration on the detectors is evaluated.

The contents of this chapter is based on the work published previously published by the author in Ref. [3].

5.1. All-optical SF-QED Experiment Layout

All-optical experiments with lower laser intensities and electron beam charge than the FOR2783 experiment have already been proposed to investigate SF-QED phenomena [3,

24, 25, 68]. It was demonstrated that the key component for such type of experiments is the magnet system which transports the pairs towards the detectors that are located at a detection region with low background noise level. Another key feature important for allo-optical experiment, such as the FOR2783, is the successful timing between the γ-ray beam and the collider laser [202].

The schematic design of the FOR2783 experiment presented in figure 5.1 implements such key components by following the basic layout of the Astra-Gemini SF-QED experiments [24], but including additional improvements on the background radiation level and on the single-particle detection system. As seen on the experimental schematic, two laser beams are required: the LWFA driver and the collider lasers which are derived from the ATLAS-3000 laser system at CALA. The ATLAS laser is a Titanium:Sapphire (Ti:Sa) laser system with central wavelength at 800 nm capable of producing single laser beams of 45 J of energy (from the the available 60 J) with a pulse duration of $\tau_{\text{laser}} = 30$ fs, resulting in a total power of 1.5 PW. This single laser output is split into the two required laser beams where the central part contains 9.5 J used on the tightly focused collider laser beam for the SF-QED interactions, and in a ring-shaped beam containing 30 J after losses that is weakly focused for driving the electron beams.

5.2. Generation of 2.5 GeV Electron Beams

The 30 J LWFA driver laser beam, which has a ring-shape with internal diameter of 12.7 cm and external diameter of 28 cm, is focused by a f/40 parabolic mirror at the LWFA target reaching powers capable of generating multi-GeV electron beam as already discussed in previous publications [90, 203, 204]. First trial experiments at the ATLAS laser have been performed with reduced laser energies of about 5 J using f/30 focusing mirrors with a 20 mm-long slit jet nozzle that produces a plateau electron density of approximately 10^{18} cm^{-3}. Applying a gas mixture of 96% hydrogen and 4% nitrogen, electrons beams are commonly generated with peak energies of 1 GeV. A typical spectrum of the this first trial is shown in figure 5.2 a). In this experiment, ionization injection in the homogeneously doped gas jet of electrons is responsible for the broad spectrum since the intensity of the driver laser beam was not sufficient to reach self-truncated ionization injection and, therefore, the injection was over the length of the jet [205]. Later, shock front injection [206] was implemented to trigger localized injection events. First, a wire stretched across the nozzle induced a supersonic gas flow which was originated by the hydrodynamic shock, however, again, a broad spectrum was observed due to the fixed electron density step limited by the Mach
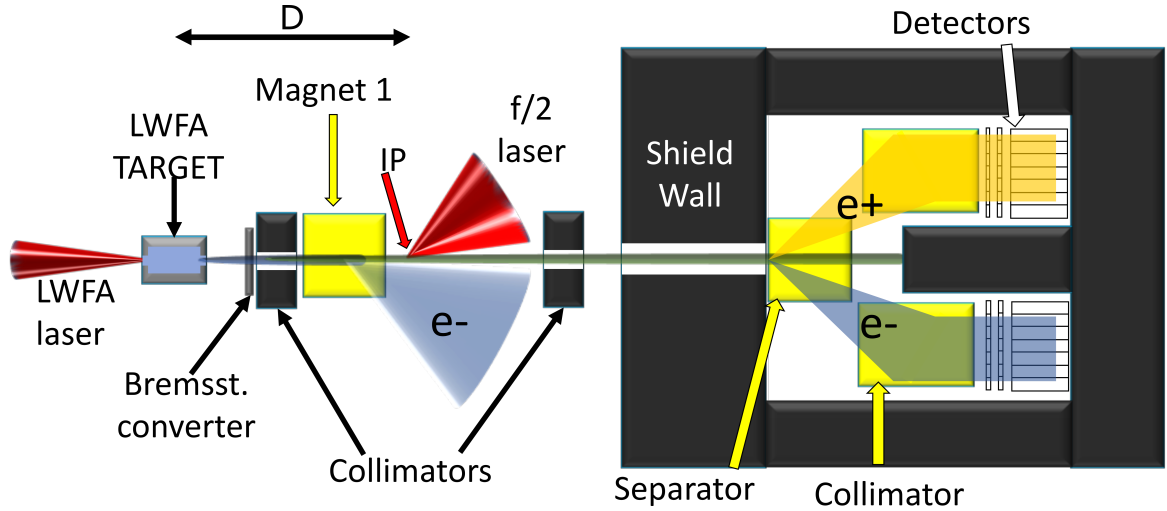
Figure 5.1.: Experimental layout of the FOR2783 experiment at the Centre for Advanced Laser Applications (CALA). Two laser beams are required for the experiment. The 'LWFA-laser' beam is responsible for accelerating monoenergetic electron beams that will interact with a converter target and generate bremsstrahlung gamma photons. The electron beam is deflected outside of the main experimental axis while the γ-beam interacts with a second tightly focus (F/2) 'collider' laser beam. The γ-photon and laser interaction triggers the creation of electron-positron pairs via nonlinear Breit-Wheeler process. The γ-photons and the created pairs co-propagate towards the detectors where a beam dump for the high-energy photons is placed. A system composed of dipole magnets guides the particles to the single-particle detectors.

number of the nozzle. The wire-generated electron spectrum is shown in figure 5.2 b). Finally, an optically-triggered shock [207–209] was tested, and a narrow-band spectrum was observed (figure 5.2 c). The optically-triggered shock injection method allows the transfer of most of the plasma wave energy to the electron beam and a narrow-band high-energy spectrum is achieved with matched charge density.

The energy of the observed electron beams approximately follows the theoretical formula for matched acceleration in the bubble regime where the peak energy gain is given by [86]

$$\Delta E_{max}\,[\text{GeV}] \approx 1.7 \cdot (P\,[100\ \text{TW}])^{1/3} \cdot (n_e\,[10^{18}/\text{cm}^3])^{-2/3} \cdot (\lambda\,[800\ \text{nm}])^{-4/3}. \quad (5.1)$$

At the design point of the FOR2783 experiment, the maximum power achieved by the LWFA laser driver (energy of 30 J, pulse duration of 30 fs and wavelength of $\lambda = 800$ nm) is about 1 PW. Hence, using equation (5.1), the maximum energy gain experienced by an electron bunch is expected to be $\Delta E_{max} \approx 3.6$ GeV, for a matched
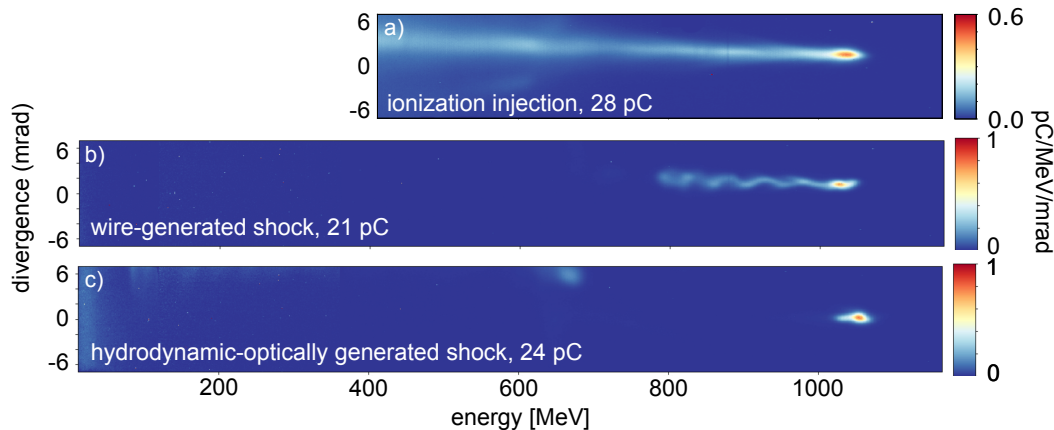
Figure 5.2.: Electron spectra for different injection methods after first LWFA trials at the ATLAS-3000 laser at CALA: a) broad spectrum due to the continuous ionization injection, charge 28 pC above 1 GeV. b) Broad spectrum produced by a wire-generated shock through shock-front injection method, charge 21 pC above 1 GeV. c) Narrow-band and high-energy spectrum produced by optically-triggered shock-front injection, charge 24 pC above 1 GeV. The beam divergence in all experiments is on the order of $\approx$ 0.5 mrad. Figure provided by our collaborators at CALA, Katinka von Grafenstein and Prof. Dr. Stefan Karsch.

plasma density of $n_e < 10^{18}$ cm^{-3}. Electron beam energy of 2.5 GeV can be achieved by varying the plasma density and the energy of the LWFA laser beam.

After generating the 2.5 GeV monoenergetic electron beam, the LWFA laser beam is reflected out of the beam axis, for example, by a tape drive, while the electrons continue their propagation. The reflection of the LWFA beam by the tape drive is important to avoid ablating and damaging the bremsstrahlung target. As the electron continues its propagation, it meets a bremsstrahlung converter target where high-energy γ-photons are produced. These high-energy photons are essential for triggering the nonlinear Breit-Wheeler pair creation processes by colliding them with the collider laser beam.

As seen in chapter 2, the bremsstrahlung radiation is composed of many 10's to 100's MeV photons that are incapable of triggering pair creation due to their low energy, however, they can still be detected by the designed Cherenkov calorimeter either by direct photons hits on the detectors or by generating secondary particles inside the calorimeter detection channel. Hence, the signal produced by these MeV-photons represents an inherent background radiation in this type of experiment that should be mitigated as much as possible.

A critical part of the experiment is to optimize the target length to obtain a high γ-photon yield with photon energies $E_\gamma > 0.9\mathcal{E}$ which is capable of triggering the pair

production process, where $\mathcal{E}$ is the energy of the primary LWFA electron beam, while not significantly reducing the signal-to-noise ratio on the detectors by the few-MeV photons inherently produced in the bremsstrahlung process.

5.3. Bremsstrahlung Conversion

The converter target is selected to be a high-Z material which allows achieving high bremsstrahlung conversion efficiency. In the FOR2783 experiment, Tungsten (W, $X_0^{\mathrm{W}} = 3.5\,\mathrm{mm}$) was chosen due to its high radiation stopping power and yield as already discussed in section 2.1.1 and in figure 2.1.

Monte-Carlo GEANT4 [108–110] simulations were performed for an incoming 10 pC collimated electron beam of $\mathcal{E} = 2.5$ GeV passing through tungsten foils of different thicknesses (50 μm, 350 μm, 1 mm and 2.5 mm). In figure 5.3 a) the evolution of the bremsstrahlung spectrum is shown for the different target thicknesses L. The simulation results show that for energies above $\mathrm{E}_\gamma > 2.25\,\mathrm{GeV}$, i.e., $\mathrm{E}_\gamma > 0.9\mathcal{E}$, a softening of the spectrum is observed as the length of the target increases due to the electron energy losses and multiple scatterings inside the material. In addition, negligible yield increase is observed above 1 mm thickness.

As the target length increases and multiple scatterings inside the target start to become significant, the full width at half maximum of the angular distribution (FWHM) of the γ-photons also becomes larger as shown in figure 5.3 b). The increase on the FWHM of the angular distribution of the γ-ray leads to a bremsstrahlung beam less collimated, and a reduced photon flux at the interaction point (IP). The photon flux of the hard-photons between 2.2 - 2.5 GeV at the IP is presented in figure 5.3 c) for different target thicknesses. The γ-flux saturates for lengths of $L < 0.4X_0$ due to the increase of the divergence and spectrum softening as the target becomes thicker. The simulated γ-flux distribution for the hard-photons between the energy range of 2.2 - 2.5 GeV for different converter target thicknesses is shown in figure 5.4 with the increased divergence and the stochastic nature of the photon distribution.

From the simulation results presented in figures 5.3 and 5.4, the optimum tungsten target thickness is found to be $L < 1\,\mathrm{mm}$ due to the high yield of photon of energies above $\mathrm{E}_\gamma > 2.2\,\mathrm{GeV}$ without saturation of the photon-flux.
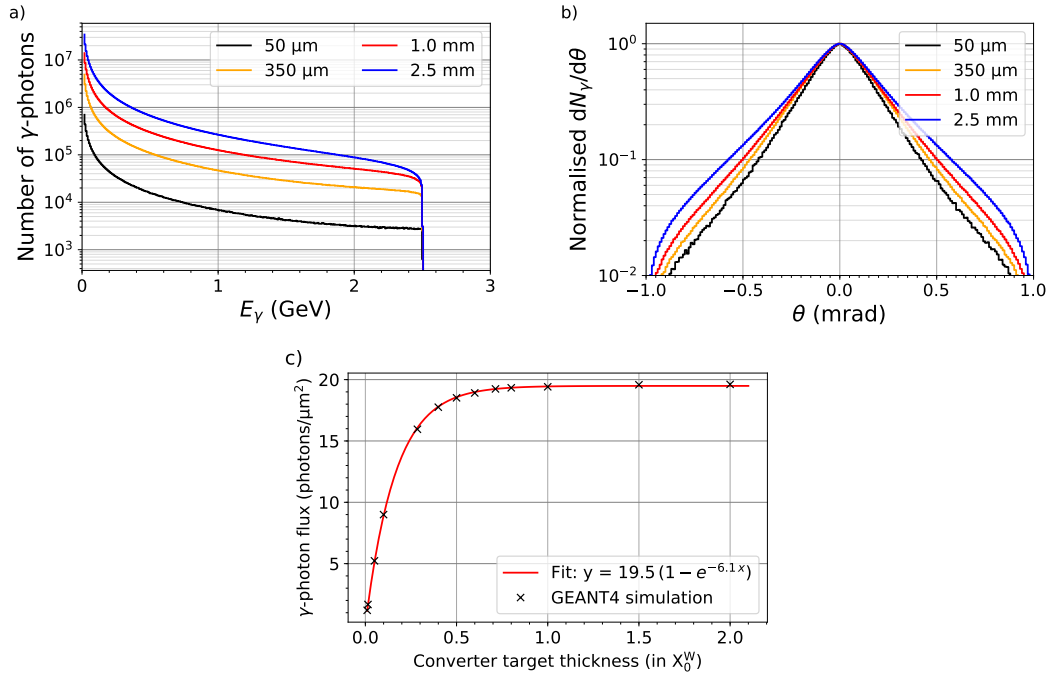
Figure 5.3.: GEANT4 simulations of a collimated electron beam of energy 2.5 GeV and 10 pC charge interacting with a tungsten converter target. (a) Bremsstrahlung spectrum, (b) angular distribution of the Bremsstrahlung γ-ray for different tungsten converter target thickness (50 µm, 1.0 mm, 350 µm, 2.0 mm). As the converter target thickness increases, the yield of γ-photons also increases and the full width at half maximum (FWHM) of the angular distribution enlarges due to the multiple scattering inside the target. (c) γ-photon flux for different target thicknesses at the focal plane of the collider laser for hard-photons of energies between 2.2 - 2.5 GeV within the 100 µrad of the bremsstrahlung emission cone. Saturation of the photon flux is observed as the target thickness increases.

5.4. Photon-Photon Interaction and Optimal Laser Intensity

After the generation of the γ-ray photons, both, electrons and photons, co-propagates through a Tantalum collimator which shapes the γ-beam profile to match the entrance of gamma-ray beam dump located downstream close to the detectors. Hence, the collimator is designed to have a 10 cm length and inner radius of 1 mm (10 mm outer radius). At the end of the Tantalum collimator, a permanent dipole magnet (magnet 1) of length 60 cm and field strength of approximately BL ≈ 0.32 T m is placed. The dipole magnet cleans the now shaped bremsstrahlung γ-ray of any charged particle by deflecting the primary electrons downwards towards a set of Lanex scintillating
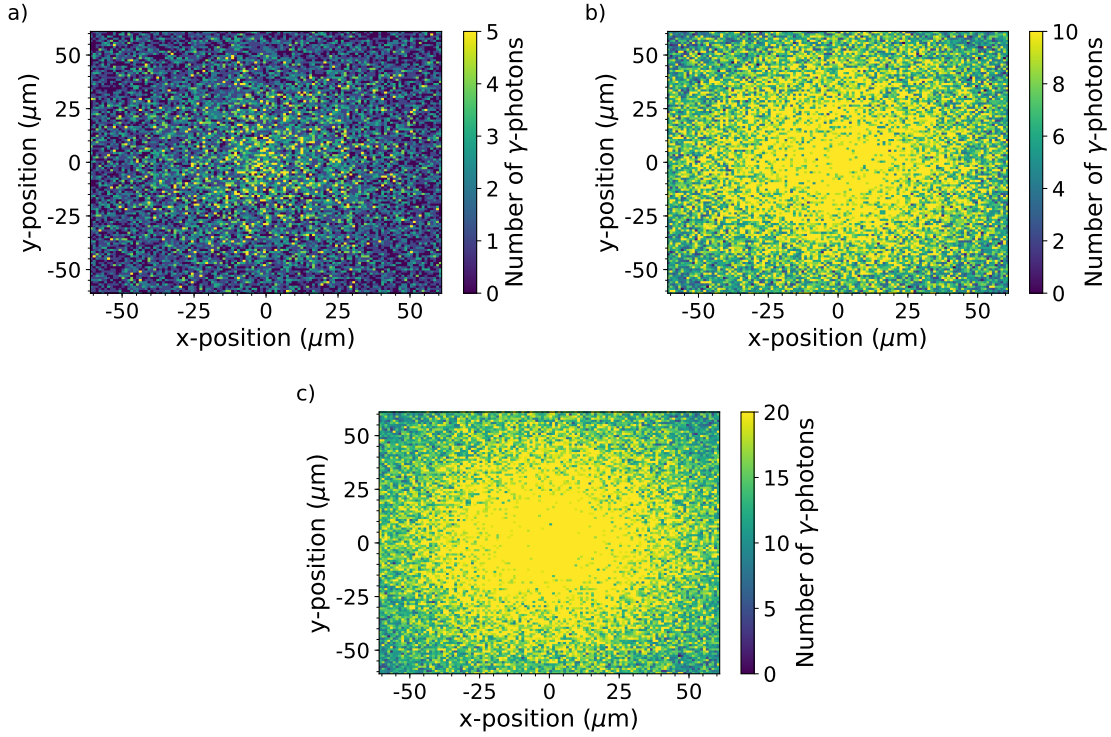
Figure 5.4.: GEANT4 Simulated flux of the γ-photons with energies within the spectral range of 2.2 - 2.5 GeV as a function of the tungsten converter target thickness: (a) 50 µm, (b) 350 µm, (c) 1000 µm. In the simulations, it was considered as input a collimated electron beam with energy of 2.5 GeV and 10 pC of charge. The increased yield for thicker targets is primarily radiated into larger angles and only increase peak flux slowly. The interaction laser only subtends a focal spot area of $\approx 2.0\,\mu m^2$ – much smaller than γ-spot size. The peak flux of the gamma-beam in the considered spectral range is 1.7 photons/µm² for a 50 µm thick target, 9.0 photons/µm² for a 350 µm thick target, and 16 photons/µm² for a 1000 µm thick target.

screens used for diagnosing their energy spectrum and charge. At about the rear of the dipole magnet it is located the interaction point (IP). Now, the next natural step is to determine the optimal collider laser intensity required to reach the highest pair-creation probability rate.

5.4.1. Optimal Collider Laser Intensity

At high laser intensities, the pair production probability rate given in equation (2.28) approximately scales as $P \propto I^q$, with q considered as an effective non-linearity parameter. In figure 5.5 is shown the logarithmic derivative of the pair production yield $q = \mathrm{d}(\log P)/\mathrm{d}(\log I)$, i.e., the effective parameter q which represents approximately the

slope of the curves already presented in figure 2.15 a). In the exponentially suppressed regime, characterized by $q > 1$, the pair yield N_{pairs} increases rapidly with the increase of the collider laser intensity. As the laser intensity I increases, the parameter q reduces significantly, and the pair production probability per cycle starts to exceed 10% per incoming γ-photon requiring depletion of the γ-photon to be taken into account. As soon as the parameter reaches values of $q < 1$, the pair yield N_γ as $N_{\text{pairs}} \propto N_\gamma \text{P}$ increases sub-linearly by raising the collider laser intensity. Hence, for this regime of a parameter $q < 1$, a larger laser spot area, which leads to a higher number of γ-photon flux, is more favorable to improve the pair production yield rather than increasing of laser intensity.
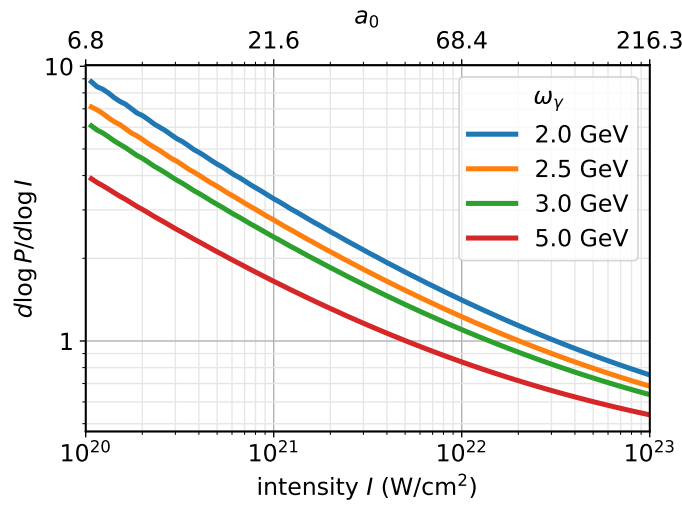
Figure 5.5.: Logarithmic derivative of the pair production yield, slope of the curves in figure 2.15 a). The ideal laser intensity is found to be in the range between $0.5 \ldots 3 \times 10^{22} \, \text{W cm}^{-2}$ for the accessible electron-beam energy range of $1 \ldots 3.6 \, \text{GeV}$ at the FOR2783 experiment for a constant density of γ-rays in a spot size much larger than the laser spot size. The design point of the experiment is chosen to be 2.5 GeV electron beam energy, and a collider laser peak intensity close to $10^{22} \, \text{W/cm}^2$ leading to an effective parameter $q \approx 1$.

For the FOR2783 experimental parameters, the optimal collider laser intensity is determined by the effective parameter q under the assumptions of a fixed high laser power, large γ-ray spot area $A_\gamma > A_{\text{laser}}$ in which the number of γ-photons scales linearly with the laser area $N_\gamma \propto A_{\text{laser}}$ while the intensity decreases as $\text{I} \propto A_{\text{laser}}^{-1}$. Hence, the ideal laser intensity is found to be in the range between $0.5 \ldots 3 \times 10^{22} \, \text{W cm}^{-2}$ for the accessible electron-beam energy range of $1 \ldots 3 \, \text{GeV}$. The design point of the experiment is chosen to be: 2.5 GeV electron beam energy which, as previously

discussed, is accessible at CALA with the LWFA laser beam (energy of 30 J, pulse duration of 30 fs and wavelength of $\lambda = 800$ nm) to produce high-energy γ-photons via bremsstrahlung capable of triggering the nonlinear Breit-Wheeler pair creation process using a collider laser peak intensity close to 10^{22} W/cm^2. The choice of such parameters leads to an effective parameter $q \approx 1$. The collision angle[1] between the γ-photons and the collider laser beam is set to 162° which, as seen in figure 2.15 b), does not reduce significantly the par yield.

At the chosen design point, the pair yield is maximized by increasing the number of high-energy γ-photons at the interaction point. To this end, the distance D between the bremsstrahlung photons and interaction point (IP), as seen in figure 5.1, should be minimized to improve the γ-photon flux at the IP, and therefore promote more photons-laser collisions. In the FOR2783 experiment, the distance D is chosen to be 600 mm leading to an expected γ-beam spot of $w_\gamma \approx 300\,\mu$m. The distance D is limited by the dimension of dipole magnet (magnet 1) placed in between the bremsstrahlung converter target and the IP. The length of the dipole magnet of 600 mm is the minimum length required to deflect the 2.5 GeV electron beam outside the IP allowing only photon-laser collisions and still having the electron beam be dumped inside the target area without creating radiation background at the location at the detectors.

To match the collider laser intensity, an f/2 off-axis parabolic mirror focus the beam in an Airy-shaped focus with diameter of the first minimum at $q_1 = 2.44 \cdot f/\# \cdot \lambda \approx 4\,\mu$m and an Airy FWHM diameter of FWHM$_{\text{Airy}} = 1.03 \cdot f/\# \cdot \lambda = 1.65\,\mu$m. Approximating the Airy focus to a Gaussian distribution, an effective waist of $w_0 = 1.4\,\mu$m and FWHM diameter of 1.6 μm are obtained. The large γ-ray spot area in comparison with the spot area of the focused laser makes the spatial overlap between them uncritical and easily achievable using a YAG:Ce scintillation signal.

The temporal overlap, namely the timing between the γ-photons and the laser beam, is also monitored interferometrically. To achieve the overlap of the high-energy photons with the collider laser beam, the use the temporal overlap between the LWFA and the collider as a baseline and compensate later the electron bunch delay inside the LWFA bubble and its duration. Hence, at first, the time-of-arrival (TOA) of the beams at the IP position of the LWFA and collider laser beams is measured using a photodiode. The diode signal allows to roughly estimate the position of the delay stage where the propagation distances of the light beams are matched, however, the precision of this measurement is limited by the response of the photodiode which

---

[1]Head-on collisions with holed parabolic mirrors were considered, however, they present a source of background noise indistinguishable from the nonlinear BW pairs generated at the border or inside the OAP hole.

corresponds to an uncertainty on the overlap of about a few 100's of femtoseconds. Then, interferometry between the beams is implemented for narrowing down the overlap precision to a few 10's of femtoseconds. An example of how to achieve spatial and temporal overlaps between laser beams derived from the same light source is shown in Appendix E. The example introduces the same technique planned to perform the spatial and temporal overlap of the LWFA and collider beams of the FOR2783 experiment. Finally, the time difference between the LWFA driver pulse and the electron beams is easily compensated using a delay stage knowing that the electron bunches are a few-fs behind the LWFA driver laser pulse and have a duration of also few-femtoseconds. The timing accuracy $\Delta\tau$ is determined by the Rayleigh range of the collider laser beam with $\Delta\tau < \pi w_0^2/(c\,\lambda) \approx 30\,\mathrm{fs}$ which is well within the stability of the system.

5.4.2. Expected Pair Yield and Spectrum

After defining the γ-photon flux at the interaction point and the optimal laser intensity, the expected pair yield N_{pairs} for the FOR2783 experiment can be evaluated as

$$N_{\mathrm{pairs}} = \Phi_{\mathrm{gamma}} \cdot A_{\mathrm{laser}} \cdot \theta_{\mathrm{div}} \cdot N_{\mathrm{cycles}} \cdot \mathrm{P}\,, \qquad (5.2)$$

where Φ_{gamma} is the γ-photon flux from figure 5.3 for different target thicknesses and a collimated 10 pC electron beam, A_{laser} is area of the collider laser focal spot, N_{cycles} is the number of laser cycles and P is the average pair production per laser cycle. The parameter θ_{div} represents the divergence loss of the bremstrahlung photon flux which in our setup is dominated by the electron beam divergence θ_{e} of about 0.5 mrad. The divergence loss constant is evaluated as $\theta_{\mathrm{div}} = \theta_\gamma^2/(\theta_\gamma^2 + \theta_{\mathrm{e}}^2)$. In the limit of thin targets, the divergence of bremsstrahlung gamma photons is determined by the Lorentz-factor $\gamma_e \approx 5000$ of the primary electron beam such that $\theta_\gamma = 1/\gamma_e = 0.2\,\mathrm{mrad}$. Hence, the divergence loss parameter evaluates to $\theta_{\mathrm{div}} = \theta_\gamma^2/(\theta_\gamma^2 + \theta_{\mathrm{e}}^2) \approx 0.14$.

The expected pair yield for a laser repetition rate of 0.1 Hz and different converter target thicknesses is shown in figure 5.6.

Based on our design point, primary LWFA electron beam of energy $\mathcal{E} = 2.5\,\mathrm{GeV}$ with divergence $\theta_{\mathrm{e}} = 0.5\,\mathrm{mrad}$, collider laser intensity of $\mathrm{I} = 9.5 \times 10^{21}\,\mathrm{W\,cm^{-2}}$, converter target thickness of $50\,\mu\mathrm{m}$, and a charge of 10 pC of primary electrons, we can achieve a maximum pair production rate of 0.22 pairs per laser shot which corresponds to about 80 pairs per hour. Higher yields on the order of $\gg 1000$ pairs/hour are possible with thicker targets and higher primary electron bunch charges which could realistic
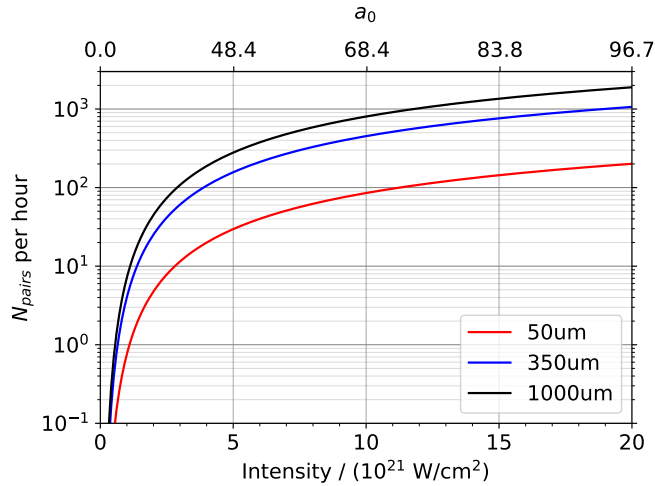
Figure 5.6.: Pair yield rate per hour for different intensities (at constant laser spot size) and converter thickness based on the following parameters: $\lambda = 800$ nm, $w_0 \approx 2$ µm, pulse duration of 30 fs, monoenergetic LWFA electron beam energy with 2.5 GeV and 0.5 mrad FWHM divergence angle. The optimal experiment pair rate, based on our design point of $I = 9.5 \times 10^{21} \, \mathrm{W\,cm^{-2}}$ and target thickness of 50 µm is 80 pairs/10 pC/h.

reach up to 100 pC per laser shot.

The evaluated pair yield assumes a constant laser spot size and γ-ray divergence of approximately 0.5 mrad which is predominately set by the LWFA beam. For the FOR2783 experimental conditions, the pair yield can be reduced by increasing the collider laser spot size which decreases the laser intensity, or improved by reducing the divergence of the γ-ray which increases the γ-photon flux at the IP. To decrease the divergence of the γ-ray beam, and, consequently, increase its flux, one should reduce the divergence of the multi-GeV electron bunch. Therefore, by adding a collimating lens after the LWFA target, the divergence of the γ-ray would be reduced to $\approx 1/\gamma = 0.2$ mrad (with negligible electron beam divergence) leading to an increase of approximately $7\times$ of the γ-photon flux and the pair yield.

The expected pair spectra are also investigated and important for the construction of the single-particle detectors. For a monoenergetic γ-ray beam of $\omega_\gamma = 2.5$ GeV, the pair spectra, as seen in figure 5.7 a), is symmetrical and centered at $\omega_\gamma/2$ as expected from the kinematics of the particle collision. For our experimental parameters, the γ-beam is broadband due to the nature of the bremsstrahlung process with the highest number of photons at low energies. Hence, for our experimental conditions, the pair spectra are determined by the γ-beam spectrum as shown in figure 5.7 b) which is an

asymmetrical pair spectra shifted towards lower energies.
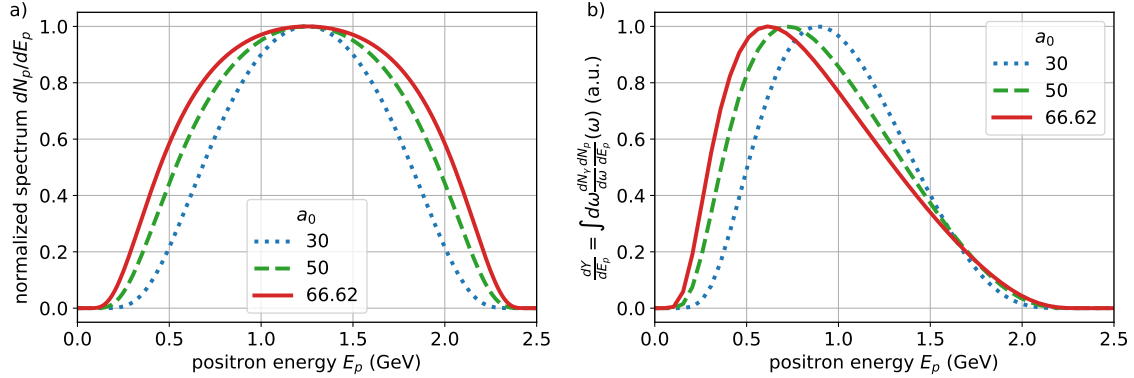
Figure 5.7.: Normalized spectra of produced pairs for different values of the normalized vector potential: $a_0 = 30$, $a_0 = 50$, and $a_0 = 66.62$: (a) a monoenergetic γ-ray with energy of $\omega_\gamma = 2.5$ GeV produces a symmetrical pair spectra centered at $\omega_\gamma/2$, and (b) for our experimental design point, the bremsstrahlung spectrum expected from a 50 µm thick converter foil broadens and shifts the pair spectra towards lower energies.

5.5. Single Pair Detection and Background Level

After the pairs are created at the interaction point through the collision of the few high-energy γ-photons and the laser beam, they co-propagate with the remaining γ-ray through a second collimator that shapes the gamma-beam profile again and a 10 cm diameter tunnel inside a 5.6 m shielding wall that separates the ATLAS laser target area and the detection bunker region as shown in figure 5.8. Inside the bunker region, a combination of separator and collimator magnets deflect and re-collimate the leptons towards the single-particle detectors while the γ-ray continues in a straight path towards a gamma-beam dump placed about 1 m behind the detectors. The designed arrangement of the separator and collimator magnets allows diagnosing particles in the range of 300 MeV to 1.3 GeV where the highest pair production probability is obtained as seen in figure 5.7 b). The timing between a single-particle hit on the detectors and a backscattered noise from the beam dump corresponds to about 7 ns which is sufficient for gating the calorimeter photomultiplier tubes and the LYSO imaging system.

The detection system used in the FOR2783 experiment was previously introduced in chapter 3. In this experiment, coincidence measurements between electrons and positrons are possible since the magnet system separates the pairs and transports them to two different sets of detectors - one for each type of charged particle.

Figure 5.8.: Detection bunker installed at CALA behind a 5.6 m radiation shielding wall of concrete. The bunker is connected to the CALA target area by a 10 cm diameter tunnel.

For the entire pair rate considered at the experiment, we expect only single pairs being produced during the photon-laser collisions. Consequently, the pairs are recorded as single events and the signal of no more than one single-particle per detector element in both LYSO screens and the Cherenkov calorimeter is expected. Therefore, the signal does not depend on the converter target thickness or beam charge since a Breit-Wheeler signal event on the detectors is well defined.

The challenge in detecting the single signal events is the reject the shower of 10's of MeV background radiation on the detectors that can significantly reduce the signal-to-noise ratio. To prevent significant background radiation on the detectors, the CALA facility offers a 5.6 m long radiation shield wall that allows separating the background radiation generated inside the target area, where the IP and the primary electron dump are located and the detection region where orders of magnitude lower radiation levels are found. To estimate the background radiation level inside the CALA target area and the detection bunker, GEANT4 Monte-Carlo simulations with the complete experimental geometry as shown in figure 5.10 were performed. Note that a numerical absorber is used to emulate temporal gating and avoid backscattered background from the gamma-beam dump inside the radiation bunker.

The simulations indicate that only a small number of events are recorded by the Cherenkov calorimeter for a 50 µm tungsten converter foil on both simulated cases in which the temporal gating of the detectors is enabled or not. The recorded particle spectra of the background noise in a single calorimeter channel are shown in figure 5.11.
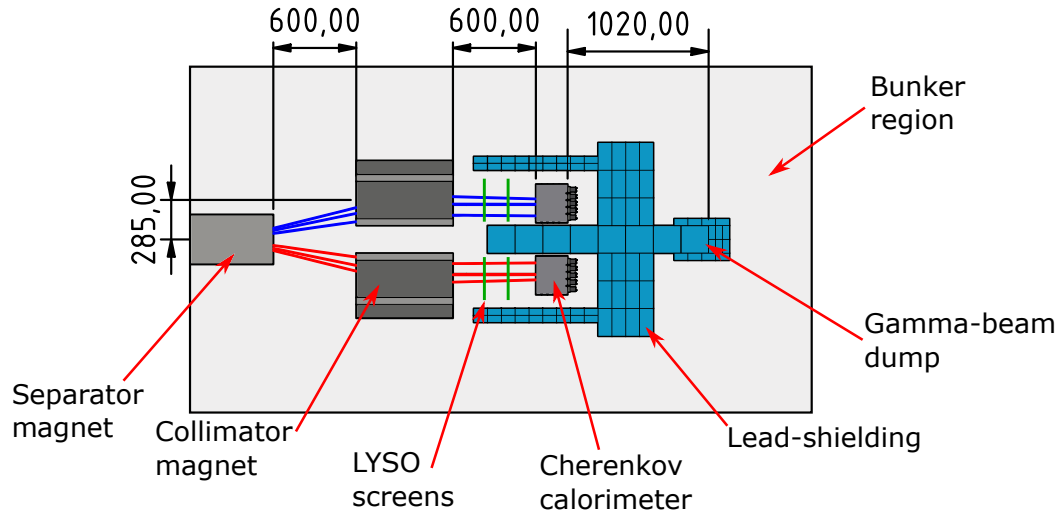
Figure 5.9.: Top view of the arrangement of the components inside the CALA bunker with distances between components. The distance between the Cherenkov calorimeter and the gamma-beam dump is about 1 m, which corresponds to a particle double pass from the Cherenkov calorimeter of about 7 ns which is sufficient for gating the devices and neglecting the background noise. Blue trajectories are the electrons and red trajectories represent the positrons. The detection system is designed to diagnose particles in the range of 300 MeV to 1.3 GeV where the highest pair production probability is obtained.

When temporal gating is not present, the number of noise particles is higher than the situation when gating is applied and noise particles originating from the gamma-beam dump are neglected.

To guard against any unknown source of background and to quantify probabilities of false-positive hits, measurements of the background noise radiation level inside the bunker are planned before the data set collection at the experiment.

According to the simulations, the background radiation on the detectors is mainly composed of few γ-photons of energy less than 15 MeV originated at the γ-beam dump that are backscattered towards the devices. The background radiation scales linearly with the primary LWFA beam charge and the thickness of the converter target. This is understood by considering the bremsstrahlung yield as previously presented. The overall bremsstrahlung yield increases linearly with converter target thickness for the range of interest of the experiment while the number of high-energy photons saturates above 2.2 GeV for small converter target thickness values of $L < 0.5X_0$. As the yield increases with the thickening of the target, the number of background photons backscattered striking the detectors also increases. Due to this reason, we find that a converter target with $L \ll X_0$ is ideal for the FOR2783 experiment, since
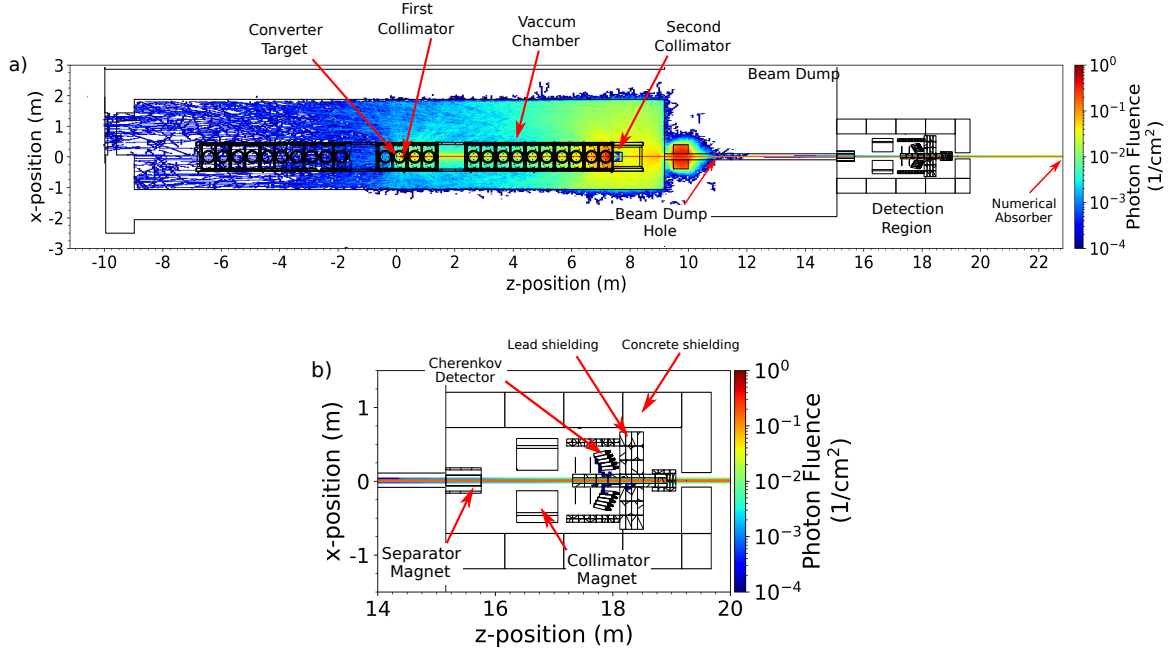
Figure 5.10.: Monte-Carlo simulations of the average γ-photon fluence at the target area and detector region at CALA. (a) shows the photon flux across the entire target area as well in the detection region, and (b) presents a detailed view inside the detection region. The photon fluence is average over 10^4 primary events where each event corresponds to a shot of a collimated electron with an energy of 2.5 GeV onto the tungsten converter target of $50\,\mu$m thickness. A numerical absorber is included in the simulations to represent the temporal gating of the detectors and mitigate all backscattered noise from the gamma-beam dump.

few hard γ-photons with energy above 2.2 GeV required for triggering the SF-QED interactions are produced, and a lower number of MeV-photons, which only contributes for generating background radiation inside the bunker, are cooled down at the γ-beam dump. Hence, a tungsten foil of $50\,\mu$m thickness is chosen as the design point and it is proven ideal for reduced background level on the detectors and significant pair yield as demonstrated by the simulations previously presented.

Finally, using the simulations results given in figure 5.11 b), the signal-to-noise ratio on the Cherenkov calorimeter can be evaluated. According to the simulation, the number of Cherenkov photons detected by the calorimeter produced due to background radiation entering the detector is $N_{bg} \approx 6$ photons with uncertainty of $\sigma_{bg} = \sqrt{N_{bg}} \approx 2.45$ photons. Assuming that a signal lepton[2] of 500 MeV hits

---

[2]A signal lepton pair of 500 MeV has a high probability of being created according to the pair creation spectrum presented in figure 5.7 b).
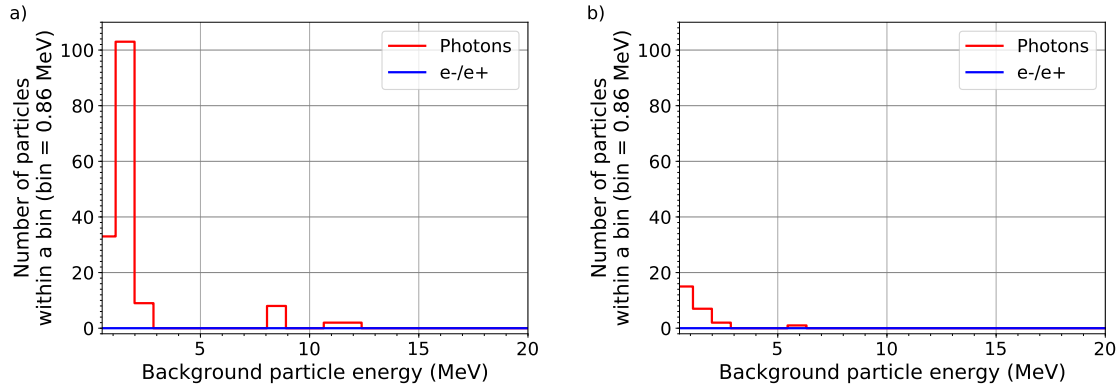
Figure 5.11.: Simulated background noise at a single Cherenkov calorimeter channel (a) without employing temporal gating and (b) using temporal gating. The backscattered noise originated at the beam dump is mitigated when temporal gating is applied on the detectors and the only noise on the detectors is forward particle noise from interactions upstream. The Monte-Carlo simulations were conducted using GEANT4 with a collimated primary monoenergetic 2.5 GeV electron beam with a charge of 10 pC interacting with a 50 μm tungsten converter target.

the Cherenkov detector, about $N_{sig} = 83$ Cherenkov photons are detected by the calorimeter with uncertainty of $<\sigma_{sig}> = \sqrt{N_{sig}} \approx 9$. Thus, the signal-to-noise ratio SNR_p is given by $SNR_p = N_{sig}/N_{bg} = 83/6 \approx 13.8$. And, the alternate SNR definition $SNR_\sigma = N_{sig} / <\sigma> = 83/9.6 \approx 8.6$, where $<\sigma> = (<\sigma_{sig}>^2 + 2 \cdot \sigma_{bg}^2)^{0.5} \approx 9.6$. On the other hand, an SNR < 1 is possible if thicker targets are considered due to its background noise level increase as the bremsstrahlung yield is higher as well but insignificant gains in the pair yield.

The response of the LYSO screens on the experiment can also be evaluated using equation (3.3). The screens are imaged by 4Picos placed 870 mm away from the crystal arrays and the cameras are attached to a f/1.4, 28 mm focal length lens with transmission efficiency of about $T_{lens} \approx 19\%$ at the LYSO peak wavelength. Hence, the light collection angle is $\Omega = (\pi \cdot 20^2)/(870^2) = 1.66 \times 10^{-3}$ sr, where $(\pi \cdot 20^2)$ is the input area of the lens. Using the the calibration values of the screens introduced in section 3.4 where an absolute light efficiency of the LYSO screens of $(9.08 \pm 0.43) \times 10^{10}$ photons/sr/pC is given, the number of detected photons by the 4Picos CCD sensor is

$$N_{ph, det} = 9.08 \times 10^{10} \cdot 1.66 \times 10^{-3} \cdot \frac{1.602 \times 10^{-19}}{10^{-12}} \cdot T_{lens} = 4.58 \text{ photons} \qquad (5.3)$$

with uncertainty of 0.21 photons calculated following the same method above.

According to the calibration of the 4Picos cameras, please see Appendix D, the number of photons per CCD counts at an average MCP gain of 1.35 kV is about 0.00259 photons/count which corresponds to about 386 counts/photon. Hence, the 4 photons expected to reach the CCD sensor of the camera will produce a signal of $4 \cdot 386 = 1544$ counts which is well above background level and easily distinguishable. Note that higher count signals are also possible by increasing the ICCD gain voltage of the camera. To avoid any unknown signal and non-linearity, calibration of the LYSO screens using back-converter foils to produce lepton pairs is planned during the FOR2783 beamtime.

5.6. Conclusions

This chapter presents a fully-evaluated all-optical setup to probe the nonlinear Breit-Wheeler process via γ-laser interactions for the first time. Background radiation is inherently generated for this type of experiment presenting a challenge to the experimental design that has been addressed and successfully solved in the design of the experiment. For this reason, GEANT4 Monte-Carlo simulations of the full experimental geometry were performed to optimize the background radiation levels at the detection region built inside the radiation bunker of CALA. According to the simulations, the background scales proportionally with the few-MeV γ-photons generated via bremsstrahlung that are dumped inside the radiation bunker and do not contribute for triggering the pair production process, while the yield of hard photons above 2.2 GeV required for the SF-QED interactions does not increase significantly. Therefore, maximizing the signal-to-noise ratio at detectable signal rates by minimizing the radiation background is an important requirement rather than maximizing the signal rate itself.

To minimize the radiation background, the simulations shows that the trade-off between signal rate and SNR is, counterintuitively, optimized for thin bremsstrahlung converter target with thickness much less than the radiation length of the converter material ($L \ll X_0$) for a moderate primary electron charge of 10 pC. Thus, a tungsten converter target of 50 μm thickness was chosen for the experiment.

Optimization of the collider laser intensity is also another major requirement of the experiment since the pair production rate scales exponentially with the laser intensity $P \propto I^q$ at high laser intensities. On the FOR2783 experiment, due to the high laser intensities, the parameter $q < 1$ and the pair yield increase sub-linearly indicating that larger laser focal spot areas have more influence on the increase of pair yield than the

laser intensity itself. Hence, the ideal laser intensity of the experiment is found to be approximately I $= 9.5 \times 10^{21}$ W/cm^2 assuming an primary electron beam of 2.5 GeV, 10 pC of charge and divergence of $\theta_e \approx 0.5$ mrad.

Finally, a SNR > 10 is possible for the chosen design point of the experiment, and pair yields of 0.22 pairs per laser shot, i.e., about 80 pairs per hour at laser repetition rate of 0.1 Hz, are achievable at the ATLAS-3000 laser system at CALA. The increase of the pair yield is possible by introducing thicker converter targets but still maintaining a controlled background noise level, or by inserting a plasma-lens stage after the LWFA target to focus the primary electron beam to reduce the divergence of the bremsstrahlung-ray and increase the number of high-energy γ-photons at the interaction point.

6. Discussions and Outlook

Electron-positron pair creation via quantum-vacuum fluctuation is one of the most puzzling and fascinating theory that remain untested in the laboratory. With the advent of high-power lasers, SF-QED process became accessible, and upcoming experiments, such as the E-320 at FACET-II (SLAC) and FOR2783 at the Centre for Advanced Laser Applications (CALA) projects, aim to experimentally investigate the pair-production phenomenon.

The challenge of the SF-QED experiments is the detection of a single particle above the noise produced by the background radiation composed of many x-rays and low-energy γ-photons generated by the beam dumps placed close to the detectors. To overcome this issue, this thesis presents the design and calibration of a single-particle detector capable of successfully diagnosing single particles with a signal-to-noise ratio of above 10.

A summary of the calibration of the designed detection system and the performance expected for the SF-QED experiments is given in the next sections. Moreover, research opportunities for SF-QED and areas beyond the scope of SF-QED are discussed.

6.1. Single-Particle Detection System

The single particle detector designed and calibrated in this work demonstrated that single particle diagnosis is possible in the upcoming SF-QED experiments. The challenge of this type of experiment is to reduce the background noise level on the detectors through clever radiation shielding geometries and by temporally gating the detectors to reject any type of background noise to achieve a signal-to-noise ration > 1 on the calorimeter.

The Cherenkov calorimeter is a high-performance device able to diagnose single signal particle hits with incoming energy in the range of a few MeV to GeV with high rejection of low energy background radiation generated from beam dumps in the experiments. The fast response of the photomultiplier tubes (PMTs) responsible to detect the Cherenkov light enables to temporally gate the signal and, therefore, neglect any noise originating from sources of secondary particles far from the device.

The LYSO scintillating screens of the designed detection system provide a high scintillation yield and fast decay time of the scintillation light of the LYSO crystal. Both features combined with a superior imaging system composed of image intensifiers or

ultra-fast ICCD 4Picos cameras, which contain built-in microchannel plate intensifiers (MCPs), enable the detection of low photon signals from a single particle hit on the scintillating screens. In addition, the image intensifiers and the MCPs also allow to temporally gate the imaging system reducing the background noise on the detection. Moreover, the screens provide a better energy resolution than the Cherenkov calorimeter and the spectrum of the detected particles can be inferred by integrating the response over many shots. The use of silicon tracking detectors present an alternative to the LYSO tracking layers. Silicon detectors are also able to detect single-particle hits with great background noise rejection due to their insensibility to low-energy particles due to their thin thickness. In the E-320 and FOR2783 experiments, large strips of silicon detectors are required increasing the cost of the tracking layer solution. Therefore, the use of pixelated scintillating screens is preferred due to its cost-benefit in diagnosing single particles as discussed in chapter 3.

The exceptional performance of the proposed single particle detection system is obtained not only from the enhanced performance of the individual components used, the LYSO tracking layers, and the calorimeter but also from the combination thereof. On the detection system, a valid event is only accounted for if the particle track is within one-pixel difference on both LYSO screens and the response of all three detectors is above 3σ of the expected signal level, resulting in 99% of true events being considered.

The accuracy of the designed detector system in diagnosing single particles is essential for the upcoming E-320 and FOR2783 experiments and can be easily implemented in other SF-QED experiments that also require probing single particles originated from SF-QED process, for example, the linear Breit-Wheeler [25] and LUXE [63].

6.2. E-320 Experiment at FACET-II (SLAC)

The Experiment-320 (E-320) at FACET-II linear accelerator (SLAC) is introduced in chapter 4. The E-320 initial run will collide with an electron beam, with a mean energy of 13 GeV and energy spread of $< 0.1\%$, with a focused laser beam of $a_0 \approx 10$. As a consequence of the interaction, electron-positron pairs will be created and later probed at the single particle detector designed in this work. At the experiment, the detectors are placed less than 10 meters from an electron and γ-ray beam dump that generates a shower of low energy (few-tens of MeV) secondary particles, however, the signals produced by this shower are easily gated away from the detection system.

On the other hand, Monte-Carlo simulations were performed to estimate the back-

ground noise promoted by the low-energy secondary particles at the detectors that are not possible to be gated. The simulations resulted in a a signal-to-noise ratio of $SNR_\sigma = 18$ at the Cherenkov calorimeter.

The single-particle detection system has been installed in the FACET beamline as designed and has been collecting data. The plot in figure 6.1 shows the signal of the central detection channel of the calorimeter (photomultiplier voltage gain set to its minimum of 500 V). The signal seen is generated by the current background radiation in the region where the calorimeter is installed. The signal of the photomultiplier tube is saturated and exhibits two time constants, τ_1 and τ_2, however, for small signals, the long decay time constant is not visible. Further analysis of the signal of the PMTs is required.
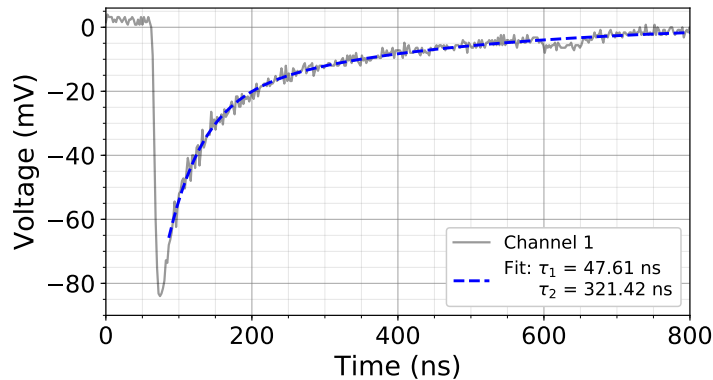
Figure 6.1.: Signal of the central detection channel of the calorimeter (photomultiplier voltage gain set to its minimum of 500 V). The signal seen is generated by the current background radiation in the region where the calorimeter is installed. The signal present two time constants: $\tau_1 = 47.61$ ns and $\tau_2 = 321.42$ ns. Note that the long decay time constant τ_2 is not visible for small photomultiplier signals. Further analysis of the signal of the PMTs is required. The Cherenkov calorimeter was designed by the author of this thesis, but its installation and signal acquisition was performed by E. Gerstmayer and S. Meuren.

According to the Monte-Carlo simulations of the full FACET beamline layout presented in chapter 4, the LYSO screens are also able to detect single particle hits above background noise with a higher energy resolution than the calorimeter of 0.02.

Figure 6.2 shows the signal from both LYSO tracking layers installed at FACET-II. The captured scintillation signal also corresponds to the background radiation that propagates across the detectors. Further analysis of the background levels on the screens is also required.
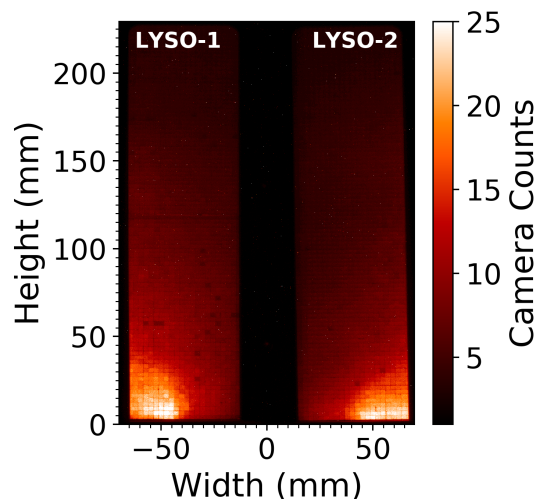
Figure 6.2.: Signal of the LYSO tracking layers installed at FACET-II as part of the designed single-particle detection system. The scintillation signal generated by large losses of the primary electron beam is seen at the bottom of the screens. Imaged captured with a Manta G-895 (8-bit mode) camera attached to a lens with focal length of 50 mm (f-number of 0.95). Further analysis of the signal is required. The LYSO screens were designed by the author of this thesis, but their installation and signal acquisition were performed by E. Gerstmayer and S. Meuren.

The background radiation observed on all three elements of the designed single-particle detector is generated by the large losses of the accelerated electron beam. With such large background radiation, the system is not capable to detect single-particle since the single-particle signal is immersed in noise. Therefore, further optimization of the electron beam is required to reduce the background radiation levels. After the optimization of the electron beam, in-situ calibration of the detectors is required as discussed in section 3.3.1 prior to data taking shots.

6.3. FOR2783 Experiment at CALA

Different from the E-320, the FOR2783 is an all-optical experiment with the ATLAS-3000 laser split into two different beams. The ring-shaped part of the beam, known as the LWFA-laser beam, is used to produce laser-accelerated electrons beams with energies of 2.5 pC and a charge of 10 pC.

Currently, the generation of the required electron beam for the FOR2783 experiment is being commissioned using a laser beam of energy of 9 J on target, pure hydrogen as

gas, and a spherical mirror with f-number $\approx$ 55 and a focal length of 10 m. The results of the first trials are shown in figure 6.3. Monoenergetic electron beams with energies above 1 GeV have been produced via hydrodynamic-optically generated shocks to induce down-ramp injection in a supersonic gas jet produced using a slit nozzle 20 mm long and 3 mm width. Results from this experimental configuration are shown in figure 6.3 a). Attempts are being made to increase the energy of the electron beams by changing the initial gas target from a slit-nozzle jet to a gas cell which increases the acceleration length to 20 mm. In this new scenario, electron beams have been accelerated to energies up to 2.3 GeV, however, with a continuous tail of low energy particles due to the ionization injection mechanism. The results representing this trial are shown in figure 6.3 b). The gas density of both acceleration experiments is under evaluation but is assumed to be between 10^{18} cm^{-3} and 10^{19} cm^{-3}.

The electron beams are then used to produce bremsstrahlung radiation by interacting with a 50 µm-thick tungsten converter target optimized using Monte-Carlo GEANT4 simulations.

The high-energy γ-photons interact with the second beam, known as the collider beam, which is tightly focused to an intensity given by an $a_0 \approx 66$. The pair yield expected from the photon-laser interactions is about 80 pairs/hour for a laser repetition rate of 0.1 Hz is predicted. In addition, the signal-to-noise ratio of the detectors was evaluated using GEANT4 Monte-Carlo simulations with the full geometry of the experiment inserted into the model, and an SNR > 10 of the Cherenkov detector was found.

As seen in figure 5.8, the radiation bunker has been built already at CALA. The next step is to assemble the lead radiation shield inside the region and place the detectors. After the installation of the components inside the bunker, calibration of the detectors as described in section 3.3.1 and measurements of the background radiation are planned.

6.4. Research Opportunities

Strong-field QED experiments provide an excellent platform to advance different fields of high-energy physics including plasma-based accelerators and particle detectors. In the following sections, some research opportunities provided by SF-QED are explored.
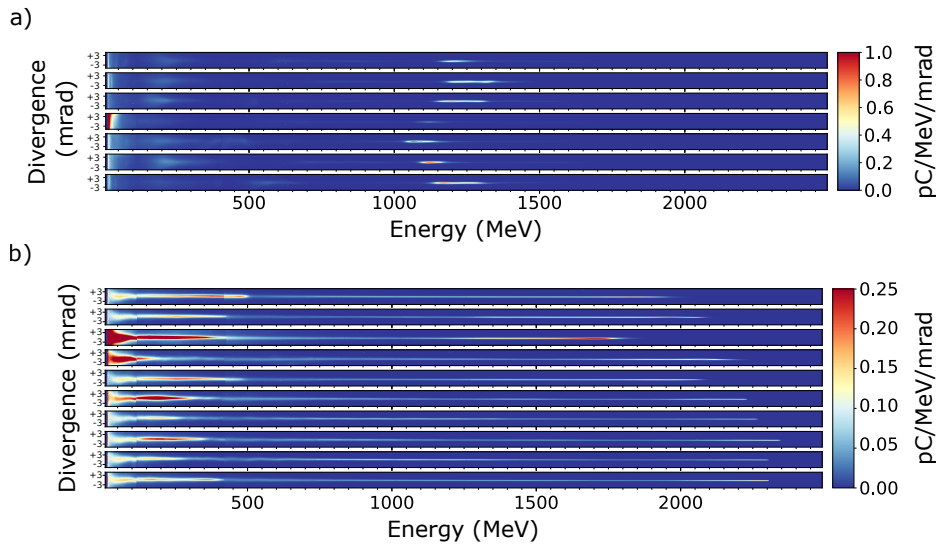
Figure 6.3.: Preliminary results during the electron beam commissioning at CALA for the FOR2783 experiment using a laser beam of energy of 9 J on target, pure hydrogen as gas, and spherical mirror with an f-number of ≈ 55 and focal length of 10 m. a) Shows the energy spectrum of the laser-accelerated electron beams produced via hydrodynamic-optically generated shocks to induce down-ramp injection in a supersonic gas jet produced using a slit nozzle 20 mm long and 3 mm width. In this target configuration, electron beams with energies above 1 GeV are produced. b) Energy spectrum of accelerated electron beams has been using a gas cell with an increased acceleration length of 20 mm. Using the gas cell target, electrons are injected via the ionization injection process with maximum energy up to 2.3 GeV but presenting a long tail of low-energy particles. The gas density of both acceleration experiments is under evaluation but is assumed to be between 10^{18} cm^{-3} and 10^{19} cm^{-3}. Data was provided by our collaborators of the FOR2783 experiment, Katinka von Grafenstein and Prof. Dr. Stefan Karsch.

6.4.1. Strong-Field QED

Investigating SF-QED interactions enables the study of fundamental questions in QED, plasma physics, and properties of extreme astrophysical environments.

The electron-positron pair production from quantum vacuum is the major driving force of SF-QED experiments. So far, such process remains untested in the laboratory, but, as discussed in this thesis, the increase of laser intensity enables probing such phenomenon. As the laser intensity grows, higher χ_e (and χ_γ) parameters are achieved, and as soon as $\chi \gg 1$, where χ represents either χ_e or χ_γ, QED cascades start to play a role in creating electron-positron pair plasma. The generation of pair plasma and QED cascades represent a new challenge to be overcome.

To achieve $\chi \gg 1$ values, ideas for co-locating petawatt laser systems with ultra-relativistic electron beam accelerators have been envisioned [210]. For example, the construction of the 100 PW laser of the Station of Extreme Light (SEL) co-located with the 25 keV superconducting x-ray free-electron laser facility (XFEL) at the Shangai Superintense-Ultrafast Laser Facility (SULF) reaching a $\chi \approx 55$ through the collision of an 8 GeV electron beam with a laser beam of $a_0 = 575$ [211, 212].

In this new generation of PW laser facilities, the collision of the ultra-relativistic electron beam with the intense laser beam can generate a continuous sequence of emissions of a high-energy γ-photons which, while still immersed in the laser field, triggers pair production. This sequence takes place increasing exponentially the number of particles forming electron-positron pair plasma until the nonlinear quantum parameter reaches $\chi \lesssim 1$ and the generation of hard γ-photons and pair production becomes less probable [213].

Despite the great challenge imposed to generate pair plasma under laboratory conditions, they represent an important step for further studying the interaction between the SF-QED and collective plasma effects [212], which are similar to the processes in the magnetosphere of magnetars [210, 214–216].

The generation of pair plasma investigates the fully nonperturbative regime where $\chi \gg 1$. On the other hand, precision measurements of the transition from the classical to the quantum regime also remain untested [57, 217–224].

In addition, electron-laser collision experiments can be used to study the spin polarization of electrons while emitting high-energy photons via the nonlinear Compton scattering process during their interaction with a high-intensity laser pulse [225–227].

6.4.2. Beyond Strong-Field QED

All-optical experiments are also capable of triggering QED cascades using laser-accelerated electron beams via the laser-wakefield technique (LWFA). However, the current LWFA electron beams are still not comparable with the beams generated by conventional accelerators. Hence, improvements on the LWFA technique and laser diagnostics are essential for improving the quality of the LWFA electron beam.

Laser Wakefield Acceleration (LWFA)

The generation of high-quality electron beams with low emittance, low energy spread, and high energy is one of the key parameters ensuring a successful strong-field QED experiment. Since the first demonstration of quasi-monoenergetic electron beams with

energy of about 100 MeV produced by LWFA [92, 228, 229], an enhancement in the beam energy up to 8 GeV has been reported due to the rapid increase of the peak intensity of the lasers available and the use of techniques such as laser guiding within a plasma channel [90].

However, plasma-based accelerators are still ongoing research and have not reached the same level of maturity as conventional linear accelerators which are capable of providing low emittance and low energy spread beams with energies above 10 GeV [195, 196]. In addition, plasma-based accelerators still cannot provide comparable high repetition rates, reproducibility shot-to-shot, and stability provided by conventional accelerators.

Efforts have been made to obtain a better understanding of the LWFA method, for example, the evolution of the bubble [230], different injection mechanisms [91, 94], how beam loading influences the spectral shape of the bunches [204], and improvements on the beam emittance and its diagnostics [93, 231, 232]. However, tailoring laser wakefield driven electron beams is still considered a challenge due to the large number of parameters to be controlled and optimized. To overcome the problem of the large number of variables to be tuned, machine learning methods together with full automatization of laser systems are promising techniques to improve the output of the laser-plasma accelerators [233, 234].

High-quality electron beams produced by laser-plasma accelerators are essential for the success of the upcoming all-optical SF-QED experiments. For example, as seen in chapter 5, monoenergetic electron beams with low emittance favor the generation of high energy and low divergence bremsstrahlung γ-rays and the increase of the number of γ-laser interactions improving the number of pairs created. High-quality electron beams also produce electron-laser interactions with a nonlinear quantum electron parameter above unit, $\chi_e > 1$, enabling signatures of radiation reaction being observed at a single-shot basis [223].

High-Intensity Laser Diagnostics

The development of high-intensity lasers is a key factor to investigate SF-QED process not only to improve the quality of LWFA electron beams but also to determine the quality of the collider laser beam of the SF-QED experiments.

To this end, it is essential to fully understand the performance of the laser beam. However, direct characterization of the laser light at its full power has not yet been performed due to damages to the optical components required for probing the beam. The usual routine to infer the laser intensity at high-power mode is to measure the

full-power energy of the collimated beam, then attenuate the laser power to measure the pulse duration and image the focused beam to determine the focus area. Knowing these three parameters, full-power energy, pulse duration, and focus area, the intensity of the laser at full-power mode is estimated. This simple method of calculating the full-power intensity of the focused laser beam may not hold at tightly focused beams, for example, the pulse duration may be longer from low-power measurements due to radial dispersion and nonlinear effects [235]. These uncertainties are still the subject of studies.

Studies, such as atomic ionization effects of gases, have been proposed to measure the peak laser intensity at focus [236, 237], nonetheless, they are only valid at non-relativistic laser intensities. At higher intensities, methods combining atomic ionization and acceleration of electrons were suggested to retrieve the size of the focus and intensity of the laser beam [238–241]. More recently, ponderomotive scattering of electrons from ionized gases was proposed to measure the peak intensity at the focus by analyzing the spatial distribution of the scattered high-energy electron beam by the laser [235]. So far, these methods previously mentioned have not yet been experimentally realized and the characterization of the peak intensity at focus remains a challenge.

Independently of the ionization of gases, another promising technique to measure the peak intensity of relativistic lasers uses the emitted radiation from the nonlinear Thomson radiation after the collision of an electron beam with a highly intense focused laser beam to be probed [222, 242, 243]. This method relies on the measurement of the ellipticity of the emitted radiation which depends mainly on the a_0 of the laser beam. However, to achieve precise measurement of the a_0 of the laser beam and its peak intensity, the quality of the colliding electron beam must be well-tailored, especially its energy spread.

In addition to the measurement of the peak intensity at the focus of the laser beam running at high-power mode, it is also important to understand how the laser amplitude and phase evolve at focus. Full-field reconstruction techniques using interferometric scans of the laser beam can be employed to obtain fringe patterns that can precisely retrieve the electric field characteristics of the laser field over many shots [244]. The real reconstructed electric field amplitude, phase, and distribution of the laser beam at the focus can be used as an input parameter of the current SF-QED theoretical models and an improved prediction of the interactions can be possible.

High-Energy Photon Diagnostics

Another essential component of pair production experiments via quantum vacuum fluctuations is the generation of γ-photons. As seen in chapters 4 and 5, γ-ray beams are intrinsically part of any SF-QED experiments but yet their profile and energy have not been successfully characterized.

Spectrometers based on pair production through the Bethe-Heitler process in high-Z targets have already been proposed, however, the detectors were not designed for the high flux of the photon beams expected at the experiments [245, 246]. Alternatively, a spectrometer based on electromagnetic cascades inside scintillation crystals has been designed and later used in SF-QED experiments to measure the γ-beam transverse and longitudinal profiles [60, 247]. However, the detector exhibited a poor energy resolution due to its insensitivity to small variations of the incoming γ-ray spectrum.

A promising solution for probing γ-beams with high-energy, high-flux with improved resolution is the pair spectrometers designed in Refs. [248, 249]. The designed spectrometers can spectrally resolve γ-ray beams up to 10 GeV by converting the incoming gamma photons into high-energy electron-positron pairs analyzed in a dipole magnet. The detectors are designed specifically for the upcoming SF-QED at LUXE (DESY) [248] and Experiment-320 [249], and are capable of performing precision measurements of the γ-ray beam spectra. Both detectors are still to be tested and calibrated, but they already provide a great advance in diagnosing high-energy photons in SF-QED experiments.

6.5. Final Remarks

The recent developments in highly intense lasers enable investigating different and exciting hitherto untested SF-QED phenomena that were not accessible before through the collision of the laser beams with electron or highly-energetic photon beams. However, to achieve the required strong field above the Schwinger critical limit, ultrarelativistic electron beams are required to produce high-energy γ-photons either by bremsstrahlung or by nonlinear inverse Compton scattering. Independently of the type of the SF-QED experiment, using conventional accelerators or all-optical, the electron beams and γ-photons are cooled down in beam dumps that scatter x-rays and low energy γ-photons towards the single-particle detectors used to diagnose the pairs created in the experiment. Therefore, the challenge for the upcoming experiments is to minimize the background radiation on the detectors by using clever radiation

shielding geometries and temporal gating techniques on the detector.

Different SF-QED effects can be also measured using the electron-laser collision geometries, for example, Compton scattering and the recoil of electrons due to the high-energy photon emission, namely radiation reaction, at different regimes of interactions are possible to be investigated. In addition, precision measurements of the transition from the classical to the quantum regime of both interactions have been proposed but are still to be realized [57, 217–224]. The realization of electron-laser experiments also provides an excellent platform to study spin polarization of electrons while emitting high-energy photons via the nonlinear Compton scattering process during their interaction with a high-intensity laser pulse [225–227]. Additionally, particle cascades and showers can also be triggered by electron-laser interactions due to SF-QED process [9, 224, 250, 251]. The cascades can further generate dense electron-positron plasma [252], similar to the ones originated by SF-QED process in the vicinity of pulsars and black holes due to their extreme intense magnetic fields [253, 254], that can be investigated under laboratory conditions.

On the contrary, collision geometries between highly energetic photons and intense laser beams offer the opportunity to investigate purely the nonlinear Breit-Wheeler pair production without the electron-laser interaction intermediate step. The FOR2783 experiment is designed to diagnose the pair production process in the non-perturbative regime for the first time using an all-optical experimental layout and pure photon-laser collisions [3].

To detect the pairs created from the quantum vacuum, sensitive detectors are essential to perform precision measurements of the SF-QED processes. The single particle detector designed in this work to be used on the upcoming SF-QED experiments E-320 and FOR2783 demonstrates superior performance ability of single particles detection with a signal-to-noise ratio well above unity. In addition to detector development, SF-QED experiments are an excellent platform to combine and promote beneficial knowledge exchanges between the recent laser and plasma-based accelerator developments with the state-of-art expertise of conventional accelerators.

A. Derivation of the Lorentz equation

First, let's recall the Lagrangian of a non-relativistic particle interacting with an electromagnetic field given by [146]

$$\mathcal{L}(\mathbf{r}, \mathbf{v}, t) = \frac{m\mathbf{v}^2}{2} + q\mathbf{v} \cdot \mathbf{A} - q\phi \tag{A.1}$$

where m and q are the charged particle mass and charge, $\mathbf{v}$ is the velocity of the particle, $\mathcal{A}$ and ϕ are the field vector and scalar potentials.

The next step, is to substitute the Lagrangian in equation (A.1) into the Euler-Lagrange equation of motion [146]

$$\frac{\partial \mathcal{L}}{\partial \mathbf{r}} - \frac{\mathrm{d}}{\mathrm{d}t}\left(\frac{\partial \mathcal{L}}{\partial \mathbf{v}}\right) = 0 \,. \tag{A.2}$$

The first term of the left-hand side of equation (A.2) becomes

$$\begin{aligned}
\frac{\partial \mathcal{L}}{\partial \mathbf{r}} &= \nabla\left(q\mathbf{v} \cdot \mathbf{A} - q\phi\right) \\
&= q\left[\nabla\left(\mathbf{v} \cdot \mathbf{A}\right) - \nabla\phi\right] \\
&= q\left[\mathbf{v} \times (\nabla \times \mathbf{A}) + (\mathbf{v} \cdot \nabla)\mathbf{A} - \nabla\phi\right] \,.
\end{aligned} \tag{A.3}$$

We solve now the partial derivative in the second term of the left-hand side of the Euler-Lagrangian equation (A.2),

$$\frac{\partial \mathcal{L}}{\partial \mathbf{v}} = m\mathbf{v} + q\mathbf{A} \tag{A.4}$$

and then take its total derivative with respect to time,

$$\begin{aligned}
\frac{\mathrm{d}}{\mathrm{d}t}\left(\frac{\partial \mathcal{L}}{\partial \mathbf{v}}\right) &= \frac{\partial}{\partial t}\left(m\mathbf{v} + q\mathbf{A}\right) + (\mathbf{v} \cdot \delta)(m\mathbf{v} + q\mathbf{A}) \\
&= \left(m\frac{\partial \mathbf{v}}{\mathrm{d}t} + q\frac{\partial \mathbf{A}}{\partial t}\right) + q(\mathbf{v} \cdot \nabla)\mathbf{A}
\end{aligned} \,. \tag{A.5}$$

Note that we use the convective derivative property $\mathrm{d}y/\mathrm{d}t = \partial y/\partial t + \mathbf{v} \cdot \nabla t$.

Finally, we plug equation (A.3) and equation (A.5) into the Euler-Lagrange equation to obtain

$$m\frac{\partial \mathbf{v}}{\partial t} = -q\frac{\partial \mathbf{A}}{\partial t} + q\mathbf{v} \times (\nabla \times \mathbf{A}) - q\nabla\phi \,. \tag{A.6}$$

Rearranging equation (A.6) in a more convenient form as

$$\frac{\partial \left(m\mathbf{v}\right)}{\partial t} = q\left[-\frac{\partial \mathbf{A}}{\partial t} - q\nabla\phi\right] + q\left[\mathbf{v} \times \left(\nabla \times \mathbf{A}\right)\right].\tag{A.7}$$

Finally, recalling the definitions of the electric $\mathbf{E}$ and magnetic $\mathbf{B}$ fields in terms of the field vector and scalar potentials,

$$\mathbf{E} = -\frac{\partial \mathbf{A}}{\partial t} - q\nabla\phi\,,\tag{A.8a}$$

$$\mathbf{B} = \nabla \times \mathbf{A}\,,\tag{A.8b}$$

we can rewrite equation (A.7) in terms of the electromagnetic fields and obtain the non-relativistic equation of motion of a charged particle interacting with an electromagnetic wave,

$$\frac{\partial \mathbf{p}}{\partial t} = q\left(\mathbf{E} + \mathbf{v} \times \mathbf{B}\right)\tag{A.9}$$

where $\mathbf{p} = m\mathbf{v}$ is the particle momentum. The term in the right-hand side of the equation of motion (A.9) is known as the Lorentz force $\mathbf{F}_{\mathrm{L}} = q\left(\mathbf{E} + \mathbf{v} \times \mathbf{B}\right)$ which gives the force exerted in a charged particle by an electromagnetic field.

B. Single Particle Motion in an Electromagnetic Field

Assume an electromagnetic field with the scalar potential ϕ and vector potential $\mathbf{A}$. The Lagrangian that describes the interaction of a non-relativistic particle with an electromagnetic field is given by $\mathcal{L}(\mathbf{r}, \mathbf{v}, t) = m\mathbf{v}^2/2 + q\mathbf{v} \cdot \mathbf{A} - q\phi$, where m and q are the particle mass and charge, $\mathbf{v}$ is the velocity of the particle [146]. By substituting the given Lagrangian into the Euler-Lagrange equation (see Appendix A for a detailed derivation), one obtains the famous Lorentz equation of motion[1]:

$$\frac{\mathrm{d}\mathbf{p}}{\mathrm{d}t} = q\left(\mathbf{E} + \mathbf{v} \times \mathbf{B}\right). \tag{B.1}$$

The right-hand side of equation (B.1) represents the force exerted on the charged particle, $\mathbf{F}_{\mathrm{L}} = q\left(\mathbf{E} + \mathbf{v} \times \mathbf{B}\right)$. One sees that the electric field $\mathbf{E}$ is responsible for direct acceleration of the particle in the same direction as the electric field, while the magnetic force in the cross-product $\mathbf{v} \times \mathbf{B}$ results in a force perpendicular to the velocity of the particle and the magnetic field $\mathbf{B}$. Solutions for specific cases such as constant electric fields ($\mathbf{E}$, $\mathbf{B} = 0$) or constant magnetic fields ($\mathbf{E} = 0$, $\mathbf{B}$) can be easily found in the literature [69, 146, 255]. Here, the focus will be to describe the motion of a charged particle in an electromagnetic plane wave which is the basic model to describe the interaction of electrons with laser light.

Particle Motion in an Electromagnetic Plane Wave

In this section, we solve the particle motion interacting with an electromagnetic plane wave. The solution can be obtained using different methods, for example with the Euler-Lagrange equation of motion as showed in Ref. [88] or using the Lorentz equation of motion given in equation (B.1). In this work, we focus on the latter method.

First, we need to express the equation of motion in its covariant form using the

---

[1]The equation of motion is given in rationalized natural units ($c = \hbar = \epsilon_0 = 1$).

four-vector notation[2], given as [146]

$$\frac{\mathrm{d}u^{\mu}}{\mathrm{d}S} = -\frac{e}{m_e}F^{\mu\nu}u_{\nu}\,, \tag{B.2}$$

where $u^{\mu} = (\gamma, \mathbf{u})$ is the normalized four-momentum, e and m_e are the absolute charge and mass of the electron, $F^{\mu\nu}$ is the electromagnetic field tensor, and S is the proper time of the particle. The electromagnetic field tensor is expressed as $F^{\mu\nu} = \partial^{\mu}A^{\nu}(K^{\mu}X_{\mu}) - \partial^{\nu}A^{\mu}(K^{\mu}X_{\mu})$, where $A^{\nu} = (0,\, 0,\, A_0\cos(K^{\mu}X_{\mu}),\, A_0\sin(K^{\mu}X_{\mu}))$ is the four-potential for an electromagnetic plane wave with scalar potential equal to zero since there are no free external charges in the system. The four-wavevector $K^{\mu} = (\omega_0,\, k_x,\, 0,\, 0)$ which results in the dispersion relation $K^{\mu}K_{\mu} = \omega_0^2 - k_x^2 = 0$ and X^{μ} is the four-position vector.

Now, substituting the definition of the electromagnetic tensor definition assuming a plane wave, the equation of motion becomes

$$\frac{\mathrm{d}u^{\mu}}{\mathrm{d}S} = -\frac{e}{m_e}\left[K^{\mu}\frac{\mathrm{d}A^{\nu}}{\mathrm{d}(K^{\mu}X_{\mu})} - K^{\nu}\frac{\mathrm{d}A^{\mu}}{\mathrm{d}(K^{\mu}X_{\mu})}\right]u_{\nu}\,. \tag{B.3}$$

Introducing the normalized the proper time $\tilde{S} = \omega_0 S$, the normalized four-potential[3] $a^{\mu} = eA^{\mu}/(m_e)$, and the four-wavevector as $n^{\mu} = (1/\omega_0)K^{\mu}$ which gives the propagation direction of the wave, equation (B.3) can be normalized as

$$\frac{\mathrm{d}u^{\mu}}{\mathrm{d}\tilde{S}} = -\left(n^{\mu}a'^{\nu} - n^{\nu}a'^{\mu}\right)u_{\nu}\,. \tag{B.4}$$

Note that the vectors $a'^{\nu} = (e/m_e)\left[\mathrm{d}A^{\nu}/\mathrm{d}(K^{\mu}X_{\mu})\right] = \mathrm{d}a^{\nu}/\mathrm{d}(K^{\mu}X_{\mu})$. Now, premultiplying equation (B.4) by the direction n_{μ}, one obtains the following equation,

$$\frac{\mathrm{d}(n_{\mu}u^{\mu})}{\mathrm{d}\tilde{S}} = -\left(n_{\mu}n^{\mu}a'^{\nu} - n_{\mu}n^{\nu}a'^{\mu}\right)u_{\nu} = 0\,, \tag{B.5}$$

since the terms $n_{\mu}n^{\mu}a'^{\nu} = 0$ and $n_{\mu}a'^{\mu}n^{\nu} = 0$. By integrating equation (B.5), we get the first constant of motion $n_{\mu}u^{\mu} = C_0$. If the particle is initially at rest, $C_0 = 1$, and the first relation is obtained:

$$\gamma = 1 + u_x\,. \tag{B.6}$$

Now, by left-multiplying equation (B.4) with a the basis vector $\alpha_{\mu} = (0,\, 0,\, 1,\, 0)$, we

---

[2]The Minkowski metric employed here is (+1, -1, -1, -1). The equations and variables are given in rationalized natural units ($c = \hbar = \epsilon_0 = 1$).

[3]Note that the normalized four-potential have already been briefly introduced as the normalized laser strength in equation (1.1).

obtain the following:

$$\frac{d(\alpha_\mu u^\mu)}{d\tilde{S}} = -\left(\alpha_\mu n^\mu a'^\nu - \alpha_\mu n^\nu a'^\mu\right) u_\nu = -\alpha_\mu n^\nu a'^\mu u_\nu\,. \tag{B.7}$$

We define new variable $\zeta = n_\mu X^\mu$ and take its derivative with respect to $\tilde{S}$ to obtain $d\zeta/d\tilde{S} = n_\mu(d\,X^\mu/d\tilde{S}) = n_\mu u^\mu$. Now, substituting the new ζ variable and its derivative in equation (B.7), we obtain

$$\frac{d}{d\zeta}(\alpha_\mu u^\mu) = \frac{d}{d\zeta}(\alpha_\mu a^\mu) \tag{B.8}$$

which results in the relation $\alpha_\mu u^\mu = \alpha_\mu a^\mu$, and, consequently, $u_y = a_y$. If we modify the basis vector to $\alpha_\mu = (0,\,0,\,0,\,1)$ and follow the same calculation steps, it is also easy to verify that $u_z = a_z$.

A solution for the u_x component of the normalized momentum, which does not depend on the Lorentz factor γ, is still required. That being so, we take the square of equation (B.6) such that $\gamma^2 = (1 + u_x)^2$. Recalling that $\gamma^2 = 1 + u^2 = u_x^2 + u_y^2 + u_z^2$, the relation $u_x = (u_y^2 + u_z^2)/2 = (a_y^2 + u_z^2)/2$ is found.

Finally, the momenta of a particle initially at rest interacting with an electromagnetic plane wave propagating in x-direction and given by the four-potential $a^\mu = (0,\,0,\,\delta a_0 \cos\phi,\,(1-\delta^2)^{0.5} a_0 \sin\phi)$, where $\phi = K_\mu X^\mu$, and polarization expressed by the δ parameter ($\delta = \{\pm 1,\,0\}$ for linear polarization, and $\delta = \pm 1/\sqrt{2}$ for circular polarization) is given by the following set of equations in the laboratory frame:

$$u_x = \frac{(a_y^2 + u_z^2)}{2} = \frac{a_0^2}{4}\left[1 + (2\delta^2 - 1)\cos 2\phi\right]\,, \tag{B.9a}$$

$$u_y = \delta\, a_0 \cos(\phi)\,, \tag{B.9b}$$

$$u_z = (1-\delta^2)^{0.5}\, a_0 \sin(\phi)\,. \tag{B.9c}$$

The trajectories of the particle is obtained by simply integrating each momentum component with respect to the phase ϕ:

$$x = \frac{1}{4}a_0^2\left[\phi + \frac{2\delta^2 - 1}{2}\,\sin 2\phi\right]\,, \tag{B.10a}$$

$$y = \delta\, a_0 \sin\phi\,, \tag{B.10b}$$

$$z = -(1-\delta^2)^{0.5}\, a_0 \cos\phi\,. \tag{B.10c}$$

121

Note that the particle travels in the same direction in which the plane wave propagates as given in equation (B.10a), and, in addition, the distance travelled by the particle increases over time due to the term ϕ. Hence, the electron drifts in x-direction while interacting with the electromagnetic field with average momentum given by $<u_x> = a_0^2/4$ which corresponds to a velocity of $<v> = a_0^2/(4 + a_0^2)$.

In the average rest frame of the electrons, $<u_x> = 0$, we can obtain $\gamma^2 = 1 + u^2$ and the Lorentz parameter $\gamma_0 = \sqrt{1 + a_0^2/2}$ from the previous relation.

If we boost the momentum solution of equation (B.9) to the rest frame of the electron by the average momentum $<u>$ in the propagation direction, we obtain

$$u_x = \frac{a_0^2}{4\gamma_0}(2\delta^2 - 1)\cos 2\phi \,, \tag{B.11a}$$

$$u_y = \delta a_0 \cos(\phi) \,, \tag{B.11b}$$

$$u_z = (1 - \delta^2)^{0.5} a_0 \sin(\phi) \,. \tag{B.11c}$$

And, by integrating the components of the momentum in equation (B.11), the particle trajectory in the average rest frame is obtained,

$$x = \frac{a_0^2}{4\gamma_0^2}\left(\delta^2 - \frac{1}{2}\right)\sin 2\phi \,, \tag{B.12a}$$

$$y = \frac{\delta}{\gamma_0}a_0 \sin \phi \,, \tag{B.12b}$$

$$z = -\frac{a_0}{2\gamma_0}(1 - \delta^2)^{0.5} \cos \phi \,. \tag{B.12c}$$

The electron motion while interacting with an electromagnetic plane wave for two different normalized field strength a_0 is shown in figure B.1. As a_0 become larger, the amplitude of the motion increases as well the drift velocity of the particle. In addition, a figure-of-eight motion is observed in the particle motion in its average rest frame.
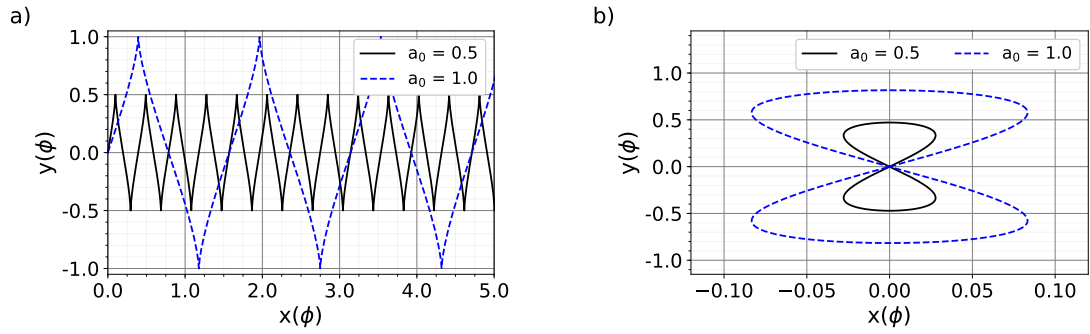
Figure B.1.: Electron trajectories while interacting with an electromagnetic plane wave in (a) the laboratory and in the (b) cycle average rest frame of the electron for two different normalized values of $a_0 = \{0.5, 1.0\}$. The amplitude of the motion becomes larger with higher values of the normalized field strength as seen in (a). In the average rest frame of the electron, the motion becomes the famous figure-of-eight. In the case of $a_0 \ll 1$, the position in x-direction of the particle reduces to $x \sim$ constant.

C. Radiation Length of Materials

Radiation length of an element of a compound is defined as the mean length required for an electron to reduce its energy by a factor of 1/e. The energy lost by the electron is transferred to photons through bremsstrahlung process or to secondary particles. Therefore, a particle propagating through a material of thickness x and radiation length X_0 loses energy with the rate:

$$\frac{\mathrm{d}\mathcal{E}}{\mathrm{d}x} = -\frac{\mathcal{E}}{X_0} \,. \tag{C.1}$$

The radiation length X_0 of an element given in units of cm^2/g can evaluated using the following analytical formula [107]:

$$\frac{1}{X_0} = 4\alpha \mathrm{r}_e^2 \frac{\mathrm{NA}}{A} \left\{ Z^2 \left[L_{\mathrm{rad}} - f(Z) \right] + Z \, L'_{\mathrm{rad}} \right\}, \tag{C.2}$$

where $4\alpha \mathrm{r}_e^2 \mathrm{NA} = 716.408\,\mathrm{g\,cm}^{-2}$, NA is Avogadro's number, A is the atomic weight of the element, Z stands for the atomic number of the element, $L_{\mathrm{rad}} = \ln(184.15 Z^{-1/3})$, $L'_{\mathrm{rad}} = \ln(1194 Z^{-2/3})$, and the function $f(Z)$ is defined as:

$$f(Z) = a^2 \left[(1 + a^2)^{-1} + 0.20206 - 0.0369a^2 + 0.0083a^4 - 0.002a^6 \right], \tag{C.3}$$

with $a = \alpha Z$. In Ref [107], tabulated values of radiation lengths for different elements are given.

The radiation length of a compound or mixture with n elements is calculated using the weight fraction w_i of each of its components and their respective radiation length X_0^i:

$$\frac{1}{X_0} = \sum \frac{w_i}{X_0^i} \,. \tag{C.4}$$

In the following sections, we calculate the radiation length for the materials used on the proposed detectors in this thesis: Schott F2 lead-glass and LYSO.

Schott F2 Lead-Glass Radiation Length

The components of the Schott F2 lead-glass and their radiation length are shown in table C.1. The radiation length of each element was taken from the reference values given in Ref. [107].

Element	Weight Fraction w_i	Radiation Length X_0 $(\mathrm{g\,cm^{-2}})$
Pb	0.422	6.37
Si	0.214	21.84
O	0.295	34.24
K	0.042	17.32
Na	0.023	27.74
As	0.004	11.94

Table C.1.: Elements present in the Schott F2 lead-glass and their respective radiation lengths. Values of the radiation length is taken from Ref. [107].

Now, applying equation equation (C.4) for the mixture,

$$\frac{1}{X_0^{\mathrm{F2}}} = \frac{0.422}{6.37} + \frac{0.214}{21.84} + \frac{0.295}{34.24} + \frac{0.042}{17.32} + \frac{0.023}{27.74} + \frac{0.004}{11.94} = 0.088\,25\,\mathrm{cm^2\,g^{-1}}. \quad (\text{C.5})$$

Hence, the radiation length of the F2 lead-glass is $X_0^{\mathrm{F2}} = 11.33\,\mathrm{g\,cm^{-2}}$. Now, if one divides the radiation length value by the density of the material ($\rho_{\mathrm{F2}} = 3.69\,\mathrm{g\,cm^{-3}}$), the radiation length only in terms of distance is obtained: $X^{\mathrm{F2}} = X_0^{\mathrm{F2}}/\rho_{\mathrm{F2}} = 3.10\,\mathrm{cm}$.

LYSO Radiation Length

Following the same method applied previously for calculating the radiation length of the F2 lead-glass, table C.2 presents the materials composing the LYSO crystal as well as their respective masses weight and radiation lengths.

Again, by applying equation equation (C.4) for the mixture, one obtains the inverse of the radiation length,

$$\frac{1}{X_0^{\mathrm{LYSO}}} = \frac{0.7100}{6.92} + \frac{0.0456}{7.02} + \frac{0.0630}{21.84} + \frac{0.1814}{34.23} = 0.117\,223\,\mathrm{cm^2\,g^{-1}}. \quad (\text{C.6})$$

Hence, the radiation length of the LYSO crystal is $X_0^{\mathrm{LYSO}} = 8.53\,\mathrm{g\,cm^{-2}}$. The radiation length of the crystal in terms of only length is given, for a material density of $\rho_{\mathrm{LYSO}} = 7.15\,\mathrm{g\,cm^{-3}}$, as $X^{\mathrm{LYSO}} = X_0^{\mathrm{LYSO}}/\rho_{\mathrm{LYSO}} = 1.19\,\mathrm{cm}$.

Note that LYSO is denser than the F2 lead-glass, hence energy is lost through radiation and secondary particles by the incoming electron in a shorter distance

Element	Weight Fraction w_i	Radiation Length X_0 $(\mathrm{g\,cm^{-2}})$
Lu	0.7100	6.92
Y	0.0456	7.02
Si	0.0630	21.84
O	0.1814	34.24

Table C.2.: Elements in the LYSO crystal with their respective mass weights. The Values of the radiation length is taken from Ref. [107].

propagated inside the material than the F2 lead-glass. Consequently, $X^{\mathrm{LYSO}} < X^{\mathrm{F2}}$.

D. Calibration of the Gated 4Picos Cameras

The Picosecond ICCD Gated 4Picos Camera

Intensified charged-coupled devices (ICCDs) are CCDs optically connected to an image intensifier, for example, a microchannel plate (MCPs) that amplifies the photon signal before reaching the CCDs chips.

The microchannel plate is considered to be a two-dimensional array of small photo-multiplier tubes that convert an incoming photon into an amplified electrical current with gains over 10^6. MCPs are devices made of glass plates with holes with diameters of a few tens of micrometers etched into the glass plates at a pitch of also a few tens of micrometers. The holes are usually angled to the normal surface of the plate so that the electron current is amplified. The MCPs are attached to a photocathode that releases photoelectrons as a photon hits the device. The photoelectrons are accelerated in the same direction as the electric field applied into the MCP. Due to the angle of the channels, the electrons can collide with the walls of the MCP, and more electrons are released amplifying the current signal. The newly released electrons are then also accelerated in the direction of the MCP electric field. This process repeats until a shower of accelerated electrons reaches a phosphor screen that scintillates. Finally, the scintillation signal of the phosphor screen is imaged by a CCD sensor. Figure D.1 presents a sketch of the 4Picos ICCD camera where the MCP output signal (image intensifier) is coupled into a CCD sensor through a set of imaging lenses.

For the upcoming SF-QED experiments to image the scintillating LYSO screens, two ICCD 4Picos cameras (serial numbers P49139 and P49218) were calibrated. The calibration setup is shown in figure D.2. Two similar setups were mounted. The first setup was used to characterize the optical density of the filters used for the second setup mounted for the 4Picos camera characterization. The same light source, a Thorlabs 532 nm continuous-wave diode-pumped laser of nominal 0.9 mW output energy [256] is used on both setups.
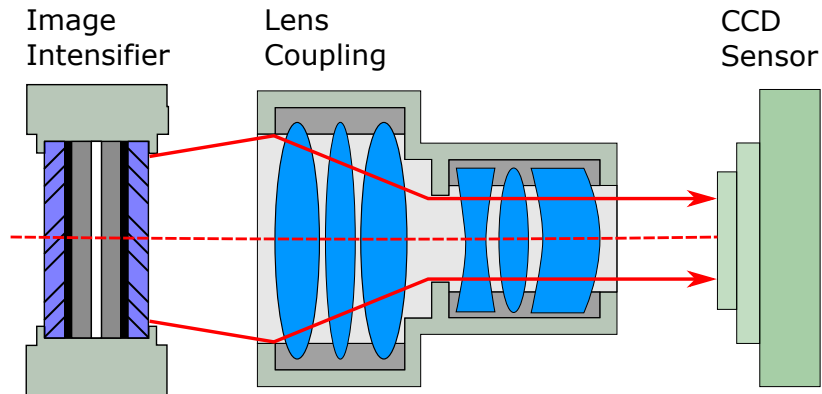
Figure D.1.: Sketch of the lens coupled intensified CCD (ICCD) 4Picos camera. The few photons signal is amplified by an image intensifier that is coupled by a set of imaging lenses that matches the image size to the CCD sensor. Image adapted from Ref. [186].
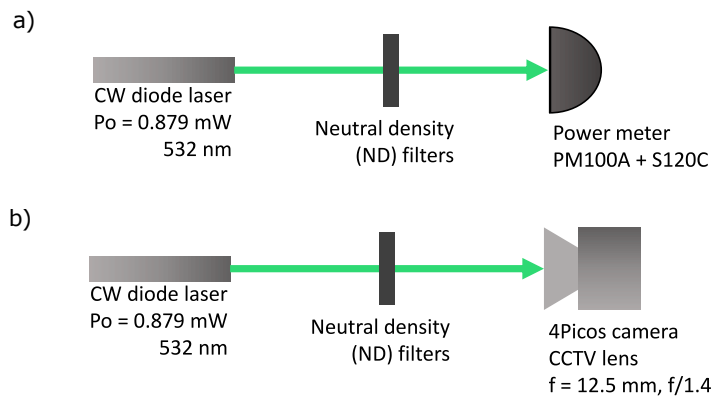
Figure D.2.: Sketch of both similar setups used during the calibration of the cameras. a) Setup for the neutral density filter characterization. It uses a power meter to record the light beam power after propagating through the filter that is later used to calculate the optical density (OD) of the filter. b) Similar setup, but the power meter is substituted by the 4Picos and the laser light imaged by the cameras.

Filter Characterization

At first, the output power of the diode laser and the optical densities (transmissions) of the filters were characterized using a Thorlabs power meter model PM100A [257] attached to a Silicon photodiode model S120C [258]. The filters used at the calibration were absorptive neutral density (ND) filters [259] and Kodak Wratten Optical Filters [260]. The setup for this characterization is similar to the 4Picos calibration setup, but the power meter is placed in the same position instead of the camera. Please see figure D.2 for details.

The measured input power P_i of the diode laser, which is measured without any attenuation, is $P_i = 0.879\,\mathrm{mW}$. Then filters are added to the light path, and the output power P_o is measured. Knowing the input and output powers for each set of filter, the optical density OD of each filter can be calculated as

$$OD = -\log_{10}\left(\frac{P_o}{P_i}\right).$$

(D.1)

Table D.1 presents the measured output power and calculated optical density for each filter used on the camera calibration. Note that the filters present a calculated optical density with less than 6% difference from the manufacturer's nominal value.

Nominal OD	Output Power P_o	Calculated OD
3.0 (1)	$0.560\,\mu\mathrm{W}$	3.20
3.0 (2)	$0.578\,\mu\mathrm{W}$	3.18
2.0	$6.52\,\mu\mathrm{W}$	2.13
1.0	$94.0\,\mu\mathrm{W}$	0.97
0.5	$0.274\,\mathrm{mW}$	0.51
0.2 (Wratten)	$0.568\,\mathrm{mW}$	0.19
0.3 (Wratten)	$0.448\,\mathrm{mW}$	0.29
0.4 (Wratten)	$0.358\,\mathrm{mW}$	0.39
0.8 (Wratten)	$0.146\,\mathrm{mW}$	0.78
1.0 (Wratten)	$86.7\,\mu\mathrm{W}$	1.00

Table D.1.: Measurement values of the neutral density filters used at the calibration of the cameras. The difference between the calculated and the nominal optical densities provided by the manufacturer is less than 6%.

Camera Calibration

In the camera calibration, as seen in figure D.2 b), the laser light is imaged by the 4Picos camera attached to a CCTV lens with a focal length of 12.5 mm and f/1.4. In the path between the light source and the camera, different neutral density filters were placed to avoid saturation of the camera CCD while capturing the light at different exposure times of the CCD sensor.

The calibration procedure of the cameras was the following:

(i) Set a MCP gain for the camera and remove the CCD sensor gain.

(ii) Select a combination of ND filter and exposure time of the CCD such that a signal without saturation on the CCD pixels is ontained.

(iii) Capture a total of 100 images for this set of MCP gain, ND filter and exposure time.

(iv) Calculate the number of photons N_p that the CCD sensor captured by applying the following simple formula

$$N_p = \frac{P_i \cdot 10^{-OD} \cdot \Delta t}{E_p} \ ,$$

where P_i is the laser output measured at the calibration of the ND filters, OD is the optical density of the combination of the filters used at this calibration configuration, Δt represents the CCD exposure time and, finally, $E_p = hc/\lambda = 3.73 \times 10^{-19}$ J is the energy of a single photon of wavelength of 532 nm.

(v) For each of the 100 images captured for this calibration configuration, select a region of interest (ROI) around the laser spot imaged and subtract the background noise. The background noise is calculated and the average CCD count number of a region of the same image that does not contain any photon hit. Note that sometimes after the subtraction, some pixels could have a negative count number that should be equated to zero.

(vi) Integrate all the counts within the region of interest of each image and divide it by the number of the photons N_p calculated above and the quantum efficiency of the used camera for the 532 nm wavelength.

(vii) Calculate the averaged and standard deviation of the calibration value counts/N_p of the 100 captured traces for this calibration configuration.

The procedure above was performed for different MCP gains of both 4Picos cameras and the calibration curves in figure D.3 is obtained. An exponential curve is fitted on the data points obtained for each camera and a mean fractional deviation for all data points from the best curve fit is less than 0.15 for both curves.
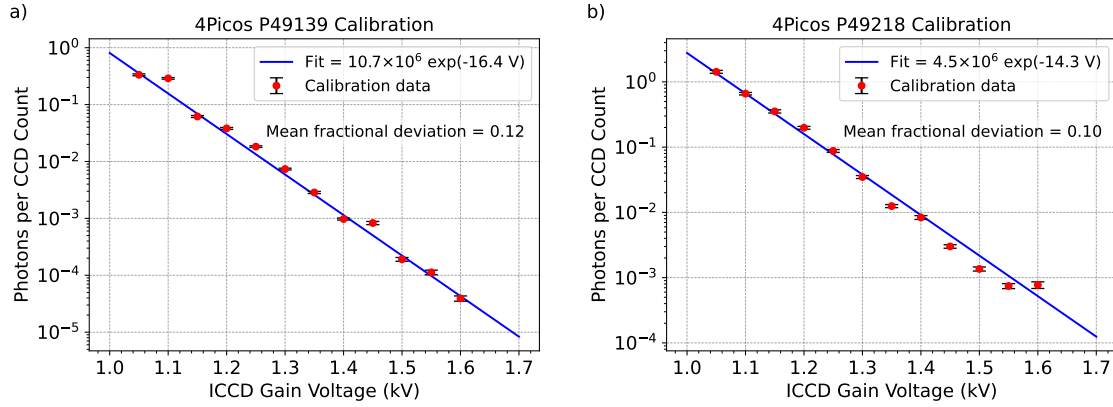

Figure D.3.: Calibration curves obtained for both 4Picos cameras (serial numbers P49139 and P49218) planned to be used on the upcoming SF-QED experiment. Exponential curves are fitted on the calibration data points, and a mean fractional deviation for all data points from the best curve fit is less than 0.15 for both curves.

E. Timing Overlap Between Laser Pulses

In this appendix, the method for interferometric spatial and timing overlaps between beams is introduced. The measurements presented here were performed during the emittance campaign at the JETi-200 laser system in the Helmholtz Institute Jena in which the author participated. However, the same measurement technique is planned to be used at the FOR2783 experiment at CALA for spatially and temporally overlapping both LWFA driver and collider beams.

Setup

The experimental setup used to perform the spatial and temporal overlap is shown in figure E.1. The JETi laser beam is split into two beams by a mirror with a hole in its center. The center of the JETi laser beam, namely the main beam, propagates through the hole of 40 mm diameter of the first mirror towards a delay stage for later to be focused by an off-axis parabola (main OAP) with a focal length of 1 meter. The portion of the JETi laser beam which is reflected by the mirror with the hole, namely the pick-off beam, has a ring shape with an inner diameter of 40 mm and outer diameter of 125 mm which propagates through a mask (pick-off mask) that selects only two spots from this ring-shaped beam each with about 15 mm. Now, both pick-off spots are focused by a second OAP (pick-off OAP) with a focal length of 40 cm. All focused laser beams are imaged on a camera by a microscope objective of $10\times$ magnification.

A delay stage is placed on the path of the main laser beam to match the propagation distance of the pick-off beams. The stage has a minimum step size of $1\,\mu m$ which corresponds to a light double pass of about $6.6\,fs$.

In the following, two methods to determine the temporal overlap of the beams are introduced. The first method uses a photodiode to determine the delay difference between the beams and the rough position of the delay linear stage where the overlap occurs. Then, an interferometric measurement is introduced, and a fine temporal overlap is achieved by observing the interference fringes which appear when matching the time-of-arrival of the beams.
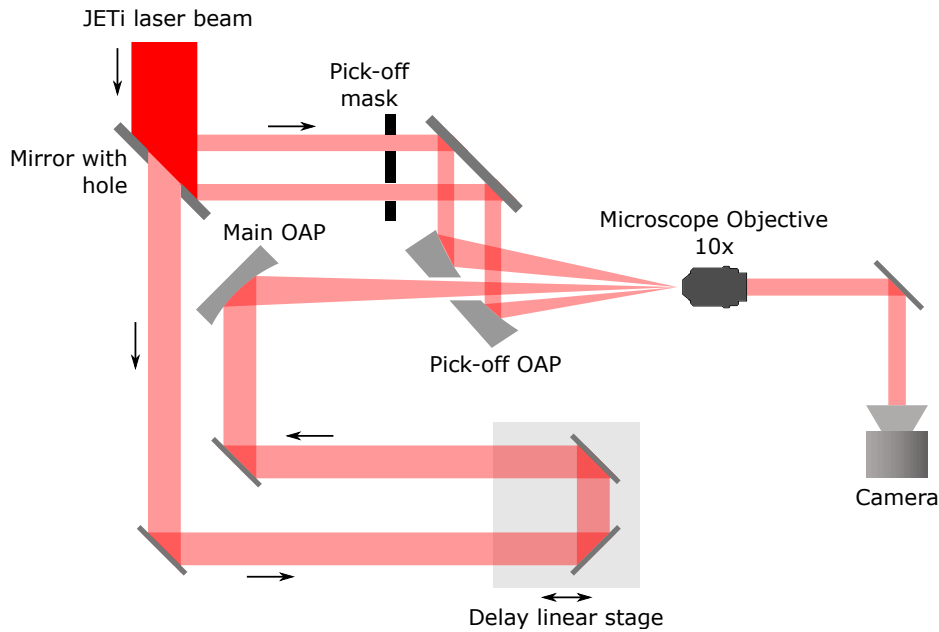
Figure E.1.: Experimental setup implemented at the emittance campaign at the JETi laser system at Helmholtz Institute Jena. The setup allows measuring the spatial and temporal overlap of three laser beams derived from the JETi laser. The laser is first split into two beams by a mirror with a hole in its center. The central part of the beam, namely the main beam, has a diameter of 40 mm and propagates through a delay stage before it is focused by an OAP (main OAP) of focal length of 1 meter. The part which is reflected by the mirror has a ring shape and propagates through a mask that selects only two round spots of about 15 mm diameter. The two selected spots, namely pick-off beams, form the pick-off beam which is later focused by an off-axis parabolic mirror of 40 cm focal length. Both beams are focused approximately at the same spot and a microscope objective (MO) with $10\times$ magnification images the beams into a camera to look at the interference fringes when the beams are spatially and temporally overlapped. To determine the rough delay between the main and pick-off beams, the MO is substituted by a photodiode, and the arrival times of the beams are correlated with the stage position.

Photodiode Timing Measurement

At first, a photodiode was placed at the focal spot (at the same position of the microscope objective in figure E.1) of the beams, and the time-of-arrival of each beam was recorded by an oscilloscope at different positions of the delay stage. The photodiode technique allows to roughly evaluate the delay between the beams and determine around which position of the delay stage the correct timing overlap is located. Note that the pick-off beams have the same delay hence are already temporally overlapped.

In this measurement, a Thorlabs DET10A/M silicon photodiode was connected to Tektronix TDS 3034C oscilloscope triggered by the laser system itself to record the time-of-arrival of the beams. The photodiode cannot resolve sub-nanosecond signals, hence, the delay between the signals was calculated by using the time difference of the peaks of the main and pick-off beams. Figure E.2 shows the delay difference for different delay stage positions. A linear relation between the delay and the stage position is observed such that a linear equation of the type $\Delta t = -6.4863 \times 10^{-3} \cdot x + 1.7603 \times 10^{-2}$ is fitted into the data points, where Δt is the delay difference between the beams and x is the linear delay stage position. From the linear fit, the temporal overlap of the beam occur at x = 2.714 mm which corresponds to a delay difference of $\Delta t = 0$.
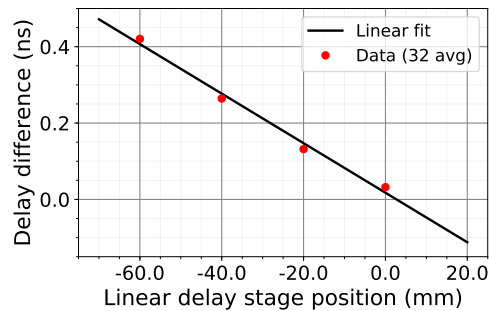
Figure E.2.: Delay difference between the main and pick-off beam time-of-arrival (TOA) for different delay stage positions. A linear fit on the points and the best fitted curve $\Delta t = -6.4863 \times 10^{-3} \cdot x + 1.7603 \times 10^{-2}$ is plotted. For the photodiode measurement, the delay difference which the temporal overlap of the main and pick-off beams is observed, i.e. $\Delta t = 0$, is at the stage position x = 2.714 mm.

Interferometric Timing Measurement

From the photodiode measurement, the temporal overlap occur at a delay linear stage position of about x = 2.714 mm. Now, the photodiode is substituted by the microscope objective of 10× magnification and a camera to image the beams. If the propagation distances are matched, all beams will have the same time-of-arrival (TOA) at the common focal spot position and fringes from the interference between the beams will occur. This interferometric method allows achieving a timing overlap with a precision of < 30 fs for the minimum step of 1 μm from the delay stage.

We drive again the delay stage in steps of 1 μm on a range close to the position x = 2.714 mm in search for images with interference fringes between the three laser beams. Figure E.3 shows the main (larger beam spot) and pick-off beams (two small bright spots) spatially overlapping and the interference fringes when the beams are also temporally overlapped. In figure E.3 a) the delay stage position is set to 3.279 mm and no temporal overlap between the main and pick-off beams was observed, only the interference between the two pick-off beams is seen. As we move the delay stage to earlier times, i.e. a delay stage position of 3.259 mm, all three beams interfere as seen in figure E.3 b). The temporal overlap occur at a linear delay stage position of x = 3.259 mm which is about 0.680 μm far from the delay position estimated by the photodiode measurement. The difference arises from the poor resolution of the diode in resolving sub-nanosecond light pulses and its slow rise time also on the order of few-ns. To confirm the interference of all three beams, the main beam was blocked and the interference fringes only between the pick-offs are observed in figure E.3 c). The delay stage position range in which the interference of all three beams is seen is about $6\,\mu$ which corresponds to a double light pass of about 40 ns matching approximately the laser pulse width.
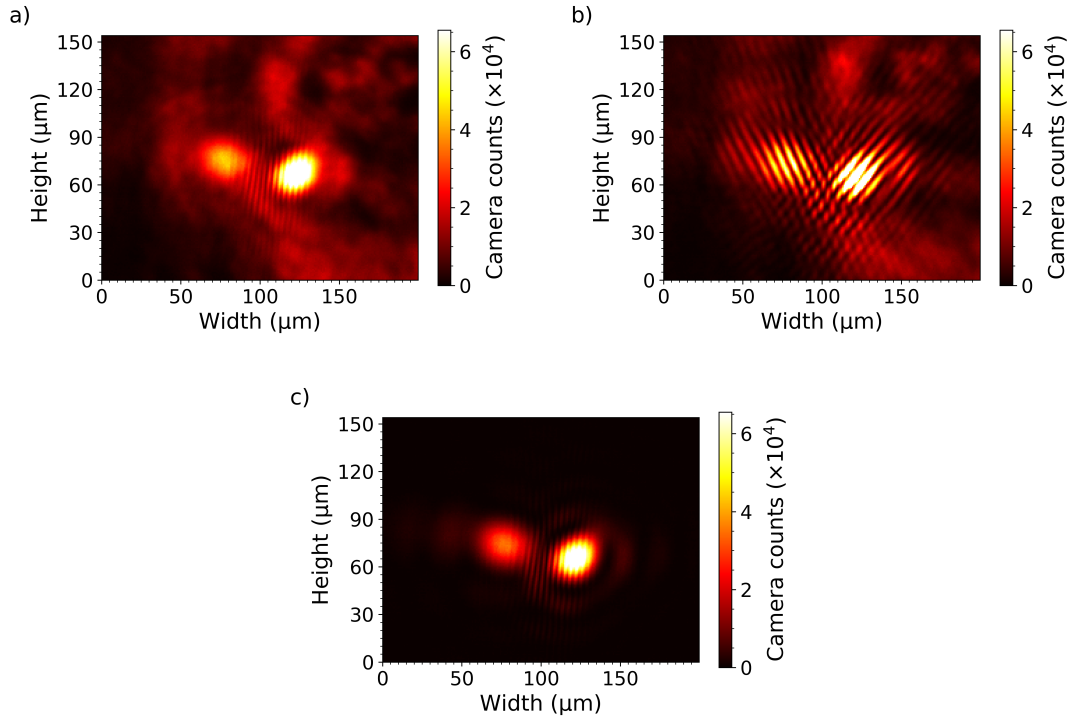
Figure E.3.: Spatial and temporal overlap between the main and pick-off beams using interferometry. The main beam is shown as the large spot in a) and b), and the pick-off beams are the two smaller spots that appear on all images. In a), the delay stage is positioned at x = 3.279 mm and no interference fringes between the pick-off and main beams is seen. As the delay stage goes to earlier times, i.e. at x = 3.259 mm, interference fringes between the beams are visible as shown in b). Finally, to confirm that the fringes appear due to the temporal overlap between the three beams, c) shows the condition when the main beam is blocked and only the fringes between the pick-offs are observed. Hence, temporal overlap is achieved at a delay stage position of x = 3.259 mm.

F. Calibration of Scintillation Screens

During the ELBE beam time, the absolute charge of different scintillation screens were characterized using a mononenergetic 27 MeV electron beam with 5.6 pC charge. The calibration of the screens follows the same method described by Refs. [123, 124, 261] where the absolute scintillation light efficiency Y^{eff} is calculated as,

$$Y^{\text{eff}} = \frac{N_{\text{p}} \cos(\phi)}{T \, \Omega \, Q_e} \, . \tag{F.1}$$

where N_{p} stands for the total number of photons within a selected region of interest (ROI) of the screens; ϕ is the angle between the incident electron beam and the normal vector of the surface of the arrays; $Q_e = 5.6\,\text{pC}$ is the charge of the incident electron beam given by diagnostics of the accelerator, Ω represents the effective collection solid angle, and, finally, T represents the transmission loss through the imaging system.

The total number of photons N_{p} is obtained from the defined region of interest of the images taken of the scintillation light emitted by the screens after being irradiated by an electron bunch. The count value of each pixel of the ROI is converted into number of photons using the using the photon transfer curve calibration of the camera given by the manufacturer. The photon transfer curve of the Hamamatsu ORCA Flash4 camera used on the experiment is give as,

$$N_{\text{p}} = \frac{\text{CF} \, (N_{\text{counts}} - 100)}{\text{QE}} \, . \tag{F.2}$$

On the photon transfer curve of the camera given in equation (F.2), the value of the conversion factor $\text{CF} = 0.48$ photons/electron is given by the calibration of the manufacturer, as well as the the quantum efficiency QE at the peak wavelength of the scintillation light. For the LYSO screens, the quantum efficiency is equal to $\text{QE} = 0.41$ which corresponds to the peak of the scintillation spectrum at $410\,\text{nm}$, and, for the CsI:Tl array, the quantum efficiency increases to $\text{QE} = 0.81$ for the maximum emission peak of the crystal at about 550 nm.

The exposure time of the camera was set to $1\,\text{ms}$ in all calibration measurements which is low enough so that the influence of the dark current electrons from the accelerator can be neglected during the experiments. For the weighted average dark current of the accelerator of (0.156 ± 0.005) electrons/RF cycle (the cycle frequency of the accelerator is 260 MHz) [103] during the $1\,\text{ms}$ of exposure time, a total of 4.1×10^4

of dark electrons are irradiated in the screen which corresponds to only 0.12% of the primary electron bunch charge of 5.6 pC proving the negligible influence of the dark current. In addition, the exposure time on the order of milliseconds allows to capture all the scintillation light from the crystals by the imaging system since it is much larger than their decay times.

Lanex Screen Cross-Calibration

The lanex BioMax MS was the first screen calibrated at the ELBE radiation source to assure that the result of calibration method employed agrees with values already reported in the literature. The experimental setup for the lanex screen assembled at the ELBE radiation source is shown in Figure F.1. The screen was placed in an angle $\phi = 45°$ with respect to the incoming electron beam with a distance of 535 mm from the macro objective lens. For this setup, the collection solid angle for the lens with f/1.4 and 28 mm focal length is $\Omega = (2\pi \cdot 20^2)/(535^2) \approx 4.390 \times 10^{-3}$ sr, where 20 mm is the radius of the macro lens. The transmission loss of the optical system is given by the sum of the Nikon lens transmittance of 19.35% which was measured prior to the experiment and the intensity loss given by Lambert's cosine law, which reduces the peak intensity by a factor of $\cos(45°)$. Hence, the total transmission photon transmission is $T = \cos(45°) \cdot 0.1935 \approx 0.14$.
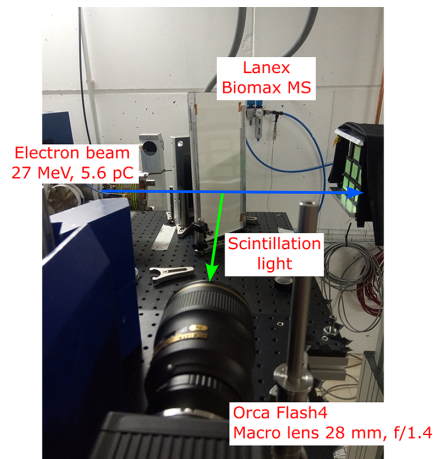
Figure F.1.: Experimental setup for the Lanex BioMax MS screen calibration installed at the ELBE radiation source. The Orca camera is imaging the screen in a 45° angle which corresponds to an intensity loss of $\cos(45°)$ as given by the Lambert's cosine law and photon collection angle of $\Omega \approx 4.390 \times 10^{-3}$ sr.

A total of 100 images were captured and post-processed to evaluate the absolute scintillation light yield. An example of a captured image (shot #20) is shown in

figure F.2. At each captured image, a region of interest was selected around the area irradiated by the primary electron beam and the count value of each pixel within this region was converted into number of photons using the camera transfer curve given in equation (F.2). Then, the number of photons of each image was integrated and the total number of emitted photon by the screen N_p was obtained. Finally, equation (F.1) is used with the setup parameters T, Ω and Q_e to estimate the absolute scintillation photon efficiency at each of the captured images. The absolute scintillation light efficiency of all data set was averaged that the average effieciency of the lanex screen is $Y_{lanex}^{eff} = 7.47 \times 10^9$ photons/sr/pC with an uncertainty given by the standard deviation of 0.43×10^9 photons/sr/pC. Note that the calculated absolute light efficiency Y_{lanex}^{eff} is only about 2% lower than the values reported in the literature [124, 261] therefore proving that the post-processing method used in the calibration experiment of the lanex screen can be extended to the other scintillation screens.
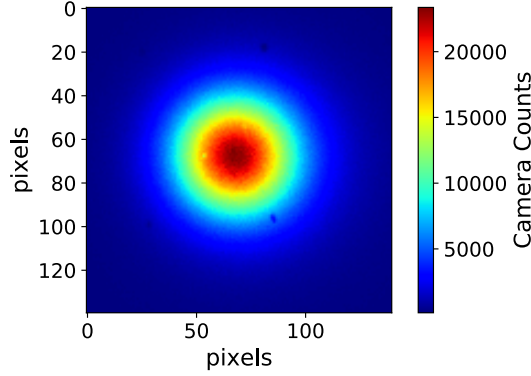
Figure F.2.: An example of a captured image (shot #20) of the Lanex BioMax MS screen irradiated by a 27 MeV electron bunch with charge of 5.6 pC. The count number of each pixel is converted into number of photons using the photon transfer curve of the camera for later the absolute scintillation light efficiency be evaluated.

Crystal Screens Calibration

Now, we employ the same calibration method described above for the lanex BioMax screen to the remain two scintillation screen arrays: LYSO and CsI:Tl. Both screens are pixelated with different pixel dimensions with the CsI providing a finer resolution than the LYSO screen. The pixel LYSO pixel dimensions are 2 mm (width)×2 mm (height)× 4 mm (thickness) which are larger than the pixel sizes of 1 mm (width)×1 mm (height)× 10 mm (thickness) for the CsI.

The parameters of the electron bunches provided by the ELBE accelerator also remained as previously, monoenergetic 27 MeV bunches with 5.6 pC, at the calibration of both screens. However, the collection solid angle and transmission of the imaging system differs from the lanex measurements. Both screens were placed on a distance D far from the imaging camera of about 820 mm which results in a collection angle $\Omega = (\pi \cdot 20^2)/(D^2) = 1.87 \times 10^{-3}$ sr, where the factor $(\pi \cdot 20^2)$ represents the area of the camera lens. The transmission loss T of the imaging system is also different and is given by the intensity loss given by the Lambertian cosine law for an angle of 19.05°, mirror reflectivity of 0.98 for the wavelength range of the scintillation light emitted, a transmission of 19.35% of the camera lens, and attenuation of the light signal by a neutral density filter with optical density of 1.8 placed in front of the camera to avoid signal saturation on the CCD sensor. Hence, the total transmission loss is calculated as $T = 0.98 \cdot \cos(19.05°) \cdot 19.355/100 \cdot 10^{-1.8} = 0.00285$. In addition, the angle ϕ between the irradiated electron beam and the normal surface of the screens is now set to $\phi = 0°$.

Examples of images of both scintillation screens after being irradiated with a single electron bunch of the accelerator is shown in figure F.3. A set of 500 images was collected for each calibration dataset the same post-processing method previously described for the calibration of the lanex screens was employed. The calculated absolute calibration light efficiency and its standard deviation of both scintillating screens are given in table F.1.
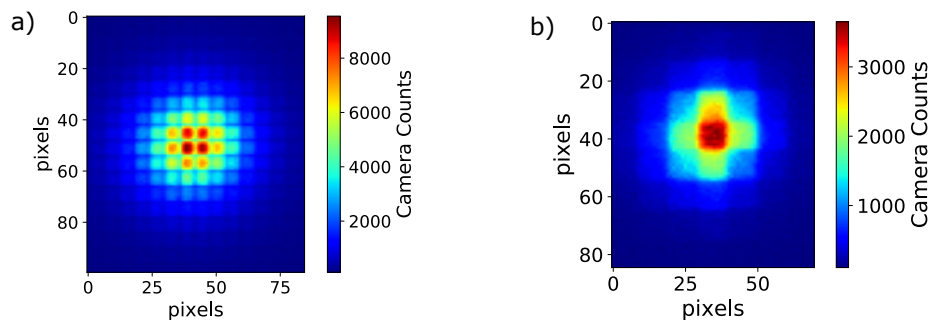
Figure F.3.: Examples of images of the scintillation screens after being irradiated with a monoenergetic bunch of 27 MeV and 5.6 pC of charge from the ELBE radiation source. a) CsI:Tl crystal with pixel size of 1 mm (width) × 1 mm (height) × 10 mm (thickness), and b) LYSO screen with pixel dimensions of 2 mm (width) × 2 mm (height) × 4 mm (thickness).

The next step is to calculate the light yield per energy deposited in each of the materials. To this end, first we calculate the number of photons produced by a single electron hit assuming a 2π collection angle of the emitted light transported to an

Screen	Absolute Light Efficiency	Uncertainty
CsI:Tl	1.17×10^{11} photons/sr/pC	0.06×10^{11} photons/sr/pC
LYSO	9.08×10^{10} photons/sr/pC	0.43×10^{10} photons/sr/pC

Table F.1.: Average absolute scintillation light efficiency calculated for a set of 500 images taken of each screen after being irradiated by a 27 MeV monoenergetic electron bunch of 5.6 pC charge. The uncertainty value is given by the standard deviation of the 500 calculated efficiencies.

imaging system attached directly at the rear of the crystal screens. This assumption assumes that detects all photons at this solid angle are collected by the sensor without loss. Thus, the number of photons emitted by a single electron is given by,

$$Y_X = 2\pi \cdot \frac{Y_X^{\text{eff}}}{E_{\text{dep, ioni}}^X} \cdot \frac{1.602 \times 10^{-19}}{10^{-12}} \; \frac{\text{photons}}{\text{MeV}} \;, \tag{F.3}$$

where Y_X is the light yield of material X = {LYSO, CsI}, Y_X^{eff} is the absolute scintillation light efficiency value from the calibration experiment and summarized in table F.1, and $E_{\text{dep, ioni}}^X$ is the energy deposited in the material by a 27 MeV electron that is transferred to secondary particles through ionization.

Monte-Carlo GEANT4 simulations were performed to estimate the energy deposited in each crystal and transferred to secondary particles through ionization. For an incident 27 MeV in a 4 mm thick LYSO screens, the average energy deposited is $E_{\text{dep, ioni}}^{\text{LYSO}} = (1.98 \pm 1.41)$ MeV. And, for the 10 mm thick CsI:Tl crystal, the simulated mean energy deposited transferred to secondaries through ionization is $E_{\text{dep, ioni}}^{\text{CsI}} = (2.25 \pm 1.50)$ MeV. The simulated results of energy deposited for the LYSO and CsI:Tl crystals that are transferred to secondaries through ionization and bremsstrahlung are plotted in figure F.4. Note that the graph in figure F.4 a) have been already presented previously in chapter 3, figure 3.12, but is reproduced again here for an easier reference of the reader.

Now, applying equation (F.3) using the absolute light efficiencies given in table F.1 and the energy deposited simulated that are shown in figure F.4, the light yield of the crystals are calculated. The LYSO crystal present a light yield of $Y_{\text{LYSO}} = (46.2 \pm 32.9)$ photons/keV deposited which is in agreement with values found in the literature [120, 121, 125–129]. And, finally, the light yield of the CsI crystal obtained from this calibration is about $Y_{\text{CsI}} = (52.3 \pm 34.9)$ photons/keV deposited which is also in agreement with values found in the literature [130–134]. The uncertainties of the
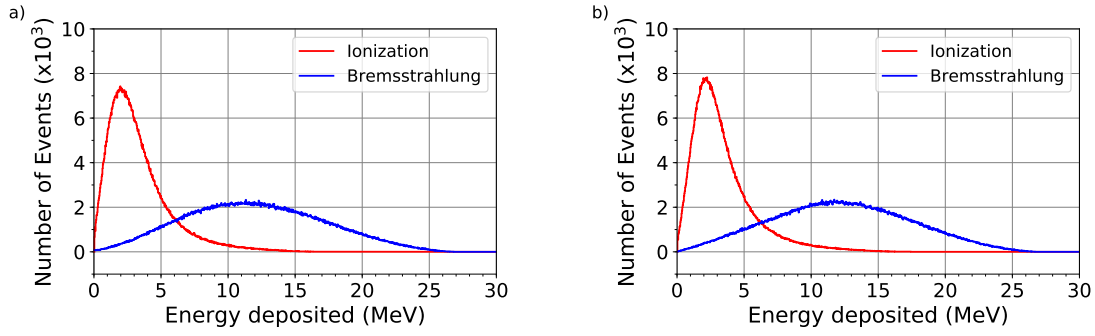
Figure F.4.: simulated results of energy deposited for the a) LYSO and b) CsI:Tl crystals that are transferred to secondaries through ionization and bremsstrahlung. The mean energy deposited for the LYSO and CsI:Tl crystal are $E_{dep, ioni}^{LYSO} = (1.98 \pm 1.41)$ MeV and $E_{dep, ioni}^{CsI} = (2.25 \pm 1.50)$ MeV, respectively. A total of 10^6 events were simulated.

light yields are calculated using the error propagation method. The uncertainties values are high due to the large uncertainty in the simulated energy deposited transferred to secondaries by ionization.

Bibliography

[1] J. Schwinger, "On Gauge Invariance and Vacuum Polarization," *Phys. Rev.*, vol. 82, no. 5, pp. 664–679, 1951.

[2] V. I. Ritus, "Quantum effects of the interaction of elementary particles with an intense electromagnetic field," *J. Russ. Laser. Res.*, vol. 6, no. 5, pp. 497–617, 1985.

[3] F. C. Salgado, K. Grafenstein, A. Golub, A. Döpp, A. Eckey, D. Hollatz, C. Müller, A. Seidel, D. Seipt, S. Karsch, and M. Zepf, "Towards pair production in the non-perturbative regime," *New J. Phys.*, vol. 23, no. 10, p. 105002, 2021.

[4] I. C. E. Turcu and et al., "High field physics and QED experiments at ELI-NP: Supplement," *Rom. Rep. Phys.*, vol. 68, p. S145, 2016.

[5] S. Gales, K. A. Tanaka, D. L. Balabanski, F. Negoita, D. Stutman, O. Tesileanu, C. A. Ur, D. Ursescu, I. Andrei, S. Ataman, M. O. Cernaianu, L. D'Alessi, I. Dancus, B. Diaconescu, N. Djourelov, D. Filipescu, P. Ghenuche, D. G. Ghita, C. Matei, K. Seto, M. Zeng, and N. V. Zamfir, "The extreme light infrastructure-nuclear physics (ELI-NP) facility: new horizons in physics with 10 PW ultra-intense lasers and 20 MeV brilliant gamma beams," *Rep. Prog. Phys.*, vol. 81, no. 9, p. 094301, 2018.

[6] D. N. Papadopoulos, J. P. Zou, C. Le Blanc, G. Chériaux, P. Georges, F. Druon, G. Mennerat, P. Ramirez, L. Martin, A. Fréneaux, A. Beluze, N. Lebas, P. Monot, F. Mathieu, and P. Audebert, "The Apollon 10 PW laser: experimental and theoretical investigation of the temporal characteristics," *High Pow Laser Sci Eng*, vol. 4, 2016.

[7] J. W. Yoon, Y. G. Kim, I. W. Choi, J. H. Sung, H. W. Lee, S. K. Lee, and C. H. Nam, "Realization of laser intensity over 10ˆ23 W/cmˆ2," *Optica*, vol. 8, no. 5, p. 630, 2021.

[8] S. S. Bulanov, M. Chen, C. B. Schroeder, E. Esarey, W. P. Leemans, S. V. Bulanov, T. Z. Esirkepov, M. Kando, J. K. Koga, A. G. Zhidkov, P. Chen, V. D. Mur, N. B. Narozhny, V. S. Popov, A. G. R. Thomas, and G. Korn, "On the design of experiments to study extreme field limits," *AIP Conf. Proc.*, vol. 1507, pp. 825–830, 2012.

[9] S. S. Bulanov, C. B. Schroeder, E. Esarey, and W. P. Leemans, "Electromagnetic cascade in high-energy electron, positron, and photon interactions with intense laser pulses," *Phys. Rev. A*, vol. 87, no. 6, 2013.

[10] R. Svensson, "Electron-Positron Pair Equilibria in Relativistic Plasmas," *Astrophys. J.*, vol. 258, p. 335, 1982.

[11] P. Laurent and L. Titarchuk, "Electron–Positron Pair Creation Close to a Black Hole Horizon: Redshifted Annihilation Line in the Emergent X-Ray Spectra of a Black Hole. I," *ApJ*, vol. 859, no. 2, p. 89, 2018.

[12] S. W. Hawking and S. F. Ross, "Pair production of black holes on cosmic strings," *Phys. Rev. Lett.*, vol. 75, no. 19, pp. 3382–3385, 1995.

[13] J. S. Heyl and L. Hernquist, "Nonlinear QED effects in strong-field magnetohydrodynamics," *Phys. Rev. D Part. Fields*, vol. 59, no. 4, 1999.

[14] A. K. Harding and D. Lai, "Physics of strongly magnetized neutron stars," *Rep. Prog. Phys.*, vol. 69, no. 9, pp. 2631–2708, 2006.

[15] R. Turolla, S. Zane, and A. L. Watts, "Magnetars: the physics behind observations. A review," *Rep. Prog. Phys.*, vol. 78, no. 11, p. 116901, 2015.

[16] A. I. Nikishov, "Absorption of high-energy photons in the universe," *Sov. Phys. JETP*, vol. 14, no. 8, p. 393, 1962.

[17] E. Schrödinger, "Quantisierung als Eigenwertproblem," *Ann. Phys.*, vol. 385, no. 13, pp. 437–490, 1926.

[18] P. A. Dirac, "The quantum theory of the electron," *Proc. R. Soc. Lond. A Math. Phys. Sci.*, vol. 117, no. 778, pp. 610–624, 1928.

[19] C. D. Anderson, "The apparent existence of easily deflectable positives," *Science*, vol. 76, no. 1967, pp. 238–239, 1932.

[20] C. D. Anderson, "The Positive Electron," *Phys. Rev.*, vol. 43, no. 6, pp. 491–494, 1933.

[21] W. H. Furry and J. R. Oppenheimer, "On the Theory of the Electron and Positive," *Phys. Rev.*, vol. 45, no. 4, pp. 245–262, 1934.

[22] W. H. Furry and J. R. Oppenheimer, "On the Limitations of the Theory of the Positron," *Phys. Rev.*, vol. 45, no. 12, pp. 903–904, 1934.

[23] G. Breit and J. A. Wheeler, "Collision of Two Light Quanta," *Phys. Rev.*, vol. 46, no. 12, pp. 1087–1091, 1934.

[24] C. H. Keitel, A. Di Piazza, G. G. Paulus, T. Stoehlker, E. L. Clark, S. Mangles, Z. Najmudin, K. Krushelnick, J. Schreiber, M. Borghesi, B. Dromey, M. Geissler, D. Riley, G. Sarri, and M. Zepf, "Photo-induced pair production and strong field QED on Gemini." (arXiv:2103.06059v1).

[25] B. Kettle, D. Hollatz, E. Gerstmayr, G. Samarin, and et al., "A laser–plasma platform for photon–photon physics: the two photon Breit–Wheeler process," *New J. Phys.*, vol. 23, no. 11, p. 115006, 2021.

[26] J. R. Oppenheimer, "Note on the Theory of the Interaction of Field and Matter," *Phys. Rev.*, vol. 35, no. 5, pp. 461–477, 1930.

[27] S. M. Dancoff, "On Radiative Corrections for Electron Scattering," *Phys. Rev.*, vol. 55, no. 10, pp. 959–963, 1939.

[28] J. A. Wheeler, "On the Mathematical Description of Light Nuclei by the Method of Resonating Group Structure," *Phys. Rev.*, vol. 52, no. 11, pp. 1107–1122, 1937.

[29] W. Heisenberg, "Über die in der Theorie der Elementarteilchen auftretende universelle Länge," *Ann. Phys.*, vol. 424, no. 1-2, pp. 20–33, 1938.

[30] P. A. M. Dirac, "Bakerian Lecture - The physical interpretation of quantum mechanics," *Proc. R. Soc. Lond. A*, vol. 180, no. 980, pp. 1–40, 1942.

[31] J. A. Wheeler and R. P. Feynman, "Interaction with the Absorber as the Mechanism of Radiation," *Rev. Mod. Phys.*, vol. 17, no. 2-3, pp. 157–181, 1945.

[32] V. Weisskopf, "The electrodynamics of the vacuum based on the quantum theory of the electron," *Kong. Dan. Vid. Sel. Mat. Fys. Med.*, vol. 14N6, pp. 1–39, 1936.

[33] W. E. Lamb and R. C. Retherford, "Fine Structure of the Hydrogen Atom by a Microwave Method," *Phys. Rev.*, vol. 72, no. 3, pp. 241–243, 1947.

[34] H. A. Bethe, "The Electromagnetic Shift of Energy Levels," *Phys. Rev.*, vol. 72, no. 4, pp. 339–341, 1947.

[35] S. Tomonaga, "On a Relativistically Invariant Formulation of the Quantum Theory of Wave Fields," *Prog. Theor. Phys.*, vol. 1, no. 2, pp. 27–42, 1946.

[36] J. Schwinger, "Quantum Electrodynamics. I. A Covariant Formulation," *Phys. Rev.*, vol. 74, no. 10, pp. 1439–1461, 1948.

[37] J. Schwinger, "On Quantum-Electrodynamics and the Magnetic Moment of the Electron," *Phys. Rev.*, vol. 73, no. 4, pp. 416–417, 1948.

[38] R. P. Feynman, "The Theory of Positrons," *Phys. Rev.*, vol. 76, no. 6, pp. 749–759, 1949.

[39] R. P. Feynman, "Space-Time Approach to Quantum Electrodynamics," *Phys. Rev.*, vol. 76, no. 6, pp. 769–789, 1949.

[40] R. P. Feynman, "Mathematical Formulation of the Quantum Theory of Electromagnetic Interaction," *Phys. Rev.*, vol. 80, no. 3, pp. 440–457, 1950.

[41] M. E. Peskin and D. V. Schroeder, *An introduction to quantum field theory: Student economy edition.* The advanced book program, Westview Press a member of the Perseus Books Group, student economy edition ed., 2016.

[42] W. Greiner and J. Reinhardt, *Quantum electrodynamics.* Springer, 4th ed. ed., 2009.

[43] F. J. Dyson, "The S Matrix in Quantum Electrodynamics," *Phys. Rev.*, vol. 75, no. 11, pp. 1736–1755, 1949.

[44] F. J. Dyson, "The Radiation Theories of Tomonaga, Schwinger, and Feynman," *Phys. Rev.*, vol. 75, no. 3, pp. 486–502, 1949.

[45] S. G. Karshenboim, "Precision physics of simple atoms: QED tests, nuclear structure and fundamental constants," *Phys. Rep.*, vol. 422, no. 1-2, pp. 1–63, 2005.

[46] B. Odom, D. Hanneke, B. D'Urso, and G. Gabrielse, "New measurement of the electron magnetic moment using a one-electron quantum cyclotron," *Phys. Rev. Lett.*, vol. 97, no. 3, p. 030801, 2006.

[47] G. Gabrielse, D. Hanneke, T. Kinoshita, M. Nio, and B. Odom, "New determination of the fine structure constant from the electron value and QED," *Phys. Rev. Lett.*, vol. 97, no. 3, p. 030802, 2006.

[48] W. H. Furry, "On Bound States and Scattering in Positron Theory," *Phys. Rev.*, vol. 81, no. 1, pp. 115–124, 1951.

[49] A. Hartin, "Strong field QED in lepton colliders and electron/laser interactions," *Int. J. Mod. Phys. A*, vol. 33, no. 13, p. 1830011, 2018.

[50] D. M. Wolkow, "Über eine Klasse von Lsungen der Diracschen Gleichung," *Z. Physik*, vol. 94, no. 3-4, pp. 250–260, 1935.

[51] A. I. Nikishov and V. I. Ritus, "Quantum process in the field of a plane electromagnetic wave and in a constant field I," *Sov. Phys. JETP*, vol. 19, no. 2, 1964.

[52] S. Meuren, C. H. Keitel, and A. Di Piazza, "Semiclassical picture for electron-positron photoproduction in strong laser fields," *Phys. Rev. D*, vol. 93, no. 8, 2016.

[53] V. Dinu and G. Torgrimsson, "Trident pair production in plane waves: Coherence, exchange, and spacetime inhomogeneity," *Phys. Rev. D*, vol. 97, no. 3, 2018.

[54] A. Ilderton, B. King, and D. Seipt, "Extended locally constant field approximation for nonlinear Compton scattering," *Phys. Rev. A*, vol. 99, no. 4, 2019.

[55] A. Di Piazza, M. Tamburini, S. Meuren, and C. H. Keitel, "Improved local-constant-field approximation for strong-field QED codes," *Phys. Rev. A*, vol. 99, no. 2, 2019.

[56] H. R. Reiss, "Production of Electron Pairs from a Zero-Mass State," *Phys. Rev. Lett.*, vol. 26, no. 17, pp. 1072–1075, 1971.

[57] Bula, McDonald, Prebys, Bamber, Boege, Kotseroglou, Melissinos, Meyerhofer, Ragg, Burke, Field, Horton-Smith, Odian, Spencer, Walz, Berridge, Bugg, Shmakov, and Weidemann, "Observation of nonlinear effects in Compton scattering," *Phys. Rev. Lett.*, vol. 76, no. 17, pp. 3116–3119, 1996.

[58] C. Bamber, S. J. Boege, T. Koffas, T. Kotseroglou, A. C. Melissinos, D. D. Meyerhofer, D. A. Reis, W. Ragg, C. Bula, K. T. McDonald, E. J. Prebys, D. L. Burke, R. C. Field, G. Horton-Smith, J. E. Spencer, D. Walz, S. C. Berridge, W. M. Bugg, K. Shmakov, and A. W. Weidemann, "Studies of nonlinear QED in collisions of 46.6 GeV electrons with intense laser pulses," *Phys. Rev. D Part. Fields*, vol. 60, no. 9, 1999.

[59] D. L. Burke, R. C. Field, G. Horton-Smith, J. E. Spencer, D. Walz, S. C. Berridge, W. M. Bugg, K. Shmakov, A. W. Weidemann, C. Bula, K. T. McDonald, E. J.

Prebys, C. Bamber, S. J. Boege, T. Koffas, T. Kotseroglou, A. C. Melissinos, D. D. Meyerhofer, D. A. Reis, and W. Ragg, "Positron Production in Multiphoton Light-by-Light Scattering," *Phys. Rev. Lett.*, vol. 79, no. 9, pp. 1626–1629, 1997.

[60] J. M. Cole and et al., "Experimental Evidence of Radiation Reaction in the Collision of a High-Intensity Laser Pulse with a Laser-Wakefield Accelerated Electron Beam," *Phys. Rev. X*, vol. 8, no. 1, 2018.

[61] K. Poder and et al., "Experimental Signatures of the Quantum Nature of Radiation Reaction in the Field of an Ultraintense Laser," *Phys. Rev. X*, vol. 8, no. 3, 2018.

[62] S. Meuren, "Probing Strong-field QED at FACET-II (SLAC E-320)," *FACET-II Science Workshop*, 2019.

[63] H. Abramowicz and et al., "Conceptual design report for the LUXE experiment," *Eur. Phys. J. Spec. Top.*, vol. 230, no. 11, pp. 2445–2560, 2021.

[64] A. Di Piazza, T. N. Wistisen, and U. I. Uggerhøj, "Investigation of classical radiation reaction with aligned crystals," *Phys. Lett. B.*, vol. 765, pp. 1–5, 2017.

[65] T. N. Wistisen, A. Di Piazza, H. V. Knudsen, and U. I. Uggerhøj, "Experimental evidence of quantum radiation reaction in aligned crystals," *Nat. Commun.*, vol. 9, no. 1, p. 795, 2018.

[66] C. F. Nielsen, J. B. Justesen, A. H. Sørensen, U. I. Uggerhøj, and R. Holtzapple, "Radiation reaction near the classical limit in aligned crystals," *Phys. Rev. D*, vol. 102, no. 5, 2020.

[67] E. Esarey, C. B. Schroeder, and W. P. Leemans, "Physics of laser-driven plasma-based electron accelerators," *Rev. Mod. Phys.*, vol. 81, no. 3, pp. 1229–1285, 2009.

[68] G. M. Samarin, M. Zepf, and G. Sarri, "Radiation reaction studies in an all-optical set-up: experimental limitations," *J. Mod. Opt.*, vol. 65, no. 11, pp. 1362–1369, 2018.

[69] J. D. Jackson, *Classical electrodynamics*. Wiley, 3rd ed., 1998.

[70] J. D. Cockcroft and E. T. S. Walton, "Experiments with high velocity positive ions.—(I) Further developments in the method of obtaining high velocity positive

ions," *Proc. R. Soc. Lond. A Math. Phys. Sci.*, vol. 136, no. 830, pp. 619–630, 1932.

[71] J. D. Cockcroft and E. T. S. Walton, "Experiments with high velocity positive ions. II. -The disintegration of elements by high velocity protons," *Proc. R. Soc. Lond. A Math. Phys. Sci.*, vol. 137, no. 831, pp. 229–242, 1932.

[72] R. L. Geng, H. Padamsee, A. Seaman, and V. D. Shemelin, "World Record Accelerating Gradient Achieved in a Superconducting Niobium RF Cavity," in *Proceedings of the 2005 Particle Accelerator Conference*, pp. 653–655, IEEE, 2005.

[73] P. W. Higgs, "Broken Symmetries and the Masses of Gauge Bosons," *Phys. Rev. Lett.*, vol. 13, no. 16, pp. 508–509, 1964.

[74] F. Englert and R. Brout, "Broken Symmetry and the Mass of Gauge Vector Mesons," *Phys. Rev. Lett.*, vol. 13, no. 9, pp. 321–323, 1964.

[75] G. S. Guralnik, C. R. Hagen, and T. W. B. Kibble, "Global Conservation Laws and Massless Particles," *Phys. Rev. Lett.*, vol. 13, no. 20, pp. 585–587, 1964.

[76] G. Aad and et al., "Observation of a new particle in the search for the Standard Model Higgs boson with the ATLAS detector at the LHC," *Phys. Lett. B.*, vol. 716, no. 1, pp. 1–29, 2012.

[77] S. Chatrchyan and et al., "Observation of a new boson at a mass of 125 GeV with the CMS experiment at the LHC," *Phys. Lett. B.*, vol. 716, no. 1, pp. 30–61, 2012.

[78] M. Benedikt, A. Blondel, P. Janot, M. Mangano, and F. Zimmermann, "Future Circular Colliders succeeding the LHC," *Nat. Phys.*, vol. 16, no. 4, pp. 402–407, 2020.

[79] A. Abada and et al., "FCC-hh: The Hadron Collider," *Eur. Phys. J. Spec. Top.*, vol. 228, no. 4, pp. 755–1107, 2019.

[80] G. A. Loew, "The SLAC linear collider and a few ideas on future linear colliders," in *Proceedings of the 1984 Linear Accelerator Conference*, p. 6 p, 1984.

[81] J. de Blas, R. Franceschini, F. Riva, P. Roloff, U. Schnoor, M. Spannowsky, J. D. Wells, A. Wulzer, and J. Zupan, eds., *The CLIC potential for new physics*, vol. 3 of *CERN Yellow Reports: Monographs.* CERN, 2018.

[82] L. Linssen, A. Miyamoto, M. Stanitzki, and H. Weerts, eds., *Physics and detectors at CLIC: CLIC conceptual design report*, vol. 2012,3 of *CERN*. Geneva: CERN, 2012.

[83] G. Aarons and et al., eds., *Physics at the ILC*, vol. 2 of *International Linear Collider Reference Design Report*. CERN, 2007.

[84] C. Joshi, "Plasma-based accelerators: then and now," *Plasma Phys. Control. Fusion*, vol. 61, no. 10, p. 104001, 2019.

[85] T. Tajima and J. M. Dawson, "Laser Electron Accelerator," *Phys. Rev. Lett.*, vol. 43, no. 4, pp. 267–270, 1979.

[86] W. Lu, M. Tzoufras, C. Joshi, F. S. Tsung, W. B. Mori, J. Vieira, R. A. Fonseca, and L. O. Silva, "Generating multi-GeV electron bunches using single stage laser wakefield acceleration in a 3D nonlinear regime," *Phys. Rev. Spec. Top. Accel Beams*, vol. 10, no. 6, 2007.

[87] S. Kuschel, M. B. Schwab, M. Yeung, D. Hollatz, A. Seidel, W. Ziegler, A. Sävert, M. C. Kaluza, and M. Zepf, "Controlling the Self-Injection Threshold in Laser Wakefield Accelerators," *Phys. Rev. Lett.*, vol. 121, no. 15, p. 154801, 2018.

[88] P. Gibbon, *Short pulse laser interactions with matter: An introduction*. Imperial College Press, 2005.

[89] W. P. Leemans, B. Nagler, A. J. Gonsalves, C. Tóth, K. Nakamura, C. G. R. Geddes, E. Esarey, C. B. Schroeder, and S. M. Hooker, "GeV electron beams from a centimetre-scale accelerator," *Nature Phys*, vol. 2, no. 10, pp. 696–699, 2006.

[90] A. J. Gonsalves, K. Nakamura, J. Daniels, C. Benedetti, C. Pieronek, T. C. H. de Raadt, S. Steinke, J. H. Bin, S. S. Bulanov, J. van Tilborg, C. G. R. Geddes, C. B. Schroeder, C. Tóth, E. Esarey, K. Swanson, L. Fan-Chiang, G. Bagdasarov, N. Bobrova, V. Gasilov, G. Korn, P. Sasorov, and W. P. Leemans, "Petawatt Laser Guiding and Electron Beam Acceleration to 8 GeV in a Laser-Heated Capillary Discharge Waveguide," *Phys. Rev. Lett.*, vol. 122, no. 8, p. 084801, 2019.

[91] S. Kuschel, *Erzeugung dichter Elektronenpulse mit Laser-Plasma-Beschleunigern für QED Experimente in hohen Feldern*. Ph.D. thesis, Friedrich-Schiller-Universität Jena, 2018.

[92] C. G. R. Geddes, C. S. Toth, J. van Tilborg, E. Esarey, C. B. Schroeder, D. Bruhwiler, C. Nieter, J. Cary, and W. P. Leemans, "High-quality electron beams from a laser wakefield accelerator using plasma-channel guiding," *Nature*, vol. 431, no. 7008, pp. 538–541, 2004.

[93] A. Seidel, J. Osterhoff, and M. Zepf, "Characterizing ultralow emittance electron beams using structured light fields," *Phys. Rev. Accel. Beams*, vol. 24, no. 1, 2021.

[94] J. Faure, C. Rechatin, A. Norlin, A. Lifschitz, Y. Glinec, and V. Malka, "Controlled injection and acceleration of electrons in plasma wakefields by colliding laser pulses," *Nature*, vol. 444, no. 7120, pp. 737–739, 2006.

[95] G. A. Mourou, T. Tajima, and S. V. Bulanov, "Optics in the relativistic regime," *Rev. Mod. Phys.*, vol. 78, no. 2, pp. 309–371, 2006.

[96] G. Mourou, "Nobel Lecture: Extreme light physics and application," *Rev. Mod. Phys.*, vol. 91, no. 3, 2019.

[97] D. Strickland and G. Mourou, "Compression of amplified chirped optical pulses," *Opt. Commun.*, vol. 56, no. 3, pp. 219–221, 1985.

[98] M. Perry, "Multilayer Dielectric Gratings: Increasing the Power of Light," *Science and Technology Review*, vol. September, 1995.

[99] S. Backus, C. G. Durfee Iii, G. Mourou, H. C. Kapteyn, and M. M. Murnane, "0.2-TW laser system at 1kHz," *Opt. Lett.*, vol. 22, no. 16, pp. 1256–1258, 1997.

[100] F. S. Englbrecht, A. Döpp, J. Hartmann, F. H. Lindner, M. Groß, H.-F. Wirth, P. G. Thirolf, S. Karsch, J. Schreiber, K. Parodi, and G. Dedes, "Radiation protection modelling for 2.5 Petawatt-laser production of ultrashort x-ray, proton and ion bunches: Monte Carlo model of the Munich CALA facility," *J. Radiol. Prot.*, 2020.

[101] A. E. Siegman, *Lasers*. University Science Books, 1986.

[102] M. H. R. Hutchinsons, T. Ditmire, E. Springate, J. W. G. Tisch, Y. L. Shao, M. B. Mason, N. Hay, and J. P. Marangos, "High–intensity lasers: interactions with atoms, molecules and clusters," *Philos. Trans. A Math. Phys. Eng. Sci.*, vol. 356, no. 1736, pp. 297–315, 1998.

[103] F. C. Salgado, N. Cavanagh, M. Tamburini, D. W. Storey, R. Beyer, P. H. Bucksbaum, Z. Chen, A. Di Piazza, E. Gerstmayr, Harsh, E. Isele, A. R. Junghans, C. H. Keitel, S. Kuschel, C. F. Nielsen, D. A. Reis, C. Roedel, G. Sarri, A. Seidel, C. Schneider, U. I. Uggerhøj, J. Wulff, V. Yakimenko, C. Zepter, S. Meuren, and M. Zepf, "Single particle detection system for strong-field QED experiments," *New J. Phys.*, vol. 24, no. 1, p. 015002, 2022.

[104] P. A. Zyla and et al., "Review of Particle Physics: 35. Particle Detectors at Accelerators," *Prog. Theor. Exp. Phys.*, vol. 2020, no. 8, pp. 551–588, 2020.

[105] S. Jayaraman and L. H. Lanzl, *Clinical Radiotherapy Physics.* Springer eBook Collection, Springer Berlin Heidelberg and Imprint Springer, 2nd ed. 2004 ed., 2004.

[106] NIST - National Institute of Standards and Technology, "ESTAR database," 2021.

[107] Y. S. Tsai, "Pair production and bremsstrahlung of charged leptons," *Rev. Mod. Phys.*, vol. 46, no. 4, pp. 815–851, 1974.

[108] S. Agostinelli and et al., "Geant4—a simulation toolkit," *Nucl. Instrum. Methods Phys. Res. A*, vol. 506, no. 3, pp. 250–303, 2003.

[109] J. Allison and et al., "Geant4 developments and applications," *IEEE Trans. Nucl. Sci.*, vol. 53, no. 1, pp. 270–278, 2006.

[110] J. Allison and et al., "Recent developments in Geant4," *Nucl. Instrum. Methods Phys. Res. A*, vol. 835, pp. 186–225, 2016.

[111] W. R. Leo, *Techniques for nuclear and particle physics experiments: A how-to approach / William R. Leo.* Springer, 2nd rev. ed. ed., 1994.

[112] J. B. Birks, *The Theory and Practice of Scintillation Counting: International Series of Monographs in Electronics and Instrumentation.* Elsevier Science, 1964.

[113] F. Maddalena, L. Tjahjana, A. Xie, Arramel, S. Zeng, H. Wang, P. Coquet, W. Drozdowski, C. Dujardin, C. Dang, and M. Birowosuto, "Inorganic, Organic, and Perovskite Halides with Nanotechnology for High–Light Yield X- and Gamma-ray Scintillators," *Crystals (Basel)*, vol. 9, no. 2, p. 88, 2019.

[114] P. A. Zyla and et al., "Review of Particle Physics: 34. Passage of Particles Through Matter," *Prog. Theor. Exp. Phys.*, vol. 2020, no. 8, pp. 535–550, 2020.

[115] C. Kim, J.-Y. Yeom, and G. Kim, "Digital n-gamma Pulse Shape Discrimination in Organic Scintillators with a High-Speed Digitizer," *J Radiat Prot Res*, vol. 44, no. 2, pp. 53–63, 2019.

[116] C. Kim, W. Lee, A. Melis, A. Elmughrabi, K. Lee, C. Park, and J.-Y. Yeom, "A Review of Inorganic Scintillation Crystals for Extreme Environments," *Crystals (Basel)*, vol. 11, no. 6, p. 669, 2021.

[117] H. Kolanoski and N. Wermes, *Teilchendetektoren: Grundlagen und Anwendungen.* Springer Spektrum, 1. aufl. 2016 ed., 2016.

[118] J. Wulff, *Construction and Calibration of a Single Particle Cherenkov Calorimeter for Strong-field QED Experiments.* Bachelor thesis, Friedrich-Schiller-Universität Jena, Jena, 2020.

[119] S. Seifert, J. H. L. Steenbergen, H. T. van Dam, and D. R. Schaart, "Accurate measurement of the rise and decay times of fast scintillators with solid state photon counters," *J. Instrum.*, vol. 7, no. 09, pp. P09004–P09004, 2012.

[120] C. W. E. van Eijk, "Inorganic scintillators in medical imaging," *Phys. Med. Biol.*, vol. 47, no. 8, pp. R85–106, 2002.

[121] M. Cieślak, K. Gamage, and R. Glover, "Critical Review of Scintillating Crystals for Neutron Detection," *Crystals (Basel)*, vol. 9, no. 9, p. 480, 2019.

[122] Y. Glinec, J. Faure, A. Guemnie-Tafo, V. Malka, H. Monard, J. P. Larbre, V. de Waele, J. L. Marignier, and M. Mostafavi, "Absolute calibration for a broad range single shot electron spectrometer," *Rev. Sci. Instrum.*, vol. 77, no. 10, p. 103301, 2006.

[123] A. Buck, K. Zeil, A. Popp, K. Schmid, A. Jochmann, S. D. Kraft, B. Hidding, T. Kudyakov, C. M. S. Sears, L. Veisz, S. Karsch, J. Pawelke, R. Sauerbrey, T. Cowan, F. Krausz, and U. Schramm, "Absolute charge calibration of scintillating screens for relativistic electron detection," *Rev. Sci. Instrum.*, vol. 81, no. 3, p. 033301, 2010.

[124] J.-P. Schwinkendorf, S. Bohlen, J. P. Couperus Cabadağ, H. Ding, A. Irman, S. Karsch, A. Köhler, J. M. Krämer, T. Kurz, S. Kuschel, J. Osterhoff, L. F. Schaper, D. Schinkel, U. Schramm, O. Zarini, and R. D'Arcy, "Charge calibration of DRZ scintillation phosphor screens," *J. Inst.*, vol. 14, no. 09, pp. P09025–P09025, 2019.

[125] Advatech-UK, "LYSO(Ce) Scintillator Crystal." https://www.advatech-uk.co.uk/lyso_ce.html. Accessed: 08.01.2022.

[126] L. Pidol, A. Kahn-Harari, B. Viana, E. Virey, B. Ferrand, P. Dorenbos, J. de Haas, and C. van Eijk, "High efficiency of lutetium silicate scintillators, Ce-doped LPS, and LYSO crystals," *IEEE Trans. Nucl. Sci.*, vol. 51, no. 3, pp. 1084–1087, 2004.

[127] C. Wanarak, W. Chewpraditkul, and A. Phunpueok, "Light yield non-proportionality and energy resolution of Lu1.95Y0.05SiO5:Ce and Lu2SiO5:Ce scintillation crystals," *Procedia Eng.*, vol. 32, pp. 765–771, 2012.

[128] J. T. M. de Haas and P. Dorenbos, "Advances in Yield Calibration of Scintillators," *IEEE Trans. Nucl. Sci.*, vol. 55, no. 3, pp. 1086–1092, 2008.

[129] R. M. Turtos, S. Gundacker, M. Pizzichemi, A. Ghezzi, K. Pauwels, E. Auffray, P. Lecoq, and M. Paganoni, "Measurement of LYSO Intrinsic Light Yield Using Electron Excitation," *IEEE Trans. Nucl. Sci.*, vol. 63, no. 2, pp. 475–479, 2016.

[130] I. Holl, E. Lorenz, and G. Mageras, "A measurement of the light yield of common inorganic scintillators," *IEEE Trans. Nucl. Sci.*, vol. 35, no. 1, pp. 105–109, 1988.

[131] J. D. Valentine, D. K. Wehe, G. F. Knoll, and C. E. Moss, "Temperature dependence of CsI (T1) absolute scintillation yield," *IEEE Trans. Nucl. Sci.*, vol. 40, no. 4, pp. 1267–1274, 1993.

[132] M. Moszyński, M. Kapusta, M. Mayhugh, D. Wolski, and S. O. Flyckt, "Absolute light output of scintillators," *IEEE Trans. Nucl. Sci.*, vol. 44, no. 3, pp. 1052–1061, 1997.

[133] M. Moszyński, W. Czarnacki, W. Klamra, M. Szawlowski, P. Schotanus, and M. Kapusta, "Application of large area avalanche photodiodes to study scintillators at liquid nitrogen temperatures," *Nucl. Instrum. Methods Phys. Res. A*, vol. 504, no. 1-3, pp. 307–312, 2003.

[134] J. de Haas, P. Dorenbos, and C. van Eijk, "Measuring the absolute light yield of scintillators," *Nucl. Instrum. Methods Phys. Res. A*, vol. 537, no. 1-2, pp. 97–100, 2005.

[135] O. Chamberlain, E. Segrè, C. Wiegand, and T. Ypsilantis, "Observation of Antiprotons," *Phys. Rev.*, vol. 100, no. 3, pp. 947–950, 1955.

[136] J. J. Aubert, U. Becker, P. J. Biggs, J. Burger, M. Chen, G. Everhart, P. Gold-hagen, J. Leong, T. McCorriston, T. G. Rhoades, M. Rohde, S. C. C. Ting, S. L. Wu, and Y. Y. Lee, "Experimental Observation of a Heavy Particle J," *Phys. Rev. Lett.*, vol. 33, no. 23, pp. 1404–1406, 1974.

[137] F. J. García de Abajo, A. G. Pattantyus-Abraham, N. Zabala, A. Rivacoba, M. O. Wolf, and P. M. Echenique, "Cherenkov effect as a probe of photonic nanostructures," *Phys. Rev. Lett.*, vol. 91, no. 14, p. 143902, 2003.

[138] F. Liu, L. Xiao, Y. Ye, M. Wang, K. Cui, X. Feng, W. Zhang, and Y. Huang, "Integrated Cherenkov radiation emitter eliminating the electron velocity threshold," *Nature Photon*, vol. 11, no. 5, pp. 289–292, 2017.

[139] X. Lin, S. Easo, Y. Shen, H. Chen, B. Zhang, J. D. Joannopoulos, M. Soljačić, and I. Kaminer, "Controlling Cherenkov angles with resonance transition radiation," *Nature Phys*, vol. 14, no. 8, pp. 816–821, 2018.

[140] P. A. Cerenkov, "Visible Emission of Clean Liquids by Action of Gamma Radiation," *Dokl. Akad. Nauk SSSR*, vol. 2, p. 451, 1934.

[141] E. P. Cherenkova, "The discovery of the Cherenkov radiation," *Nucl. Instrum. Methods Phys. Res. A*, vol. 595, no. 1, pp. 8–11, 2008.

[142] I. E. Tamm and I. M. Frank, "Coherent Radiation of Fast Electrons in a Medium," *Dokl. Akad. Nauk SSSR*, vol. 14, p. 107, 1937.

[143] M. F. L'Annunziata, *Radioactivity*. Elsevier, 2007.

[144] J. V. Jelley, "Čerenkov radiation: Its origin, properties and applications," *Contemp. Phys.*, vol. 3, no. 1, pp. 45–57, 1961.

[145] C. Leroy and P.-G. Rancoita, *Principles of radiation interaction in matter and detection*. World Scientific, 2nd ed. ed., 2009.

[146] L. D. Landau and E. M. Lifshitz, *The classical theory of fields*, vol. 4 of *Course of Theoretical Physics*. Butterworth-Heinemann, 4th ed., 1987.

[147] O. Klein and Y. Nishina, "Über die Streuung von Strahlung durch freie Elektronen nach der neuen relativistischen Quantendynamik von Dirac," *Z. Angew. Phys.*, vol. 52, no. 11-12, pp. 853–868, 1929.

[148] C. Itzykson and J. B. Zuber, *Quantum field theory.* International series in pure and applied physics, McGraw-Hill, 1980.

[149] G. R. Blumenthal and R. J. Gould, "Bremsstrahlung, Synchrotron Radiation, and Compton Scattering of High-Energy Electrons Traversing Dilute Gases," *Rev. Mod. Phys.*, vol. 42, no. 2, pp. 237–270, 1970.

[150] M. S. Longair, *High energy astrophysics.* Cambridge University Press, 3rd ed., 2011.

[151] H. Bradt, *Astrophysics processes: The physics of astronomical phenomena / Hale Bradt.* Cambridge University Press, 2008.

[152] Esarey, Ride, and Sprangle, "Nonlinear Thomson scattering of intense laser pulses from beams and plasmas," *Phys. Rev. E*, vol. 48, no. 4, pp. 3003–3021, 1993.

[153] S. K. Ride, E. Esarey, and M. Baine, "Thomson scattering of intense lasers from electron beams at arbitrary interaction angles," *Phys. Rev. E*, vol. 52, no. 5, pp. 5425–5442, 1995.

[154] A. Jochmann, A. Irman, M. Bussmann, J. P. Couperus, T. E. Cowan, A. D. Debus, M. Kuntzsch, K. W. D. Ledingham, U. Lehnert, R. Sauerbrey, H. P. Schlenvoigt, D. Seipt, T. Stöhlker, D. B. Thorn, S. Trotsenko, A. Wagner, and U. Schramm, "High resolution energy-angle correlation measurement of hard x rays from laser-Thomson backscattering," *Phys. Rev. Lett.*, vol. 111, no. 11, p. 114803, 2013.

[155] A. Debus, S. Bock, M. Bussmann, T. E. Cowan, A. Jochmann, T. Kluge, S. D. Kraft, R. Sauerbrey, K. Zeil, and U. Schramm, "Linear and non-linear Thomson-scattering x-ray sources driven by conventionally and laser plasma accelerated electrons," in *Harnessing relativistic plasma waves as novel radiation sources from terahertz to x-rays and beyond* (D. A. Jaroszynski and A. Rousse, eds.), Proceedings of SPIE, 0277-786X, (Bellingham, Wash.), p. 735908, SPIE, 2009.

[156] C. Harvey, T. Heinzl, and A. Ilderton, "Signatures of high-intensity Compton scattering," *Phys. Rev. A*, vol. 79, no. 6, 2009.

[157] R. Ruffini, G. Vereshchagin, and S.-S. Xue, "Electron–positron pairs in physics and astrophysics: From heavy nuclei to black holes," *Phys. Rep.*, vol. 487, no. 1-4, pp. 1–140, 2010.

[158] L. D. Landau, E. M. Lifshitz, L. P. Pitaevskii, and V. B. Berestetskii, *Quantum electrodynamics*. Course of Theoretical Physics, Pergamon, 1982.

[159] R. J. Gould and G. P. Schréder, "Pair Production in Photon-Photon Collisions," *Phys. Rev.*, vol. 155, no. 5, pp. 1404–1407, 1967.

[160] F. Sauter, "Über das Verhalten eines Elektrons im homogenen elektrischen Feld nach der relativistischen Theorie Diracs," *Z. Physik*, vol. 69, no. 11-12, pp. 742–764, 1931.

[161] W. Heisenberg and H. Euler, "Folgerungen aus der Diracschen Theorie des Positrons," *Z. Physik*, vol. 98, no. 11-12, pp. 714–732, 1936.

[162] G. V. Dunne, "New strong-field QED effects at extreme light infrastructure," *Eur. Phys. J. D*, vol. 55, no. 2, pp. 327–340, 2009.

[163] W. Greiner, B. Müller, and J. Rafelski, *Quantum electrodynamics of strong fields*. Texts and monographs in physics, Springer-Verlag, 1985.

[164] D. Seipt, *Strong-Field QED Processes in Short Laser Pulses: One- and Two-Photon Compton Scattering*. Ph.D. thesis, Technischen Universität Dresden, 2012.

[165] L. V. Keldysh, "Ionization in the Field of a Strong Electromagnetic Wave," *Sov. Phys. JETP*, vol. 20, no. 5, 1965.

[166] V. S. Popov, "Tunnel and multiphoton ionization of atoms and ions in a strong laser field (Keldysh theory)," *Phys.-Usp.*, vol. 47, no. 9, pp. 855–885, 2004.

[167] A. I. Nikishov and V. I. Ritus, "Ionization of systems bound by short-range forces by the field of an electromagnetic wave," *Sov. Phys. JETP*, vol. 23, no. 1, pp. 168–177, 1966.

[168] A. M. Perelomov, V. S. Popov, and M. V. Terent'ev, "Ionization of atoms in an alternating electric field," *Sov. Phys. JETP*, vol. 23, no. 5, pp. 924–934, 1966.

[169] E. Brezin and C. Itzykson, "Pair Production in Vacuum by an Alternating Field," *Phys. Rev. D Part. Fields*, vol. 2, no. 7, pp. 1191–1199, 1970.

[170] H. R. Reiss, "Limits on tunneling theories of strong-field ionization," *Phys. Rev. Lett.*, vol. 101, no. 4, p. 043002, 2008.

[171] H. R. Reiss, "Absorption of Light by Light," *J. Math. Phys.*, vol. 3, no. 1, pp. 59–67, 1962.

[172] R. Schützhold, H. Gies, and G. Dunne, "Dynamically assisted Schwinger mechanism," *Phys. Rev. Lett.*, vol. 101, no. 13, p. 130404, 2008.

[173] G. V. Dunne, H. Gies, and R. Schützhold, "Catalysis of Schwinger vacuum pair production," *Phys. Rev. D*, vol. 80, no. 11, 2009.

[174] A. Di Piazza, E. Lötstedt, A. I. Milstein, and C. H. Keitel, "Barrier control in tunneling e+-e- photoproduction," *Phys. Rev. Lett.*, vol. 103, no. 17, p. 170403, 2009.

[175] A. Monin and M. B. Voloshin, "Semiclassical calculation of photon-stimulated Schwinger pair creation," *Phys. Rev. D*, vol. 81, no. 8, 2010.

[176] A. Monin and M. B. Voloshin, "Photon-stimulated production of electron-positron pairs in an electric field," *Phys. Rev. D*, vol. 81, no. 2, 2010.

[177] G. Torgrimsson, C. Schneider, and R. Schützhold, "Sauter-Schwinger pair creation dynamically assisted by a plane wave," *Phys. Rev. D*, vol. 97, no. 9, 2018.

[178] G. Torgrimsson, "Perturbative methods for assisted nonperturbative pair production," *Phys. Rev. D*, vol. 99, no. 9, 2019.

[179] H. Taya, "Dynamically assisted Schwinger mechanism and chirality production in parallel electromagnetic field," *Phys. Rev. Research*, vol. 2, no. 2, 2020.

[180] A. Otto, *The Dynamically Assisted Schwinger Process: Primary and Secondary Effects.* Ph.D. thesis, Technischen Universität Dresden, 2017.

[181] Hamamatsu, "Technical Note: ORCA-Flash4.0 V3 Digital CMOS camera C13440-20CU." https://www.hamamatsu.com/resources/pdf/sys/SCAS0134E_C13440-20CU_tec.pdf. Accessed: 02.01.2022.

[182] P. Allport, "Applications of silicon strip and pixel-based particle tracking detectors," *Nat. Rev. Phys.*, vol. 1, no. 9, pp. 567–576, 2019.

[183] K. Kirsebom and R. Sollie, "Radiation of F2 lead glass and consequences for the monitoring of the absolute calibration of lead glass calorimeters," *Nucl. Instrum. Methods Phys. Res. A*, vol. 245, no. 2-3, pp. 351–360, 1986.

[184] L. Bartoszek, V. Bharadwaj, M. D. Church, A. A. Hahn, and et al., "The E760 lead-glass central calorimeter: design and initial test results," *Nucl. Instrum. Methods Phys. Res. A*, vol. 301, no. 1, pp. 47–60, 1991.

[185] Et-Enterprises, "9111b series data sheet." https://et-enterprises.com/images/data_sheets/9111B.pdf. Accessed: 06.01.2022.

[186] Stanford Computer Optics, "Brochure: 4Picos Ultra High Speed ICCD Camera." https://stanfordcomputeroptics.com/download/Brochure-4Picos.pdf. Accessed: 06.01.2022.

[187] Ashland Inc., "Gafchromic Dosimetry Media, Type EBT-3." http://www.gafchromic.com/documents/EBT3_Specifications.pdf. Accessed: 10.04.2021.

[188] PicoTech, "PicoScope 6000 - high performance USB scope." https://picotech.com/oscilloscope/6000/picoscope-6000-overview. Accessed: 07.01.2022.

[189] C. I. Clarke, F. J. Decker, R. J. England, R. Erikson, C. Hast, M. J. Hogan, S. Z. Li, M. Litos, Y. Nosochkov, J. Seeman, J. C. Sheppard, U. Wienands, M. Woodley, and G. Yocky, eds., *FACET: SLAC's New User Facility*, 2012.

[190] S. Gessner, E. Adli, J. M. Allen, W. An, C. I. Clarke, C. E. Clayton, S. Corde, J. P. Delahaye, J. Frederico, S. Z. Green, C. Hast, M. J. Hogan, C. Joshi, C. A. Lindstrøm, N. Lipkowitz, M. Litos, W. Lu, K. A. Marsh, W. B. Mori, B. O'Shea, N. Vafaei-Najafabadi, D. Walz, V. Yakimenko, and G. Yocky, "Demonstration of a positron beam-driven hollow channel plasma wakefield accelerator," *Nat. Commun.*, vol. 7, p. 11785, 2016.

[191] U. Wienands, S. Gessner, M. J. Hogan, T. W. Markiewicz, T. Smith, J. Sheppard, U. I. Uggerhøj, J. L. Hansen, T. N. Wistisen, E. Bagli, L. Bandiera, G. Germogli, A. Mazzolari, V. Guidi, A. Sytov, R. L. Holtzapple, K. McArdle, S. Tucker, and B. Benson, "Channeling and radiation experiments at SLAC," *Nucl. Instrum. Methods Phys. Res. B*, vol. 402, pp. 11–15, 2017.

[192] A. Deng, O. S. Karger, T. Heinemann, A. Knetsch, P. Scherkl, G. G. Manahan, A. Beaton, D. Ullmann, G. Wittig, A. F. Habib, Y. Xi, M. D. Litos, B. D. O'Shea, S. Gessner, C. I. Clarke, S. Z. Green, C. A. Lindstrøm, E. Adli, R. Zgadzaj, M. C. Downer, G. Andonian, A. Murokh, D. L. Bruhwiler, J. R. Cary, M. J. Hogan,

V. Yakimenko, J. B. Rosenzweig, and B. Hidding, "Generation and acceleration of electron bunches from a plasma photocathode," *Nat. Phys.*, vol. 15, no. 11, pp. 1156–1160, 2019.

[193] R. Zgadzaj, T. Silva, V. K. Khudyakov, A. Sosedkin, J. Allen, S. Gessner, Z. Li, M. Litos, J. Vieira, K. V. Lotov, M. J. Hogan, V. Yakimenko, and M. C. Downer, "Dissipation of electron-beam-driven plasma wakes," *Nat. Commun.*, vol. 11, no. 1, p. 4753, 2020.

[194] D. Ullmann, P. Scherkl, A. Knetsch, T. Heinemann, A. Sutherland, A. F. Habib, O. S. Karger, A. Beaton, G. G. Manahan, A. Deng, G. Andonian, M. D. Litos, B. D. O'Shea, J. R. Cary, M. J. Hogan, V. Yakimenko, J. B. Rosenzweig, and B. Hidding, "All-optical density downramp injection in electron-driven plasma wakefield accelerators," *Phys. Rev. Research*, vol. 3, no. 4, 2021.

[195] SLAC National Accelerator Laboratory, "Technical Design Report for the FACET-II Project at SLAC National Accelerator Laboratory." 2016.

[196] V. Yakimenko, L. Alsberg, E. Bong, G. Bouchard, C. Clarke, C. Emma, S. Green, C. Hast, M. J. Hogan, J. Seabury, N. Lipkowitz, B. O'Shea, D. Storey, G. White, and G. Yocky, "FACET-II facility for advanced accelerator experimental tests," *Phys. Rev. Accel. Beams*, vol. 22, no. 10, 2019.

[197] FACET, "S20 laser schematic." https://stanford.io/3G3AdPl. Accessed: 30.12.2021.

[198] A. Ferrari, P. R. Sala, A. Fasso, and J. Ranft, "FLUKA: A Multi-Particle Transport Code."

[199] T. T. Böhlen, F. Cerutti, M. Chin, A. Fassò, A. Ferrari, P. G. Ortega, A. Mairani, P. R. Sala, G. Smirnov, and V. Vlachoudis, "The FLUKA Code: Developments and Challenges for High Energy and Medical Applications," *Nucl. Data Sheets*, vol. 120, pp. 211–214, 2014.

[200] FOR 2783, "Probing the Quantum vacuum." http://quantumvacuum.org/. Accessed: 14.01.2022.

[201] A. Pukhov and J. Meyer-ter Vehn, "Laser wake field acceleration: the highly non-linear broken-wave regime," *Appl. Phys. B: Lasers Opt.*, vol. 74, no. 4-5, pp. 355–361, 2002.

[202] D. J. Corvan, T. Dzelzainis, C. Hyland, G. Nersisyan, M. Yeung, M. Zepf, and G. Sarri, "Optical measurement of the temporal delay between two ultra-short and focussed laser pluses," *Opt. Express*, vol. 24, no. 3, pp. 3127–3136, 2016.

[203] W. P. Leemans, A. J. Gonsalves, H.-S. Mao, K. Nakamura, C. Benedetti, C. B. Schroeder, C. Tóth, J. Daniels, D. E. Mittelberger, S. S. Bulanov, J.-L. Vay, C. G. R. Geddes, and E. Esarey, "Multi-GeV electron beams from capillary-discharge-guided subpetawatt laser pulses in the self-trapping regime," *Phys. Rev. Lett.*, vol. 113, no. 24, p. 245002, 2014.

[204] J. Götzfried, A. Döpp, M. F. Gilljohann, F. M. Foerster, H. Ding, S. Schindler, G. Schilling, A. Buck, L. Veisz, and S. Karsch, "Physics of High-Charge Electron Beams in Laser-Plasma Wakefields," *Phys. Rev. X*, vol. 10, no. 4, 2020.

[205] J. P. Couperus, R. Pausch, A. Köhler, O. Zarini, J. M. Krämer, M. Garten, A. Huebl, R. Gebhardt, U. Helbig, S. Bock, K. Zeil, A. Debus, M. Bussmann, U. Schramm, and A. Irman, "Demonstration of a beam loaded nanocoulomb-class laser wakefield accelerator," *Nat. Commun.*, vol. 8, no. 1, p. 487, 2017.

[206] A. Buck, J. Wenz, J. Xu, K. Khrennikov, K. Schmid, M. Heigoldt, J. M. Mikhailova, M. Geissler, B. Shen, F. Krausz, S. Karsch, and L. Veisz, "Shock-front injector for high-quality laser-plasma acceleration," *Phys. Rev. Lett.*, vol. 110, no. 18, p. 185006, 2013.

[207] J. Faure, C. Rechatin, O. Lundh, L. Ammoura, and V. Malka, "Injection and acceleration of quasimonoenergetic relativistic electron beams using density gradients at the edges of a plasma channel," *Phys. Plasmas*, vol. 17, no. 8, p. 083107, 2010.

[208] P. Brijesh, C. Thaury, K. T. Phuoc, S. Corde, G. Lambert, V. Malka, S. P. D. Mangles, M. Bloom, and S. Kneip, "Tuning the electron energy by controlling the density perturbation position in laser plasma accelerators," *Phys. Plasmas*, vol. 19, no. 6, p. 063104, 2012.

[209] S. Fourmaux, K. Ta Phuoc, P. Lassonde, S. Corde, G. Lebrun, V. Malka, A. Rousse, and J. C. Kieffer, "Quasi-monoenergetic electron beams production in a sharp density transition," *Appl. Phys. Lett.*, vol. 101, no. 11, p. 111106, 2012.

[210] S. Meuren, D. A. Reis, R. Blandford, P. H. Bucksbaum, N. J. Fisch, F. Fiuza, E. Gerstmayr, S. Glenzer, M. J. Hogan, C. Pellegrini, M. E. Peskin, K. Qu, G. White, and V. Yakimenko, "MP3 White Paper 2021 – Research Opportunities Enabled by Co-locating Multi-Petawatt Lasers with Dense Ultra-Relativistic Electron Beams." (arXiv:2105.11607v1).

[211] E. Cartlidge, "The light fantastic," *Science (1979)*, vol. 359, no. 6374, pp. 382–385, 2018.

[212] S. Meuren, P. H. Bucksbaum, N. J. Fisch, F. Fiúza, S. Glenzer, M. J. Hogan, K. Qu, D. A. Reis, G. White, and V. Yakimenko, "On Seminal HEDP Research Opportunities Enabled by Colocating Multi-Petawatt Laser with High-Density Electron Beams." (arXiv:2002.10051v1).

[213] K. Qu, S. Meuren, and N. J. Fisch, "Signature of Collective Plasma Effects in Beam-Driven QED Cascades," *Phys. Rev. Lett.*, vol. 127, no. 9, p. 095001, 2021.

[214] A. Y. Chen, F. Cruz, and A. Spitkovsky, "Filling the Magnetospheres of Weak Pulsars," *ApJ*, vol. 889, no. 1, p. 69, 2020.

[215] A. N. Timokhin and A. K. Harding, "On the Maximum Pair Multiplicity of Pulsar Cascades," *ApJ*, vol. 871, no. 1, p. 12, 2019.

[216] R. Gueroult, Y. Shi, J.-M. Rax, and N. J. Fisch, "Determining the rotation direction in pulsars," *Nat. Commun.*, vol. 10, no. 1, p. 3232, 2019.

[217] C. P. Ridgers, T. G. Blackburn, D. Del Sorbo, L. E. Bradley, C. Slade-Lowther, C. D. Baird, S. P. D. Mangles, P. McKenna, M. Marklund, C. D. Murphy, and A. G. R. Thomas, "Signatures of quantum effects on radiation reaction in laser–electron-beam collisions," *J. Plasma Phys.*, vol. 83, no. 5, 2017.

[218] A. G. R. Thomas, C. P. Ridgers, S. S. Bulanov, B. J. Griffin, and S. P. D. Mangles, "Strong Radiation-Damping Effects in a Gamma-Ray Source Generated by the Interaction of a High-Intensity Laser with a Wakefield-Accelerated Electron Beam," *Phys. Rev. X*, vol. 2, no. 4, 2012.

[219] M. Vranic, J. L. Martins, J. Vieira, R. A. Fonseca, and L. O. Silva, "All-optical radiation reaction at 10^{21} W/cm^2," *Phys. Rev. Lett.*, vol. 113, no. 13, p. 134801, 2014.

[220] V. Dinu, C. Harvey, A. Ilderton, M. Marklund, and G. Torgrimsson, "Quantum Radiation Reaction: From Interference to Incoherence," *Phys. Rev. Lett.*, vol. 116, no. 4, p. 044801, 2016.

[221] T. G. Blackburn, A. Ilderton, C. D. Murphy, and M. Marklund, "Scaling laws for positron production in laser–electron-beam collisions," *Phys. Rev. A*, vol. 96, no. 2, 2017.

[222] W. Yan, C. Fruhling, G. Golovin, D. Haden, J. Luo, P. Zhang, B. Zhao, J. Zhang, C. Liu, M. Chen, S. Chen, S. Banerjee, and D. Umstadter, "High-order multiphoton Thomson scattering," *Nature Photon*, vol. 11, no. 8, pp. 514–520, 2017.

[223] C. D. Baird, C. D. Murphy, T. G. Blackburn, A. Ilderton, S. P. D. Mangles, M. Marklund, and C. P. Ridgers, "Realising single-shot measurements of quantum radiation reaction in high-intensity lasers," *New J. Phys.*, vol. 21, no. 5, p. 053030, 2019.

[224] T. G. Blackburn, E. Gerstmayr, S. P. D. Mangles, and M. Marklund, "Model-independent inference of laser intensity," *Phys. Rev. Accel. Beams*, vol. 23, no. 6, 2020.

[225] D. Seipt, D. Del Sorbo, C. P. Ridgers, and A. G. R. Thomas, "Theory of radiative electron polarization in strong laser fields," *Phys. Rev. A*, vol. 98, no. 2, 2018.

[226] D. Del Sorbo, D. Seipt, T. G. Blackburn, A. G. R. Thomas, C. D. Murphy, J. G. Kirk, and C. P. Ridgers, "Spin polarization of electrons by ultraintense lasers," *Phys. Rev. A*, vol. 96, no. 4, 2017.

[227] Y.-F. Li, R. Shaisultanov, K. Z. Hatsagortsyan, F. Wan, C. H. Keitel, and J.-X. Li, "Ultrarelativistic Electron-Beam Polarization in Single-Shot Interaction with an Ultraintense Laser Pulse," *Phys. Rev. Lett.*, vol. 122, no. 15, p. 154801, 2019.

[228] S. P. D. Mangles, C. D. Murphy, Z. Najmudin, A. G. R. Thomas, J. L. Collier, A. E. Dangor, E. J. Divall, P. S. Foster, J. G. Gallacher, C. J. Hooker, D. A. Jaroszynski, A. J. Langley, W. B. Mori, P. A. Norreys, F. S. Tsung, R. Viskup, B. R. Walton, and K. Krushelnick, "Monoenergetic beams of relativistic electrons from intense laser-plasma interactions," *Nature*, vol. 431, no. 7008, pp. 535–538, 2004.

[229] J. Faure, Y. Glinec, A. Pukhov, S. Kiselev, S. Gordienko, E. Lefebvre, J.-P. Rousseau, F. Burgy, and V. Malka, "A laser-plasma accelerator producing monoenergetic electron beams," *Nature*, vol. 431, no. 7008, pp. 541–544, 2004.

[230] E. Guillaume, A. Döpp, C. Thaury, K. Ta Phuoc, A. Lifschitz, G. Grittani, J.-P. Goddet, A. Tafzi, S. W. Chou, L. Veisz, and V. Malka, "Electron Rephasing in a Laser-Wakefield Accelerator," *Phys. Rev. Lett.*, vol. 115, no. 15, p. 155002, 2015.

[231] R. Weingartner, S. Raith, A. Popp, S. Chou, J. Wenz, K. Khrennikov, M. Heigoldt, A. R. Maier, N. Kajumba, M. Fuchs, B. Zeitler, F. Krausz, S. Karsch, and F. Grüner, "Ultralow emittance electron beams from a laser-wakefield accelerator," *Phys. Rev. ST Accel. Beams*, vol. 15, no. 11, 2012.

[232] G. R. Plateau, C. G. R. Geddes, D. B. Thorn, M. Chen, C. Benedetti, E. Esarey, A. J. Gonsalves, N. H. Matlis, K. Nakamura, C. B. Schroeder, S. Shiraishi, T. Sokollik, J. van Tilborg, C. Toth, S. Trotsenko, T. S. Kim, M. Battaglia, T. Stöhlker, and W. P. Leemans, "Low-emittance electron bunches from a laser-plasma accelerator measured using single-shot x-ray spectroscopy," *Phys. Rev. Lett.*, vol. 109, no. 6, p. 064802, 2012.

[233] R. J. Shalloo, S. J. D. Dann, J.-N. Gruse, C. I. D. Underwood, A. F. Antoine, C. Arran, M. Backhouse, C. D. Baird, M. D. Balcazar, N. Bourgeois, J. A. Cardarelli, P. Hatfield, J. Kang, K. Krushelnick, S. P. D. Mangles, C. D. Murphy, N. Lu, J. Osterhoff, K. Põder, P. P. Rajeev, C. P. Ridgers, S. Rozario, M. P. Selwood, A. J. Shahani, D. R. Symes, A. G. R. Thomas, C. Thornton, Z. Najmudin, and M. J. V. Streeter, "Automation and control of laser wakefield accelerators using Bayesian optimization," *Nat. Commun.*, vol. 11, no. 1, p. 6355, 2020.

[234] J. Lin, Q. Qian, J. Murphy, A. Hsu, A. Hero, Y. Ma, A. G. R. Thomas, and K. Krushelnick, "Beyond optimization—supervised learning applications in relativistic laser-plasma experiments," *Phys. Plasmas*, vol. 28, no. 8, p. 083102, 2021.

[235] F. Mackenroth, A. R. Holkundkar, and H.-P. Schlenvoigt, "Ultra-intense laser pulse characterization using ponderomotive electron scattering," *New J. Phys.*, vol. 21, no. 12, p. 123028, 2019.

[236] A. Link, E. A. Chowdhury, J. T. Morrison, V. M. Ovchinnikov, D. Offermann, L. van Woerkom, R. R. Freeman, J. Pasley, E. Shipton, F. Beg, P. Rambo,

J. Schwarz, M. Geissel, A. Edens, and J. L. Porter, "Development of an in situ peak intensity measurement method for ultraintense single shot laser-plasma experiments at the Sandia Z petawatt facility," *Rev. Sci. Instrum.*, vol. 77, no. 10, p. 10E723, 2006.

[237] C. Smeenk, J. Z. Salvail, L. Arissian, P. B. Corkum, C. T. Hebeisen, and A. Staudte, "Precise in-situ measurement of laser pulse intensity using strong field ionization," *Opt. Express*, vol. 19, no. 10, pp. 9336–9344, 2011.

[238] A. L. Galkin, M. P. Kalashnikov, V. K. Klinkov, V. V. Korobkin, M. Y. Romanovsky, and O. B. Shiryaev, "Electrodynamics of electron in a superintense laser field: New principles of diagnostics of relativistic laser intensity," *Phys. Plasmas*, vol. 17, no. 5, p. 053105, 2010.

[239] M. Kalashnikov, A. Andreev, K. Ivanov, A. Galkin, V. Korobkin, M. Romanovsky, O. Shiryaev, M. Schnuerer, J. Braenzel, and V. Trofimov, "Diagnostics of peak laser intensity based on the measurement of energy of electrons emitted from laser focal region," *Laser Part. Beams*, vol. 33, no. 3, pp. 361–366, 2015.

[240] K. A. Ivanov, I. N. Tsymbalov, O. E. Vais, S. G. Bochkarev, R. V. Volkov, V. Y. Bychenkov, and A. B. Savel'ev, "Accelerated electrons for in situ peak intensity monitoring of tightly focused femtosecond laser radiation at high intensities," *Plasma Phys. Control. Fusion*, vol. 60, no. 10, p. 105011, 2018.

[241] K. Krajewska, F. Cajiao Vélez, and J. Z. Kamiński, "High-energy ionization for intense laser pulse diagnostics," *Plasma Phys. Control. Fusion*, vol. 61, no. 7, p. 074004, 2019.

[242] M. Babzien, I. Ben-Zvi, K. Kusche, I. V. Pavlishin, I. V. Pogorelsky, D. P. Siddons, V. Yakimenko, D. Cline, F. Zhou, T. Hirose, Y. Kamiya, T. Kumita, T. Omori, J. Urakawa, and K. Yokoya, "Observation of the second harmonic in Thomson scattering from relativistic electrons," *Phys. Rev. Lett.*, vol. 96, no. 5, p. 054802, 2006.

[243] O. Har-Shemesh and A. Di Piazza, "Peak intensity measurement of relativistic lasers via nonlinear Thomson scattering," *Opt. Lett.*, vol. 37, no. 8, pp. 1352–1354, 2012.

[244] G. Pariente, V. Gallet, A. Borot, O. Gobert, and F. Quéré, "Space–time characterization of ultra-intense femtosecond laser beams," *Nature Photon*, vol. 10, no. 8, pp. 547–553, 2016.

[245] W. Schumaker, G. Sarri, M. Vargas, Z. Zhao, K. Behm, V. Chvykov, B. Dromey, B. Hou, A. Maksimchuk, J. Nees, V. Yanovsky, M. Zepf, A. G. R. Thomas, and K. Krushelnick, "Measurements of high-energy radiation generation from laser-wakefield accelerated electron beams," *Phys. Plasmas*, vol. 21, no. 5, p. 056704, 2014.

[246] F. Barbosa, C. Hutton, A. Sitnikov, A. Somov, S. Somov, and I. Tolstukhin, "Pair spectrometer hodoscope for Hall D at Jefferson Lab," *Nucl. Instrum. Methods Phys. Res. A*, vol. 795, pp. 376–380, 2015.

[247] K. T. Behm, J. M. Cole, A. S. Joglekar, E. Gerstmayr, J. C. Wood, C. D. Baird, T. G. Blackburn, M. Duff, C. Harvey, A. Ilderton, S. Kuschel, S. P. D. Mangles, M. Marklund, P. McKenna, C. D. Murphy, Z. Najmudin, K. Poder, C. P. Ridgers, G. Sarri, G. M. Samarin, D. Symes, J. Warwick, M. Zepf, K. Krushelnick, and A. G. R. Thomas, "A spectrometer for ultrashort gamma-ray pulses with photon energies greater than 10 MeV," *Rev. Sci. Instrum.*, vol. 89, no. 11, p. 113303, 2018.

[248] K. Fleck, N. Cavanagh, and G. Sarri, "Conceptual Design of a High-flux Multi-GeV Gamma-ray Spectrometer," *Sci. Rep.*, vol. 10, no. 1, p. 9894, 2020.

[249] B. Naranjo, G. Andonian, N. Cavanagh, A. Di Piazza, A. Fukasawa, E. Gerstmayr, R. Holtzapple, C. Keitel, N. Majernik, S. Meuren, C. Nielsen, M. Oruganti, D. Reis, J. Rosenzweig, Y. Sakai, G. Sarri, D. Storey, O. Williams, M. Yadav, and V. Yakimenko, eds., *Pair Spectrometer for FACET-II: JACoW Publishing, Geneva, Switzerland*, 2021.

[250] A. Ilderton, "Trident pair production in strong laser pulses," *Phys. Rev. Lett.*, vol. 106, no. 2, p. 020404, 2011.

[251] B. King and H. Ruhl, "Trident pair production in a constant crossed field," *Phys. Rev. D*, vol. 88, no. 1, 2013.

[252] C. P. Ridgers, C. S. Brady, R. Duclous, J. G. Kirk, K. Bennett, T. D. Arber, A. P. L. Robinson, and A. R. Bell, "Dense electron-positron plasmas and ultrain-

tense gamma-rays from laser-irradiated solids," *Phys. Rev. Lett.*, vol. 108, no. 16, p. 165006, 2012.

[253] R. D. Blandford and R. L. Znajek, "Electromagnetic extraction of energy from Kerr black holes," *Mon. Not. R. Astron. Soc.*, vol. 179, no. 3, pp. 433–456, 1977.

[254] P. Goldreich and W. H. Julian, "Pulsar Electrodynamics," *Astrophys. J.*, vol. 157, p. 869, 1969.

[255] A. O. Barut, *Electrodynamics and classical theory of fields and particles.* Dover Publications, 1980.

[256] Thorlabs, "S120C - Standard Photodiode Power Sensor." https://www.thorlabs.de/thorproduct.cfm?partnumber=S120C. Accessed: 11.01.2022.

[257] Thorlabs, "NEK02 - Box with 12 Absorptive Ø1/2" ND Filters." https://www.thorlabs.de/thorproduct.cfm?partnumber=NEK02. Accessed: 11.01.2022.

[258] Thorlabs, "CPS532-C2 - Collimated Laser-Diode-Pumped DPSS Laser Module." https://www.thorlabs.de/thorproduct.cfm?partnumber=CPS532-C2. Accessed: 11.01.2022.

[259] Thorlabs, "PM100A - Compact Power Meter Console." https://www.thorlabs.de/thorproduct.cfm?partnumber=PM100A. Accessed: 11.01.2022.

[260] KODAK, "Wratten 2 Filters." https://www.kodak.com/en/motion/page/wratten-2-filters. Accessed: 25.07.2021.

[261] T. Kurz, J. P. Couperus, J. M. Krämer, H. Ding, S. Kuschel, A. Köhler, O. Zarini, D. Hollatz, D. Schinkel, R. D'Arcy, J.-P. Schwinkendorf, J. Osterhoff, A. Irman, U. Schramm, and S. Karsch, "Calibration and cross-laboratory implementation of scintillating screens for electron bunch charge determination," *Rev. Sci. Instrum.*, vol. 89, no. 9, p. 093303, 2018.

List of Publications

Unpublished

(i) S. Kuschel, C. Zepter, A. Seidel, **F. C. Salgado**, X. Huang, Y. Zhao, G. Schaefer, A. Saevert, M. Zepf, "Generation and focusing of orbital angular momentum laser beams from joule-class laser systems," *in preparation.*

Published

(i) **F. C. Salgado**, N. Cavanagh, M. Tamburini, D. W. Storey, R. Beyer, P. H. Bucksbaum, Z. Chen, A. Di Piazza, E. Gerstmayr, Harsh, E. Isele, A. R. Junghans, C. H. Keitel, S. Kuschel, C. F. Nielsen, D. A. Reis, C. Roedel, G. Sarri, A. Seidel, C. Schneider, U. I. Uggerhøj, J. Wulff, V. Yakimenko, C. Zepter, S. Meuren, and M. Zepf, "Single particle detection system for strong-field QED experiments," *New J. Phys.*, vol. 24, no. 1, p. 015002, 2022.

(ii) **F. C. Salgado**, K. Grafenstein, A. Golub, A. Döpp, A. Eckey, D. Hollatz, C. Müller, A. Seidel, D. Seipt, S. Karsch, and M. Zepf, "Towards pair production in the non-perturbative regime," *New J. Phys.*, vol. 23, no. 10, p. 105002, 2021.

(iii) B. Kettle, D. Hollatz, E. Gerstmayr, G. M. Samarin, A. Alejo, S. Astbury, C. Baird, S. Bohlen, M. Campbell, C. Colgan, D. Dannheim, C. Gregory, H. Harsh, P. Hatfield, J. Hinojosa, Y. Katzir, J. Morton, C. D. Murphy, A. Nurnberg, J. Osterhoff, G. Pérez-Callejo, K. Põoder, P. P. Rajeev, C. Roedel, F. Roeder, **F. C. Salgado**, G. Sarri, A. Seidel, S. Spannagel, C. Spindloe, S. Steinke, M. J. V. Streeter, A. G. R. Thomas, C. Underwood, R. Watt, M. Zepf, S. J. Rose, and S. P. D. Mangles, "A laser–plasma platform for photon–photon physics: the two photon Breit–Wheeler process," *New J. Phys.*, vol. 23, no. 11, p. 115006, 2021.

(iv) H. Abramowicz, U. Acosta, M. Altarelli, R. Aßmann, Z. Bai, T. Behnke, Y. Benhammou, T. Blackburn, S. Boogert, O. Borysov, M. Borysova, R. Brinkmann, M. Bruschi, F. Burkart, K. Büßer, N. Cavanagh, O. Davidi, W. Decking, U. Dosselli, N. Elkina, A. Fedotov, M. Firlej, T. Fiutowski, K. Fleck, M. Gostkin, C. Grojean, J. Hallford, H. Harsh, A. Hartin, B. Heinemann, T. Heinzl, L. Helary, M.

Hoffmann, S. Huang, X. Huang, M. Idzik, A. Ilderton, R. Jacobs, B. Kämpfer, B. King, H. Lahno, A. Levanon, A. Levy, I. Levy, J. List, W. Lohmann, T. Ma, A. J. Macleod, V. Malka, F. Meloni, A. Mironov, M. Morandin, J. Moron, E. Negodin, G. Perez, I. Pomerantz, R. Pöschl, R. Prasad, F. Quéré, A. Ringwald, C. Rödel, S. Rykovanov, **F. Salgado**, A. Santra, G. Sarri, A. Sävert, A. Sbrizzi, S. Schmitt, U. Schramm, S. Schuwalow, D. Seipt, L. Shaimerdenova, M. Shchedrolosiev, M. Skakunov, Y. Soreq, M. Streeter, K. Swientek, N. T. Hod, S. Tang, T. Teter, D. Thoden, A. I. Titov, O. Tolbanov, G. Torgrimsson, A. Tyazhev, M. Wing, M. Zanetti, A. Zarubin, K. Zeil, M. Zepf, and A. Zhemchukov, "Conceptual design report for the LUXE experiment," *Eur. Phys. J. Spec. Top.*, vol. 230, no. 11, pp. 2445–2560, 2021.

(v) H. Abramowicz, M. Altarelli, R. Aßmann, T. Behnke, Y. Benhammou, O. Borysov, M. Borysova, R. Brinkmann, F. Burkart, K. Büßer, O. Davidi, W. Decking, N. Elkina, H. Harsh, A. Hartin, I. Hartl, B. Heinemann, T. Heinzl, N. TalHod, M. Hoffmann, A. Ilderton, B. King, A. Levy, J. List, A. R. Maier, E. Negodin, G. Perez, I. Pomerantz, A. Ringwald, C. Rödel, M. Saimpert, **F. Salgado**, G. Sarri, I. Savoray, T. Teter, M. Wing, and M. Zepf, "Letter of Intent for the LUXE Experiment." (arXiv:1909.00860).

(vi) J. A. Cardarelli, M. J. V. Streeter, C. Colgan, D. Hollatz, A. Alejo, C. Arran, C. D. Baird, M. D. Balcazar, E. Gerstmayr, H. Harsh, B. Kettle, E. Los, C. Roedel, **F. Salgado**, G. M. Samarin, G. Sarri, A. G. R. Thomas, C. I. D. Underwood, M. Zepf, and S. P. D. Mangles, "Shock injection producing narrow energy spread, GeV electron beams from a laser wakefield accelerator," in *APS Division of Plasma Physics Meeting Abstracts*, vol. 2019 of APS Meeting Abstracts, p. BO6.006, 2019.

Danksagung

Who said that doing a Ph.D. is not fun? Maybe I got lucky in the choice of topic and workgroup. For this reason, I gratefully thank my supervisor Matt for offering me this very interesting topic of strong-field QED. I appreciate your guidance, suggestions and ideas, patience, and criticisms during the project.

I wish to thank my collaborators from the E-320 and FOR2783 projects. In special, I thank Katinka, Stefan Karsch, Elias, Sebastian, and David Reis for their input and positive criticism.

Performing all the work described in the thesis was not possible without my colleagues and friends who helped me during my Ph.D. studies to design, assemble, and calibrate the particle detectors and the experiments. With them, I also engaged in fruitful discussions about physics and had a great time together. If I forget to name someone here, my apologies for my forgetful mind.

First, thanks to Pooyan, Zhao, Neus, and Ivan for your friendship and conversations about physics since our first lecture of the master's course. A warm thank you to Carola and Christian, for our dinners and drinks, movie nights, and great adventures together. By the way, some advice for the reader, do not touch the probe table otherwise Carola can be angry at you! A shout-out to Daniel Seipt for his incredible patience and ability to explain to me complicated physics theories. I cannot forget to thank my walkie-talkie partner Daniel Ullmann for the countless time together in the lab late at night trying not to explode things around. I also thank Andreas and Dominik for sharing their enormous knowledge and experience inside the lab, and for their patience every time I had not-so-clever questions for them. Also, thanks to Harsh for sharing with me the Ph.D. journey (and office!) during these years.

Thanks to Georg, and Alex Sävert who invested their time and work to help me understand the JETI-200 laser and how not to break it.

I would like to thank my friend Eric, who even thousands of kilometers and several different time zones away, always encouraged me. Also, a thank you to Morten (and his blue decks) and Tom for all the great mtg games, drinking experience, and life-sharing on Sundays.

Finally, my enormous thank you to my family, in special my parents and brother, who, even far away, are always supportive, giving me great advice, and motivating me in every step of my life never letting me stop on the way.

Ehrenwörtliche Erklärung

Ich erkläre hiermit ehrenwörtlich, dass ich die vorliegende Arbeit selbständig, ohne unzulässige Hilfe Dritter und ohne Benutzung anderer als der angegebenen Hilfsmittel und Literatur angefertigt habe. Die aus anderen Quellen direkt oder indirekt übernommenen Daten und Konzepte sind unter Angabe der Quelle gekennzeichnet.

Weitere Personen waren an der inhaltlich-materiellen Erstellung der vorliegenden Arbeit nicht beteiligt. Insbesondere habe ich hierfür nicht die entgeltliche Hilfe von Vermittlungs- bzw. Beratungsdiensten (Promotionsberater oder andere Personen) in Anspruch genommen. Niemand hat von mir unmittelbar oder mittelbar geldwerte Leistungen für Arbeiten erhalten, die im Zusammenhang mit dem Inhalt der vorgelegten Dissertation stehen.

Die Arbeit wurde bisher weder im In- noch im Ausland in gleicher oder ähnlicher Form einer anderen Prüfungsbehörde vorgelegt.

Die geltende Promotionsordnung der Physikalisch-Astronomischen Fakultät ist mir bekannt.

Ich versichere ehrenwörtlich, dass ich nach bestem Wissen die reine Wahrheit gesagt und nichts verschwiegen habe.

Ort, Datum   Felipe Cezar Salgado